

The role of resting Ca^{2+} in astrocyte Ca^{2+} signalling.

Claire Marianne King

Dissertation submitted for the degree of

Doctor of Philosophy

of the

University College London

Department of Clinical and Experimental Epilepsy

Institute of Neurology

DECLARATION

I, Claire Marianne King, confirm that the work presented in this thesis is my own. Where information has been derived from other sources, I confirm that this has been indicated in the thesis.

February 2016

ABSTRACT

Astrocytes form gap-junction coupled networks and their fine processes cover many synapses enabling astrocytes to powerfully modulate synapse function. Such modulation is thought to involve Ca^{2+} -dependent release of signalling molecules from astrocytes. However, astrocyte Ca^{2+} signalling and its role in synaptic physiology remains a matter of debate. An incomplete and mostly qualitative understanding of the fundamental mechanisms of intracellular Ca^{2+} signalling in astrocytes could be a knowledge-limiting factor.

Previous studies predict that astrocyte resting $[\text{Ca}^{2+}]$ profoundly affects astrocyte Ca^{2+} signalling, especially IP_3 and store-dependent Ca^{2+} transients. I therefore quantitatively investigated the role of resting $[\text{Ca}^{2+}]$ in shaping spontaneous and evoked Ca^{2+} transients in astrocytes. I used two-photon excitation fluorescence microscopy and whole-cell patch clamp to document Ca^{2+} signalling of individual passive astrocytes in the CA1 *stratum radiatum* of acute hippocampal slices in young adult rat. I used fluorescence lifetime imaging to obtain a quantitative readout of astrocyte $[\text{Ca}^{2+}]$ and reveal the relationship between resting $[\text{Ca}^{2+}]$ and Ca^{2+} transients. I combined these techniques with UV-uncaging of Ca^{2+} or Ca^{2+} buffer to manipulate the astrocyte resting $[\text{Ca}^{2+}]$ to further investigate its effect on Ca^{2+} signalling.

Using these methods, we have found that low resting $[\text{Ca}^{2+}]$ were associated with smaller amplitudes of spontaneous Ca^{2+} transients. This was also true for metabotropic glutamate receptor agonist (DHPG) evoked Ca^{2+} transients when different cells or regions of interest of the same cell were compared. The well-established increase of most IP_3 receptors' open probability at higher cytosolic $[\text{Ca}^{2+}]$ could explain this observation. In contrast, changes of resting $[\text{Ca}^{2+}]$ within a single astrocyte region were associated with inverse changes in amplitude of evoked Ca^{2+} transients. The DHPG-induced equilibration of $[\text{Ca}^{2+}]$ across cytosol and store compartments could be a potential explanation for this effect. Thus, resting $[\text{Ca}^{2+}]$ could shape the amplitude of astrocyte Ca^{2+} transients by at least two distinct mechanisms.

Keywords: calcium, FLIM, astrocytes, DHPG, hippocampus

TABLE OF CONTENTS

| | |
|--|-----------|
| Chapter1: INTRODUCTION..... | 17 |
| ASTROCYTE STRUCTURAL AND PHYSIOLOGICAL PROPERTIES..... | 19 |
| A. Astrocyte heterogeneity..... | 19 |
| B. Morphology | 19 |
| i. General morphology and structural interactions of protoplasmic astrocytes in the stratum radiatum of the rodent hippocampus | 19 |
| ii. Astrocyte ultrastructural morphology shows functional plasticity | 20 |
| C. Gap junction coupling..... | 22 |
| i. Gap-junction connected astrocytes form Ca ²⁺ permeable syncytia..... | 22 |
| ii. Connexin expression also regulates astrocyte processes coverage of excitatory synapse..... | 24 |
| D. Passive electrophysiological properties..... | 24 |
| PHYSIOLOGICAL FUNCTIONS OF NEURON-GLIA INTERACTIONS..... | 26 |
| A. Homeostasis | 26 |
| i. Astrocytes and regulation of extracellular potassium..... | 26 |
| ii. Transmitter Synthesis/Removal by Astrocytes | 26 |
| iii. Additionally to a supportive role, these functions also enable astrocytes to actively shape neuronal transmission | 27 |
| B. Tripartite synapse: | 27 |
| Reciprocal, modulable communication between astrocytes and neurons | 27 |
| i. Astrocytes can integrate neuronal activity..... | 28 |
| ii. Astrocytes can in turn modulate neuronal activity through gliotransmission | 29 |
| ASTROCYTE CALCIUM SIGNALLING | 32 |
| A. Definition of “Resting” [Ca ²⁺], as used in this thesis | 32 |
| B. Intra and inter cellular calcium fluctuations are the basis of astrocyte excitability 33 | |
| i. Astrocyte calcium transients | 33 |
| ii. Calcium micro-domains: possible functional spatial segregation of astrocytic calcium oscillations | 34 |
| C. Current controversy over the physiological relevance of gliotransmission: the mechanisms underlying astrocyte calcium signalling..... | 36 |
| i. Does astrocyte Ca ²⁺ signalling really affect neuronal activity?..... | 36 |
| ii. mGluR / IP ₃ R disruption does not affect all astrocyte Ca ²⁺ signalling | 37 |
| D. Developing the tools to investigate astrocyte calcium signalling | 38 |
| i. High resolution imaging reveals the complexity of astrocyte Ca ²⁺ signalling..... | 38 |
| ii. Physiological approach..... | 38 |

| | | |
|------|---|-----------|
| E. | Resting calcium and astrocyte IP ₃ R mediated calcium signalling..... | 39 |
| i. | Inositol-triphosphate receptor (IP ₃ R) dependent Ca ²⁺ events in astrocytes | 39 |
| ii. | Inositol- tri-phosphate receptors (IP ₃ R) are gated by cytosolic calcium concentration 40 | |
| iii. | Cytoplasmic [Ca ²⁺] gating of IP ₃ R could modulate the amplitude of calcium events in astrocytes | 41 |
| | OBJECTIVES | 43 |
| | Chapter2: RECORDING ASTROCYTE CALCIUM SIGNALING WITH HIGH RESOLUTION AND SENSITIVITY | 44 |
| | ACUTE HIPPOCAMPAL SLICE PREPARATION..... | 44 |
| A. | Why the hippocampus? | 44 |
| B. | Animals used..... | 44 |
| C. | Dissection and slicing procedure..... | 45 |
| | WHOLE CELL PATCH CLAMP OF ASTROCYTES | 46 |
| A. | Rig configuration..... | 46 |
| B. | Whole cell patch clamp..... | 46 |
| C. | Confirming astrocyte identity..... | 47 |
| | CALCIUM IMAGING | 49 |
| A. | Setup configuration..... | 49 |
| B. | Calcium indicator dye selection | 50 |
| i. | Dye diffusion | 50 |
| ii. | Affinity for calcium | 50 |
| iii. | Dynamic range..... | 50 |
| | DISCUSSION | 51 |
| A. | Patch clamp loading vs ester-loading vs genetic-targeting..... | 51 |
| B. | Astrocyte preparation: slices vs culture vs in vivo | 52 |
| | Chapter3: QUANTITATIVE ESTIMATION OF CALCIUM CONCENTRATIONS..... | 53 |
| | FLUORESCENCE INTENSITY [Ca ²⁺] CALIBRATION..... | 54 |
| A. | Background correction..... | 54 |
| B. | F _{MAX} : indicator fluorescence for near dye saturation [Ca ²⁺] _{free} | 54 |
| i. | Calcium ionophore method | 54 |
| ii. | High [Ca ²⁺] calibration probe method | 56 |
| C. | F _{MIN} , calcium indicator fluorescence for zero free calcium..... | 57 |
| D. | Fluorescence intensity based estimation of [Ca ²⁺] using F _{MIN} and F _{MAX} probes | 58 |

| | |
|--|-----------|
| INDICATOR INDEPENDENT CALCIUM IMAGING..... | 59 |
| A. Fluorescence Lifetime Imaging Microscopy | 59 |
| B. FLIM acquisition..... | 59 |
| i. Configuration and principle | 59 |
| ii. Fast- FLIM | 60 |
| C. OGB-2 lifetime vs $[Ca^{2+}]$ calibration | 61 |
| i. $[Ca^{2+}]$ calibration in cuvette (sealed glass slides and coverslips)..... | 61 |
| ii. $[Ca^{2+}]$ calibration in cells..... | 65 |
| iii. Background correction..... | 65 |
| DISCUSSION | 68 |
| A. Summary..... | 68 |
| B. Other methods tested: Ratiometric Dyes | 68 |
| Chapter 4: SPONTANEOUS ASTROCYTE CALCIUM EVENTS | 69 |
| INTRODUCTION | 69 |
| A. Objective | 69 |
| B. Endogenous astrocyte spontaneous Ca^{2+} activity..... | 69 |
| METHODS | 70 |
| A. Recording protocol..... | 71 |
| B. Manual ROI selection..... | 71 |
| C. Endogenous Ca^{2+} events..... | 72 |
| i. Ca^{2+} event identification..... | 72 |
| ii. Ca^{2+} event characterisation/properties | 72 |
| iii. Testing for correlation relationships with linear fitting and Spearman test | 73 |
| RESULTS..... | 77 |
| A. Spontaneous Ca^{2+} events..... | 77 |
| B. Ca^{2+} event activity in relationship to ROI morphology..... | 78 |
| C. Ca^{2+} event characteristics relationship with ROI resting $[Ca^{2+}]$ | 79 |
| i. Resting $[Ca^{2+}]$ distribution | 79 |
| ii. Ca^{2+} event characteristics and pre-event resting $[Ca^{2+}]$ | 79 |
| DISCUSSION | 83 |
| A. Summary..... | 83 |
| B. Larger spontaneous Ca^{2+} event amplitude was associated with higher pre-event resting $[Ca^{2+}]$ | 83 |
| i. Possible mechanisms | 83 |
| ii. Possible physiological relevance (see chapter 7)..... | 87 |
| iii. Further investigation..... | 87 |

| | | |
|---|--|-----------|
| C. | Frequency of Ca ²⁺ events detected and experimental limitations..... | 88 |
| i. | Technical and analysis limitations may underestimate the frequency of astrocyte spontaneous Ca ²⁺ events | 88 |
| ii. | Frequency of Ca ²⁺ events is similar to bulk of previously reported values | 90 |
| D. | Conclusion..... | 91 |
| Chapter5: | MANIPULATING CALCIUM CONCENTRATIONS | 92 |
| INTRODUCTION | | 92 |
| A. | Objective | 92 |
| B. | UV uncaging of NPEGTA or Diazo2 | 92 |
| C. | UV LED setup | 93 |
| METHODS | | 93 |
| A. | UV uncaging setup | 93 |
| i. | UV light source | 93 |
| ii. | UV light control..... | 94 |
| - | Positioning the optical fibre..... | 94 |
| - | Setting UV pulse parameters | 94 |
| - | Reducing UV mediated autofluorescence | 94 |
| B. | Protocol..... | 96 |
| i. | Fluorescence lifetime recording of OGB-2 in Astrocytes | 96 |
| ii. | Uncaging compounds..... | 96 |
| C. | Data extraction and analysis | 97 |
| i. | Regions of Interest..... | 97 |
| - | Pixel binning | 97 |
| - | Selection of representative ROIs..... | 97 |
| ii. | Quantifying the effect of UV photolysis of caged Ca ²⁺ or Ca ²⁺ buffer | 99 |
| UNCAGING EFFECT ON ASTROCYTE [Ca ²⁺]..... | | 101 |
| A. | KMS-only cells: quantifying UV exposure photodamage and non-uncaging related changes in astrocyte resting [Ca ²⁺]..... | 101 |
| B. | Diazo2 cells: quantifying the uncaging related decrease in astrocyte resting [Ca ²⁺] 101 | |
| C. | NPEGTA cells: quantifying the uncaging related increase in astrocyte resting [Ca ²⁺] | 104 |
| DISCUSSION | | 106 |
| A. | Summary..... | 106 |

| | | |
|--|---|------------|
| B. | UV exposure adjustments..... | 106 |
| i. | Improving the coupling between UV LED and optical fibre to increase the output power at slice..... | 106 |
| ii. | UV exposure optimisation..... | 106 |
| C. | Caged compound concentrations..... | 107 |
| D. | Conclusion..... | 107 |
| Chapter 6: ASTROCYTE CALCIUM EVENTS EVOKED BY ACTIVATION OF METABOTROPIC GLUTAMATE RECEPTORS..... | | 108 |
| INTRODUCTION..... | | 108 |
| A. | Objective..... | 108 |
| B. | DHPG activation of group I mGluRs in astrocytes..... | 108 |
| METHODS..... | | 110 |
| A. | Acquisition..... | 110 |
| i. | Recording protocol..... | 110 |
| ii. | Pressure application..... | 111 |
| B. | ROI selection..... | 112 |
| C. | DHPG mediated Ca ²⁺ response and resting [Ca ²⁺] analysis..... | 112 |
| i. | Quantifying DHPG-puff Ca ²⁺ response and resting [Ca ²⁺]..... | 112 |
| ii. | DHPG pressure applications 1 and 2: before and after changing the resting [Ca ²⁺]... .. | 113 |
| iii. | Statistical analysis..... | 113 |
| RESULTS..... | | 114 |
| A. | DHPG-evoked Ca ²⁺ response and resting [Ca ²⁺]..... | 115 |
| i. | Correlations tested across all ROIs..... | 115 |
| ii. | Exclusion of non-responsive ROIs..... | 115 |
| iii. | Correlations tested across DHPG-responsive ROIs..... | 115 |
| iv. | DHPG-response across individual ROI..... | 116 |
| B. | Mean cell DHPG-evoked Ca ²⁺ response after changing the resting [Ca ²⁺]..... | 119 |
| i. | Aim..... | 119 |
| ii. | Stability of Ca ²⁺ response to repeated DHPG pressure applications (KMS-only cells) 119 | |
| iii. | Effect of Ca ²⁺ uncaging: NPEGTA/CaCl ₂ cells..... | 121 |
| iv. | Effect of Ca ²⁺ buffer uncaging: Diazo2 cells..... | 121 |

| | | |
|------|---|------------|
| C. | DHPG-evoked Ca^{2+} response after changing the resting $[\text{Ca}^{2+}]$: individual ROIs | 124 |
| | 124 | |
| i. | Aim..... | 124 |
| ii. | DHPG response peak $[\text{Ca}^{2+}]$ after changing the pre-event resting $[\text{Ca}^{2+}]$ in individual ROIs | 124 |
| iii. | DHPG response amplitude after changing the pre-event resting $[\text{Ca}^{2+}]$ in individual ROIs | 124 |
| iv. | Equilibration of Ca^{2+} stores and cytosol: possible qualitative explanation..... | 125 |
| v. | Further qualitative analysis confirms these correlations between change of response to DHPG and change of resting $[\text{Ca}^{2+}]$ in individual ROIs..... | 131 |
| D. | Ratio of endoplasmic reticulum to cytosol in an astrocyte model..... | 136 |
| | DISCUSSION | 138 |
| A. | Peak $[\text{Ca}^{2+}]$ and amplitude astrocyte Ca^{2+} response to a given DHPG-application are positively correlated to the resting $[\text{Ca}^{2+}]$ | 138 |
| B. | The change in response amplitude is negatively correlated to the change in resting $[\text{Ca}^{2+}]$ in individual ROI..... | 139 |
| | i. Individual ROIs..... | 139 |
| | ii. Possible mechanisms | 140 |
| C. | Methodology limitations..... | 141 |
| | i. DHPG pressure application caveats | 141 |
| | ii. Caged compounds are Ca^{2+} buffers | 142 |
| D. | Conclusion and remarks/perspectives | 143 |
| | Chapter 7: GENERAL DISCUSSION..... | 144 |
| | Summary..... | 144 |
| A. | Higher pre-event resting $[\text{Ca}^{2+}]$ may be associated with larger amplitudes of Ca^{2+} events..... | 144 |
| B. | Within a ROI, increasing resting $[\text{Ca}^{2+}]$ decreases the amplitude of evoked Ca^{2+} events..... | 145 |
| | Resting $[\text{Ca}^{2+}]$ variability in astrocytes..... | 146 |
| A. | Astrocyte resting $[\text{Ca}^{2+}]$ recorded in this thesis | 146 |
| | i. Resting $[\text{Ca}^{2+}]$ in whole-cell patch clamped astrocytes..... | 146 |
| | ii. Resting $[\text{Ca}^{2+}]$ in gap-junction coupled astrocytes | 146 |
| | iii. Resting $[\text{Ca}^{2+}]$ in astrocytes in vivo | 148 |
| B. | Previously reported astrocyte resting $[\text{Ca}^{2+}]$ | 148 |
| | i. Reported astrocyte resting $[\text{Ca}^{2+}]$ | 148 |
| | ii. Physiological changes in astrocyte resting $[\text{Ca}^{2+}]$ | 149 |

| | |
|--|----------------|
| Physiological relevance of the observed evoked or spontaneous astrocyte Ca^{2+} event amplitudes..... | 150 |
| A. Comparing changes in $[Ca^{2+}]$ and changes in Ca^{2+} indicator fluorescence intensity (F/F_0) | 150 |
| i. Estimation of 'Fluo-4 equivalent F/F_0 ' from OGB-2 FLIM $[Ca^{2+}]$ | 150 |
| ii. Comparison with previously reported Fluo-4 $\Delta F/F_0$ recordings of astrocyte Ca^{2+} events 151 | |
| B. Possible consequences of increased astrocyte event peak $[Ca^{2+}]$ through the example of astrocyte Ca^{2+} dependent vesicular release..... | 152 |
| i. Ca^{2+} dependent exocytosis in neurons..... | 152 |
| ii. Ca^{2+} dependent exocytosis in astrocytes | 153 |
| - astrocytes exhibit functional Ca^{2+} dependent exocytosis | 153 |
| - astrocytes, relative to neurons, may require lower $[Ca^{2+}]$ for Ca^{2+} dependent exocytosis..... | 153 |
| iii. Other astrocyte Ca^{2+} dependent impacts..... | 154 |
| C. Discrepancy in quantitative $[Ca^{2+}]$ recorded in astrocytes and neurons for Ca^{2+} dependent vesicular release. | 155 |
| i. Limitations of the estimation of $[Ca^{2+}]$ in this thesis..... | 155 |
| ii. Astrocyte $[Ca^{2+}]$ requirements for Ca^{2+} dependent release could be different..... | 157 |
| CONCLUSIONS AND PERSPECTIVES | 158 |
| REFERENCES | 178 |

ANNEX:

Bassoon-RPB interaction regulates Cav1.2 synaptic transmission recorded in acute hippocampal slice field recordings..... 160

INTRODUCTION160

- A. Objective:.....160
- B. Brief overview of the Hippocampus anatomy.....161
- C. Extracellular field recordings of CA3 to CA1 synaptic transmission.....162
- D. Ca²⁺, CavS and synaptic transmission.....162
 - i. The role of Ca²⁺ and CaVs in synaptic transmission 162
 - ii. Voltage-gated Ca²⁺ channels in the hippocampus..... 163
 - iii. Presynaptic active zone structure 164
 - iv. Bassoon is a large structural component of the presynaptic active zone which is also thought to be involved in regulating synaptic transmission..... 165

METHODS167

- A. Acute hippocampal slice preparation.....167
 - i. Animals used..... 167
 - ii. Slice preparation 167
- B. Recording protocol.....167
 - i. Experimental groups 167
 - ii. Field recordings..... 168
 - iii. fEPSP analysis..... 168

RESULTS.....170

- A. Acute interference with Bassoon-RBP interaction weakens evoked synaptic transmission reliant on Cav2.1 at the CA3 Schaffer-collaterals to CA1 synapses.....170
- B. Synaptic Transmission Relies More on CaV2.2 upon Bassoon Deletion173

DISCUSSION175

- A. Summary.....175
- B. The contribution of CaV2.2 to synaptic transmission is increased in Bsn^{-/-}mice, compensating for reduced CaV2.1 contribution in these animals.....175
- C. Functional relevance of the Bassoon-mediated specific recruitment of CaV2.1 for synaptic transmission.....176

Table of Figures

| | |
|---|-----|
| Figure 1.1 Protoplasmic astrocytes in the CNS: structure, properties and interactions. | 18 |
| Figure 1.2 astrocyte ultrastructure: fine astrocyte processes are present surrounding hippocampal synapses in rodents and humans..... | 21 |
| Figure 1.3 astrocyte to astrocyte interactions..... | 23 |
| Figure 1.4 passive electrophysiology properties of protoplasmic adult astrocytes | 25 |
| Figure 1.5 astrocyte Ca^{2+} signalling is implicated in astrocyte interactions with neurons, local environment and vasculature | 31 |
| Figure 6.6 astrocyte Ca^{2+} events, examples..... | 35 |
| Figure 1.7 IP_3R2 dependent spontaneous calcium events in astrocytes | 40 |
| Figure 1.8 Bell-shaped calcium response curves of IP_3R | 41 |
| Figure 1.9 simulation of calcium concentration effect | 42 |
| on calcium oscillations in astrocytes..... | 42 |
| Figure 2.1 Acute hippocampal slice preparation | 45 |
| Figure 2.2 Identification of astrocytes in acute hippocampal slices..... | 48 |
| Figure 2.3 normalisation of fluorescence intensity of Fluo-4 to A594, principle. | 49 |
| Figure 3.1 Ionomycin is not a reliable means of determining F_{MAX} in situ, | 55 |
| in my hands..... | 55 |
| Figure 3.2 High $[Ca^{2+}]$ KMS solution in pipette may be used as a probe | 56 |
| for estimating F_{MAX} in situ | 56 |
| Figure 3.3 F_{MIN} is determined by imaging pipettes containing KMS + 10mM EGTA. | 57 |
| Figure 3.4 example use of F_{MIN} and F_{MAX} pipette probes to estimate $[Ca^{2+}]$ from | 58 |
| fluorescence intensity recording of Fluo-4 in a whole-cell patch clamped astrocyte, in situ | 58 |
| Figure 3.5 OGB-2 Fluorescence Lifetime Imaging (FLIM) principle..... | 62 |
| $[Ca^{2+}]$ calibration in cuvette (glass slides) | 62 |
| Figure 3.6 OGB-2 photon count ratio (fast-FLIM) principle..... | 63 |
| $[Ca^{2+}]$ calibration in cuvette (glass slides) | 63 |
| Table 3.1 $[Ca^{2+}]$ calibration solutions | 64 |
| Figure 3.7 Cell correction of OGB-2 photon count ratio $[Ca^{2+}]$ calibration..... | 66 |
| Figure 3.8 Background autofluorescence | 67 |
| Figure 4.1 identifying endogenous Ca^{2+} events | 74 |
| Figure 4.2 ROI characterisation..... | 75 |
| Figure 4.3 spontaneous calcium transient characterisation..... | 76 |
| Table 4.1 Proportion of events per morphological category (n=11 cells) | 78 |
| Figure 4.4 resting $[Ca^{2+}]$ distribution in patched astrocytes | 81 |
| Figure 4.5 Relationship between resting $[Ca^{2+}]$ and spontaneous Ca^{2+} event..... | 82 |
| Fig. 5.1 UV LED uncaging of caged calcium or calcium buffers to modulate resting $[Ca^{++}]$ in astrocytes, Setup..... | 95 |
| Fig. 5.2 automatically defined Regions Of Interest (ROI)..... | 98 |
| Fig. 5.3 Quantifying the effect of uncaging method | 100 |
| Fig. 5.4 UV LED effect on KMS-only, 'no cage' cells..... | 102 |
| Fig. 5.5 UV LED uncaging of 2.5mM Diazo2 reduces resting $[Ca^{2+}]$ in patched astrocyte. | 103 |

| | |
|---|-----|
| Fig. 5.6 UV LED uncaging of 5mM NP-EGTA/3mM CaCl ₂ increases resting [Ca ²⁺] in patched astrocyte. | 105 |
| Figure 6.1 DHPG-pressure application (DHPG-p) evoked Ca ²⁺ response in patched astrocyte method illustration. | 114 |
| Figure 6.2 mean response to a single DHPG-p vs pre-event resting [Ca ²⁺] in each cell..... | 117 |
| Figure 6.3 Response to a single DHPG-p vs pre-event resting [Ca ²⁺] in each ROI..... | 118 |
| Figure 6.4 mean response to DHPG-p before and after time in KMS-only cells..... | 120 |
| Figure 6.5 mean response to DHPG-p before and after Ca ²⁺ uncaging in NPEGTA cells | 122 |
| Figure 6.6 mean response to DHPG-p before and after Ca ²⁺ buffer uncaging | 123 |
| in Diazo2 cells..... | 123 |
| Figure 6.7 change in DHPG-puff response vs change in resting [Ca ²⁺] | 126 |
| for all ROI from cells with no uncaging (KMS-only, no UV exposure)..... | 126 |
| Figure 6.8 change in DHPG-p response vs change in resting [Ca ²⁺]..... | 127 |
| for all ROI from cells with Ca ²⁺ uncaging (NPEGTA/CaCl ₂) | 127 |
| Figure 6.9 change in DHPG-p response vs change in resting [Ca ²⁺]..... | 128 |
| for all ROI from cells with Ca ²⁺ -buffer uncaging (Diazo2) | 128 |
| Figure 6.10 change in DHPG-p response vs change in resting [Ca ²⁺] for all ROI..... | 129 |
| Figure 6.11 Equilibration of Ca ²⁺ stores and cytosol qualitatively explains correlations between change of resting [Ca ²⁺] and response peak [Ca ²⁺] or amplitude | 130 |
| Figure 6.12 change in DHPG-p response in all DHPG-responsive ROI according to qualitative change in resting [Ca ²⁺] groups in KMS-only ROI..... | 133 |
| Figure 6.13 change in DHPG-puff response in all DHPG-responsive ROI according to qualitative change in resting [Ca ²⁺] in ROI with Ca ²⁺ uncaging (NPEGTA/CaCl ₂)..... | 134 |
| Figure 6.14 change in DHPG-p response in all DHPG-responsive ROI according to qualitative change in resting [Ca ²⁺], in ROI with Ca ²⁺ buffer uncaging (Diazo2). | 135 |
| Figure 6.15 The ratio of endoplasmic reticulum (ER) to cytosol volumes determines resting [Ca ²⁺] and event peak [Ca ²⁺] and amplitude in an astrocyte model. | 137 |

ANNEX figures

| | |
|--|-----|
| Figure A.1 the tri synaptic hippocampal network..... | 161 |
| Figure A.2 simplified interactions at the presynaptic active zone | 166 |
| Figure A.3 recording fEPSPs in acute hippocampal slices..... | 169 |
| Figure A.4 acute interference with Bassoon-RBP interaction weakens synaptic transmission | 172 |
| Figure A.5 synaptic transmission relies more on Ca _v 2.2 in slices from Bsn ^{-/-} mice | 174 |

ABBREVIATIONS

Resting $[Ca^{2+}]$ (in this thesis): basal $[Ca^{2+}]$; *see page for further detailed definition*

[X] concentration of X compound

A594 Alexa Fluor 594

A647 Alexa Fluor 647

APV (2*R*)-amino-5-phosphonopentanoate, NMDAR antagonist

Bsn^{-/-} bassoon null mutant

Ca²⁺ calcium

DHPG (s)-3,5-dihydroxyphenylglycine, group1 mGluR agonist

DHPG-p pressure application of DHPG

fEPSP field excitatory post-synaptic potential

FLIM fluorescence lifetime imaging microscopy

Fluo-4, Fluo-4, pentopotassium salt, cell impermeant

KMS potassium methane sulfonate solution

mGluR metabotropic glutamate receptor, numbered 1-8 for the subtype considered

NMDAR N-methyl-D-aspartate receptor

NPEGTA o-nitrophenyl-EGTA, tetrapotassium salt, cell impermeant

OGB-1 Oregon Green® BAPTA-1, hexapotassium salt, cell impermeant

OGB-2 Oregon Green® BAPTA-2, octapotassium salt, cell impermeant

OGB-AM, cell permeant version of Oregon Green® BAPTA

P1-36 Postnatal days 1 to 36

PTX picrotoxin, GABA_AR antagonist

RBM/P RIM-binding molecule/protein

RIM Rab-3 interacting molecule

TCSPC Time correlated single photon counting

TTX tetrodotoxin

UV ultra-violet

WT wild-type

Scientific contributions during PhD

International conferences

- **International Astrocyte School 2012**
10 minute student project presentation: "Quantify Ca^{2+} signalling in astrocytes using fluorescence intensity"
- **Frontiers in Neurophotonics 2013**
poster presentation: "manipulating $[\text{Ca}^{2+}]$ in astrocytes with UV uncaging of Diazo2 and NPEGTA"

UCL Grand Challenges internal training

- 5 minute thesis presentation
- 10 minute mock grant-application presentation

Publication contributions

- Davydova D¹, Marini C¹, **King C²**, Klueva J³, Bischof F¹, Romorini S¹, Montenegro-Venegas C¹, Heine M³, Schneider R³, Schröder MS¹, Altmann WD⁴, Henneberger C⁵, Rusakov DA², Gundelfinger ED⁶, Fejtova A⁷. 2014, **Bassoon specifically controls presynaptic P/Q-type Ca^{2+} channels via RIM-binding protein.** *Neuron*, 82. pp181-94

I performed extracellular field recordings of excitatory post synaptic potentials at the CA3 to CA1 synapses, in the presence of N or P/Q-type voltage gated Ca^{2+} channel blockers, in acute hippocampal slices from rats or either Bassoon knock out and wild-type mice. These experiments contributed to understanding the Bassoon mediated structural interactions underlying the relative contribution of voltage gated Ca^{2+} channel subtypes 2.1 and 2.2 to synaptic transmission. This work was published in *Neuron*, 2014 (see above) and is presented as an annex to this thesis.

- Henneberger C¹, Bard L², **King C²**, Jennings A², Rusakov DA². 2013, **NMDA receptor activation: two targets for two co-agonists.** *Neurochemical Research*, 38. pp 1156-62.

I wrote a bibliographical review of how NMDA receptor subunit distribution contributes to defining how NMDA receptors will interact with co-agonists Glycine or D-serine. This section contributed to a review on NMDAR co-agonist signalling with was published in *Neurochemical Research*, 2013 (see above).

- Zheng K¹, Bard L¹, Reynolds J¹, **King C¹**, Jensen T¹, Gourine A², Rusakov D¹. 2015 **Time-resolved imaging reveals heterogeneous landscapes of nanomolar Ca^{2+} in neurons and astroglia.** *Neuron*, 88. pp 277-288

I contributed to the design and acquisition of in vivo fluorescence lifetime imaging recordings of astrocyte and neuron resting $[\text{Ca}^{2+}]$ which is discussed in the general discussion, chapter 7 of this thesis and currently in minor format revision as accepted for publication in *Neuron*. In the text of this thesis, this paper is referenced as (Zheng et al. 2015).

ACKNOWLEDGEMENTS

Many thanks to my supervisors, Prof Christian Henneberger and Prof Dmitri Rusakov, and to the UCL Grand Challenges PhD program. Thank you to both my PhD examiners, Professors Josef Kittler and Alexei Verkhratsky, for their advice and discussion opportunities during my viva and thesis corrections.

I would also like to thank the Rusakov synaptic imaging lab team and the Henneberger lab in Bonn for their help, advice and support.

Specifically, I wish to thank to Dr Kaiyu Zheng for his patience whilst rekindling my interest in optics and his help and advice with fixing software and hardware crashes.

Secondly, thanks to Drs Lucie Bard and Thomas Jensen for their imaging, electrophysiology and academia expertise.

Thanks to Drs Yamina Bakiri and Piotr Michaluck for both their technical and emotional support.

I would also like to thank all the PIs, postdocs, PhD students, technicians and administration staff in the DCEE and ION for their advice, fascinating insight and great scientific discussion opportunities.

Thanks to my BSc and MSc teachers and supervisors, Prof Daniel Voisin, Prof Philippe de Deurvadere, Prof Andreas Frick, who have together contributed over the years to getting me interested, educating me and developing my interest in cell biology, specifically Neuroscience.

Special thanks to Prof Jonathan Weber, Prof Richard Ribchester and Prof Charles Bourque who all kindly took the time to further my scientific culture, experience, skills and knowledge during the respective summer placements in their laboratories. These were truly inspirational placements and experiences.

Much gratitude to all.

I dedicate this PhD to my family for their excellent education skills, letting me grow up on an organic vineyard and who greatly helped finance my education despite everything. To Philip who makes life worthwhile despite everything and his parents who gave me somewhere to write this. Thank you.

'Ever tried, ever failed, no matter.

Try again, fail again, fail better.'

Samuel Beckett

Chapter1: INTRODUCTION

Astrocytes are a subtype of the macroglial cells of the central nervous system (see Fig.1.1.A) which also comprise oligodendrocytes, responsible for the myelin sheath surrounding neuronal axons, and progenitor cells such as NG2 cells (Bignami & Dahl 1974; Jessen 2004). The coining of the term glia is commonly attributed to Virchow in the mid-19th century as reported in (Virchow 1856). According to Virchow, the term neuroglia describes the supporting “substance distinct from the proper nervous parts”. The term astrocyte, etymologically referring to the characteristic star-like dense arborisation of this subtype of neuroglia cells (see Fig.1.1.B), is thought to be coined by Lenhossek (Lenhossek 1895). Indeed, staining methods developed in the 19th century enabled the morphological identification of these cells as illustrated for example in the “nevroglië” chapter in Ramon y Cajal’s 2nd volume on Human Histology (Ramon y Cajal, translation by Azoulay 1909). A detailed historical account of the concept of glia is given for example in (Kettenmann & Verkhratsky 2008).

Astrocytes play an important role in brain homeostasis and metabolism. Experimental evidence since the early 1990s, has further revealed some of the properties and functions of astrocytes helping to establish the nature of their interactions with neurons and vasculature (illustration Fig. 1.1.D), which could be essential for physiological brain function. Indeed astrocytes, particularly astrocyte calcium (Ca^{2+}) signalling, were shown to play an important role in synaptic plasticity (for example Henneberger et al. 2010 however also see Agulhon et al. 2010), behaviour (for example Halassa et al. 2009 however also see Petravicz et al. 2014). Understanding the properties of astrocytes and their role in brain physiology, could contribute to reveal novel therapeutic strategies or targets for treatment of diseases such as epilepsy for example as reviewed in Crunelli et al. 2015.

However, in addition to their supportive role, the extent to which these astrocyte-neuron interactions play a more proactive role in manipulating the processing and storage of information in physiological brain functions, perhaps through Ca^{2+} signalling, remains controversial, as suggested by the above mentioned examples of possible conflicting studies and as reviewed in Agulhon et al. 2008. The lack of consensus or understanding of the mechanisms that underlie a more active role of astrocytes in shaping neuronal activity (reviewed in Hamilton & Attwell 2010) suggest that further investigation into astrocyte physiology and its mechanisms could contribute to establishing the role of these cells in brain physiology.

In this thesis, we propose to contribute to the understanding of astrocyte Ca^{2+} signalling through a quantitative method to study astrocyte resting $[\text{Ca}^{2+}]$ and its relationship with astrocyte Ca^{2+} events in situ. This introduction aims to describe astrocytes, the functions, importance and controversies in the current understanding of astrocyte Ca^{2+} signalling for brain physiology and how resting $[\text{Ca}^{2+}]$ may contribute to shape astrocyte Ca^{2+} signalling.

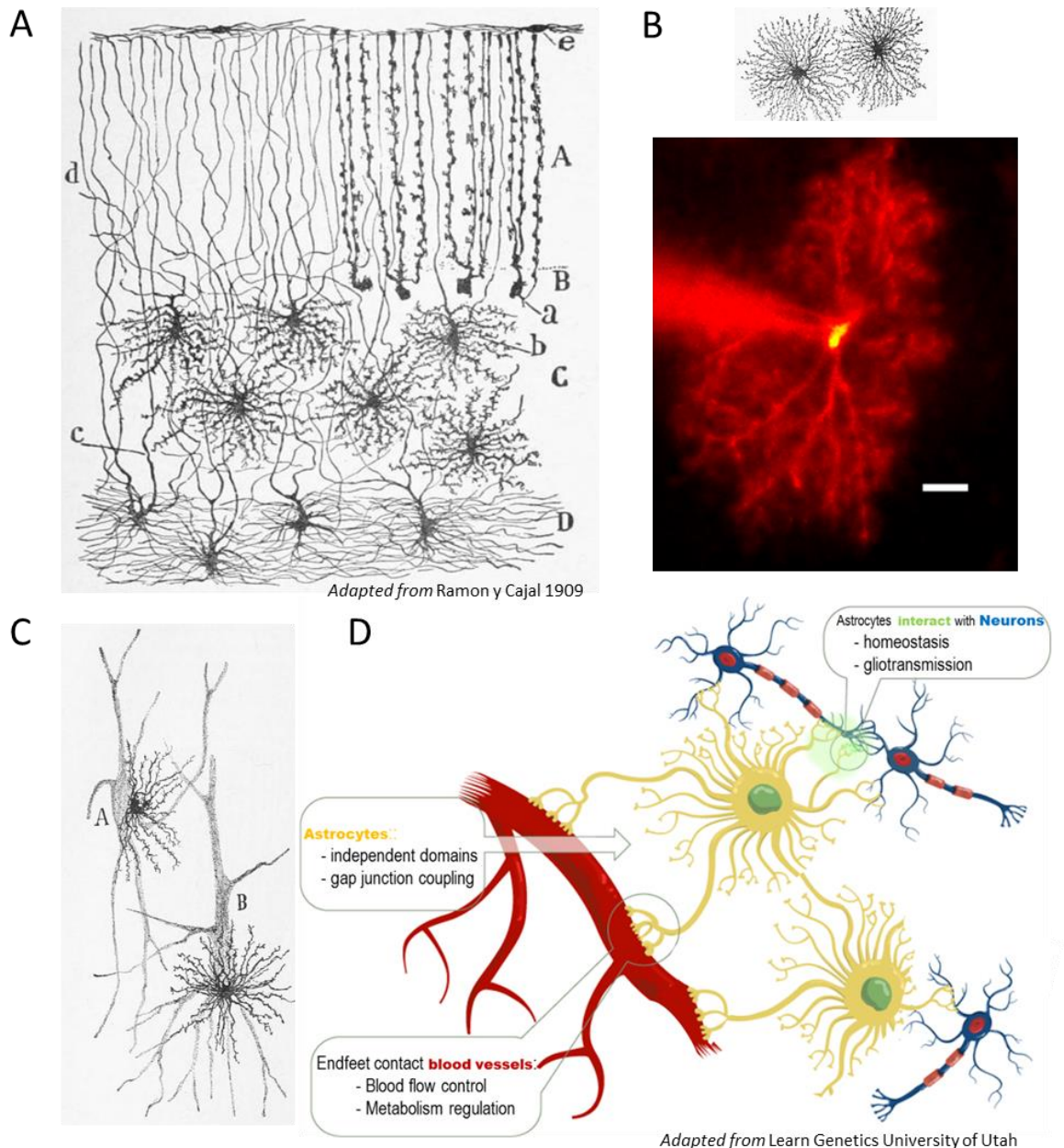


Figure 1.1 Protoplasmic astrocytes in the CNS: structure, properties and interactions.

A. Golgi staining of neuroglia in the Human cerebellum (adapted from Ramon y Cajal 1909)

Illustration of the morphological heterogeneity of astrocytes in cerebellum (layers from the bottom up): fibrous astrocytes (c) in white matter (D), protoplasmic astrocytes (b) in granule cell layer (C), Bergmann glia (a) cells in the molecular layer (A).

B. Example of whole cell patched protoplasmic astrocyte, star-like arborisation

Top: Golgi staining of star shaped independent Glial cells (adapted from Ramon y Cajal 1909).
Bottom: Whole cell patch clamp of protoplasmic astrocyte in CA1 stratum radiatum of acute hippocampal rat slices loaded with 350 μ M TexasRed-Dextran for morphological identification (scale bar 10 μ m).

C. Golgi staining of astrocytes and neurons in the Human cortex (adapted from Ramon y Cajal 1909)

Glial cells (smaller) can be found in periphery of neurons (elongated, larger cells).

D. Astrocytes at the heart of brain physiology (adapted from Learn. Genetics, University of Utah)

Schematic illustration of gap junction coupled (orange), non-overlapping, astrocytes (yellow), their endfeet projections onto brain vasculature (red), for blood flow and neuronal metabolism regulation, and their interactions, homeostasis and gliotransmission, (green) with neurons (blue).

ASTROCYTE STRUCTURAL AND PHYSIOLOGICAL PROPERTIES

A. Astrocyte heterogeneity

Astrocytes are non-excitabile, non-neuronal cells in the central nervous system alongside neurons, oligodendrocytes, NG2 cells and microglia. This broad definition encompasses many potentially different cells as illustrated for example in terms of morphology in figure 1.1.A. Indeed, as further investigation into their properties progresses, there is increasing evidence that astrocytes form a heterogeneous population. For example: in terms of morphology (Fig.1.1.A), intracellular compartments (Di Castro et al. 2011), inter-cellular coupling (Nagy et al. 2011) and electrophysiological properties (Zhou et al. 2006). This heterogeneity could be a function of species (Oberheim et al. 2009) or development (Sun et al. 2013) for example. Furthermore, such heterogeneity may have functional consequences for astrocyte physiology and their roles in the central nervous system (Matyash & Kettenmann 2010; Martin et al. 2015). Further investigation into the morphological, biochemical and electrophysiological properties should help define sub-population characteristics. Until then, stringent documentation or definition of the glial cells under investigation is therefore necessary.

A relative consensus has been reached to some extent for the structural and physiological properties of protoplasmic astrocytes. These characteristics and their nuances are described below and were used to identify the astrocytes in this study.

B. Morphology

i. General morphology and structural interactions of protoplasmic astrocytes in the stratum radiatum of the rodent hippocampus

Astrocytes have a distinctive anatomic appearance: a small soma ($\approx 10 \mu\text{m}$ diameter) from which multiple fine processes, create an intricate and extensive star-like arborisation (illustrated in figure 1.1.B). Protoplasmic astrocytes, in grey matter as opposed to fibrous astrocytes in white matter (*Peters 1976, Miller Raff 1984*), have profuse, short stubby primary processes ($\approx 1 \mu\text{m}$ thick) from which leaf-like ultrathin flat ($\approx 50 \text{ nm}$ wide) peripheral processes expand into minute extracellular gaps often beyond classical light microscopy resolution (fuzzy appearance figures 1.1.B; 1.3).

On the one hand, astrocytic end-feet contact blood vessels and the pial surface covering the entire surface of intraparenchymal capillaries (Mathiisen et al. 2010) helping delineate the blood-brain barrier. On the other hand, astrocytic peripheral processes are intimately intertwined with neuronal processes at synapses as was originally suggested by Cajal (illustration figure 1.1.C).

Indeed in the hippocampus, a single astrocyte is thought to contact $\approx 100\,000$ synapses (Bushong et al. 2002). Similarly, cortical astrocytes could interact with up to 8 different neuronal somas or ≈ 600 different dendrites suggesting functional groups of synapses (within or across different neurons) could be coordinated by individual astrocytes (Halassa et al. 2007).

ii. Astrocyte ultrastructural morphology shows functional plasticity

At the ultrastructural level, astrocyte morphology is more sponge-like, with leaf-like ultrathin processes that can ensheath synapses (figure 1.2). These peri-synaptic astrocyte processes are thought to be particularly motile. Indeed, cultured astrocytes, which have a more two-dimensional morphology than astrocytes in situ, were found to form and extend filopodia when exposed to glutamate (Cornell-Bell et al. 1990b). In slices, peripheral astrocyte small processes have been shown to be highly motile relative to changes in neuronal dendritic spines: extending and retracting their coverage of a given synapse over minutes (timelapse recordings in organotypic, cultured hippocampal slices; Haber et al. 2006). Moreover, both the proportion of synapses covered and the extent of astrocyte coverage of neuronal synapses are not constant across different regions of the central nervous system (reviewed in Reichenbach et al. 2010). Approximately 60% of rat hippocampal synapses were found to be in immediate contact with astrocyte processes, predominantly at larger synapses in CA1 area (Ventura & Harris 1999). However more recently astrocyte processes were found to preferentially tightly ensheath synapses onto thin postsynaptic spines in the hippocampus dentate gyrus (Medvedev et al. 2014). Pathologically, astrocyte synapse coverage may be disrupted with increasing severity of epilepsy as suggested in an electron microscopy study of hippocampus samples from resected tissue of human epilepsy patients (Witcher et al. 2010). However, electron microscopy in these studies relies on fixed tissue samples. Such preparations could be detrimental to the preservation of such small structures through loss of extracellular medium which could perhaps bias the extent of astrocyte synapse coverage or differences in percentage of astrocyte coverage of synapses in different electron microscopy studies (reviewed in Bernardinelli et al. 2014).

These changes in astrocyte coverage of synapses have been suggested as a mechanism that may contribute to the regulation of some aspects of synaptic transmission, plasticity or pathology. For example, increased extension of astrocyte processes is correlated with a dampening of excitatory synaptic transmission in hippocampal slices (Pannasch et al. 2014).

Preliminary studies suggest that structural plasticity of astrocyte coverage of neuronal synapses could be Ca^{2+} dependent. Indeed, in astrocyte hippocampal cultures, Ca^{2+} uncaging induced an actin dependent outgrowth of these perisynaptic astrocyte processes (Molotkov et al. 2013). Electron microscopy in hippocampal slices from mice genetically engineered to show reduced astrocyte Ca^{2+} signalling revealed reduced astrocyte synaptic coverage (Tanaka et al. 2013).

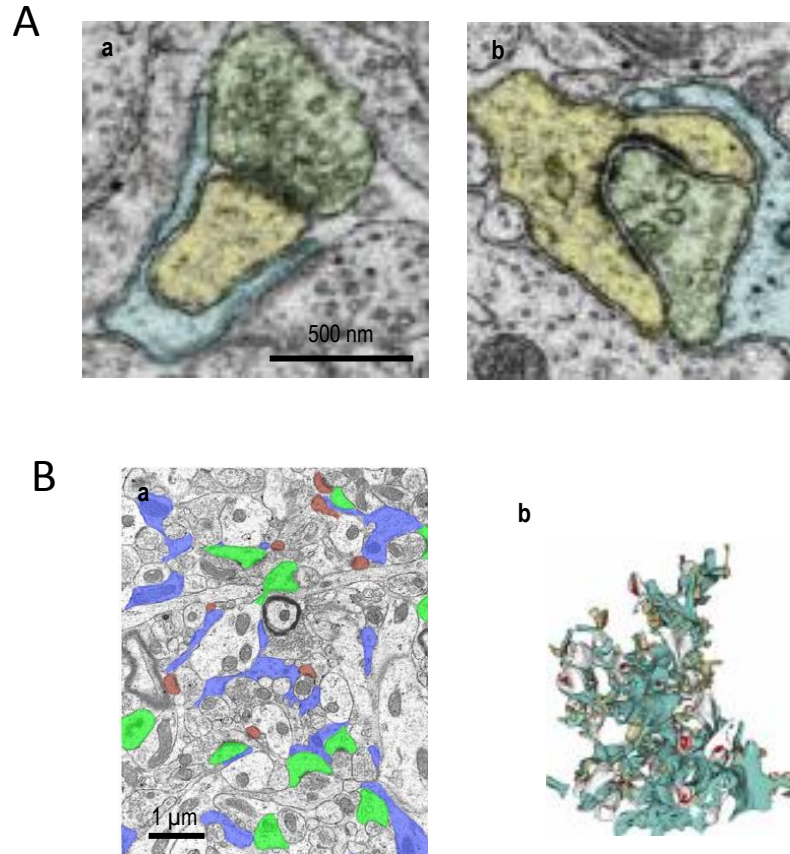


Figure 1.2 astrocyte ultrastructure: fine astrocyte processes are present surrounding hippocampal synapses in rodents and humans.

This illustration is adapted from Witcher et al. 2010 in a,b and Medvedev et al. 2014 in c,d.

A : electron microscopy of astrocyte peri synaptic processes in hippocampal human tissue

Electron microscopy reveals that astrocytes processes (blue) surround both thin (a) and mushroom (b) spines (presynaptic axon bouton, green and post synaptic dendritic spine, yellow) in human hippocampus slices taken from hippocampal resection samples in patients with mild epilepsy (Witcher et al. 2010).

B: electron microscopy and 3D reconstruction of rodent astrocyte peri synaptic processes

Three dimensional reconstructions (b) of contiguous astrocyte fine process (blue) and surrounding dendritic spines (thin spines in brown, mushroom spines in grey, post synaptic density in red) illustrates the astrocyte peripheral processes ultrastructure. This was reconstructed from electron microscopy of dentate gyrus rat hippocampal slices (a) where astrocyte processes are in blue, thin spines in brown, mushroom spines in green. (Medvedev et al. 2014)

C. Gap junction coupling

i. Gap-junction connected astrocytes form Ca^{2+} permeable syncytia

Hippocampal astrocytes in both 1 month old rats (Bushong et al. 2002) and 2 month old mice (Ogata & Kosaka 2002), as well as cortical astrocytes in 3 month old mice (Halassa et al. 2007) are thought to have individual, mostly non overlapping domains (illustration in figure 1.3.A). However one of the defining characteristics of these astrocytes is their capacity to form syncytia mediated by their extensive coupling to one another through gap junctions (illustrated in figures 1.3.B; 2.2.B). These junctions consist of two apposed connexin based hemichannels connecting adjacent membranes. Astrocyte gap junctions are have been shown to be mainly made of connexin proteins 30 (Nagy et al. 1999) and 43 (Yamamoto et al. 1990). These connexin mediated connections form pores permeable to ions and other small molecules (up to $\approx 1000\text{Da}$ molecular weight) including secondary messengers such as calcium (Ca^{2+}) and inositol triphosphate (IP_3) (reviewed in Giaume & McCarthy 1996). Such intercellular communication is believed to mediate the coordinated action of adjacent but individual cells in terms of electrical and biochemical activity and equalizes their intracellular ion concentrations (Rose & Ransom 1997).

Ca^{2+} waves propagating across networks of astrocytes were the first phenomena to be investigated in astrocyte Ca^{2+} signalling in culture (Cornell-Bell, Finkbeiner, et al. 1990). A number of mechanisms have been suggested to underlie the propagation of these inter-cellular Ca^{2+} waves. Indeed although these gap-junctions are permeable to both Ca^{2+} and IP_3 , Ca^{2+} diffusion is tightly regulated by cytosolic Ca^{2+} buffers, uptake into internal stores or extrusion into the extracellular space. This has led to the suggestion that IP_3 may propagate across these gap-junctions and initiate the spread of a Ca^{2+} signal, through the activation of ER receptors, across gap-junction coupled astrocytes (Boitano et al. 1992).

Furthermore, such inter-cellular Ca^{2+} waves could also occur independently from gap-junction coupling. A given astrocyte can release ATP into the extracellular space which in turn could activate Ca^{2+} signals in neighbouring astrocytes through activation of G-protein coupled P2Y receptors for example (Guthrie et al. 1999).

In the hippocampus in vivo, glissandi waves (propagating faster than waves observed in situ) were shown to be sensitive to both gap-junction and purinergic receptor blockade (Kuga et al. 2011) suggesting that, in these conditions, both mechanisms may coexist.

Gap junction permeability is strongly reduced by intracellular acidification (Francis et al. 1999) or large, "pathophysiological", increases in intracellular $[\text{Ca}^{2+}]$ of $>100\mu\text{M}$ (Dakin et al. 2005). More recent studies in more intact preparation suggest these astrocyte Ca^{2+} waves may occur more frequently in pathological conditions as recorded in vivo mouse model of Alzheimer's disease (Kuchibhotla et al. 2009).

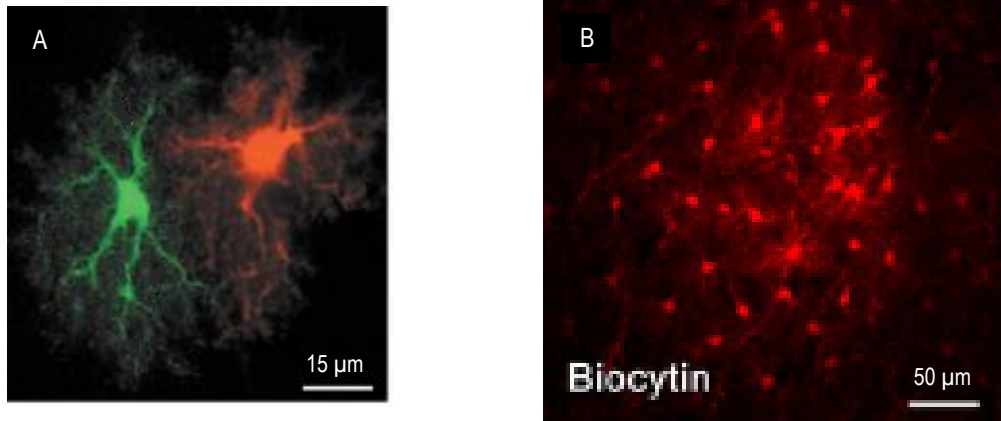


Figure 1.3 astrocyte to astrocyte interactions

This illustration is adapted from Bushong et al. 2002 in a and Houades et al. 2008 in b.

A: Example individual astrocyte domains in rat hippocampus slices

Astrocytes in the rodent hippocampus and neocortex are thought to occupy individual domains with limited overlap (A). Two astrocytes in the rat hippocampus are injected with two different dyes to reveal their individual domains (Bushong et al. 2002).

B: Example gap-junction coupled astrocytes in mouse barrel cortex

Astrocytes are characteristically strongly coupled via gap-junctions to form a syncytium (B). Astrocyte was loaded with gap junction permeable biocytin in the barrel cortex of mice (Houades et al. 2008). See figure 2.2.B for illustration in the hippocampus.

ii. Connexin expression also regulates astrocyte processes coverage of excitatory synapse.

Independently of their channel function, more recent investigation into the role of these connexins has revealed how they may also play a role in regulating astrocyte morphology. Indeed, connexin 30 deletion in mice has revealed increased and extended astrocyte process coverage of excitatory synapses in the hippocampus which in turn led to a dampening of excitatory synaptic transmission (Pannasch et al. 2014). Models of glutamate transporter density in astrocytes lead Pannasch et al to suggest that the increase in astrocyte coverage observed in connexin 30 depleted astrocytes could increase the local astrocyte glutamate uptake at these synapses thus reducing glutamate available for postsynaptic neuronal receptors (as suggested by Oliet et al. 2001). In more physiological terms, the expression of connexin 30 is thought to appear later in development than connexin 43 which is already present in radial glia (> postnatal day 10, Nagy et al. 1999). Its expression may also be increased following seizures (Condorelli et al. 2002) or decreased in reactive astrocytes surrounding local injury (Koulakoff et al., 2008). Once again, this highlights the importance of considering the developmental stage alongside the experimental model used when considering individual astrocytes as these parameters may functionally alter their structural properties and interactions.

D. Passive electrophysiological properties

The resting membrane potential (RMP) of astrocytes is generally low and hyperpolarised, close to potassium equilibrium potential (originally shown in amphibian model, Kuffler et al. 1966). For example, protoplasmic astrocytes in situ in the adult rat hippocampus have a RMP around -80 to -90 mV (Henneberger et al. 2010; Zhou et al. 2006). Although astrocytes express a variety of potassium (K^+) channels, inwardly rectifying K^+ (Kir 1.4) channels seem to be important in setting the resting potential (Steinhauser 1993). Due to this “ K^+ leak” and extensive cell volume (through the large number of processes and gap junction coupling), astrocytes exhibit a characteristically low ($\leq 10 \text{ M}\Omega$) input resistance (Steinhauser et al. 1992). Astrocytes express many other voltage-activated ion channels (reviewed in Sontheimer 1994; Verkhratsky & Steinhäuser 2000), yet the low ratio of sodium (Na^+) to K^+ channels in adult astrocytes suggests these cells are not capable of regenerative electrical responses like the action potential: hence the term “passive” astrocytes and the characteristic linear relationship of current to voltage in these mature passive protoplasmic astrocytes (linear I/V curve; figure 1.3; Zhou et al. 2006).

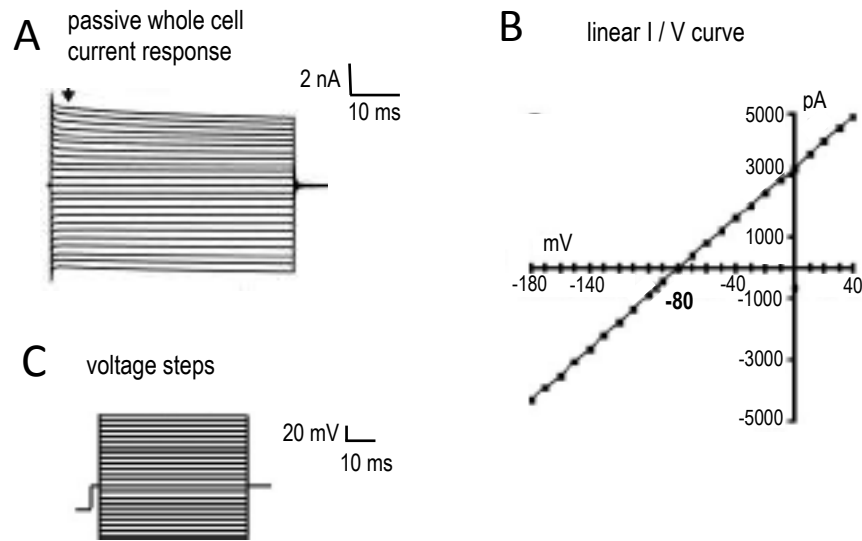


Figure 1.4 passive electrophysiology properties of protoplasmic adult astrocytes

This illustration is adapted from figure 2 in Zhou et al. 2006.

A: passive astrocyte whole cell current response in rat hippocampus slices

The passive current profile of a whole cell patched protoplasmic astrocyte in the CA1 region of P35 rat (adult) hippocampal slice is shown in A. This current profile is recorded in response to 50 ms pulses in 10mV voltage steps from -180 to +60 mV, as shown in C.

B: linear relationship between current amplitude and voltage command in passive astrocytes

The current amplitudes at 5ms (arrow in A) are plotted against the command voltage in B for each response (A) to the voltage steps (C) in order to illustrate the relationship between current and voltage (I/V curve).

C: example voltage step protocol for induction of current profile in A

This illustrates the voltage steps command protocol: 50 ms pulses in 10mV voltage steps from -180 to +60 mV.

The predominant leak-type K⁺ channel current expressed in these passive astrocytes leads to their characteristic linear I / V relationship, B.

The structural properties of protoplasmic astrocytes put astrocytes in a strong position to sense, integrate and modulate synaptic transmission (as discussed in the next sections) through the extensive lamellar processes that surround synaptic contacts and endfeet projections onto the brain vasculature (Fig. 1.1.D).

We used the properties described in this section to identify individual astrocytes in the CA1 stratum radiatum area of P21-26 rat acute hippocampal slices studied in this thesis within the limits of the tools used and described in chapter 2.

Furthermore, these structural properties of astrocytes are susceptible to change which in turn may have functional impact on their interactions. Astrocyte-neuron interaction functions are detailed in the next sections, specifically highlighting the role of astrocyte Ca²⁺.

PHYSIOLOGICAL FUNCTIONS OF NEURON-GLIA INTERACTIONS

A. Homeostasis

Astrocytes have widespread physiological roles in the brain such as the maintenance and formation of the blood-brain barrier for example. Some of the mechanisms of astrocyte support of physiological neuronal activity are briefly and non-exhaustively described here as the main focus of this thesis is on astrocyte Ca^{2+} signalling. Astrocytes support neuronal activity through metabolic support (as a source of lactate and glucose for neighbouring neurons; Pellerin & Magistretti 1994) and homeostatic regulation of the extracellular space through uptake of extracellular potassium (K^+) and neurotransmitters which is paramount for physiological neuronal transmission (reviewed in Allaman et al. 2011).

i. Astrocytes and regulation of extracellular potassium

Astrocytes help prevent the extracellular accumulation of K^+ which can occur secondary to neural activity (Newman et al. 1984). Extracellular $[\text{K}^+]$ is thought to be tightly regulated to a resting level of ≈ 3 mM. A single action potential may increase extracellular $[\text{K}^+]$ by 0.75 mM, whereas a “ceiling” level of K^+ accumulation (≈ 10 to 12 mM) is only reached or exceeded under pathologic conditions of intense neuronal activity such as temporal lobe epilepsy (Benninger et al. 1980; Heinemann et al. 2000). The astrocyte mediated regulation of extracellular K^+ is thought to occur both by local K^+ uptake and spatial buffering (K^+ transfer from high to low $[\text{K}^+]$ regions). Net uptake of K^+ into glial cells depends on the active glial Na^+ pump. This is a cation transporter that uses adenosine tri phosphate (ATP) for exchange of 2K^+ and 3Na^+ . The glial Na^+ pump has a slightly higher affinity for extracellular K^+ in comparison to neuronal isoforms. Cl^- - Na^+ - K^+ cotransporters and K^+ channels are also involved. Spatial buffering of K^+ is in part attributed to astrocytes forming a syncytium (through previously described gap junctions; Wallraff et al. 2006) of highly K^+ selective and permeable membranes (Kir 4.1 channels); reviewed in Kofuji & Newman 2004; Söhl et al. 2004).

ii. Transmitter Synthesis/Removal by Astrocytes

The glutamate-glutamine cycle is a clear example of cooperativity between astrocytes and neurons. Astrocyte glutamate transporters remove potentially toxic excess glutamate, the predominant excitatory neurotransmitter, from the extracellular space. In turn, astrocytic glutamine synthetase provides neurons with glutamine: a synaptically inert precursor for re-synthesis of glutamate. After release from the presynaptic terminal, glutamate is taken up primarily by astrocytes processes (Danbolt et al. 1992; Bergles & Jahr 1997) where it is converted to glutamine through the ATP-dependent enzyme glutamine synthetase, located exclusively in the astrocytic processes surrounding glutamatergic synapses (Derouiche & Frotscher 1991). Astrocyte-expressed high affinity glutamate transporters (GLAST and GLT-1) are considered as quantitatively the most important in regulating glutamate at synapses and in the extracellular space (review in Anderson & Swanson 2000).

Indeed, in the absence of astrocytes, neurons are 100-fold more vulnerable to glutamate toxicity (Rosenberg & Aizenman 1989) and genetic down-regulation of GLAST or GLT-1, but not the neuronal subtype EAAC1, causes elevated extracellular levels of glutamate and neurotoxicity (Rothstein et al. 1996).

iii. Additionally to a supportive role, these functions also enable astrocytes to actively shape neuronal transmission

Much more can be said about the supportive role of astrocytes and glia in general; however an equally important focus in astrocyte research is understanding if and how astrocytes and neurons actively interact to shape synaptic transmission and its plasticity.

As these glutamate transporters are expressed in peripheral astrocyte processes (Rothstein et al. 1994), in conjunction with the previously described structural plasticity of these processes (Oliet et al. 2001; Pannasch et al. 2014), differential astrocyte glutamate uptake may be a mechanism by which astrocytes not only support but play a role in shaping neuronal transmission. Indeed, the local availability of astrocyte high affinity glutamate uptake could impact extracellular glutamate diffusion (Piet et al. 2004). In turn, disruption of astrocytic glutamate transporters in astrocytes located near hippocampal interneurons enhanced the inhibition of nearby excitatory neurons (Huang et al. 2004) suggesting astrocyte glutamate transport plays a role in synaptic plasticity. Indeed, uptake of glutamate by astrocytes may lead them to release the principle inhibitory neurotransmitter γ -aminobutyric acid (GABA) through glial GABA transporters (GAT2/3) in situ in hippocampus slices (Heja et al. 2009). More recent studies in mice where Kir 4.1 expression was disrupted in GFAP expressing glia reveal that K^+ clearance by astroglia through Kir 4.1 channels during synaptic activity may contribute to dampen synaptic transmission and affect short term synaptic transmission (Sibille et al. 2013). Astrocyte mediated potassium clearance and uptake of neurotransmitters (as described here for glutamate for example) are therefore mechanisms by which astrocytes not only support but also shape synaptic transmission and its plasticity. These mechanisms contribute to the concept of the tripartite synapse.

B. Tripartite synapse:

Reciprocal, modulable communication between astrocytes and neurons

The extensive studies of the roles of astrocytes in neuronal function and its plasticity over the last decades have led to the concept of a tripartite synapse where astrocyte-neuron interactions combine to shape synaptic transmission of information in the central nervous system (originally reviewed in Araque et al. 1999). Indeed, although astrocytes support neurons through homeostasis and metabolism as alluded to above, their functions have been revised to suggest a more active role in shaping neuronal activity. Astrocyte Ca^{2+} signalling in particular may be a key mechanism by which astrocytes could integrate and impact on neuronal function as discussed below.

i. Astrocytes can integrate neuronal activity

Astrocytes in culture were first shown to respond to external application of glutamate, the main excitatory neurotransmitter (Cornell-Bell et al. 1990a;b). Similarly, exogenous applications of many other neurotransmitters induced responses in cultured astrocytes. For example: astrocytes respond to the main inhibitory neurotransmitter, γ -aminobutyric acid (GABA; Nilsson et al. 1993) and serotonin (Jalonen et al. 1997) amongst many others. Importantly, astrocytes are also shown to respond (in terms of increased internal Ca^{2+}) in situ.

In hippocampal slices, where astrocyte-neuron morphology, structure and interactions are better preserved than in culture, astrocytes were shown to respond to neurotransmitters endogenously released at CA3 to CA1 synapses following high frequency electrical stimulation of neuronal release (Porter & McCarthy 1996; Henneberger et al. 2010). Similarly, astrocytes in hippocampus slices responded to endogenous release of acetylcholine (Araque et al. 2002) and endocannabinoids (Navarrete & Araque 2010). Moreover, in vivo experiments which allow for perhaps more intact approach to brain physiology also revealed astrocyte responses to physiological stimulus. Indeed astrocytes in the barrel cortex responded to whisker stimulation (Lind et al. 2013).

It has also been suggested that astrocytes may be able to distinguish information from distinct population of neighbouring synapses. Indeed, the astrocytic response to activation of both glutamate and acetylcholine neuronal release in the hippocampus was significantly different from the linear summation of the astrocyte response to the individual activation of these pathways (Perea & Araque 2005). This suggests that not only are astrocytes responsive to neuronal activity but that this is a complex transfer of information, whereby the astrocyte can integrate different neuronal inputs through distinct positive and negative actions of neurotransmitters on astrocyte calcium signalling. These differences could perhaps result in activation of different downstream Ca^{2+} dependent phenomena in order to modulate neuronal activity through gliotransmission for example (see next section). Indeed recent evidence suggests that in the striatum, sub-populations of astrocytes form selective functional bi-directional interactions with specific neuron and synapse subtypes (Martin et al. 2015).

The mechanisms enabling astrocytes to respond and integrate neuronal activity may be numerous. As astrocytes respond via transient Ca^{2+} cytosolic increases to many different experimental stimuli, understanding and specifying the mechanisms by which they respond could help determine the physiological role of these cells in neurotransmission. Astrocytes express a large number of functional receptors to many neurotransmitters (reviewed in Porter & McCarthy, 1997). In this thesis, we address the metabotropic receptor activation mediated IP_3R pathway which is further discussed in the section on astrocyte Ca^{2+} signalling.

ii. Astrocytes can in turn modulate neuronal activity through gliotransmission

Astrocytes have been found to release, through a number of possible mechanisms, chemical compounds which can interact with neighbouring neurons. This process defines the concept of gliotransmission.

External activation of astrocytes in culture revealed that these cells could release a plethora of compounds such as glutamate (Parpura et al. 1994), adenosine triphosphate (ATP; Guthrie et al. 1999) and D-serine, an endogenous co-agonist of the NMDA receptor (Schell et al. 1995). More physiological release has been confirmed by astrocytes in acute slices: for example astrocytes release D-serine in situ preparations of both the hypothalamus (Panatier et al. 2006) and the hippocampus (Henneberger et al. 2010). Furthermore, in vivo preparations also support astrocyte mediated purinergic release for example (Halassa et al. 2009).

In turn, these chemicals released by astrocytes are thought to modulate synaptic transmission. In neuronal and astrocyte co-cultures, glutamate released through artificial stimulation (mechanical or via UV photolysis) of astrocyte Ca^{2+} could trigger slow inward currents in co-cultured neurons (Araque et al. 2000; Parpura & Haydon 2000). At excitatory synapses onto granule cells of the dentate gyrus in hippocampal slices, Jourdain et al. 2007 suggested that astrocyte glutamate release could activate nearby extrasynaptic NMDAR on the presynaptic terminal and thus potentiate synaptic transmission. Astrocytes in the stratum radiatum were found to play an important role in synaptic plasticity as long term potentiation required their Ca^{2+} dependent release of D-serine (Henneberger et al. 2010).

Astrocytes have been shown to release these compounds through varied mechanisms such as Ca^{2+} dependent vesicle exocytosis (similar as in neurotransmission) or through permeable channels which can also be activated by Ca^{2+} signalling such as the glutamate permeable Ca^{2+} activated channel Best1 for example (Woo et al. 2012). Other suggested mechanisms involve permeable channels such as: pannexin and connexin hemichannels which may release glutamate or ATP (Ye et al. 2003; Kang et al. 2008) and such release may also be enhanced (indirectly) by Ca^{2+} (Vuyst et al. 2009); or transporters such as reversal of glutamate uptake by astrocyte glutamate transporters (Szatkowski et al. 1990) which is not Ca^{2+} dependent.

Further experimental evidence has been found to support vesicle exocytosis as a mechanism underlying Ca^{2+} dependent gliotransmission. Jourdain et al. 2007 used electron microscopy to suggest that vesicles were present in astrocyte processes opposite presynaptic terminal which would support the role of astrocyte vesicle glutamate release on extrasynaptic NMDAR mentioned above. More recently, immunogold electron microscopy revealed that these vesicles in small peri-synaptic astrocytic processes contained glutamate and, separately, D-serine (Bergersen et al. 2012).

Furthermore, astrocytes in culture were found to contain many of the structural components for vesicle docking prior to exocytosis such as the SNARE proteins: synaptobrevin, syntaxin and cellubrevin (Parpura et al. 1995) as well as an astrocyte equivalent of the neuronal SNAP25, SNAP 23 (Hepp et al. 1999). These components were shown to be functional as fluorescent tagged vesicle associated glutamate transporter allowed for dynamic imaging of vesicle exocytosis following metabotropic activation of astrocytes in culture (Bezzi et al. 2004). Indeed, astrocyte ATP release was disrupted using GFAP to specifically target glia and disrupt vesicle fusion in these cells through genetic disruption of SNARE proteins (dnSNARE), in vivo (Halassa et al. 2009). Similarly, cleavage of the vesicle associated SNARE protein synaptobrevin (which contributes to docking of vesicles for exocytosis, see figure 8.2) by botulin B toxin application (Schiavo et al. 1992) in astrocytes affected astrocyte glutamate (Araque et al. 2000) and D-serine (Henneberger et al. 2010) release as measured through the reduction in astrocyte induced neuronal activity (respectively: slow inward currents and long term potentiation).

However, the extent to which this astrocyte vesicular release is physiologically relevant has been controversial as reviewed and discussed in Hamilton & Attwell 2010. They suggest that lack of quantitative and structural knowledge of astrocyte vesicle exocytosis may raise issues about whether this mechanism alone releases sufficient quantities of neurotransmitter to impact neuronal transmission in physiological conditions of astrocyte activation. Indeed, the raises in astrocyte Ca^{2+} previously reported in cultured astrocytes (Parpura & Haydon 2000) are of nM order of magnitude, lower than the μM affinity of synaptotagmin 1 involved in sensing $[Ca^{2+}]$ in neuronal Ca^{2+} dependent exocytosis (see general discussion, chapter 7). This raises the issue of improving the quantitative knowledge of astrocyte $[Ca^{2+}]$ in more physiological conditions which this thesis aims to contribute to. Additionally, the other mechanisms such as release via hemichannels for example may be able to release neurotransmitters in larger quantities. Furthermore, Hamilton suggest that disruption of SNARE proteins or astrocyte Ca^{2+} protocols are necessary but not sufficient on their own as other release mechanisms may also be affected by these disruptions. Indeed, constitutive exocytosis of proteins to the plasma membrane is mediated by endosomes which may also express toxin sensitive SNARE proteins synaptobrevin or cellubrevin. Thus toxin disruption of these SNARE proteins could non-specifically affect both vesicle exocytosis as well as the possible insertion of other transmitter permeable channels in the astrocyte cell membrane. Furthermore, as previously mentioned, transmitter release through hemichannels is also Ca^{2+} sensitive and thus Ca^{2+} disruption alone may affect multiple pathways for gliotransmission, not only Ca^{2+} dependent vesicle exocytosis.

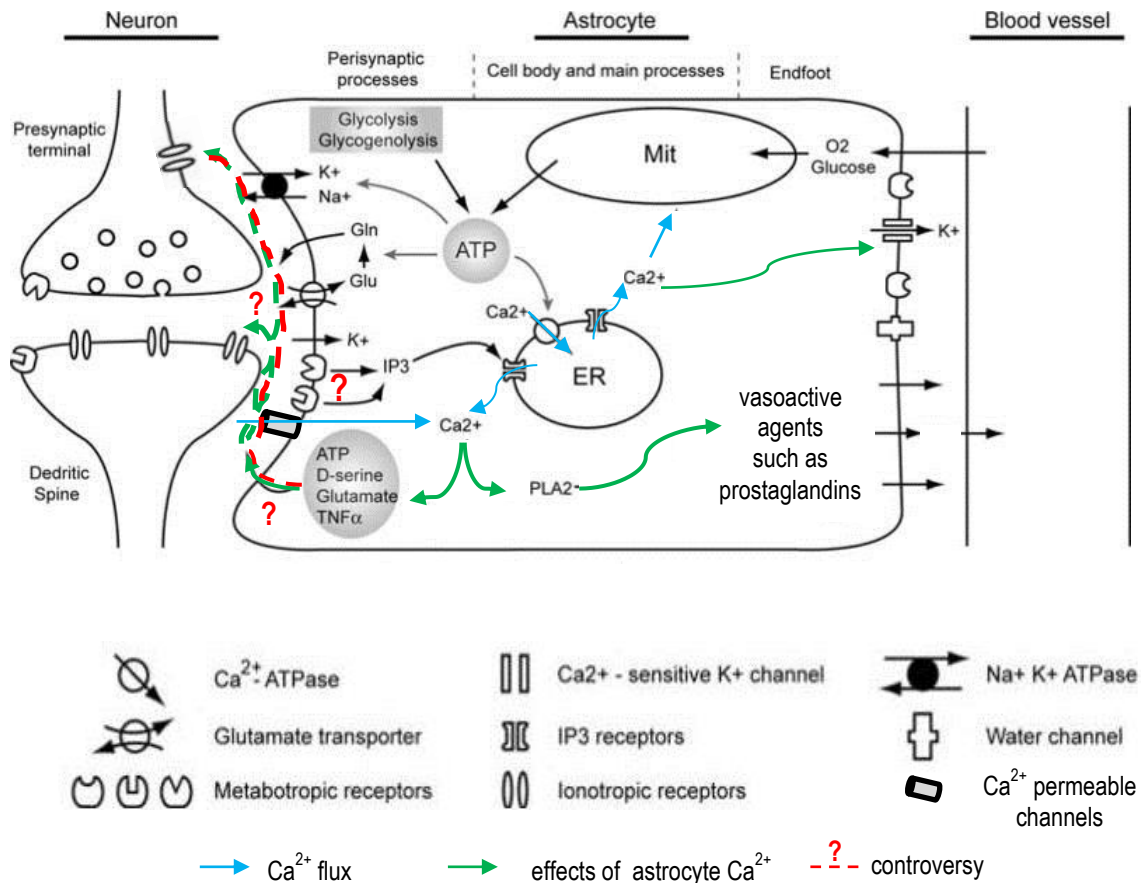


Figure 1.5 astrocyte Ca^{2+} signalling is implicated in astrocyte interactions with neurons, local environment and vasculature

This illustration is adapted from (Wang et al. 2009).

Astrocytes help mediate regulation of the peri synaptic extracellular environment through uptake of K^+ (via Na^+/K^+ pumps for example) and neurotransmitters (such as glutamate transporters) which may be released during synaptic transmission. Astrocyte Ca^{2+} signalling may contribute to the regulation of some of these metabolic processes via interactions with mitochondria and uptake of metabolites from the bloodstream.

Astrocytes can respond to neuronal activity through the release of Ca^{2+} from internal stores through IP_3 released via direct activation of metabotropic receptors by neurotransmitters for example. Additional mechanisms for entry into astrocytes include direct entry through permeable channels, as an indirect consequence of raises in extracellular $[\text{Ca}^{2+}]$ or through activation of channels such as TRPA1.

In turn, astrocytes may release chemicals into the peri synaptic extracellular space through various Ca^{2+} dependent mechanisms. These compounds, such as D-serine or glutamate for example, may in turn affect synaptic transmission and its plasticity through direct activation of ionotropic receptors on the pre or postsynaptic neuronal terminals. Thus gliotransmission is another consequence of astrocyte Ca^{2+} signalling.

Furthermore astrocyte Ca^{2+} signalling can in turn activate the release of vasoactive compounds such as prostaglandins in order to regulate local vasoconstriction of blood vessels.

Astrocyte Ca^{2+} signalling therefore plays a key role in local regulation of blood flow and components of the extracellular space. However, there is some controversy over the physiological relevance of an active role of astrocyte Ca^{2+} signalling for neuronal activity (Algulhon 2008).

ASTROCYTE CALCIUM SIGNALLING

Many of the mechanisms by which astrocytes can integrate and modulate synaptic transmission described above have been shown to involve astrocyte Ca^{2+} signalling. Additionally, astrocyte Ca^{2+} signalling is also thought to mediate local control of cerebral blood flow (Mulligan & MacVicar 2004). Understanding the basis of astrocyte Ca^{2+} signalling is, therefore, paramount for the understanding of the role of astrocyte interactions in brain physiology as illustrated in figure 1.5. Indeed, the mechanisms (reviewed in Hamilton & Attwell, 2010) and the physiological relevance (Agulhon et al. 2008; Agulhon et al. 2010; Petracicz et al. 2014) of astrocyte Ca^{2+} signalling for shaping neuronal transmission and plasticity remain under debate as is discussed in this section, paragraph B (example areas of controversy are highlighted in red question marks in illustration 1.5).

A. Definition of “Resting” $[\text{Ca}^{2+}]$, as used in this thesis

Before going into further detail with regards to astrocyte calcium signalling in the paragraphs below, it is important to clarify what is meant by the term “resting $[\text{Ca}^{2+}]$ ” throughout this thesis. In this thesis, we consider the term “resting $[\text{Ca}^{2+}]$ ” to reflect a basal state of equilibrium between the mechanisms for Ca^{2+} entry and extrusion across the cytosol, extracellular space and the different internal Ca^{2+} stores which are reviewed in (Verkhatsky et al. 2012). These mechanisms may be heterogeneously distributed either across or within astrocytes which may account for resting $[\text{Ca}^{2+}]$ variability reported in Zheng et al. 2015. In simpler terms, we defined it here as the average basal $[\text{Ca}^{2+}]$ during which no apparent Ca^{2+} events occurred. The absence of Ca^{2+} transients can be detected visually for recordings over a few seconds long, as in this thesis in chapters 4, 6 and 7. Or, as in the case of Zheng et al. 2015, the estimation of the resting $[\text{Ca}^{2+}]$ can be gathered as the average value over longer acquisition times (≈ 10 minutes).

Importantly, this definition differs slightly from the more general concept of ‘resting’ state which could perhaps refer to a cell in a state of minimal optimal energy use and deprived of any environmental stimuli (which may potentially only be achieved using an isolated cell in a controlled environment).

Further discussion on the physiological relevance and heterogeneity of astrocyte resting $[\text{Ca}^{2+}]$ can be found in chapter 7.

B. Intra and inter cellular calcium fluctuations are the basis of astrocyte excitability

i. Astrocyte calcium transients

Astrocyte calcium signalling can be observed as many different forms of variations in intracellular calcium: single calcium transient with or without a plateau, repetitive transients or irregular raises in cytoplasmic calcium, as shown for example in spontaneous calcium event recordings (Nett et al. 2002).

These different temporal and spatial forms of calcium transients could result as a function of the type or concentration of the primary messenger (Perea & Araque 2005). Secondly, as gap junctions are permeable to calcium, these transients could also propagate across networks of astrocytes generating intercellular calcium waves which could coordinate the activity of these glial cells (Dani et al. 1992).

The single and repetitive rises of cytosolic calcium play a complex role for initiating intracellular signalling cascades, modulating astrocytic function and intercellular interaction. Indeed, inducible calcium waves, by glutamate or mechanical stimulus, were first described in cultured astrocytes (Cornell-Bell et al. 1990a; Nedergaard 1994). Using astrocyte and neuron co-cultures, Parpura et al. 1994 suggested that evoked Ca^{2+} events in astrocytes could enable these cells to release glutamate leading to the observation of raised Ca^{2+} in the co-cultured neurons. Furthermore, Pasti et al. 1997 demonstrated that such mechanisms enabling Ca^{2+} entry, propagation and removal also occurred in astrocytes in situ. Together, these experiments laid early foundations for the era in which astrocytes would become a recognized functional partner of neurons in information transmission, in particular through Ca^{2+} signalling.

Since then, as described above (see section: astrocytes integrate neuronal activity), many mechanisms mediate astrocyte activation in the form of Ca^{2+} events. Neuronal activity can generate transient astrocyte Ca^{2+} events through Ca^{2+} release from internal stores via activation of metabotropic or TREK1 receptors or directly through Ca^{2+} permeable membrane channels.

Spontaneously occurring Ca^{2+} transients, without experimental stimulation prior to recording, have been recorded in astrocytes in culture (Shigetomi et al. 2012), in situ slice preparations (Parri et al. 2001; Di Castro et al. 2011) and in animals in vivo (Hirase et al. 2004; Srinivasan et al. 2015). These astrocyte Ca^{2+} events may also contribute to shaping neuronal transmission (Parri et al. 2001).

Astrocyte Ca^{2+} transients can also arise independently from neuronal input. Indeed, Ca^{2+} events were recorded in astrocytes in situ in the presence of reduced neuronal activity through TTX mediated block of action potentials (Nett et al. 2002; Hausteine et al. 2014). Such events were also found to occur despite pharmacological blockade of metabotropic (mGluR) or ionotropic (such as N-Methyl D-Aspartate, NMDAR) glutamate receptors (Hausteine et al. 2014).

This could suggest that astrocyte calcium signalling is not merely a means of passively integrating neuronal activity but also, a means of independently initiating the modulation of neuronal function. However, there are also alternative means of mediating neuron-astrocyte interactions without activation of membrane bound receptors. The extracellular calcium concentrations, which decrease for example during neuronal activity, could directly serve as a signal for interaction between neurons and astrocytes (Torres et al. 2012). Another form of receptor-independent Ca^{2+} store release via an IP_3R in astrocytes of the cortex, hippocampus and midbrain, is thought to be mediated by the production of reactive oxygen species that in turn activate the synthesis of IP_3 through the activation of phospholipase C by lipid peroxidase (Vaarmann et al. 2010). Agonist evoked activation of TRPA1 in astrocytes also trigger transient Ca^{2+} events, a potential non neuronal astrocyte activation pathway (Shigetomi et al. 2012).

ii. Calcium micro-domains: possible functional spatial segregation of astrocytic calcium oscillations

Many of the experimental investigations into astrocyte Ca^{2+} signalling have focused on overall cytoplasmic increases in astrocytic Ca^{2+} (for example Cornell-Bell et al. 1990a) with the general observation of Ca^{2+} increases in the soma (for example Navarrete & Araque 2010). However, recent studies have started to further investigate into the spatial-temporal aspects of these Ca^{2+} events. Local small Ca^{2+} transients in small astrocytic processes, the structures that are actually physically surrounding the neuronal synapse, have been identified in situ ('focal' Ca^{2+} events; Di Castro et al. 2011) and in vivo ('twinkle' Ca^{2+} events; Kanemaru et al. 2014). See illustration in figure 1.6. The combination of the local expression of membrane receptors or Ca^{2+} permeable channels, distribution of internal stores as well the local availability (Ca^{2+} affinity and mobility) of cytosolic Ca^{2+} buffers are generally thought to be the molecular determinants of intracellular Ca^{2+} microdomains (reviewed in Rizzuto & Pozzan 2006; Rusakov et al. 2014).

Ca^{2+} increases in these fine astrocyte processes or potential micro-domains, have also been shown to result from single-synapse neuronal stimulation in situ (Panatier et al. 2011). This study suggests that events in astrocyte processes enable astrocytes to detect endogenous basal neuronal activity (potentially through mGluR5 activation) and can upregulate neuronal activity through adenosine activation of presynaptic A_{2A} receptors. In vivo, these small Ca^{2+} events in astrocyte fine processes were recorded following sensory stimulation (Kanemaru et al. 2014; Otsu et al. 2015). Together, these investigations have shown evidence for functional Ca^{2+} signalling micro-domains in astrocyte processes surrounding synapses that could potentially mediate physiological astrocytic neuronal interaction.

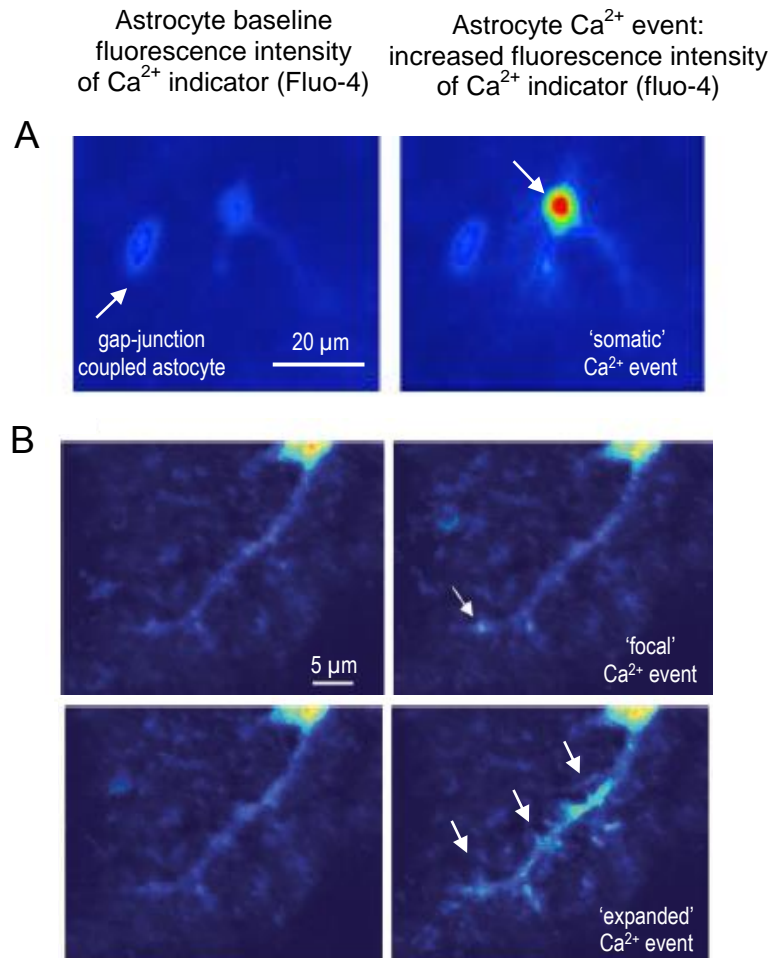


Figure 2.6 astrocyte Ca²⁺ events, examples

This illustration is adapted from recordings in astrocytes in situ by Navarrete & Araque 2010 and Di Castro et al. 2011. See figure 1.7 for example astrocyte Ca²⁺ event traces.

These panels show the fluorescence intensity (pseudocolours) of the Ca²⁺ indicator Fluo-4, loaded into astrocytes in hippocampal slices. The left panels are illustrations of Fluo-4 fluorescence intensity in baseline conditions, prior to any astrocyte Ca²⁺ events. The right panels show illustrations of the same astrocyte during Ca²⁺ events (arrows) as indicated by increased Fluo-4 fluorescence intensity.

Astrocytes show transient raises in their cytosolic [Ca²⁺]. These Ca²⁺ events can occur as a generalised raise across the cell, including the soma (as in A) as well as individual events within the fine astrocyte processes (B). These may be small fast 'focal' localised Ca²⁺ events or larger 'expanded' Ca²⁺ events which could propagate within the larger astrocyte branch or across a larger area of a given astrocyte.

A: astrocyte Ca²⁺ event in response to neuronal depolarisation (Navarrete & Araque 2010)

Average Fluo-4 fluorescence intensity in an individual astrocyte, before (left) and after (right) the electrophysiological depolarisation of a nearby single neuron (to 0mV for 5s) to stimulate endocannabinoid release. Left panel also shows a nearby gap-junction coupled astrocyte (arrow); scale bar 20 μm. The evoked Ca²⁺ event, right panel, appears to be mainly somatic (arrow).

B: spontaneous events in astrocyte processes (Di Castro et al. 2011)

Fluo-4 fluorescence intensity in an individual astrocyte process (scale bar 5 μm). A small localised 'focal' Ca²⁺ event is seen in top left panel whereas an 'expanded' Ca²⁺ event is shown in bottom left panel.

C. Current controversy over the physiological relevance of gliotransmission: the mechanisms underlying astrocyte calcium signalling

i. Does astrocyte Ca^{2+} signalling really affect neuronal activity?

Numerous studies have used pharmacological induced calcium depletion of the endoplasmic reticulum to show that astrocyte calcium signalling generally requires calcium release by internal stores, often in an IP_3R dependent manner. Indeed, both spontaneous astrocyte calcium transients (Nett et al. 2002) and exogenous activation induced astrocyte calcium transients with modulatory influences of the functioning of nearby excitatory synapses (Pasti et al. 1997) were suggested to rely on inositol 1,4,5-triphosphate (IP_3)-dependent cascades.

However, genetic models of this IP_3R pathway have triggered some debate over the physiological relevance of astrocyte calcium signalling, specifically IP_3R dependent gliotransmission. Indeed, increasing astrocyte Ca^{2+} via IP_3R pathway, through the astrocyte specific expression of an artificial Gq protein, did not appear to affect synaptic transmission (Fiacco et al. 2007). Furthermore, the astrocyte-specific genetic suppression of the IP_3R subtype 2 (IP_3R_2) failed to exert any detectable effects on excitatory synaptic transmission in the hippocampus in situ (Petraovicz et al. 2008) leading to questioning the physiological relevance of astrocyte IP_3R mediated calcium modulation of neuronal transmission (reviewed in Agulhon et al. 2008). Similarly, astrocyte specific suppression or enhancement of IP_3R_2 failed to affect synaptic plasticity (Agulhon et al. 2010) and mice with IP_3R_2 -disrupted astrocytes were shown to not exhibit altered behaviours (Petraovicz et al. 2014). However, concomitantly, suppression of endogenous Ca^{2+} activity in individual astrocytes was reported to affect neighbouring synapses in organized brain tissue (Jourdain et al. 2007; Henneberger et al. 2010). Additionally, investigation into the more local astrocyte Ca^{2+} activity in these IP_3R_2 deficient animals suggested that spontaneous astrocytic Ca^{2+} transients in situ mostly, but not entirely, relied on IP_3R_2 (Di Castro et al. 2011). Recently, evidence for differential expression of glutamate receptors in young versus older rodent astrocytes seemed to suggest that there may be an age dependency in the induction of astrocyte calcium oscillations by this specific mGluR/ IP_3R pathway. Indeed this particular mechanism of neuron to astrocyte communication may only occur in young astrocytes due to the lack of mGluR5 (group I protein-Gq coupled mGluR, see chapter 6) expression in older animals (Sun et al. 2013). Olfactory bulb in situ preparations of 2-3 month old mice also revealed a lack of effect of group I mGluRs agonist in eliciting Ca^{2+} events in these adult astrocytes (Otsu et al. 2015). However, Otsu et al. 2015 show that these astrocytes are still able to respond to sensory stimulation in vivo, via Ca^{2+} events in astrocyte fine processes. They also suggest that such Ca^{2+} events, though independent of mGluR, occur sufficiently fast enough to enable these astrocytes to contribute to the regulation of neurovascular coupling and resting vessel tone. These studies suggest that the controversy over the physiological role of astrocyte Ca^{2+} signalling in shaping neuronal activity or indeed neurovascular coupling may arise from an incomplete knowledge of the mechanisms underlying astrocyte Ca^{2+} signalling itself.

ii. mGluR / IP₃R disruption does not affect all astrocyte Ca²⁺ signalling

The specific disruption of the IP₃R₂ pathway does not preclude the possibility of either other IP₃R subtypes or other pathways altogether linking astrocyte Ca²⁺ signalling and neuronal transmission. For example, astrocyte Ca²⁺ signalling is not necessarily always mediated by IP₃R activation. Although significantly reduced, spontaneous Ca²⁺ activity was detected in the IP₃R₂ deficient astrocytes recorded in situ (Di Castro et al. 2011). IP₃R₂ independent Ca²⁺ activity was also recorded in astrocytes in vivo in these animals (Srinivasan et al. 2015). Recordings using the ratiometric high-affinity (K_D ≈50 nM) Ca²⁺ indicator yellow Cameleon-Nano 50, revealed that IP₃R₂-disrupted astrocytes in vivo displayed a reduction in the frequency of Ca²⁺ events in their fine processes ('Twinkle' Ca²⁺ events) yet some of these Twinkle events did persist and their amplitude was not much affected (Kanemaru et al. 2014). IP₃R₂ are therefore involved in the generation of small Ca²⁺ events both in situ and in vivo but other mechanisms also contribute to astrocyte Ca²⁺ signalling.

These advances in imaging astrocyte Ca²⁺ signalling in small fine astrocyte processes in situ and in vivo, contribute to suggest that there are alternatives to the classical understanding whereby neurotransmitters mediate IP₃R dependent release of calcium from astrocytic endoplasmic reticulum to trigger astrocytic modulation of neurons through Ca²⁺ dependent gliotransmission. Indeed, Ca²⁺ entry into astrocytes (reviewed in Verkhratsky et al. 2012) can occur independently of IP₃R mediated activation of the endoplasmic reticulum. Indeed Ca²⁺ can enter astrocytes directly from the extracellular space through Ca²⁺ permeable channels such as voltage activated calcium channels (Parri and Crunelli 2003), cation permeable transient receptor potential receptors A1 (Shigetomi et al. 2011), hemichannels or sodium/calcium exchanger for example. These multiple means to trigger astrocyte Ca²⁺ signals may arise independently or both as direct and indirect result of neuronal activity. Furthermore, astrocyte Ca²⁺ signalling requiring Ca²⁺ release from internal stores does not necessarily require IP₃R activation as store operated Ca²⁺ entry mechanisms (whereby low [Ca²⁺] in the endoplasmic reticulum trigger direct Ca²⁺ entry through channels on the cell membrane) may also exist in astrocytes (reviewed in Verkhratsky & Parpura 2014).

Further understanding of the Ca²⁺ events within these astrocytes may contribute to help bridge the gap between these multiple means of triggering astrocyte Ca²⁺ signalling and the multiple possible consequences of these astrocyte Ca²⁺ events on neuronal activity. Better understanding of astrocyte Ca²⁺ signalling itself (reviewed in Rusakov 2015) may resolve the controversies (as reviewed for example in Agulhon et al. 2008; Hamilton & Attwell 2010) with regards to its role in shaping neuronal transmission and neurovascular coupling (as suggested in Otsu et al. 2015) in brain physiology. In this thesis we aim to use a quantitative approach (fluorescence lifetime imaging microscopy; FLIM) to focus on one aspect of astrocyte Ca²⁺ signalling that has been relatively ignored which is how resting [Ca²⁺] may contribute to shape astrocyte Ca²⁺ signalling.

D. Developing the tools to investigate astrocyte calcium signalling

Technical advances and their adaptation or use in investigating astrocyte Ca^{2+} signalling could contribute to a better understanding of this key component in the interaction between astrocytes, neurons and vasculature in brain physiology (Volterra et al. 2014; Rusakov 2015). Optimising advanced technical tools could help to quantitatively assess the spatial and temporal aspects of defined astrocyte Ca^{2+} events with high resolution in physiologically relevant models such as done by Kanemaru et al. 2014 for example.

i. High resolution imaging reveals the complexity of astrocyte Ca^{2+} signalling

Two-photon imaging has already helped contribute to more precisely decode some of the spatial aspects of astrocyte calcium events in situ (acute brain slices). Indeed, studies such as Di Castro et al. 2011; Panatier et al. 2011; Shigetomi et al. 2013 have shifted the focus from general somatic events to potential micro-domains in the fine processes of astrocytes. These were previously not resolved with techniques such as bath loading of calcium dyes for example (Parri & Crunelli 2003).

Similarly, adapting super-resolution imaging techniques to study astrocyte calcium dynamics could possibly reveal further connections between the specific morphology of astrocytes and their calcium excitability. For example, stimulated emission depletion (STED) could be adapted (Tønnesen & Nägerl 2013) and used to resolve morphological changes in fine peri-synaptic astrocyte processes. 3-dimensional 2-photon calcium imaging would also greatly benefit this investigation as it could reveal true 3-dimensional spatial calcium dynamics within astrocytes in situ or in vivo (Katona et al. 2012).

ii. Physiological approach

Another potential source of conflict within the field is the actual physiological relevance of the current investigations into astrocyte Ca^{2+} signalling.

To counteract this, advances such as in the tools to measure calcium activity are highly relevant. For example, developing better calcium dyes with a higher dynamic range or faster timescale. Genetically encoded dyes (Akerboom et al. 2012) offer additional tools to investigate calcium dynamics at a high spatial resolution without the disruption of whole-cell patch clamp. This approach could facilitate studies in astrocyte processes in vivo, as shown in (Srinivasan et al. 2015). These methods are not without limitations: as well as potential un-physiological effects of genetic overexpression, the tagging of the dye to the membrane could lead to inhomogeneous distribution and perhaps artificially generating local areas of additional Ca^{2+} buffer. Such variations in indicator concentration could bias the assessment of the location of detected Ca^{2+} events for example. However, identifying Ca^{2+} activity in fine astrocyte processes using both methods of patch clamp mediated dye loading (Di Castro et al. 2011) and genetically encoded dye expression (Shigetomi et al. 2013) does give more relevance to the physiological possibility that these Ca^{2+} events actually do occur at the tripartite synapse. In future, the combination of these tools could help towards studying possible functions of these events (for example Hausteine et al. 2014).

Similarly, the better accessibility to in vivo Ca^{2+} imaging has enabled the study of astrocyte Ca^{2+} dynamics in potentially more physiological relevant models revealing the complexities and potential lack of understanding of astrocyte Ca^{2+} signalling (Srinivasan et al. 2015; Kanemaru et al. 2014). Furthermore, The in vivo pathophysiology study of a mouse model of Alzheimer's disease using fluorescence lifetime imaging (FLIM) revealed that the astrocyte Ca^{2+} in this model was generally elevated (Kuchibhotla et al. 2009). Such attempts to quantitatively and physiologically describe specific disease induced alterations in astrocyte Ca^{2+} dynamics could help discern new aspects in the potential mechanisms of such diseases.

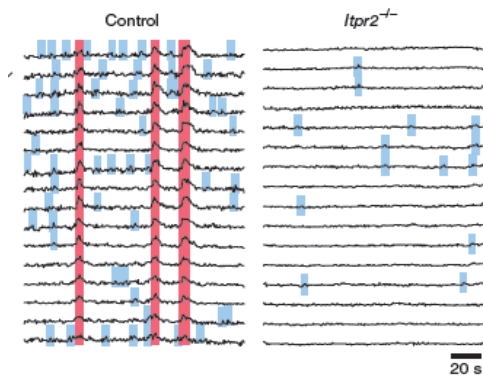
E. Resting calcium and astrocyte IP_3R mediated calcium signalling

The available cytoplasmic $[\text{Ca}^{2+}]$ is determined by a dynamic equilibrium between Ca^{2+} entry from the extracellular space or internal stores, the interaction with cytosolic Ca^{2+} buffers and the Ca^{2+} extrusion mechanisms (into internal stores or the extracellular space) as reviewed in Verkhratsky et al. 2012. Changes in resting $[\text{Ca}^{2+}]$ could contribute to set the availability of some of the mediators of astrocyte Ca^{2+} signalling and thus contribute to shape astrocyte Ca^{2+} events in terms of amplitude, propagation or frequency (as suggested for the generation of neuronal sparks in review Ross 2012). In turn the characteristics of these Ca^{2+} events such as amplitude or frequency may be important to determine the impact of astrocyte Ca^{2+} signalling. For example, the amplitude of a Ca^{2+} event is thought to be important for Ca^{2+} dependent release of synaptic vesicles mediating neuronal transmission (Augustine et al. 1991) and a similar mechanism could mediate Ca^{2+} dependent gliotransmission in astrocytes.

As some evoked and spontaneous astrocyte Ca^{2+} signalling could be mediated by IP_3R dependent Ca^{2+} release from internal stores, the relationship between IP_3R and resting $[\text{Ca}^{2+}]$ could be a possible mechanism that contributes to shape astrocyte Ca^{2+} events and perhaps increase our understanding of astrocyte Ca^{2+} signalling as discussed below.

i. Inositol-triphosphate receptor (IP_3R) dependent Ca^{2+} events in astrocytes

Astrocyte Ca^{2+} events are often found to be dependent on IP_3Rs . For example, there is a reduction in the occurrence of spontaneous Ca^{2+} events in astrocytes after infusing the tissue with heparin (Saleem et al. 2014), an IP_3R blocker (Nett et al. 2002; Parri & Crunelli 2003). A further reduction in frequency of Ca^{2+} events per intracellular region was seen in $\text{IP}_3\text{R}2$ knock-out animals in situ (illustrated in Fig.1.7; Di Castro et al. 2011) and in vivo (Kanemaru et al. 2014). Deletion of these IP_3R dependent Ca^{2+} events in astrocytes in animals genetically created to buffer IP_3 (' IP_3 sponge' mice) is correlated with a loss of astrocyte coverage of synapses in this region (Tanaka et al. 2013). These studies suggest that, although there may be other pathways involved, (Di Castro et al. 2011; Kanemaru et al. 2014; Otsu et al. 2015; Srinivasan et al. 2015) as discussed above, the IP_3R dependent astrocyte Ca^{2+} events are essential to the structure at least of the tripartite synapse.



(Adapted from Di Castro et al. 2011)

Illustration of $\Delta G/R$ calcium dependent fluorescence intensity over time (as measured by Fluo4/TexasRed Dextran) in control astrocytes (left panel) and astrocytes from IP₃R₂ knock-out animals.

The frequency of events (focal in blue, $p < 0.001$, and expanded in red, $p < 0.01$) was significantly reduced in the IP₃R₂ knock-out astrocytes.

Figure 1.7 IP₃R₂ dependent spontaneous calcium events in astrocytes

ii. Inositol- tri-phosphate receptors (IP₃R) are gated by cytosolic calcium concentration

IP₃R_s are key calcium regulators of internal store dependent Ca²⁺ signalling (reviewed in Berridge 1993). The IP₃R is a tetrameric ligand gated Ca²⁺ channel expressed in the membrane of the endoplasmic reticulum across many cell types. IP₃ is synthesised intracellularly by phospholipase-C (PLC) which hydrolyses the membrane phosphatidylinositol-4,5-bisphosphate to generate IP₃. PLC can be induced by the activation of G-protein coupled receptors (GPCR; such as group I mGluRs) on the cell membrane or by reactive oxygen species (ROS). Upon binding of IP₃ the channel is opened which allows for the liberation of Ca²⁺ along the electrochemical gradient from the internal stores into the cytosol (reviewed in Berridge 1993).

IP₃R_s are also sensitive to cytosolic Ca²⁺ concentrations (Bezprozvanny et al. 1991; reviewed in Foskett et al. 2007). The calcium modulation of IP₃R open probability is bell shaped or biphasic where generally submicromolar $< 1 \mu\text{M}$ cytosolic [Ca²⁺] activate IP₃R_s and high cytosolic [Ca²⁺] $> 10 \mu\text{M}$ inhibit IP₃R_s. The extent of this biphasic relationship between calcium concentration levels and open probability depends on the subtype of IP₃R (Fig.1.8). Indeed, with some variation as to the model/protocol used and with all IP₃R_s displaying an initial positive relationship between [Ca²⁺] and open probability, it appears that only IP₃R_s type 1 and 2 exhibit a biphasic relationship in a physiological range of [Ca²⁺] (10 to 1000 nM). Although both IP₃R_s type 1 and 2 exhibit this biphasic relationship, their sensitivity to Ca²⁺ could be differentially regulated by ATP (Wagner & Yule 2012). The type of IP₃R expressed in the astrocyte of interest may therefore play an important role in how the resting [Ca²⁺] could gate IP₃R dependent Ca²⁺ signalling. Astrocytes in culture were shown to express type 2 IP₃R (IP₃R₂; Sheppard et al. 1997; Holtzclaw et al. 2002). Genetic disruption of these IP₃R₂ in hippocampal astrocytes in situ was shown to have a strong reduction of astrocyte Ca²⁺ signalling (as previously described; Petravic et al. 2008). IP₃R₂ opening is thought to be enhanced at cytosolic [Ca²⁺] levels of $\approx 10\text{-}200 \text{ nM}$ (similar to the range of resting [Ca²⁺] recorded in this thesis) whereas higher [Ca²⁺] up to $\approx 1000 \text{ nM}$ may reduce IP₃R₂ open probability (Fig.1.8, traces J-K).

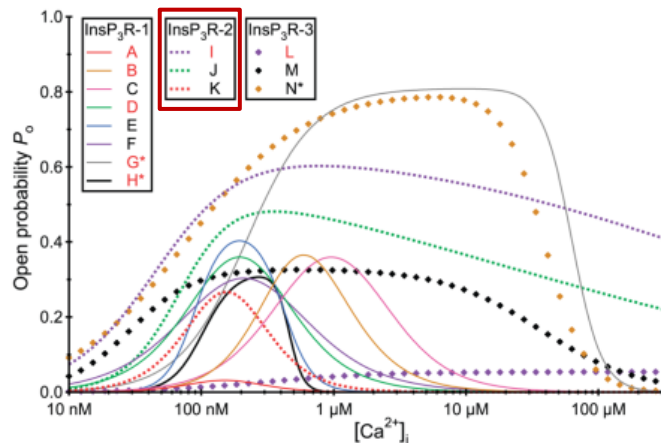


Figure 1.8 Bell-shaped calcium response curves of IP₃R

(Adapted from Foskett et al. 2007)

IP₃R subtypes 1, 2 and 3 show bell-shaped calcium response curves. (first shown by Bezprozvanny et al. 1991)

The letters A-N refer to the vertebrate animal species and cell type where this was tested.

Rodent IP₃R calcium responses are shown in D, H, J, K, where the bell shape of the IP₃R open probability is defined within the 10 to 1000nM [Ca²⁺]_i range.

iii. Cytoplasmic [Ca²⁺]_i gating of IP₃R could modulate the amplitude of calcium events in astrocytes

The non-linear [Ca²⁺]_i sensitivity of IP₃R suggests that cytosolic [Ca²⁺]_i could contribute to regulate or shape the Ca²⁺ transients that determine astrocytic Ca²⁺ signalling. Indeed, alongside the spatial distribution of internal stores and IP₃R, it is possible that the local cytosolic [Ca²⁺]_i could enhance IP₃ activated neighbouring IP₃Rs and perhaps affect the frequency or magnitude of astrocyte Ca²⁺ events which in turn could impact the astrocyte Ca²⁺ dependent phenomenon such as Ca²⁺ dependent gliotransmission. In astrocytes, a computational model (Lavrentovich & Hemkin 2008) has been suggested to explain how small changes in cytosolic [Ca²⁺]_i in combination with the mechanisms for Ca²⁺ release by internal stores could underlie spontaneous Ca²⁺ oscillations in astrocytes with IP₃ generated independently from neuronal activation (through Ca²⁺ activation of PLC as suggested in a model by Meyer 1988). According to this model, small variations in the flux of extracellular Ca²⁺ across the plasma membrane into the cytosol this can cause enough change in the local cytosolic [Ca²⁺]_i to activate Ca²⁺ release from internal stores for the initiation and propagation of Ca²⁺ transients in astrocytes.

In cultured astrocytes, bulk loading of a high affinity Ca²⁺ buffer (based on BAPTA: 1,2-bis(o-aminophenoxy)ethane-N,N,N,N-tetraacetic acid) attenuated the propagation of mechanically induced Ca²⁺ waves across astrocytes (but not the mechanically evoked initial increase in [Ca²⁺]_i in the given astrocyte). This led the authors to suggest that the buffering capacity of a given astrocyte may reduce the [Ca²⁺]_i to below the level required for the propagation of a Ca²⁺ wave (Z. Wang et al. 1997).

Preliminary simulations by Dr C. Henneberger (PhD supervisor), based on the Lavrentovich & Hemkin 2008 model, suggest that there could be an optimal range of cytosolic $[Ca^{2+}]$ for the occurrence of Ca^{2+} transients (Fig. 1.9). High amplitude Ca^{2+} oscillations occurred when the concentration of cytosolic Ca^{2+} buffers was relatively low (black line). Increasing the cytosolic buffer concentration reduced amplitude and frequency of Ca^{2+} oscillations. In both conditions the $[Ca^{2+}]$ before initiation of a Ca^{2+} transient is around 50 nM. Introducing an additional Ca^{2+} buffer equilibrated with Ca^{2+} clamped the resting $[Ca^{2+}]$ to about 100 nM (blue line). No Ca^{2+} oscillations occurred under these conditions. Similarly, lowering the resting $[Ca^{2+}]$ by increasing the rate by which Ca^{2+} is extruded from the cytosol also abolished Ca^{2+} oscillations (green line).

These simulations illustrate that there could be an optimal range of cytosolic $[Ca^{2+}]$ that allows Ca^{2+} transients in astrocytes to occur.

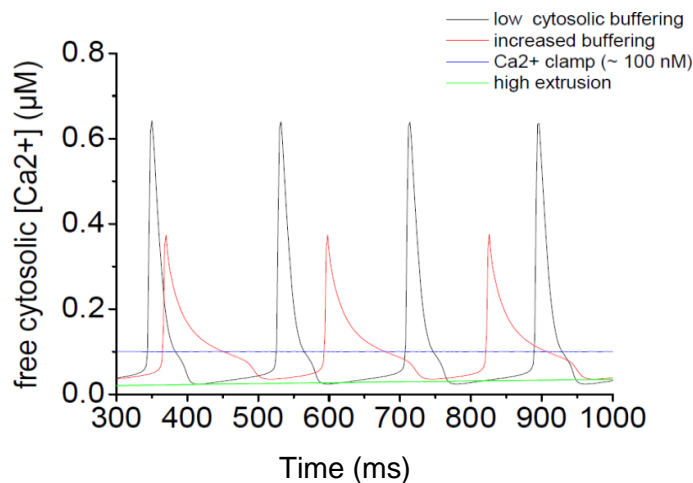


Figure 1.9 simulation of calcium concentration effect on calcium oscillations in astrocytes

Simulation by Dr C. Henneberger

Simulation of how different levels of buffering of cytosolic calcium (low (black), medium (red), calcium clamp (blue), high extrusion (green)) may affect the frequency or the amplitude of calcium transients in astrocytes.

Simulation by Dr C. Henneberger based on a model for the occurrence of spontaneous calcium transients in astrocytes based on a receptor independent IP_3 production and release from internal stores (Lavrentovich & Hemkin 2008)

Taken together, the published properties of IP_3R and exploratory simulations suggest that resting $[Ca^{2+}]$ could be a strong determinant of astrocyte Ca^{2+} signalling. This is a hypothesis that remains, to our knowledge, largely unexplored despite its potential physiological implications for Ca^{2+} dependent astrocyte-neuron communication.

OBJECTIVES

Astrocyte Ca^{2+} signals are strong modulators of synapses and neuronal circuits. However, their physiological role remains an issue of intense research and debate. Recent findings suggest that properties and determinants of astrocyte Ca^{2+} signalling are incompletely understood. One important but largely unexplored factor that could profoundly shape astrocyte Ca^{2+} signalling is the resting $[\text{Ca}^{2+}]$ itself. Therefore, the main goal of this thesis is to understand the role of resting $[\text{Ca}^{2+}]$ in controlling properties astrocyte Ca^{2+} transients *in situ*. To achieve this, we set the following objectives.

- 1) My first objective was to develop, optimise and verify a method to quantitatively monitor $[\text{Ca}^{2+}]$ in astrocytes *in situ* at near-physiological temperatures (33-35 C) in the hippocampus (CA1, stratum radiatum). In chapter 3, I present advantages and disadvantages of several experimental approaches. A modified photon count ratio analysis method (Systma et al. 1998; Agronskaia et al. 2004) of fluorescence lifetime imaging (Wilms et al. 2006) of astrocytes loaded with Ca^{2+} sensitive dyes via patch pipettes was found to optimally measure $[\text{Ca}^{2+}]$ with high spatial and temporal resolution.
- 2) Manipulating resting $[\text{Ca}^{2+}]$ is required to establish a causal relationship between resting $[\text{Ca}^{2+}]$ and properties of astrocyte Ca^{2+} transients. As described in chapter 5, I setup and used a UV LED in combination with fluorescence lifetime imaging for photolysis of caged Ca^{2+} or caged Ca^{2+} buffer within astrocytes to respectively increase or decrease resting Ca^{2+} levels in astrocytes.
- 3) These techniques were then used to investigate the relationship between resting $[\text{Ca}^{2+}]$ and Ca^{2+} transient properties. Chapter 4 investigates how resting $[\text{Ca}^{2+}]$ prior to a transient shapes properties of spontaneously occurring events. Chapter 6 analyses how Ca^{2+} transients evoked by pressure application of an mGluR-agonist (DHPG) are affected by modulation of resting $[\text{Ca}^{2+}]$ mediated by UV photolysis.

Experiments and results are summarized and discussed in chapter 7.

Additionally, I have included the presentation of my work on the presynaptic modulation of synaptic transmission at the Schaffer collateral to CA1 synapse as an annex to this thesis. This work was carried out during my PhD as part of collaboration on a separate project and is therefore not included as a main chapter of this thesis.

Chapter2: RECORDING ASTROCYTE CALCIUM SIGNALING WITH HIGH RESOLUTION AND SENSITIVITY

ACUTE HIPPOCAMPAL SLICE PREPARATION

A. Why the hippocampus?

The hippocampus plays a pivotal role in memory formation. Historically, the case study of patient H.M. epitomises its role in long term memory. Indeed, in order to alleviate his temporal lobe epilepsy, approximately two thirds of his hippocampal formation and para-hippocampal gyrus were removed. Following this treatment he suffered from severe amnesia and even though his short-term memory was still intact he could not allocate new events to long-term memory (Scoville & Milner 1957) . Acute hippocampal slices were used to identify changes in the strength of synaptic connections such as the long term potentiation of synaptic transmission (Bliss & Lomo 1973). LTP and LTD have subsequently been suggested to underlie the cellular basis of learning (for reviews see Bliss & Collingridge 1993; Bliss & Collingridge 2013)

Therefore investigation of the impact of resting calcium concentration on astrocyte calcium signalling in acute hippocampal slices may lay the groundwork for future further understanding of basic neuronal transmission in a cellular near physiological model of learning and memory encoding (Henneberger et al. 2010). Furthermore, the laminar structure of the hippocampus (Andersen et al. 1971; see annex, figure A.1) enables ease of identification of potentially anatomically and functionally similar astrocytes across slice preparations. Always selecting astrocytes of the stratum radiatum of the Cornu Amonis 1 region of the hippocampal slices studied could contribute to reduce the heterogeneity of the astrocyte population investigated in this thesis.

B. Animals used

We used acute hippocampal slices from young adult, three to four week old, male Sprague Dawley rats to investigate astrocyte calcium signalling in situ. The animals are anaesthetised with an intraperitoneal injection of pentobarbitol. Once they are fully deeply anaesthetised, as seen by lack of reflexes and slower breathing, cervical dislocation followed by decapitation was performed before extracting the brain for slicing (described below). All of the animal work was carried out in compliance with the UK Home Office schedule-1 guidelines for the humane treatment of animals used in scientific experimentation as verified by the Denny Brown Laboratory animal husbandry staff at the Institute of Neurology.

C. Dissection and slicing procedure

Following decapitation, a size 20 scalpel is used to cut through the skin and reveal the skull. Incisions are made following the sagittal, occipital and frontal cranial sutures, with care to not damage the brain underneath. The brain is gently removed from the cranium and a rough dissection is made to remove the prefrontal cortex and cerebellum and to separate the two hemispheres. This will speed up the slicing procedure as the blade will have to cut through less tissue. Another cut is made parallel to the middle cerebral artery to remove part of the dorsal cortex. This flat surface will be glued on to the slicing chamber in order to stabilise the hippocampus-brain block which should help produce even slices to minimise damage to cell projections in Z axis. The 350 μ m acute horizontal hippocampal slices (Fig. 2.1.A) are obtained using a Leica VT1200S automated vibrating single use blade microtome set at 0.10mm/s speed with 0.85mm XY amplitude. The Z axis vertical vibration amplitude is set to be less than 1 μ m using the Leica vibrocheck tool.

All the dissection procedures from the moment of decapitation are carried out whilst submerging the tissue in ice cold (0-4°C) sucrose slicing solution containing (in mM): NaCl 60, sucrose 105, KCl 2.5, MgCl₂·6H₂O 7, NaH₂PO₄ 1.25, CaCl₂ 0.5, NaHCO₃ 26, Ascorbic acid 1.3, Sodium pyruvate 3 and glucose 10 (osmolarity adjusted to approximately 310mOsm with additional glucose).

After an initial incubation of 15-20 minutes at 34°C submerged in sucrose solution, the slices are transferred and stored for at least 50 minutes at room temperature (21°C) in a submerged chamber containing artificial cerebrospinal fluid, ACSF, (in mM): NaCl 131, KCl 2.5, MgSO₄·7H₂O 1.3, NaH₂PO₄ 1.25, NaHCO₃ 21, CaCl₂ 2, and glucose 10 (osmolarity adjusted to 295-305 with glucose).

All solutions are continuously saturated with 95% O₂ / 5% CO₂. The CO₂ and NaHCO₂ react to stabilise the pH at approximately 7.4.

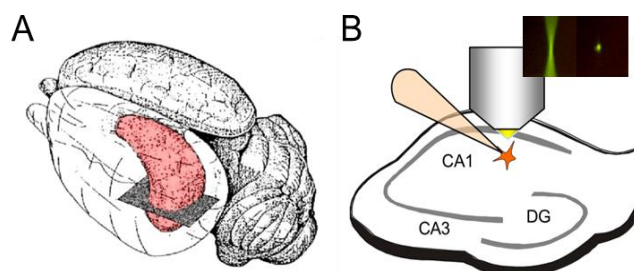


Figure 2.1 Acute hippocampal slice preparation

A. Transverse hippocampal slice, see figure 8.1 for further illustration

(adapted from Cornell University website)

Three dimensional relative position of the hippocampus (pink) in the left hemisphere of the rodent brain and example of the horizontal slicing plane (grey). A further description of the hippocampal formation anatomy is given in figure 8.1.

B. Experimental setup, see figure 5.1 for further illustration

(adapted from Henneberger et al. 2010)

Two photon excitation of whole cell patched astrocytes in the CA1 stratum radiatum of acute hippocampal slices. A photograph of the recording configuration is given in figure 5.1.

WHOLE CELL PATCH CLAMP OF ASTROCYTES

A. Rig configuration

The acute hippocampal slices were placed in an immersion chamber and held in place with a handmade harp (nylon single strands placed every 2mm glued onto a C-shaped flattened piece of platinum). A peristaltic pump (Masterflex L/S, Cole Parmer model 77200-60) was used to perfuse the slice under observation with oxygenated (95% O₂ / 5% CO₂) ACSF at ≈ 2mL/min. The ACSF was pumped through a BC1 heater (Joker communications?) to maintain bath temperature at 32-35°C for recordings at near physiological temperatures. Each slice was allowed to settle in these conditions for at least 25 minutes before recording.

The bath was mounted in a Scientifica motorised platform for X/Y axis positioning and placed above an upright Olympus microscope with built in motorised Z-axis focusing (BX61WI).

Visualisation of the slice was enabled through transmitted light from the halogen lamp in the microscope. This light was collected through an Olympus XLPlanN 25X 1.05 NA water immersion multiphoton adapted objective connected to a near infrared sensitive high resolution camera (Watec, WAT-902H Ultimate) and visualised through Scientifica PatchVision 2.0 software. The stage, microscope, camera were mounted on an antivibration table (Newport).

B. Whole cell patch clamp

The hippocampus slice was visualised through differential interference contrast microscopy. Focusing on the stratum radiatum in the region of the cornu ammonis 1 (CA1) apical dendrites, astrocyte cell bodies were identified as circular structures of approximately 10µm in diameter. They were often easier to spot nearby blood vessels. Not much more than the soma was visible under these conditions (occasionally, it was possible to distinguish larger branches).

Whole cell patch clamp of these astrocyte somas was performed using a 1.5mm outer diameter borosilicate glass with filament (G150F-4, Warner Instruments) pipette made to optimal taper and tip opening (2-5 MΩ) with a horizontal micropipette puller (either DMZ Universal, Zeitz or P-97, Sutter Instruments). The patch electrode was filled with 3-6µL of a low sodium, potassium methane sulfonate (KMS) based internal solution containing (in mM): KMS 135, HEPES 10, MgCl₂ 4, Na-ATP 4, Na-GTP 0.4, di-tris-phosphocreatine 10, (osmolarity 290-295mOsm, pH adjusted to 7.2 with KOH), a calcium indicator fluorophore (100-200 µM) and a morphological indicator (20-300 µM).

The patch pipette was inserted into a microelectrode holder (DB-S-1.5G, G23 Instruments) containing a chloride-coated silver wire connected to a CV-7B headstage (CAT1 <3Vpk, Axon Instruments, Molecular Devices). This ensemble was mounted onto a micromanipulator (PatchStar, Scientifica) on the stage in order to position the electrode near the astrocyte soma.

A small amount of positive pressure was applied before entering the bath. As the pipette was lowered into the slice, the positive pressure was increased and held using a homemade stopcock and syringe combination in order for the pipette to approach the cell with ease through the tissue and without clogging the tip opening. When the tip of the pipette was in contact with the cell, as visualised through a moving dimple in the somatic cell membrane, the pipette offset was set to 0 mV and the positive pressure was released for formation of stable giga-ohm seal. After compensating for pipette capacitance, whole cell patch clamp configuration was achieved by applying negative suction in order to rupture the cell membrane contained within the pipette tip, allowing for diffusion of the indicators and internal solution inside the cell.

The ion flow across the pipette tip opening was measured as the difference between the chlorided silver wire electrode in the pipette and a similar reference electrode placed in the bath. The current was measured in response to a voltage 10 mV square pulse step. The response was amplified (Multiclamp 700B, Axon Molecular Devices) and converted from analogue to digital signal at 10 kHz sampling rate (Digidata 1440A, Axon Molecular Devices) in order to be monitored and controlled with Clampex 10.2 software. 50 Hz noise was eliminated with a HumBug, Quest Scientific.

C. Confirming astrocyte identity

We used the following criteria to define and select protoplasmic astrocytes: small soma (10 μ m), resting membrane potential between -80 and -90 mV (no liquid junction potential compensation), electrically passive cell, input resistance 15 M Ω or less, gap-junction coupling and stereotypical morphology (illustrated in Fig2.2).

The resting membrane potential was taken as the voltage recorded for no current injection. It was closely monitored in current clamp during the imaging recordings and any cell depolarised above -80mV was discarded as an indication of ill-health or a non-astrocyte cell. Access resistance was kept at less than 20M Ω in order to help sufficient diffusion of the calcium indicator within the cell. Access resistance was estimated through the current response to 10 mV square pulse in voltage clamp for 15 minutes after going whole cell, cells were discarded if the access resistance changed by more than 20% and pressure application or pipette positioning were not able to restore good access to the cell. It was monitored during recordings in current clamp by using the automatic bridge balance compensation in the Multiclamp 700B software.

In current clamp mode, 6x 200 pA current steps (from – to +) were injected. The voltage response was used to identify electrically passive cells and measure input resistance with Ohm's law having tried to compensate for the access resistance and pipette resistance. The input resistance being so small in astrocytes, it can be hard to distinguish it from the series resistance for an accurate estimation. However, astrocytes have such low input resistance that the whole cell current response to a square pulse is very characteristic, so even if the estimated input resistance value is not exact it is still easy to determine that the patched cell has a lower than 20 M Ω input resistance.

After 15 minutes to allow for a stable loading of the dyes and equilibration of the patched cell with the internal solution in the pipette, further confirmation is achieved based on the characteristic morphology as well as the loading of Gap-junction coupled cells (Fig. 2.2.B). Indeed, this further step allows for distinction from NG2 cells which may have similar passive properties and small somas but lack extensive Gap-junction coupling and exhibit finer main processes with less extensive arborisation. The combination of these properties allows for the selection of protoplasmic passive astrocytes under the current consensus definition (International Astrocyte School, 2012).

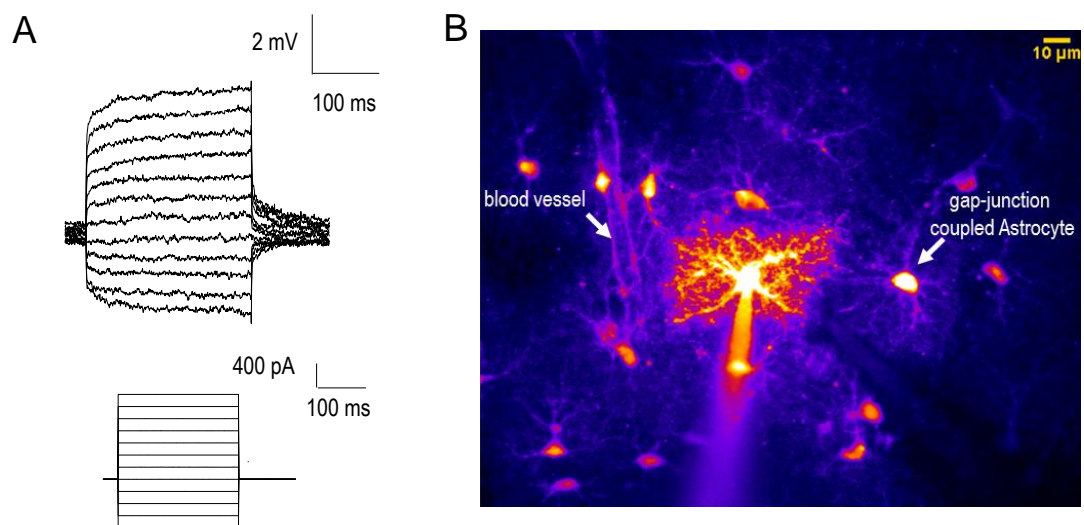


Figure 2.2 Identification of astrocytes in acute hippocampal slices

A. Passive electrophysiological properties, example trace

The top traces show the voltage response (scale bars 2mV and 100ms) recorded in a whole-cell patched astrocyte in the CA1 stratum radiatum of a P21-26 male rat acute hippocampal slice perfused with oxygenated ACSF at 32-34°C. This passive voltage profile is recorded in response to 250ms current injection in steps of 200pA from -800 to +1400 pA (as shown in lower trace; scale bar 400pA, 100ms).

Similar protocols were used for each whole-cell patched cell (although generally current injections were in 200pA steps from -600 to +600pA). This enabled to verify that the patched cell had both low input resistance (<20MΩ; calculated with Ohm's law; $R=U/I$) and was electrophysiologically passive. These electrophysiological criteria contributed to characterise cells recorded in this thesis as protoplasmic astrocytes (also see figure 1.4).

B. Morphological characterisation, example illustration

The loading of the patched cell with a morphological dye, such as A594, allows for identification of the distinct astrocyte morphology as well as evidence of gap junction coupling and occasionally endfeet projections onto neighbouring blood vessels (see arrows). This illustration is an average of the fluorescence intensity of morphology indicator A594 (100 μM) in a whole cell patched astrocyte. Single frames were taken every 1 μm between ≈ 30 μm and 100 μm from the surface of an acute hippocampal slice of a P22 male rat at 32-35°C, scale bar 10μm.

CALCIUM IMAGING

A. Setup configuration

A SpectroPhysics Maitai Ti:Sapphire 200 femtosecond pulsed laser (80 MHz repetition rate) at a suitable infrared wavelength (800 nm) is used for two photon excitation of fluorophores loaded into the patched astrocyte. 2-photon excitation enables the imaging of cells deeper in organised tissue by reducing excitation scattering. In acute brain slices this should help image more physiological properties supposing that these deeper cells and their connections are less exposed to the trauma of slicing procedure relative to more superficial tissue. Infrared excitation is less prone to scattering, causes less photodamage and less autofluorescence compared to more visible-blue light. Combined with the reduction of background noise as only a reduced set of fluorophores in the focal plane will absorb both photons (Fig. 2.1.B), 2photon excitation allows for a high resolution and sensitivity imaging of astrocyte calcium signalling (principle reviewed in Svoboda & Yasuda 2006).

The resulting emission is split using an appropriate dichroic across two photomultiplier tubes, that enable amplification of the resulting excitation of the fluorophores, equipped with appropriate emission filters to distinguish fluorescence emitted by the different dyes used. I used either Bio-Rad Radiance 2100 for calcium intensity measurements or the Olympus Fluoview FV1000MPE for calcium intensity and lifetime measurements.

A calcium sensitive fluorophore, dyes whom upon binding to calcium show a notable and linear increase in fluorescence emission for a given excitation across a range of free $[Ca^{2+}]$, is used as an indicator of changes in free Ca^{2+} levels. For fluorescence intensity measures, calcium indicator fluorescence emission needs to be normalised to a calcium insensitive dye, such as Alexa 594, in order to account for non-calcium related changes in emission such as fluctuations in cell volume and depth (Yasuda et al. 2004; Fig. 2.3). This also allows for morphological identification in order to assess the spatial characteristics of the calcium signal under investigation such as volume fraction or defining soma versus process calcium signalling (for example Di Castro et al. 2011).

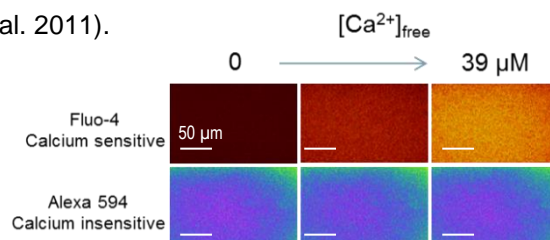


Figure 2.3 normalisation of fluorescence intensity of Fluo-4 to A594, principle.

Normalisation of a calcium sensitive dye (Fluo-4, top row) to a calcium insensitive dye (A594, bottom row) helps account for changes in cell depth or volume when considering fluorescence intensity Ca^{2+} imaging. Using a set of internal-like solutions and a decreasing concentration of Ca^{2+} buffer, here EGTA, one can calibrate the fluorescence intensity of the dye to known free $[Ca^{2+}]$. This is done for a specific imaging setup with the desired dye concentration. Although this is an illustration of a Ca^{2+} calibration I recorded in solution in glass slides (scale bar 50 μm), the aim is to be able to similarly calibrate the fluorescence intensity for free $[Ca^{2+}]$ in a given astrocyte in situ.

B. Calcium indicator dye selection

In order to gain realistic insight into astrocyte calcium signalling, an appropriate balance between imaging optimisation and physiological considerations needs to be established. Choosing the appropriate calcium imaging dye is one of the key factors for this purpose.

As illustrated in figure 2.3, both a morphological calcium insensitive dye and a calcium indicator are needed for estimating calcium transients with high spatial resolution and sensitivity using fluorescence intensity imaging.

i. Dye diffusion

In order to provide an accurate indication of calcium dye concentration for normalisation, the calcium insensitive dye needs to have similar interactions with the cell environment to the calcium indicator. An indication for this is assessing the diffusion rate of both dyes across the astrocyte the gap coupled cells. Timelapse intensity measures of the saturated calcium dye and the morphological indicator from the point of breaking into whole cell configuration indicate that the commonly used dyes (Fluo4 and A594) do not diffuse at the same rate (experiments performed by Dr L Bard, in the lab). Indeed, despite both dyes having similar molecular weight, A594 seems to leak into gap junction coupled cells faster than Fluo4. This has the additional issue of rendering morphological identification more complex. The use of 3000 Dalton dextran conjugated dyes (such as Texas Red for morphology and Calcium green for calcium) sequesters the indicators to the patched cell as they are no longer able to diffuse through gap junctions.

ii. Affinity for calcium

This leads to the second issue which is the selection of the optimal calcium indicator for detecting spontaneous astrocytic calcium transients. Calcium indicators can be selected by their affinity for calcium (K_d for calcium, which is strongly dependent on the indicator environment). Indeed, for this project we need a dye with medium affinity (K_d 300-400nM, such as Fluo-4) in order to detect both changes in basal cytosolic calcium concentration and the amplitude of calcium transients.

iii. Dynamic range

The shift in fluorescence intensity of the calcium indicator as a function of free $[Ca^{2+}]$ needs to be large enough for a sensitive measurement of physiological changes in cytosolic $[Ca^{2+}]$. This is a function of the intrinsic properties of the dye, as a result in part of its quantum yield. Therefore, fluo-4 seems like an optimal dye as its fluorescence intensity increases 40-100fold (Invitrogen) between free and saturating levels of $[Ca^{2+}]$ compared to calcium green for example which only exhibits a 5fold increase in intensity.

Dye selection is key to calcium imaging and requires constant optimisation with the development of new indicators (Teflabs). Alternatives are discussed in the next chapter.

DISCUSSION

A. Patch clamp loading vs ester-loading vs genetic-targeting

Although patch clamp loading dyes is by definition disruptive due to mechanical damage during patch procedure as well as artificial wash out of internal astrocyte constituents, it does have advantages over ester-dye loading and potentially genetic-dye targeting. Indeed, it provides an additional means of qualifying both cell health (through RMP monitoring for example) and cell identification (see above mentioned astrocyte characteristics).

Ester-loading requires incubating the astrocytes in pluronic acid and DMSO, which are potentially disruptive of cell health. More importantly, ester-loading is not cell type specific. This is particularly important in the periphery of the astrocyte where thin astrocyte processes, which often cannot be resolved by diffraction-limited microscopy, extensively overlap with neuronal processes. The recorded Ca^{2+} dependent fluorescence may thus originate from both astrocytes and neurons in the astrocyte periphery which makes it difficult to ascertain the cellular origin of the recorded Ca^{2+} signal. For this technical reason a substantial number of studies have relied entirely on somatic recordings from astrocytes in conjunction with an astrocyte marker such as SR101. Thus, using this non-astrocytic specific ester loading method, it would be difficult to distinguish neuronal from astrocyte processes when investigating the finer processes, where most calcium activity is thought to occur (Di Castro et al. 2011; Kanemaru et al. 2014). This is also the region which is probably most relevant for understanding astrocyte-neuron interactions.

Genetically targeting dye expression to specific cell types offers a whole new range of experimental approaches (Akerboom et al. 2012). This method allows easy access to detect Ca^{2+} events across the whole of the astrocyte domain (Shigetomi et al. 2013)

However, as with the above mentioned techniques, this method is also likely to impact cell health/function primarily due to genetic overexpression. The genetic overexpression of a Ca^{2+} indicator, and thus a Ca^{2+} buffer, takes place over time and therefore may affect development. It is also possible that compensatory mechanisms are put in place to insure cell function/viability. Significantly, in the context of this thesis, the current genetically encoded Ca^{2+} indicators do not show $[\text{Ca}^{2+}]$ dependent lifetimes so cannot be used for fluorescence lifetime imaging. Therefore, it is difficult to distinguish heterogeneities of indicator distribution from variable resting $[\text{Ca}^{2+}]$ in a cell. This approach to indicator delivery into astrocyte is therefore not currently suitable for the quantitative investigation of astrocyte Ca^{2+} signalling.

The whole-cell patch clamp dye-loading method was therefore used as the best compromise to achieve a quantitative readout of calcium signalling with appropriate spatial resolution.

B. Astrocyte preparation: slices vs culture vs in vivo

In principle, it would be possible to investigate the role of resting $[Ca^{2+}]$ in shaping Ca^{2+} signalling in astrocytes in culture, in situ and in vivo.

Astrocytes in culture are very accessible compared to astrocytes in situ or in vivo. This would ease pharmacological manipulations and control of the local environment for example. However, in cultured astrocytes the development and morphology for example greatly differ from that of astrocytes in situ. In contrast with cultures, acute slice preparations preserve some of the tissue organisation and structure. Until the point of slicing, the astrocyte's local environment, interactions and development are indeed preserved. This model enables relatively easy access to individual cells whilst preserving a potentially more physiological environment in comparison to culture preparations. However, acute slicing is a traumatic event and from the point of starting this preparation, tissue viability slowly degrades. Using controlled extracellular environment (such as high osmolarity, cold temperatures, reduced $[Ca^{2+}]$ or the addition of antioxidants) whilst slicing the tissue can help reduce or slow the trauma.

In vivo models (Kanemaru et al. 2014; Srinivasan et al. 2015) in awake (Thrane et al. 2012) animals may have higher physiological relevance. Indeed, this model would allow access to physiological stimulation protocols with potentially minimal disruption to the astrocyte's physiological environment when compared to culture or in-situ models. However, single-cell quantitative studies would be more technically challenging. Bulk-loading or genetically encoding dye-loading techniques would be easier to implement in vivo than whole cell-patch clamp of individual astrocytes due to their small size, difficulty in access and movement (such as breathing) related issues. However, as described above, these techniques are not well-suited to this project.

Despite their shortfalls, astrocytes in acute in-situ preparations are a common compromise between physiological relevance and cell access when investigating astrocyte calcium signalling. We therefore used the whole-cell patch clamp loading of calcium indicators in individual astrocytes in acute hippocampal slices to quantitatively dissect the potential relationship between resting $[Ca^{2+}]$ and astrocyte Ca^{2+} signalling in this thesis.

Chapter3: QUANTITATIVE ESTIMATION OF CALCIUM CONCENTRATIONS

The main objective in this chapter was to adapt and calibrate a method for a quantitative readout of astrocyte $[Ca^{2+}]$ recorded in situ (acute hippocampal slices of young adult, P21-25, rats) at near physiological temperature (32-34°C).

Classically, the steady state calcium concentrations can be estimated from the following equation:

$$[Ca]_i = K_d \cdot \frac{F - F_{min}}{F_{max} - F}$$

Where K_d is the dissociation constant and F_{MAX} , F and F_{MIN} represent maximum, steady state and calcium independent fluorescence of the calcium indicator (for experimental example see (Scott & Rusakov 2006).

This relationship depends on the assumptions that the calcium indicator forms a simple one to one complex with calcium, that the K_d in cells is similar to in calibration solutions and that it is sufficiently dilute for fluorescence intensity to be linearly proportional to the concentration of the fluorescent dye. It therefore requires that F , F_{MIN} and F_{MAX} all be determined at the same instrumental sensitivity, optical path length and effective concentration of the calcium indicator (Grynkiewicz et al. 1985).

Indeed, in order to compare calcium levels across cells acquired using similar protocols, we need to be able to calibrate the normalised calcium indicator fluorescence intensity to differences in cell depth or laser power across recordings. Although calibration of the fluorescence intensity for known free $[Ca^{2+}]$ is a useful indication of the range of dynamic, estimating F_{MAX} and F_{MIN} in the actual cellular environment will help account for the behaviour of the indicators in pH, temperature, other divalent ion concentration and buffering capacity inside the cell.

In this chapter I report fluorescence intensity calibration method we first tried to develop in order to quantify $[Ca^{2+}]$ in astrocytes in situ. The first section of this chapter is an illustration of this potential method. However, the subsequent recordings presented throughout the thesis use a second method for a quantitative readout of $[Ca^{2+}]$ in astrocytes in situ, described in the second section of this chapter: fluorescence lifetime imaging. Therefore, more detailed description of the recording setup and calibration procedures are given for FLIM recordings. This method was adapted for OGB-1 by Dr K. Zheng (Zheng et al 2015) and in this chapter I describe the FLIM method and the Ca^{2+} calibration I performed for OGB-2 with the help of Dr C. Henneberger for analysis and simulations.

FLUORESCENCE INTENSITY $[Ca^{2+}]$ CALIBRATION

A. Background correction

Analysis of the acquired timelapse calcium images is performed using ImageJ software (NIH). Selection of the region of interest is based on the morphology of the astrocyte (soma versus processes). The peak intensity per frame for this region is measured in both the calcium indicator and morphology channels. Correction for the instrumental offset to the fluorescence intensity is achieved by subtraction of the intensity in a large region selected at the beginning of a frame while the shutter is still closed. Indeed, due to the substantial arborisation of astrocytes as well as the extensive gap junction coupling, it seems unlikely that using a region in the background of the actual frame would reflect solely system noise. After normalisation by the background corrected morphology indicator intensity, the results are displayed as normalised fluorescence intensity per unit of time (as set during acquisition).

B. F_{MAX} : indicator fluorescence for near dye saturation $[Ca^{2+}]_{free}$.

i. Calcium ionophore method

The common tool for the measure of F_{MAX} inside the cell is the use of a ionophore (Fig.3.1) such as Ionomycin (Invitrogen, I-24222, reviewed in Pressman 1976) which creates supposedly calcium specific pores in the cell membrane allowing for a flow of calcium from the extracellular space according to chemical gradient (extracellular $[Ca^{2+}] > intracellular [Ca^{2+}]$). Indeed, ACSF contains 2mM $CaCl_2$ versus KMS with little or highly buffered calcium, basal resting calcium being roughly 50nM (see chapter 7; Zheng et al, 2015). More recently, it has been shown that it also increases Ca^{2+} through emptying internal stores (Muller et al. 2013). Whichever mechanism is involved for Ca^{2+} entry into the cytoplasm, this is an attractive method as it can lead to measuring F_{MAX} inside the cell (thus accounting for intracellular Ca^{2+} buffering mechanisms) for the same given parameters of the fluorescence intensity calcium imaging experiment (such as excitation laser power, cell depth, temperature).

However, we found that in our hands, a bath application of 200 μ M Ionomycin did not always lead to the saturation of Fluo-4 / A594 (200 μ M and 10 μ M respectively; Fig. 3.1.B). Indeed, this method seemed unreliable specifically as it did not always induce dye saturation (calcium transients of larger amplitude than the Ionomycin induced plateau (Fig. 3.1.B, right) or no plateau (Fig.3.1.B, left). One possibility would be to increase the external calcium concentration after recording an Ionomycin induced plateau to make sure that there is no further increase in calcium indicator intensity. One could also expect that a more localised application through pressure application of Ca^{2+} ionophore would lessen the potential hindrance due to the layers of organised tissue above the patched cell. Given these difficulties, we devised another method altogether for the estimation of F_{MAX} fluorescence intensity measurements inside whole-cell patched astrocytes in acute slices.

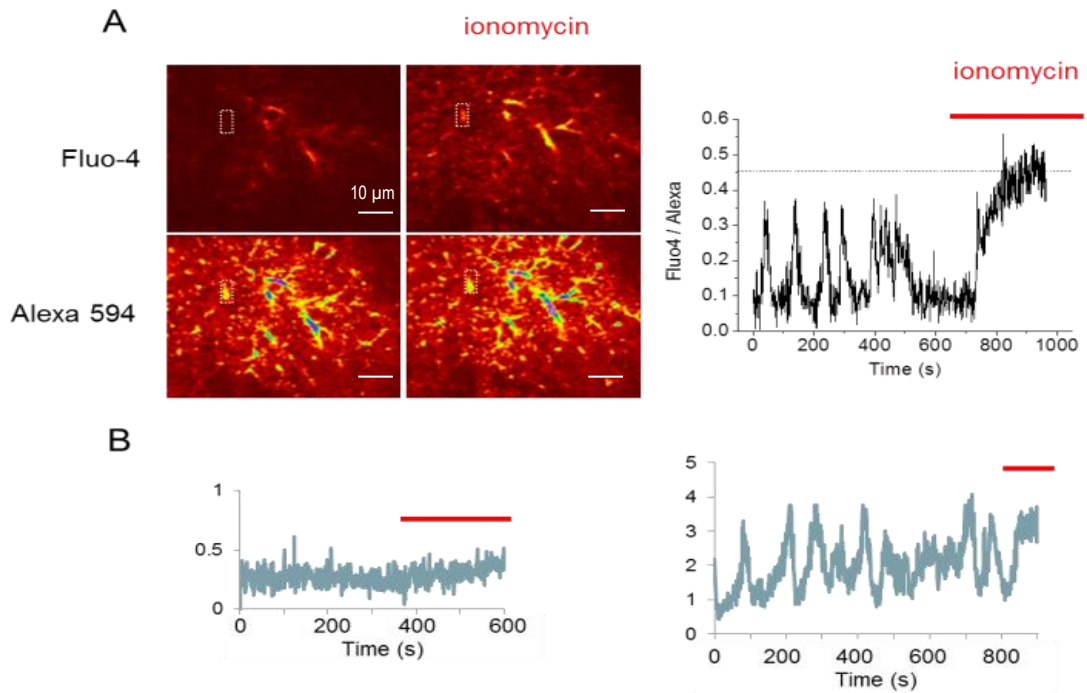


Figure 3.1 Ionomycin is not a reliable means of determining F_{MAX} in situ, in my hands.

A. Principle of Ionomycin method for F_{MAX} in situ.

The picture illustrates the average fluorescence intensity of Fluo-4 (top panels) and Alexa594 (bottom panels) in the same cell, same field of view (periphery processes; scale bar 10μm) recorded over 50 continuous frames (≈ 1 frame/second) either immediately before (right) or 5 minutes after (left) ionomycin bath application (200μM). The trace (A, right) shows the normalised fluorescence intensity (Fluo4/A594; $\Delta G/R$) over time recorded in the region of interest highlighted on the cell picture. Ionomycin application is marked in red. This region shows spontaneous Ca^{2+} transients and then a plateau increase in normalised fluorescence intensity after Ionomycin application. Time lapse fluorescence intensity/ Ca^{2+} imaging was acquired at 1 frame/ second from individual whole cell patched astrocyte in the stratum radiatum of the CA1 region of acute hippocampal slices (male rat, P21-26) perfused with oxygenated ACSF at 32-34°C (see chapter 2).

B. Examples of possible in situ bath application of Ionomycin issues

In some cases of this bath application method of Ionomycin, I failed to record saturating levels of fluorescence intensity. Example timelapse traces of such issues are illustrated here.

The left panel illustrates the failure to increase fluorescence intensity after Ionomycin application (red): either this particular cell was at already saturating $[Ca^{2+}]$ for Ca^{2+} indicator used (due to patch or slice quality for example) or the Ionomycin application failed, perhaps insufficiently penetrating the slice resulting in too fewer permeable pores in the cell of interest.

The right panel illustrates an increase in fluorescence intensity after Ionomycin application (red) that is below dye saturation level as previous transients reach higher fluorescence intensity levels.

ii. High $[Ca^{2+}]$ calibration probe method

In a second approach to estimate F_{MAX} in non-excitable cells, as close as possible to cell conditions, we proceeded to use a high known calcium concentration KMS solution in a pipette as a reference calibration probe. This required a high-calcium KMS based internal solution containing (in mM): KMS 140, EGTA 10, $CaCl_2$ 9, HEPES 10, di-tris-phosphocreatine 10, MgCl 4, Na₂-ATP 4, Na-GTP 0.4. According to WebmaxC program (MaxChelator, Stanford) for dissociation constants in pH of 7.2 at 34°C conditions, this solution should have an approximate free $[Ca^{2+}]$ of 1.3 μ M which should be roughly 80-90% saturation of Fluo-4. To see the effect of intracellular composition on this high calcium solution we then proceeded to patch astrocytes with the high calcium KMS and measured the normalised calcium indicator fluorescence in the pipette tip, soma and large processes (Fig. 3.2). As these intensity values were roughly similar in both the pipette and the patched cell, we thought to use a patch pipette with this high calcium solution as F_{MAX} or calibration probe. By placing such a pipette nearby the patched cell after recording astrocyte calcium signalling, we have a simple approximation of F_{MAX} value for given experimental conditions.

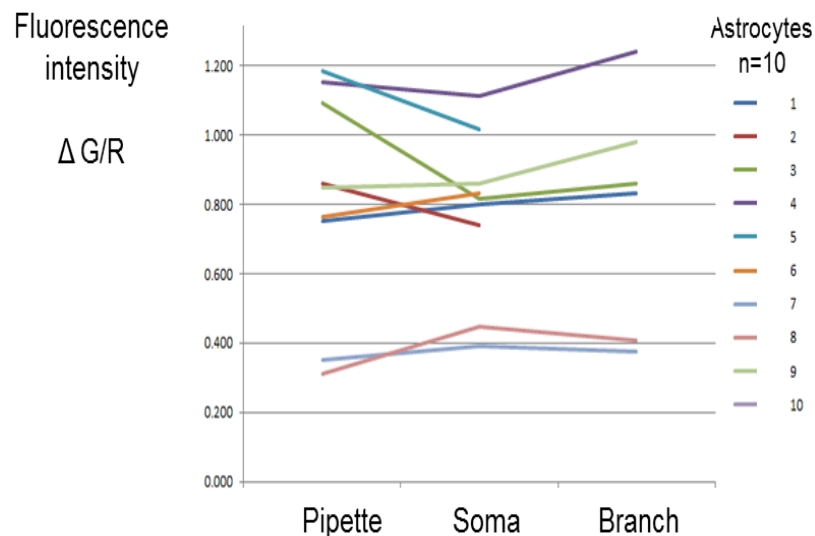


Figure 3.2 High $[Ca^{2+}]$ KMS solution in pipette may be used as a probe for estimating F_{MAX} in situ

10 astrocytes (individual colours, right axis) were whole-cell patched with a high $[Ca^{2+}]$ KMS internal solution (composition described in text). Recordings were done using 2-photon Ca^{2+} imaging in acute hippocampal slices of P21-26 male rats (in CA1 stratum radiatum) superfused with oxygenated ACSF at 32-34°C (chapter 2). The fluorescence intensity (left axis), Ca^{2+} indicator (Fluo-4) normalised to the morphological indicator (A594; $\Delta G/R$), was measured at three different visually identified regions: pipette tip, astrocyte soma and large astrocyte branch (horizontal axis).

C. F_{MIN} , calcium indicator fluorescence for zero free calcium

KMS based internal solutions are ideal for investigating astrocyte calcium signalling due to the fact that methanesulfonate is less likely to affect calcium levels than gluconate for example (Christoffersen & Skibsted 1975) which is also a commonly used internal solution. When measuring the indicator fluorescence of the internal solution only in a patch pipette as would be the case prior to patching the astrocyte, the intensity was surprisingly high as opposed to a “high calcium internal solution” (Fig.3.3.B). This was also the case in the pipette of the whole cell patched astrocyte, at least at the beginning of the recordings. Although this could be a means of testing the health or buffering capacity of the patched cell, when measuring calcium concentrations, one would hope to limit additional exogenous calcium.

It was observed that internal solutions prepared from KOH and methane sulfonic acid as opposed to salt forms of KMS had a tendency to show less calcium contamination. This could be due to the purity and multiple use of the salts. Despite extra care taken in the preparation of KMS internal solution (use of calcium free distilled water, higher purity salts), for calibration purposes an additional KMS based internal solution was made containing a high concentration of EGTA, calcium buffer, (in mM): KMS 140, EGTA 10, HEPES 10, di-tris-phosphocreatine 10, MgCl 4, Na₂-ATP 4, Na-GTP 0.4. In this case, F_{MIN} was found to be close to zero although occasional checks should be repeated using the previously described calcium probe.

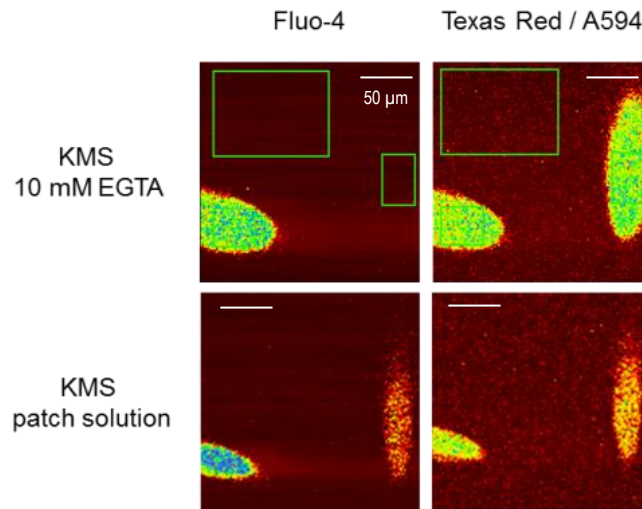


Figure 3.3 F_{MIN} is determined by imaging pipettes containing KMS + 10mM EGTA.

This illustration shows 2-photon excitation at 800nm of Ca^{2+} indicator (right panels; 200 μM Fluo-4) and morphology indicator (left panels; 300 μM Texas red and 5 μM A594; for normalisation and position) in the same field of view (from left to right) of borosilicate glass pipettes containing KMS-based internal solutions. The rectangles indicate example regions of interest (outside of pipettes for background fluorescence intensity and within pipette); scale bar 50 μm in all panels.

Top panels: F_{MIN} solution

The vertical pipettes are loaded with KMS to which 10 mM of the Ca^{2+} buffer EGTA has been added in order to measure the fluorescence intensity of the Ca^{2+} indicator (200 μM Fluo-4) at minimal [Ca^{2+}].

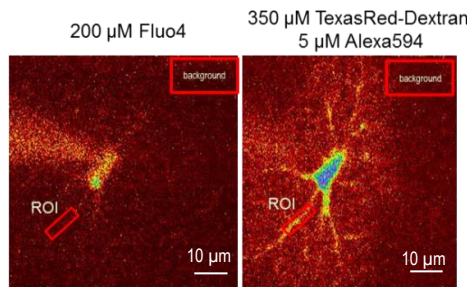
Bottom panels: patch solution

The vertical pipettes are loaded with the KMS based internal solution used routinely for whole cell patch clamp of astrocytes throughout this thesis (no additional Ca^{2+} buffers other than Ca^{2+} indicator 200 μM Fluo4; chapter 2). The residual fluorescence could result from Ca^{2+} contamination from the external ACSF or during the internal solution preparation (although no single component was identified, not shown).

The horizontal pipettes in all panels contain high [Ca^{2+}] KMS (see F_{MAX}) to indicate the range of fluorescence intensity.

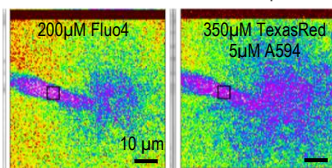
D. Fluorescence intensity based estimation of $[Ca^{2+}]$ using F_{MIN} and F_{MAX} probes

A. Record Ca^{2+} transients



B. Calibration

High $[Ca^{2+}]$ probe pipette
 -same cell depth
 -same excitation/detection parameters



C. Estimate calcium concentration

Fmax: Fluo4/Texas Red Intensity Ratio: 1.03

$$[Ca]_i = K_d \cdot \frac{F - F_{min}}{F_{max} - F}$$

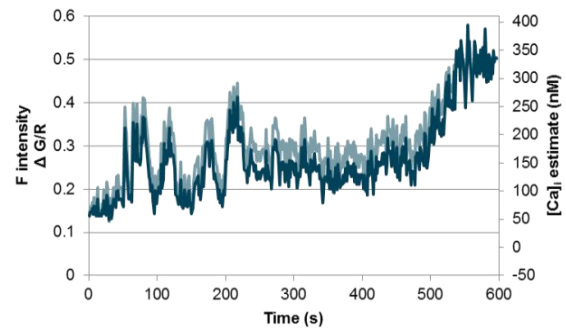


Figure 3.4 example use of F_{MIN} and F_{MAX} pipette probes to estimate $[Ca^{2+}]$ from

fluorescence intensity recording of Fluo-4 in a whole-cell patch clamped astrocyte, in situ

A. Fluorescence intensity timelapse recording of astrocyte Ca^{2+} in situ

2-photon excitation of a Ca^{2+} indicator (left panel; 200 μ M Fluo-4) and morphology indicator (right panel; 350 μ M TexasRed-Dextran, 5 μ M A594) enables the timelapse (1frame/s) acquisition of fluorescence intensity Ca^{2+} imaging of resting Ca^{2+} and Ca^{2+} transients in a whole cell patched astrocyte in the CA1 stratum radiatum of P21-25 rat acute hippocampal slices perfused with oxygenated ACSF at 32-34°C. Fluorescence intensity in the region of interest (ROI) is corrected for background noise from a region outside of the patched cell (background rectangle). Illustration is a single frame of fluorescence intensity; scale bar 10 μ m.

B. Calibration using F_{MAX} and F_{MIN} probes

After timelapse recording, a high $[Ca^{2+}]$ KMS solution containing pipette is placed at the same position (in X, Y and Z, depth) as the patched cell to serve as a calibration probe for the determination of F_{MAX} at the same excitation/detection parameters. The panels show the fluorescence intensity acquired for this F_{MAX} probe (right: Ca^{2+} indicator; left: morphology indicator; ROI inside probe in black; scale bar 10 μ m). Similar process was done with a pipette containing KMS+ 10mM EGTA as a means of determining F_{MIN} in situ (not shown, taken to be ≈ 0).

C. Estimate calcium concentration

Using the given equation for estimation of steady state $[Ca^{2+}]$ and the probe determined values for F_{MAX} in situ, we estimated the $[Ca^{2+}]$ (right axis; nM) from the normalised fluorescence intensity (indicator/morphology, $\Delta G/R$) timelapse recording in the given whole-cell patched astrocyte in the CA1 stratum radiatum of acute (P21-25 rat) hippocampal slice perfused with oxygenated ACSF at 32-34°C. According to this method, the average resting $[Ca^{2+}]$ in this astrocyte was ≈ 50 nM with Ca^{2+} transient peak $[Ca^{2+}]$ up to ≈ 250 nM.

Taken together, these estimations of F_{MIN} and F_{MAX} for a given astrocyte should enable us to have a rough estimation of the resting $[Ca^{2+}]$ recorded via fluorescence intensity timelapse imaging of astrocytes in situ. For example, in figure 3.4.C, the estimated resting $[Ca^{2+}]$ for that particular astrocyte seems to be within the 50-150 nM range, comparable to estimations myself and others in the lab have found using fluorescence lifetime imaging method, see below.

INDICATOR INDEPENDENT CALCIUM IMAGING

A. Fluorescence Lifetime Imaging Microscopy

Fluorescence Lifetime Imaging Microscopy (FLIM) acquires the fluorescence lifetime, which is the decay time from an excited fluorescent state to a ground state, as opposed to the fluorescence intensity of a fluorophore. The principle advantage of this imaging technique is that it enables the removal of fluorophore concentration and slight Z-shift emission intensity issues from the experimental design (no need for normalization of a calcium indicator to a morphology indicator). Indeed, fluorescence lifetime measurements have the advantage of not being influenced by internal settings such as laser intensity or detector gain.

Fluorescence intensity and fluorescence lifetime properties do not necessarily vary in the same way in relation to the ion environment of the indicators. For calcium imaging, the lifetime of some common Ca^{2+} indicators, such as Oregon Green BAPTA dyes (Agronskaia et al. 2004; Wilms & Eilers 2007) and Indo-1 (Szmajcinski et al. 1993) is sensitive to the free calcium concentration whereas Fluo4 lifetime for example, is not. Dr Kaiyu Zheng and others in the synaptic imaging lab are currently developing the methodology for the use of FLIM to investigate intracellular basal concentrations of calcium in neurons and astrocytes in situ and in vivo with Oregon green BAPTA-1 for which the difference in mean lifetime is especially sensitive in the 10^1 to 10^2 nM free $[\text{Ca}^{2+}]$ range (Zheng et al, 2015).

We used similar FLIM approach using Oregon green BAPTA-2. Oregon green BAPTA-2 has similar lifetime $[\text{Ca}^{2+}]$ sensitivity (Fig 3.5) to Oregon green BAPTA-1 but its affinity for calcium is slightly lower (Agronskaia et al. 2004). We expected this to be suitable for attempting to record resting as well as activity $[\text{Ca}^{2+}]$ changes in astrocytes without respectively being below dye detection sensitivity or saturating the dye.

B. FLIM acquisition

i. Configuration and principle

Fluorescence lifetime measurements require timing the occurrence of each single photon detected. We added a Time-Correlated Single Photon Counting (TCSPC, provided by PicoQuant) system to detect this information to the intensity imaging Olympus BX61WI/Fluoview10000 and the Spectraphysics Maitai 2-photon laser setup described in chapter 2. The system upgrade components are described below.

TCSPC electronics (PicoHarp 300, PicoQuant) measure the timing of a single photon arrival onto a detector in relation to the time of excitation of the fluorophore. This requires a reliable excitation start timepoint, which in our case is the laser pulse from the Spectraphysics MaiTai femtosecond Ti:Sa 2-photon excitation laser. This laser operates at a fixed repetition rate of approximately 80 MHz. The number of photons that it is possible to use without biasing the photon count and thus the statistics required for measuring changes in decay rates of fluorophores is therefore a proportion, commonly 1%, of the pulse rate of the excitation laser used (less than 800 000 photons per second for the Maitai laser).

The endpoint for TCSPC is the detection of a single photon by the photon detector. In our case, we used a single channel PMA Hybrid detection unit (version 1.0, PicoQuant). To detect OGB-2 emission photons only as far as is as possible, the PicoQuant detector was equipped with a 520 ± 35 nm bandpass filter (Semrock FF01). The excitation light (800 nm 2photon laser excitation) was cut off from entering the detector by a 600nm dichroic, provided in the FV1000 Non-Descanned Detection PicoQuant upgrade kit for Olympus Fluoview laser scanning microscope.

The acquisition software (Symphotime 64, version 1.5, PicoQuant) enabled the combination of the time of photon occurrence after laser excitation pulse with the pixel information (line or frame stamp) provided by the Olympus Fluoview laser scanning system settings. We used continuous frame scans of approximately 300ms in duration, $0.310 \mu\text{m}/\text{pixel}$ resolution and a laser excitation dwell time of $4 \mu\text{s}/\text{pixel}$ at 800nm and less than 8 mW under the objective. Physiological considerations such as laser power damage/stimulation and duration of astrocyte spontaneous activity (slow >1 s events) determined the settings used for acquisition.

ii. Fast-FLIM

The conditions for acquiring enough photons to measure the fluorescence lifetime and changes in lifetime over time with reasonable spatial (distinguish astrocyte processes) and time (distinguish slow astrocyte calcium events and resting calcium) resolution are a limitation of FLIM. To reduce the necessary lifetime acquisition time without increasing laser power, we used a gating approach. In this 'fast-FLIM' approach, we bin together all the slow photons on the one hand and all the fast photons on the other. The bin timepoints were artificially set at 0- 1.7 and 1.7 to 10 ns for fast and slow photons respectively. These are the time points in nanoseconds at which each individual emission photon is detected after a laser excitation pulse which ends at timepoint 0ns. The ratio of slow over fast photons (photon count ratio, Fig.3.6.A) is used to differentiate slower lifetimes (high ratio) from faster lifetimes (low ratio). The timepoints for binning were selected in order to have maximum range between the slowest and fastest estimated lifetimes for this particular indicator (OGB-2). This method requires less photons, thus can be faster than lifetime imaging (Fig.3.6.C for OGB-2, see Systma et al. 1998; Agronskaia et al. 2004 for principle and other applications).

C. OGB-2 lifetime vs $[Ca^{2+}]$ calibration

As with fluorescence intensity measurements, the fluorescence lifetime measurements need to be calibrated against known $[Ca^{2+}]$ in order to be able to use measured photon count ratios as a means to quantify changes in resting $[Ca^{2+}]$ in astrocytes. The aim of using FLIM is to enhance the ability to reflect these changes across different regions of a single astrocyte and across different astrocytes without influence of the changes in setup between cell regions or cells.

i. $[Ca^{2+}]$ calibration in cuvette (sealed glass slides and coverslips)

In first instance, OGB-2 lifetimes were acquired in solutions of known $[Ca^{2+}]$. We followed the method used in commercial calcium calibration kit (Invitrogen, C-3008MP) but used our own solutions to best reflect the environment used in our experiments. We used the same recipe as for the internal solution used to patch astrocytes to which calcium buffers and calcium were added.

We performed a series dilution of an internal solution containing 0 nM $[Ca^{2+}]$ with gradually increasing volumes of a similar internal solution containing 19.2 μ M $[Ca^{2+}]$ to measure intermediate $[Ca^{2+}]$ in the range of interest for astrocyte $[Ca^{2+}]$ (0-1000nM). Both solutions contained the same concentrations of ions and OGB-2. The internal solutions composition, as well as the volumes of low $[Ca^{2+}]$ solution removed and replaced by high $[Ca^{2+}]$ solution, are listed in table 3.1. The estimated $[Ca^{2+}]$ was calculated using WebmaxC program (MaxChelator, Stanford) using constants at temperature of 34°C, pH 7.2 and ionic strength 0.16.

As soon as each $[Ca^{2+}]$ solution was prepared, 20 μ L of it was placed between a glass slide and coverslip, sealed and placed under the objective for lifetime acquisition. Care was taken to acquire sufficient and similar number of photons for each $[Ca^{2+}]$, this meant acquiring for slightly longer and with higher laser power for the lower $[Ca^{2+}]$ compared to higher $[Ca^{2+}]$.

In order to mimic the experimental conditions, the calibration slides were placed above a heated water perfusion set so that the temperature in the water meniscus under the objective would be between 33-34°C during lifetime acquisition. The OGB-2 lifetimes acquired in these conditions are shown in figure 3.5.A and plotted against each estimated $[Ca^{2+}]$ in figure 3.5.B.

This shows that in the range of approximately 20 to 1000 nM, OGB-2 lifetimes exhibit a near linear relationship to $[Ca^{2+}]$, with a K_D of \approx 350 nM.

As described in the previous paragraph, OGB-2 photon count ratios were used for acquiring astrocyte calcium changes. The ratios were calculated for these calibration lifetimes (Fig3.6.A) and plotted against each calculated $[Ca^{2+}]$ in figure 3.6.B. Similarly, in the range of approximately 20 to 1000 nM, OGB-2 photon count ratios exhibit a near linear relationship to $[Ca^{2+}]$, with a K_D of \approx 150 nM. This enabled us to use the 'fast-FLIM' method to estimate astrocyte $[Ca^{2+}]$. This method enables a more physiological acquisition in terms of time and space resolution as fewer photons are required than in lifetime acquisitions, to estimate $[Ca^{2+}]$ with the same level of variability (Fig.3.6.C).

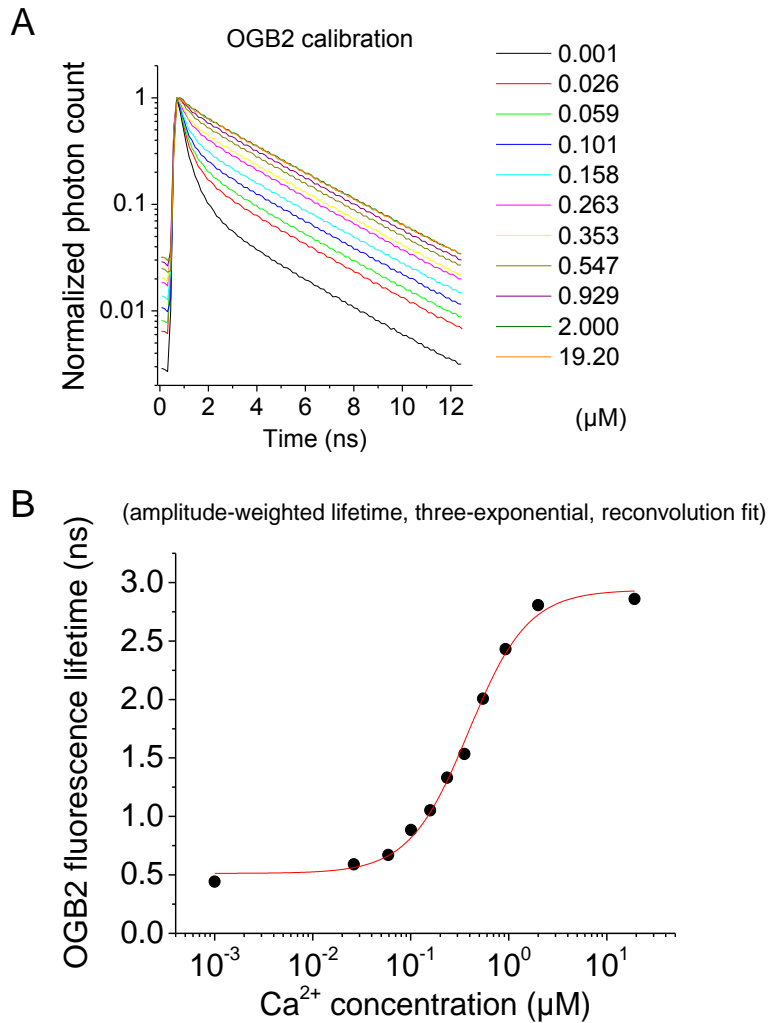


Figure 3.5 OGB-2 Fluorescence Lifetime Imaging (FLIM) principle [Ca^{2+}] calibration in cuvette (glass slides)

All the measurements in this figure are made at 34°C, using FLIM of known [Ca^{2+}] KMS internal solutions (see table 3.1) in sealed glass slides and coverslips (cuvette calibration, not cells). FLIM is acquired using the Olympus FV1000 in combination with PicoQuant TCSPC photon detection setup and 2-photon MaiTai 800nm excitation laser (see text). Whilst I recorded the lifetimes and performed the [Ca^{2+}] calibrations, my supervisor Dr C. Henneberger (C.H.) contributed to the analysis.

A. OGB-2 fluorescence lifetimes for different known [Ca^{2+}] in cuvette at 34°C

OGB2 lifetime is the decay time for the dye to return to its non-excited fluorescent state after emitting fluorescence upon binding calcium (OGB dyes exhibit some baseline fluorescence). FLIM measures the photon count of this dye at ns time bins in relation to the single pulse provided by the multiphoton laser every $\approx 12.5\text{ns}$ in our case (MaiTai 2-photon laser, 800nm emission, 80MHz repetition rate). OGB2 shows long lifetimes for higher [Ca^{2+}] and short lifetimes for lower [Ca^{2+}]. Importantly, the lifetime of OGB-2 fluorescence recorded in cuvette is a function of the [Ca^{2+}] of the calibration solution (μM). The lifetimes for each Ca^{2+} calibration solution were normalised to the peak of OGB2 fluorescence (amplitude weighted).

B. Linear relationship between OGB-2 lifetimes in cuvette and [Ca^{2+}] in the ≈ 20 to 1000nM range

OGB2 lifetimes show a linear relationship to [Ca^{2+}] in ≈ 20 to 1000nM range (logarithmic scale). This makes OGB2 a suitable indicator for quantifying [Ca^{2+}] in astrocytes using FLIM. The dots refer to the normalised lifetimes (amplitude weighted) I recorded in cuvette at 34°C for known KMS [Ca^{2+}] (see table 3.1). The red line indicates the best fit (three exponential reconvolution) using OriginPro v8 by C.H.

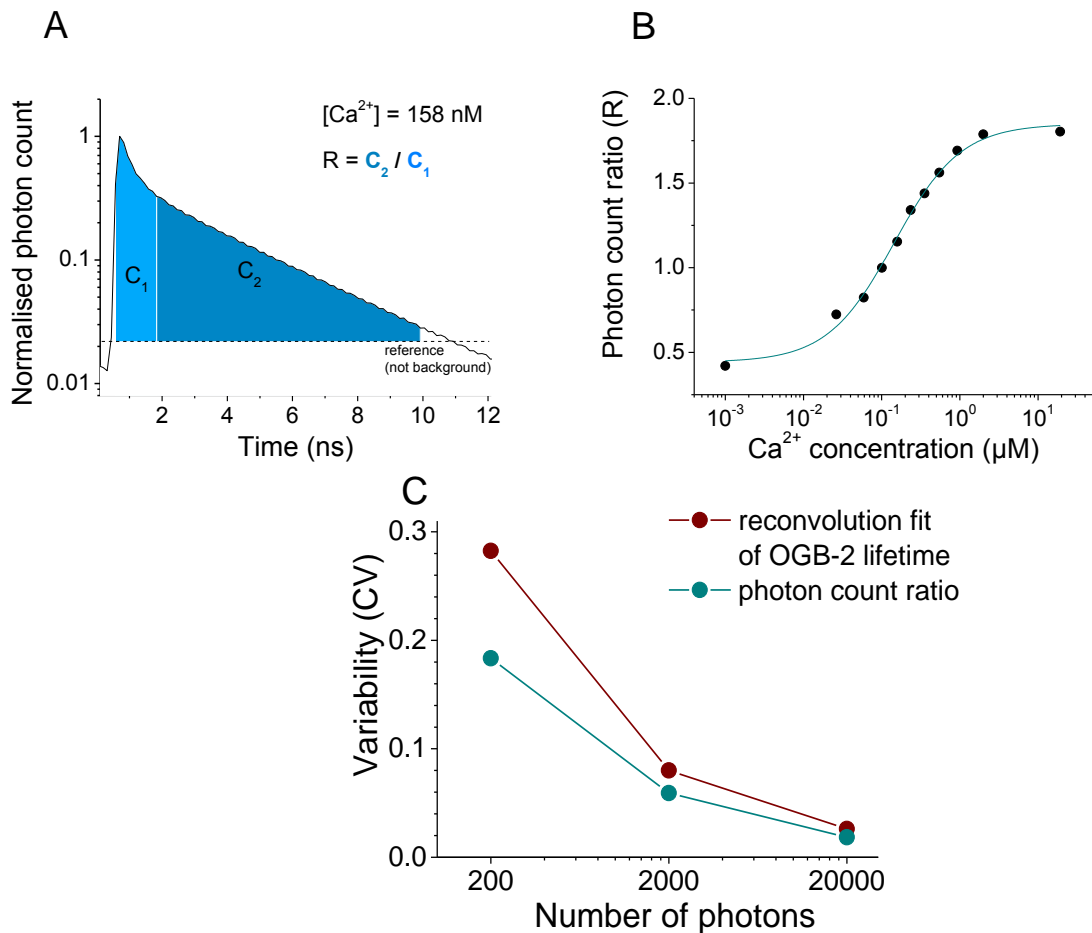


**Figure 3.6 OGB-2 photon count ratio (fast-FLIM) principle
[Ca²⁺] calibration in cuvette (glass slides)**

All the measurements in this figure are made at 34°C, using FLIM of known [Ca²⁺] KMS internal solutions (see table 3.1) in sealed glass slides and coverslips (cuvette calibration, not cells). FLIM is acquired using the Olympus FV1000 in combination with PicoQuant TCSPC photon detection setup and 2-photon MaiTai 800nm excitation laser (see text). Whilst I recorded the lifetimes and performed the [Ca²⁺] calibrations, my supervisor Dr C. Henneberger (C.H.), contributed to the analysis by design of a Matlab script to automatically calculate the photon count ratio from the acquired lifetimes. He also provided the variability simulation (C) based on my [Ca²⁺] calibration curves for lifetime and photon count ratio.

A. Fast FLIM: photon count ratio calculation

In order to reduce the acquisition time needed to quantify [Ca²⁺], we used a 'fast FLIM' method. This method calculates the ratio between two photon lifetime bins, $R=C_2/C_1$: all recorded slower photons (dark blue; C₂) divided by all recorded faster photons (light blue; C₁). For OGB-2, we found that using time bins of 0-1.8ns and 1.8-10ns gave us the best dynamic range (ratio for low [Ca²⁺] is roughly 3.5x less than ratio for high [Ca²⁺]). Photon detection times (detected by PicoQuant TCSPC) are given in ns from each excitation photon (t=0ns) emitted every 12.5ns by the MaiTai 2-photon laser.

B. Linear relationship of OGB2 photon count ratio and [Ca²⁺] in ~20 to 1000nM range

The photon count ratios of OGB2 lifetimes of known [Ca²⁺] solutions recorded in cuvette at 34°C also show a linear relationship to [Ca²⁺] in the ~ 20 to 1000nM range (logarithmic scale; best fit in teal using OriginPro v8). This enables us to use OGB2 photon count ratios to quantify [Ca²⁺] in astrocytes rather than lifetime imaging which is slower.

C. [Ca²⁺] estimation variability according to number of photons used (provided by Dr C. Henneberger, C.H.)

Lifetime (dark red) measurements require more photons to accurately estimate [Ca²⁺] than photon count ratios (teal), simulation by C.H. based on the [Ca²⁺] calibration curves in 3.5.B and 3.6.B. Photon count ratio analysis allows faster acquisition times as less photons are required to estimate [Ca²⁺] with a given estimation variability. We used a cut-off point of a minimum of 1500-2000photons /ROI for photon count ratio estimation of [Ca²⁺] in astrocytes in this thesis.

A

| [Ca²⁺] calibration internal solutions, concentrations for final volume of 50mL | | |
|--|--|---|
| | Low [Ca ²⁺] internal solution compound concentration (mM) | High [Ca ²⁺] internal solution compound concentration (mM) |
| Metasulphonic acid | 105 | 105 |
| Potassium Hydroxide | 105* | 105* |
| HEPES | 10 | 10 |
| Magnesium chloride - 6H ₂ O | 4 | 4 |
| Di(tris)-phosphocreatine | 10 | 10 |
| Na ₂ -ATP | 4 | 4 |
| Na-GTP | 0.4 | 0.4 |
| BAPTA | 10 | 5 |
| BAPTA tetrapotassium salt | 0 | 5 |
| Potassium chloride | 20 | 0 |
| Calcium chloride - 2H ₂ O | 0 | 10 |

B

| [Ca²⁺] calibration series dilution for a 1mL total volume | | | | | |
|---|---|-----|-----|-----|-----|
| Sample number | 1 | 2 | 3 | 4 | 5 |
| Estimated [Ca ²⁺] | 0 | 26 | 59 | 101 | 158 |
| Volume to remove and replace with high [Ca ²⁺] solution | 0 | 100 | 111 | 125 | 143 |

| [Ca²⁺] calibration series dilution for a 1mL total volume, <i>continued</i> | | | | | | |
|---|-------|-----|-----|-------|------|-------|
| Sample number | 6 | 7 | 8 | 9 | 10 | 11 |
| Estimated [Ca ²⁺] | 236 | 353 | 547 | 929 | 2000 | 19200 |
| Volume to remove and replace with high [Ca ²⁺] solution | 166.5 | 200 | 250 | 333.5 | 500 | 1000 |

Table 3.1 [Ca²⁺] calibration solutions

A. [Ca²⁺] calibration internal solution composition

High and low [Ca²⁺] internal solutions were prepared using the same composition as regular internal solution used for patch experiments. BAPTA and CaCl₂ were added to set [Ca²⁺]. * KOH was used to adjust the pH to 7.2.

B. Cuvette [Ca²⁺] calibration sample preparation

The range of [Ca²⁺] was created by removing a set volume from the low [Ca²⁺] and replacing it with the same volume of high [Ca²⁺]. The volumes to remove and replace are given for a total sample size of 1mL. For OGB2 calibration, 20μM of the indicator was added to each sample and the lifetime was acquired. The [Ca²⁺] for each sample was estimated using Webmaxc program (Maxchelator, Stanford) with constants for pH 7.2, ionic strength 0.16 and 34°C conditions.

ii. $[Ca^{2+}]$ calibration in cells

Our next objective was to calibrate $[Ca^{2+}]$ inside astrocytes in situ (Fig.3.7), to account for possible changes to OGB-2 lifetime due to the environment in the patched astrocyte such as pH, endogenous buffers and extrusion mechanisms. The first patched astrocytes with known $[Ca^{2+}]$ such as the high and low $[Ca^{2+}]$ solutions in table 3.1.A. I acquired OGB-2 lifetime in astrocytes loaded with KMS-internal solution (chapter 2) at either low $[Ca^{2+}]$ (KMS + 10mM BAPTA) and high $[Ca^{2+}]$ (KMS+10mM BAPTA and 10mM $CaCl_2$). The lifetimes were similar to those estimated with calibration solutions in slides (Fig.3.7.A). I also patched astrocytes with intermediate $[Ca^{2+}]$ KMS internal solutions using the same series dilution principal as in table 3.1.B. However, this approach had little success in part because it was hard to clamp $[Ca^{2+}]$ at a given value in solution across the cell body as this depended on internal solution diffusion in itself and over time, as it is possible that the different cell compartments extrude added Ca^{2+} over time for example. Additionally intermediate solutions had to be compared to the high and low $[Ca^{2+}]$ in patched astrocytes for every experimental day, which made the task harder to achieve as these high [buffer] and $[Ca^{2+}]$ containing solutions did not ease astrocyte whole-cell patch clamp.

In addition to high $[Ca^{2+}]$ patched astrocytes, I also repeated similar approach as with intensity F_{max} values. Indeed, I applied repeated and continuous puffs of 300 μ M Ionomycin (creates Ca^{2+} permeable pores in cell membranes, see Fig.3.1.A) and 500 μ M ATP (enables Ca^{2+} entry through P2X receptor activation). I tried to increase the likelihood of inducing a saturating level of $[Ca^{2+}]$ by puffing this solution close to the patched astrocyte, using the combination of Ionomycin and ATP, increasing laser excitation exposure and mechanical stimulation by removing the patch pipette without losing the integrity of the astrocyte.

We compared the photon count ratios from a simulated data set (Fig.3.7.B-C) using the $[Ca^{2+}]$ calibrations from either OGB-2 lifetimes acquired inside astrocytes or acquired in solutions only. Although tightly correlated, the simulation performed by Dr. C. Henneberger, allowed to correct the original (Fig.3.6.B) $[Ca^{2+}]$ calibration of OGB-2 photon count ratios obtained in cuvette for the slight differences seen in situ calibrated $[Ca^{2+}]$ measurements as shown in figure 3.7.D.

iii. Background correction

To further refine the estimation of $[Ca^{2+}]$ using OGB-2 fluorescence lifetime imaging, we aimed to quantify the autofluorescence lifetime in the model we are using for astrocyte recordings: acute hippocampal slices of P21-26 male rats (Fig.3.8). We simply acquired lifetime measurements from these slices in the similar recording conditions as for patched astrocytes but without dyes (34°C ACSF perfusion, 800 nm 4-7 mW excitation, 20-70 μ m depth, FLIM) as illustrated in figure 3.8.A.

We compared this to the minimum OGB-2 lifetimes acquired in patched astrocytes with low $[Ca^{2+}]$ (10 mM BAPTA). The photon rate was 2 orders of magnitude below the rate in OGB-2-low $[Ca^{2+}]$ lifetimes (Fig.3.8.B). This changes the estimation of $[Ca^{2+}]$ by less than 0.5 nM $[Ca^{2+}]$ in this case.

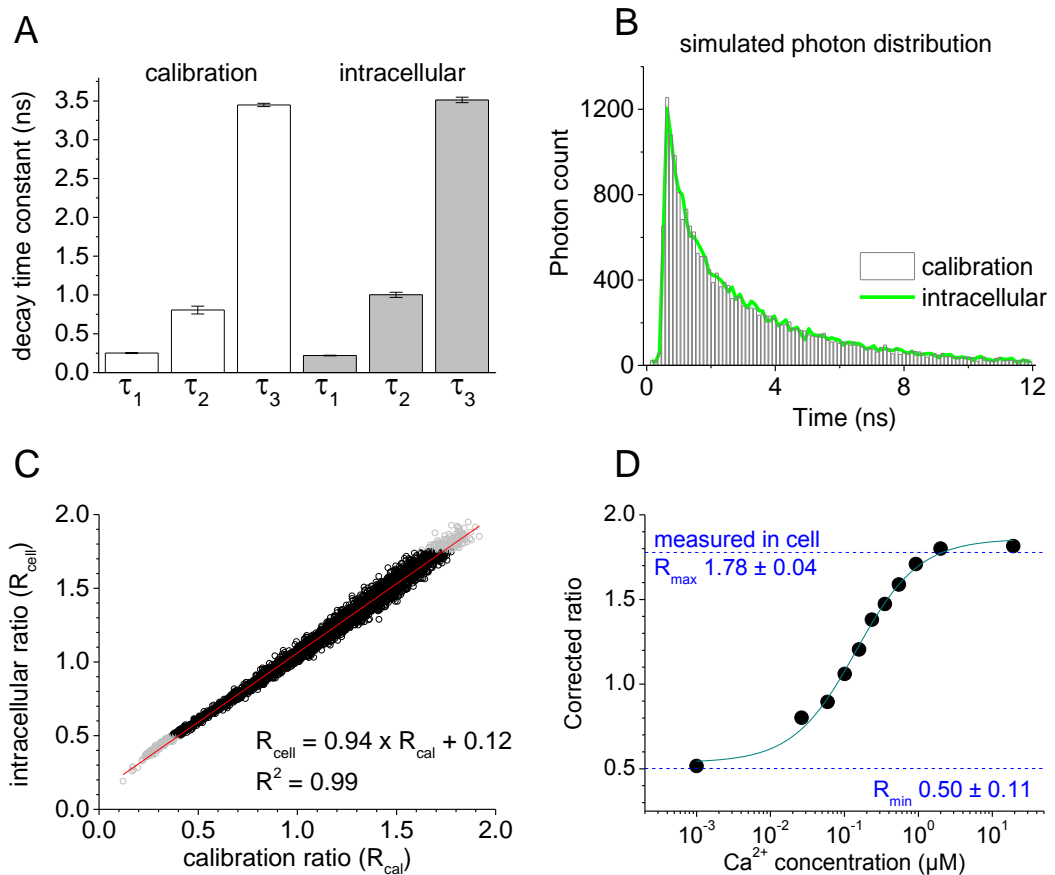


Figure 3.7 Cell correction of OGB-2 photon count ratio $[Ca^{2+}]$ calibration

Analysis by Dr. C. Henneberger

FLIM recording setup as previously described: MaiTai 2-photon excitation at 800nm, Olympus FV1000 acquisition, PicoQuant TCSPC photon detector. All recorded at 32-34°C. I recorded the data in these graphs using FLIM measurements of OGB-2 of the following items.

Cuvette calibration (see figures 3.5-6; table 3.1): internal solutions only in sealed glass slides at 34°C (cuvette, not cells).

In situ calibration: I recorded FLIM of OGB-2 loaded whole-cell patched astrocytes in the CA1 stratum radiatum of acute male P21-25 rat hippocampal slices perfused with oxygenated ACSF at 32-34°C.

Rmin: patched astrocytes using KMS-internal solution with added 10mM EGTA ($\approx 0nM [Ca^{2+}]$)

Rmax: patched astrocytes using a 10mM EGTA and 10mM $CaCl_2$ ($\approx 19\mu M [Ca^{2+}]$) KMS-internal solution and in separate experiments, patched astrocytes with normal patch internal solution after pressure application of 300 μM Ionomycin and 500 μM ATP.

Dr C. Henneberger (C.H.) contributed to the data analysis and provided simulations and cell corrected OGB-2 photon count ratio $[Ca^{2+}]$ calibration curve.

A. Time constants for fitting calibration or patched astrocyte OGB2 lifetimes and $[Ca^{2+}]$ (provided by C.H.)

Individual decay time constants components of the reconvolution fit obtained from calibration data (white) and from OGB2-filled astrocytes (grey), small but significant differences

B. Simulation of photon distribution in calibration or patched astrocytes (provided by C.H.)

Simulated experimental data for a set of lifetime components (x, y, z) with lifetimes from calibration (bar) and from patched astrocyte measured lifetime components (green line). small difference.

C. Simulation of photon count ratios in calibration or patched astrocytes (provided by C.H.)

The photon count ratios from a set of simulations shown in B for both calibration (X axis) and intracellularly measured $[Ca^{2+}]$ (Y axis). These ratios were highly correlated and this was used to estimated how to correct ratios for cell differences.

D. Cell corrected photon count ratio for $[Ca^{2+}]$ concentrations of ≈ 20 to 1000nM (provided by C.H.)

OGB2 photon count ratios from the calibration data are corrected for differences found in patched astrocyte calibration data as determined in the previous simulations (A, B and C). There appears to be a linear relationship between 'cell-corrected' OGB2 photon count ratio and $[Ca^{2+}]$ in the 20 to 1000nM range.

Rmin and Rmax are the average minimum and maximum photon count ratios measured in patched astrocytes as described above.

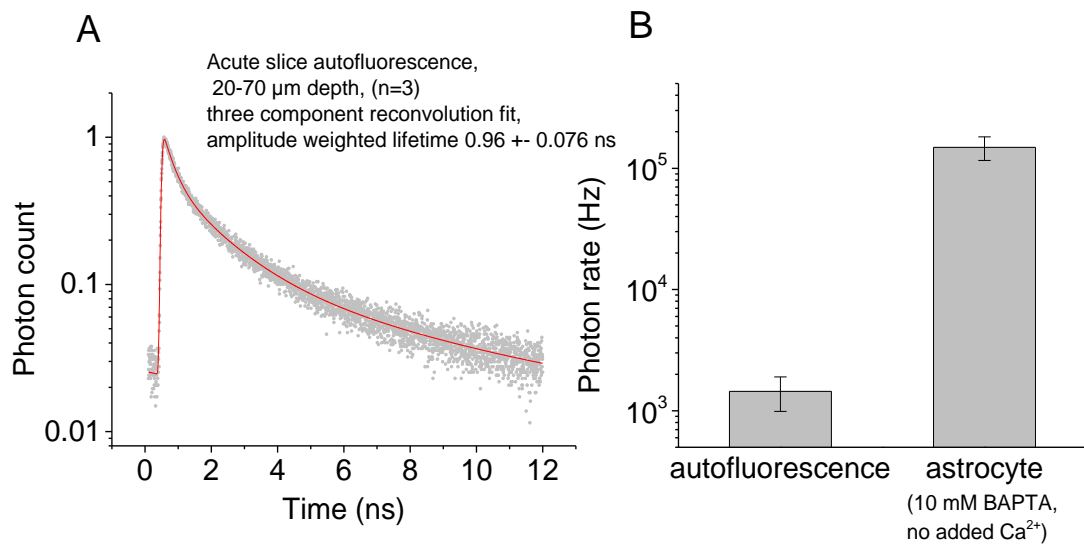


Figure 3.8 Background autofluorescence

Analysis by C.H.

I acquired the data using Olympus FV1000, 2-photon MaiTai laser excitation at 800nm and PicoQuant TCSPC photon detector as with all other FLIM experiments. Hippocampal P21-25 male rat acute slices were perfused with oxygenated ACSF at 32-34°C. Astrocytes in the CA1 stratum radiatum of these slices were patched in whole-cell configuration using KMS-internal solution with added 10mM BAPTA. My supervisor, C.H., contributed to the analysis of the data I extracted.

A. Autofluorescence lifetime in acute hippocampal slices at 20-70 μm depth

Acute hippocampal slices only were imaged from 20 to 70 μm deep, in the same conditions as for FLIM experiments of whole-cell patched astrocytes but with no patch clamp and no dyes. This was to image the contribution of background fluorescence when acquiring OGB2 lifetimes in other experiments. This graph illustrates autofluorescence average, normalised to the peak (amplitude weighted), decay lifetime recorded from 3 acute slices, 1 animal. The red line is the best fit using a three component reconvolution in OriginPro v9 software by C.H.

B. Photon rate in slice only and in patched astrocyte with 10mM BAPTA

This bar graph (average \pm SEM) presents the number of photons (photon rate, Hz) obtained when imaging the slice only (autofluorescence) and number of photons in a patched astrocyte where most of the calcium (at least in the soma, where these values were measured) should be clamped as the internal solution contains 10mM BAPTA). The contribution of autofluorescence to OGB2 lifetime is relatively small as for example, at an estimated $[\text{Ca}^{2+}] = 101$ nM, a contribution of autofluorescence of 1% changes the calculated $[\text{Ca}^{2+}]$ by less than 0.4% (simulation by C.H.).

DISCUSSION

A. Summary

In this chapter, I describe the methods we applied in order to estimate $[Ca^{2+}]$ in astrocytes in situ as accurately as possible. I originally attempted to use fluorescence intensity imaging which has the advantages of a large range of available Ca^{2+} indicators with excellent dynamic range such as Fluo-4 and faster time resolution. However, despite making some progress with $[Ca^{2+}]$ calibrations, I opted for the advantages of the indicator/setup independent fluorescence lifetime imaging to ease comparison across cell regions and cells. I calibrated OGB-2 photon count ratios against calculated $[Ca^{2+}]$ in internal solutions which I then attempted to adjust for differences due to recordings in patched astrocytes and autofluorescence of acute hippocampal slices. I used this method to acquire and monitor resting astrocyte $[Ca^{2+}]$ and astrocyte Ca^{2+} activity in whole-cell patched astrocytes in acute hippocampal slices at near physiological temperatures as will be described in the following chapters.

B. Other methods tested: Ratiometric Dyes

Ratiometric dyes, like FLIM, also allow for concentration/setup independent imaging with the advantage of not requiring additional components to regular fluorescence imaging setup and better time resolution than FLIM. A ratiometric Ca^{2+} dye has two distinguishable spectral properties: when bound to Ca^{2+} and when free from Ca^{2+} . The classical Fura2 ratiometric Ca^{2+} dyes unfortunately have ratiometric absorption properties which are not well suited for two photon excitation. Indo-1, an older ratiometric Ca^{2+} dye with a lower quantum yield and thus much dimmer than fura2, has ratiometric emission properties. Indo-1 has a K_D of approximately 350 nM (similar to OGB-2) and exhibits a shift in emission wavelengths upon binding to calcium after two photon excitation at 702 nm (Szmecinski et al. 1993). However, due to lower power of excitation laser in the 700 nm range and the low quantum yield of this dye, the fluorescence intensity was too dim in the $[Ca^{2+}]$ range of interest. Similarly, I tried to test Asante Calcium Red™ potassium salt (Teflabs, TEF3040), a more recent far red excitation ratiometric dye which may be more suited to our 2-photon excitation current setup (Krzysztof et al. 2013). However, in my hands the dynamic range was below resolution for setup used: I could not see a fluorescence intensity difference between Asante Calcium Red™ in a low $[Ca^{2+}]$ solution compared to a high $[Ca^{2+}]$ solution (1 nM vs 19 μ M). This could be due to many technical issues but others have also independently found that this dye had insufficient dynamic range (another postdoc in the synaptic imaging lab Dr. Thomas Jensen, as well as a postdoc in a different lab, Dr. Christian Wilms who mentioned issues such as “very low quantum efficiency” in a personal email communication). *Interestingly, this dye has been used for FLIM (Jahn & Hille 2014) where the low number of photons may not be such an issue.*

Chapter 4: SPONTANEOUS ASTROCYTE CALCIUM EVENTS

INTRODUCTION

A. Objective

In this chapter I quantified the characteristics of spontaneously occurring endogenous Ca^{2+} events (this refers to Ca^{2+} events occurring without applying a stimulation protocol to trigger them) in whole cell-patched astrocytes in acute hippocampal slices recorded using FLIM of OGB-2 at near physiological temperatures 32-34°C (see methods described in chapters 2 and 3). I explored the relationship between characteristics of the visually identified spontaneous Ca^{2+} events and the resting $[\text{Ca}^{2+}]$ across all astrocytes I recorded. The resting $[\text{Ca}^{2+}]$ is defined here as the average basal $[\text{Ca}^{2+}]$ recorded over 2 to 3 seconds immediately preceding each visually identified, spontaneously occurring Ca^{2+} event.

B. Endogenous astrocyte spontaneous Ca^{2+} activity

Astrocytes have been shown to exhibit endogenous spontaneous calcium events. These events are increases in cytosolic $[\text{Ca}^{2+}]$ that may have a variety of forms as defined by their duration and average amplitude. They may occur independently from neuronal activity (Nett et al. 2002) as shown for example, with recordings showing Ca^{2+} events in astrocytes in slices whilst using the voltage gated sodium channel blocker, tetrodotoxin (TTX), to inhibit neuronal activity through the block of action potential firing. Depletion of pre-synaptic vesicles to block neurotransmitter release can also not affect occurrence of astrocyte events Ca^{2+} (Parri & Crunelli 2003). Spontaneous Ca^{2+} events also occurred in astrocytes in the hippocampus in situ, after application of glutamate receptor antagonists (Haustein et al. 2014). These experiments suggest that astrocyte Ca^{2+} events can occur endogenously without experimental stimulation and possibly independently from neuronal activity. However, DiCastro et al. 2011 suggest the existence of different astrocyte Ca^{2+} events, possibly previously undistinguishable in earlier astrocyte Ca^{2+} imaging studies investigating only somatic astrocyte Ca^{2+} events. These Ca^{2+} events could occur as function of neuronal action potentials (TTX sensitive) or spontaneous, action-potential-independent, quantal release of neurotransmitters (BafilomycinA1 sensitive but TTX insensitive). This second mechanism has been suggested to underlie spontaneous astrocyte Ca^{2+} activity, although the nature of the neurotransmitter is unclear (Sun et al. 2014). Furthermore, it is not necessarily clear if and how these spontaneous Ca^{2+} transients shape neuronal transmission (Nett et al. 2002; Haustein et al. 2014).

Many mechanisms are thought to enable Ca^{2+} entry into astrocytes, whether this is a direct (DiCastro et al. 2011; Panatier et al. 2011; Tang et al. 2015) or indirect (Torres et al. 2012) result of neuronal activity or possibly independently through activation of TRPA1 channels

(Shigetomi et al. 2012) for example. A quantitative approach to characterise these endogenous spontaneous Ca^{2+} events, regardless of the cause of activation, may contribute to further understanding some of the mechanisms of astrocyte signalling in situ, perhaps in more physiological conditions than using artificial (exogenous or endogenous) stimulation protocols. Additionally, using acute hippocampal slice preparations and acquisition at near physiological temperature also contributes to the physiological relevance of the astrocyte Ca^{2+} events recorded, though the preservation of some of the physiological interactions and environment. Further quantitative characterisation of spontaneous Ca^{2+} events that engage the endogenous mechanisms for Ca^{2+} event initiation could lead to better understanding of how astrocyte Ca^{2+} can impact on such a range of neuronal transmission (from integrating basal neuronal activity (DiCastro et al. 2011; Panatier et al. 2011) to shaping synaptic plasticity such as long term potentiation (Henneberger et al. 2010)).

In this chapter, we investigate the hypothesis that the characteristics of these spontaneous Ca^{2+} events should correlate with the astrocyte resting $[\text{Ca}^{2+}]$. If the amplitude or kinetics of IP_3R -dependent Ca^{2+} events are determined by resting $[\text{Ca}^{2+}]$ (see chapter 1; reviewed in Foskett et al. 2007); then such characteristics (amplitude for example) of these spontaneous Ca^{2+} events in astrocytes should also correlate with resting $[\text{Ca}^{2+}]$ as there is evidence that some endogenous astrocyte Ca^{2+} signalling is IP_3R -dependent. For example, the diffusion of IP_3 across gap-junctions has been suggested as a mechanism for the propagation of inter-astrocyte calcium waves (Giaume & Venance 1998). Within individual astrocytes, the occurrence of spontaneous Ca^{2+} events was significantly reduced in astrocytes deprived of IP_3R (Di Castro et al. 2011) or following IP_3R acute pharmacological inhibition through 2-APB application (membrane permeable IP_3R inhibitor (Saleem et al. 2014); Parri & Crunelli 2003). However more recent studies such as in vivo Ca^{2+} imaging of mice with astrocytes genetically deprived of IP_3R still show spontaneous Ca^{2+} events, particularly in peripheral astrocyte processes (Srinivasan et al. 2015; Kanemaru et al. 2014). These studies suggest IP_3R -alternative mechanisms could underlie endogenous astrocyte Ca^{2+} signalling, specifically for the small localised events in astrocyte processes which may not have been detected in earlier studies acutely. However, it could also be possible that these potential IP_3R -alternative mechanisms result from developmental compensatory recruitment or expression in these genetically modified mice. Such changes could simply not happen on the time scale of acute inhibition of IP_3R dependent Ca^{2+} signalling in earlier studies.

METHODS

The astrocyte Ca^{2+} events presented in this chapter were recorded in astrocytes ≈ 5 minutes after they were subjected to other experiments (described in chapters 5, 6). During these other experiments, astrocytes were exposed to pressure application of DHPG (mGluR agonist; chapter 6) and in some cases, UV-photolysis of caged Ca^{2+} or Ca^{2+} buffer (chapters 5, 6). All Ca^{2+} event characteristics are presented per ROI regardless of the cell of origin as we were interested in describing the relationship of a particular Ca^{2+} event and the resting $[\text{Ca}^{2+}]$ within

that ROI. To reduce the potential impact of these artificial differences in astrocytes, we also analysed the main result considering only Ca^{2+} events that were recorded in astrocytes that contained no additional Ca^{2+} or Ca^{2+} buffer.

A. Recording protocol

Astrocytes in the CA1 stratum radiatum of submerged acute hippocampal slices were whole-cell patched with KMS based internal solution (see chapters 2,5,6), perfused with oxygenated ACSF at 32-34°C (as described in chapter 2).

Astrocyte calcium activity was acquired through fluorescence lifetime imaging of 200 μM OGB-2 (chapter 3) added to the internal KMS solution. Using the Olympus FV1000 customised setup (see chapters 2 and 3), 1000 frames were acquired continuously for approximately five minute timelapse recordings (≈ 300 ms per frame as a function of frame size) with a resolution of 0.310 $\mu\text{m}/\text{pixel}$, 4 μs excitation laser dwell time per pixel and 2-photon excitation at 800 nm (MaiTai Spectraphysics Ti:S laser; chapters 2-3) with 3-8mW laser power under the objective (Olympus 40x). The resulting OGB-2 fluorescence lifetime was acquired using the PicoQuant single photon time correlated detector (further described in chapter 3, FLIM) equipped with a band pass filter (520 \pm 35 nm range; FF01 Semrock) to allow detection of OGB-2 fluorescence emission. The PicoQuant FLIM upgrade also includes a 600nm dichroic filter helping to prevent TCSPC detection of photons emitting at wavelengths above 600nm.

Astrocyte morphology identification was enabled through the acquisition of Alexa 594 (100 μM Alexa Fluor @ 594 hydrazide, sodium salt; A10433- Invitrogen Life Technologies) fluorescence intensity using the Olympus FV1000 setup described in chapter 2. Alexa594 emission, above 600 nm, was recorded simultaneously to OGB-2 FLIM using a separate detector: a photon multiplier tube equipped with a band pass filter allowing detection of emission within the 660 to 740 nm range built-in the Olympus FV1000 system.

B. Manual ROI selection

Spontaneous events by definition do not occur at a specific time or area; therefore we opted for a manual selection of regions of interest. To represent the astrocyte's spontaneous calcium we characterised the calcium activity in manually identified regions of interest selected to reflect the different areas of the individual astrocyte.

As described in chapter 3, we reduced the variability in $[\text{Ca}^{2+}]$ estimation by selecting ROIs with a similar number of photons across the cell and between all cells. We used a minimum cut off number of photons of 1000 photons per ROI. This resulted in occasionally using a frame bin of 2 frames for cells where OGB-2 fluorescence emission was particularly low (usually a consequence of imaging cells slightly deeper in the tissue, ≈ 80 μm or more from the slice surface).

Finally, we took astrocyte morphology into account when determining the pixel bins to create the ROI. We used the Alexa594 fluorescence intensity to visually identify the morphology of the astrocyte and determine where to position ROI. We visually distinguished four morphological

compartments in each cell: soma, large main process, small secondary process and periphery fine processes. We identified one somatic ROI and three ROI for each type of process morphology for each cell, as illustrated in figure 4.2.B.

C. Endogenous Ca²⁺ events

i. Ca²⁺ event identification

For each ROI, I plotted the OGB-2 fluorescence photon count, the OGB-2 photon count ratio and the resulting estimated [Ca²⁺] over time. Using all of these traces, I manually identified spontaneous Ca²⁺ events. I used the following criteria for a change in [Ca²⁺] to be considered as a spontaneous astrocyte Ca²⁺ event.

Spontaneous Ca²⁺ events may escape detection as both the photon count ratio traces as a function of time recorded in these ROI were noisy and the dynamic range of OGB indicators is lesser than Fluo4 for example, which may reduce visual identification of Ca²⁺ events using the timelapse video of recorded OGB-2 fluorescence intensity. Therefore I used the trace of OGB-2 photon count (fluorescence intensity as opposed to fluorescence lifetime) over time, which has a better dynamic range and signal to noise ratio than the photon count ratio trace, to visually identify when Ca²⁺ events occurred. Spontaneous transient Ca²⁺ events were considered as visually identifiable increases in OGB-2 photon count relative to resting levels, which then returned to resting levels within the time of recording. I then checked these identified timepoints in the photon count ratio and [Ca²⁺] estimation traces. Indeed, these traces (as opposed to the photon count fluorescence intensity trace) should not be influenced by slight changes in dye concentration, dye photobleaching or focal plane depth drift of the selected ROI (Zheng et al, under revision). Provided the ROI still reflected the same astrocyte compartment (as confirmed through morphology indicator Alexa 594 fluorescence intensity timelapse recording), only events identified in both photon count and photon count ratio traces were taken into consideration. Indeed, verifying that the Ca²⁺ events identified in intensity traces also occurred in the FLIM traces insured that such Ca²⁺ events were not an artefact of intensity measurements. In order to be considered as an event and distinguished from baseline noise, the increase in Ca²⁺ had to occur over at least three continuously recorded timepoints which is approximately one second in the case of the acquisition protocol we used.

In order to be considered a transient Ca²⁺ event (usually lasting less than a minute) as opposed to a long-lasting increase in resting [Ca²⁺] (such as may occur during photodamage induced cell death for example), the [Ca²⁺] had to return to resting levels within the five minute recording.

ii. Ca²⁺ event characterisation/properties

Each visually identified spontaneous Ca²⁺ event was analysed to characterise the following properties, as illustrated in figure 4.3.A-B.

The region of interest where the spontaneous Ca²⁺ event occurred was qualified for morphology subtype as described above: soma, large, small and peripheral processes (figure 4.2.B).

The time of occurrence relative to the beginning of the recording was noted to identify spontaneous Ca^{2+} events occurring concomitantly across different ROI in a particular cell.

The frequency of occurrence of spontaneous Ca^{2+} events was measured as the number of events identified divided by the total recording time (≈ 5 minutes) in events $\times \text{min}^{-1}$ for each ROI.

The duration of the spontaneous Ca^{2+} event was measured as the time in seconds between initial increase in Ca^{2+} and the return to resting $[\text{Ca}^{2+}]$ levels.

The spontaneous Ca^{2+} event peak $[\text{Ca}^{2+}]$ was estimated by calculating the average $[\text{Ca}^{2+}]$ over ≈ 1.5 seconds around the maximum $[\text{Ca}^{2+}]$ value at the start of the Ca^{2+} event.

The amplitude of the spontaneous Ca^{2+} event was defined as the difference between peak $[\text{Ca}^{2+}]$ and the estimated pre-event resting $[\text{Ca}^{2+}]$.

Resting $[\text{Ca}^{2+}]$ was defined as the average estimated $[\text{Ca}^{2+}]$ across 2-3 seconds outside of any visually identified $[\text{Ca}^{2+}]$ changes. Initial resting $[\text{Ca}^{2+}]$ was estimated for each ROI at the beginning of the recording. The pre-event resting $[\text{Ca}^{2+}]$ was defined as the average estimated $[\text{Ca}^{2+}]$ across 2-3 seconds immediately prior to the Ca^{2+} event.

iii. Testing for correlation relationships with linear fitting and Spearman test

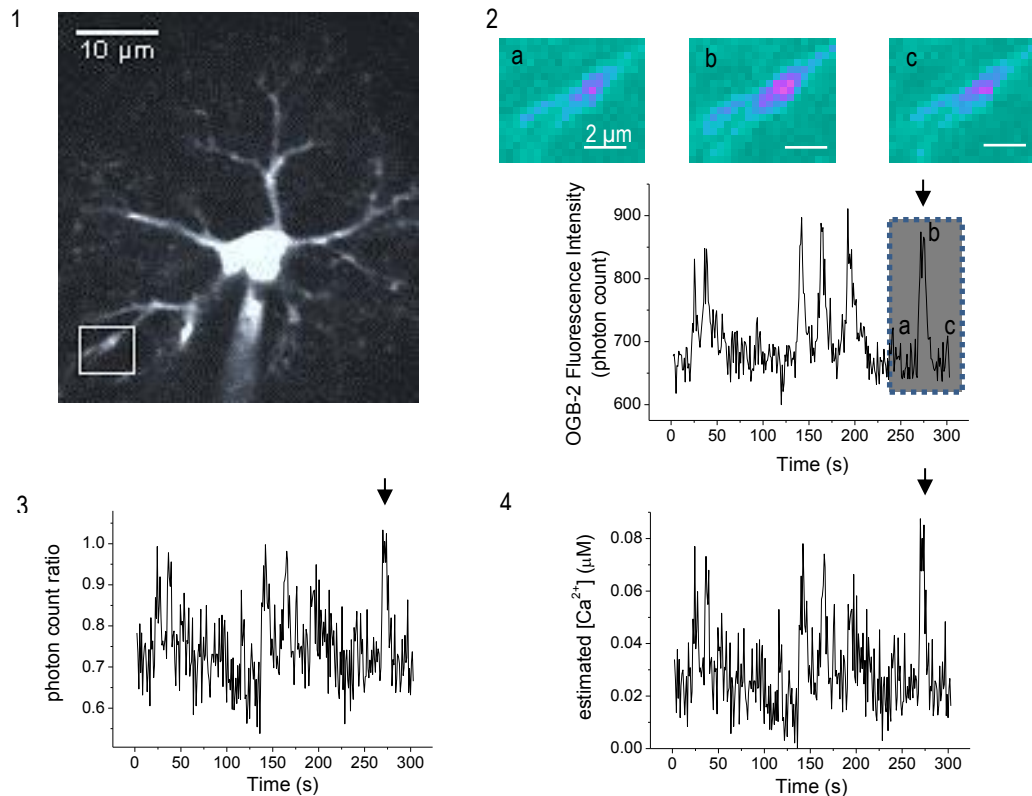
Correlations were tested and indicated by Spearman correlation coefficient (calculated in OriginPro.8 software) and its two-tailed test of significance p value. The Spearman correlation coefficient (ρ) for a sample size n , is calculated by the following equation where d_i represents the difference between the ranks of the raw data X and Y ($d_i = x_i - y_i$) so that:

$$\rho = 1 - \frac{6 \sum d_i^2}{n(n^2 - 1)}$$

If the Spearman coefficient is close to ± 1 , then it indicates that the two variables are related but does not presume a linear relationship between the two. The Spearman correlation coefficient is a non-parametric test that does not assume normal distribution or linearity or homoscedasticity (equal variance) of the data sets. These assumptions, which do not necessarily reflect the data in this chapter, are made when using linear regression or Pearson r correlation. The Spearman rank test is also less sensitive to outliers in comparison to linear regression.

I also used linear fitting in OriginPro.8 software to test the relationship of pre-event resting $[\text{Ca}^{2+}]$ to Ca^{2+} event characteristics. The pre-event resting $[\text{Ca}^{2+}]$ was set as X axis and event characteristic as Y axis. I used the slope of the best linear fit to give an indication of the strength of the correlation (higher slope value for strong correlation). The sign of the slope indicated positive or negative correlation. The P value gives an indication of how significantly the slope of the proposed best linear fit differs from 0 at 95% confidence interval (slope =0 suggests Y is not a linear function of X). The R^2 value indicated how well or not the data points measured actually fit the proposed curve: R measures the distance of the points from the linear fit curve. R^2 value of 1 suggests all data points are on the linear fit curve, R^2 value of 0.5 suggests that most of the data points are represented by the linear fit, indicating a possible relationship between X and Y. R^2 values close to 0 suggests that the data points are best fitted by a horizontal line across the mean which suggests no correlation between X and Y.

A. Endogenous Ca^{2+} events identification



B. Total endogenous Ca^{2+} events recorded

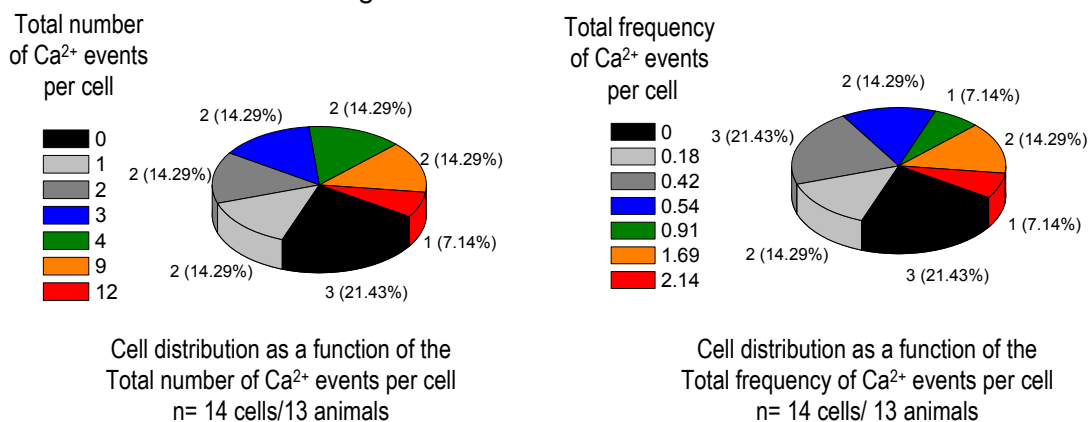


Figure 4.1 identifying endogenous Ca^{2+} events

A. Endogenous Ca^{2+} event identification

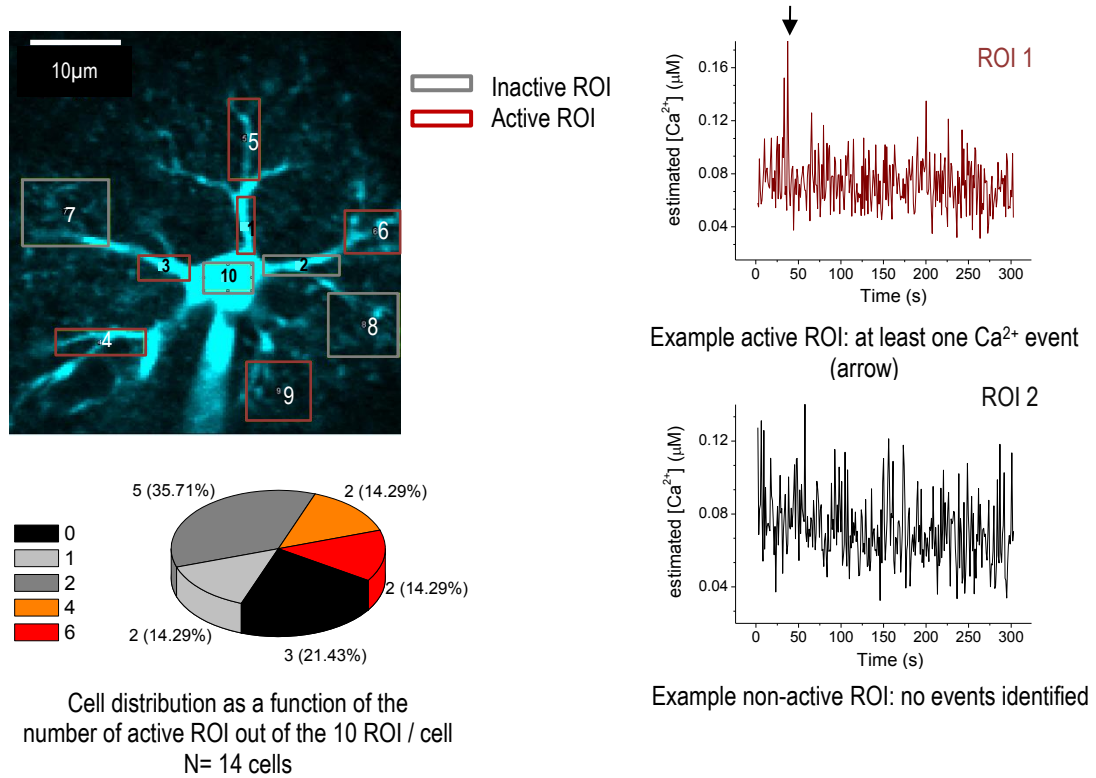
A594 fluorescence was used to identify ROI (illustration A1). The OGB-2 fluorescence intensity (photon count, A2), calculated photon count ration (A3) and estimated $[\text{Ca}^{2+}]$ timelapse traces were extracted for each ROI. Events were visually identified in intensity traces: increase in photon count (A2b) relative to baseline (A2a) which returns to baseline (A2c) within the recording; scale bar $2\mu\text{m}$. The pseudocolours illustrate low (green/ blue) and high (pink) average photon counts measured over 5 frames for the selected event (grey highlight, A2) for the selected ROI (A1). Only events that also occurred in the photon count ratio traces were taken into account. The events were quantified using the FLIM-estimated $[\text{Ca}^{2+}]$ traces.

B. Total endogenous Ca^{2+} events recorded across all 14 cells analysed

The first chart indicates the distribution of the cells analysed according to the total number of events across all ROI for each cell.

The second chart indicates the distribution of the cells analysed according to the average frequency: events per minute (total number of events / total recording duration) recorded per cell.

A. Active ROI: at least 1 endogenous Ca²⁺ event



B. Manual ROI morphology classification

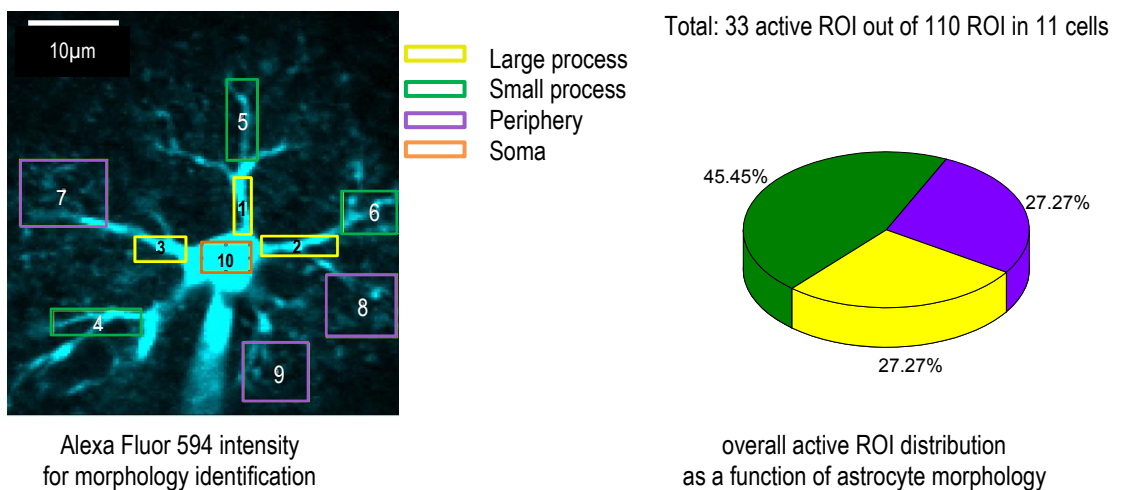


Figure 4.2 ROI characterisation

A. Active ROI

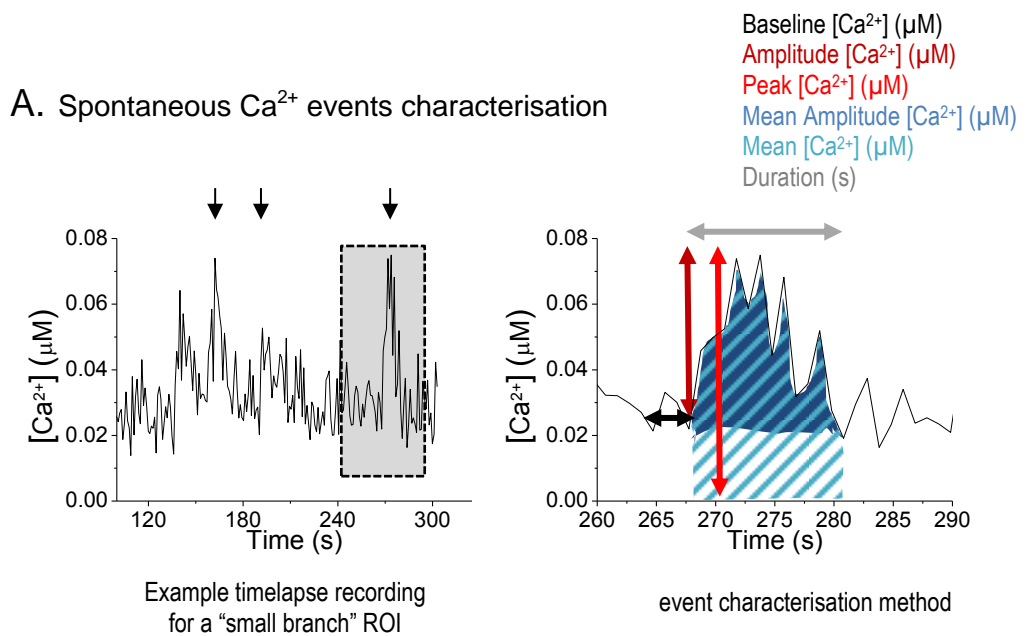
10 ROI were selected manually to represent each cell (illustrated in A1). The timelapse [Ca²⁺] recordings for each ROI were analysed for endogenous events. ROI were qualified as active (red, example trace for ROI 1) if they displayed at least one event during the total recording time. If no events were identified by the manual method described previously, the ROI was qualified as inactive (black, example trace for ROI 2).

The chart represents the distribution of all the analysed cells according to the number of ROI that were active out of the 10 ROI analysed for each cell.

B. ROI characterised by the selected area cell morphology

10 ROI were selected manually to equally represent each cell. ROI were taken across the cell and each visually determined cell area morphology type (large primary process in yellow, secondary small process in green, periphery process in purple) was represented by 3 ROI (illustrated in B1).

The chart represents the distribution of the total number of active ROI, regardless of the originating cell, as a function of the cell morphology type for each active ROI.



B. Spontaneous Ca²⁺ events characterisation in all active ROI

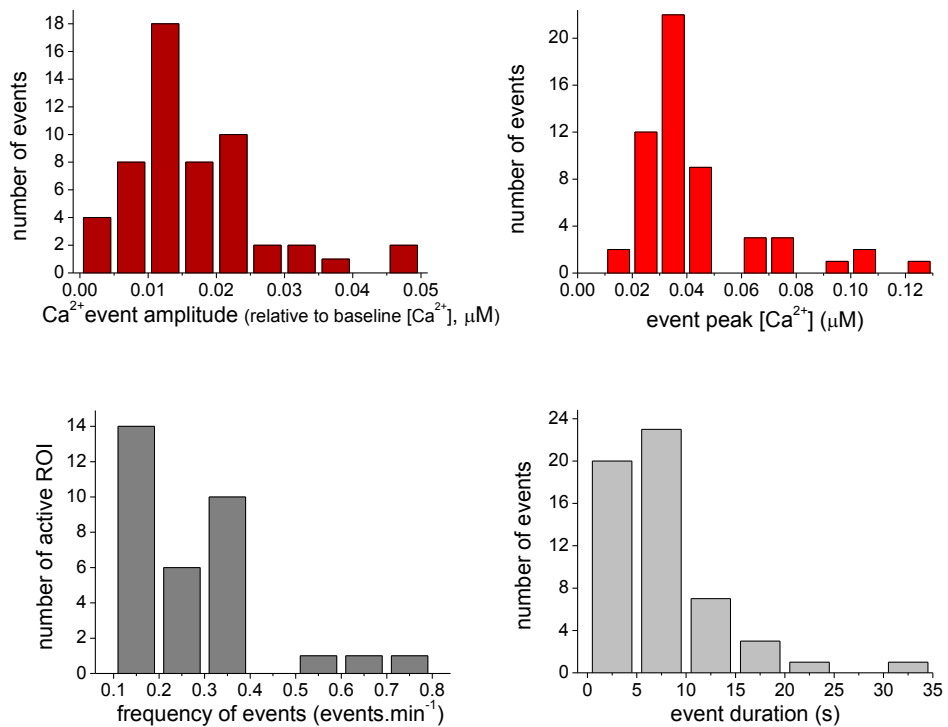


Figure 4.3 spontaneous calcium transient characterisation

A. Characterisation method

The first illustration shows the estimated [Ca²⁺] over time recorded in a small branch ROI, black arrows mark identified spontaneous Ca²⁺ events as described in the methods section of this chapter.

The event highlighted in grey is taken in the second illustration to show the characteristics measured for each Ca²⁺ event: duration (grey), pre-event baseline [Ca²⁺] (black), absolute and relative peak amplitude (red), absolute and relative average amplitude (blue).

B. Spontaneous calcium transients characteristics distribution across all active ROI

To assess the variability of these Ca²⁺ event characteristics, we plotted the distribution of the total number of events recorded across the range of each characteristic.

The first graphs show the distribution of the total number of events recorded across the range of event amplitude (dark red) and peak [Ca²⁺] (red) recorded (μM).

The distribution of the number of active ROI across the range of event frequencies per ROI recorded is in dark grey. The distribution of the total number of events recorded across the range of Ca²⁺ event duration recorded is in light grey.

RESULTS

The following section will describe the characteristics of the endogenous Ca^{2+} events in patched astrocytes as I detected through OGB-2 lifetime timelapse recordings. I will discuss the possible relationship between these characteristics and ROI morphology or resting $[\text{Ca}^{2+}]$.

A. Spontaneous Ca^{2+} events

Five minute timelapse recordings were performed and analysed for spontaneous Ca^{2+} events in 14 astrocytes. However, only 11 astrocytes showed any Ca^{2+} activity: at least one event in the 10 ROI analysed per cell. In the 114 ROI analysed for these 11 cells, only 33 ROI showed at least one Ca^{2+} event (referred to as active ROI). 55 Ca^{2+} events were analysed in total over all these active ROI. The properties of these Ca^{2+} events were analysed as described above and illustrated in figure 4.1.A; the distribution of these characteristics across the active ROI recorded are displayed in figure 4.1.B.

The frequency of events in active ROI was 0.29 ± 0.025 events per minute on average or 1-2 events/ 5 minute recording. 30% of active ROI had an average frequency of ≈ 0.35 events per minute and 42% had lower frequencies of ≈ 0.15 events per minute. Three regions from three different cells showed a slightly higher frequency of ≈ 0.65 events per minute.

On average, the Ca^{2+} events lasted for 7.7 ± 0.75 seconds. 42% of the 55 Ca^{2+} events analysed lasted between 7 and 10 seconds, 36% lasted between 1.5 and 5 seconds, 22% were lasted more than 12.5 seconds.

The average Ca^{2+} event amplitude was 16.4 ± 1.4 nM increase in $[\text{Ca}^{2+}]$. 47% of the total number of Ca^{2+} events increased their peak $[\text{Ca}^{2+}]$ by 5 to 15 nM and 33% of the total number of Ca^{2+} events increased by 15 to 25nM $[\text{Ca}^{2+}]$. The average Ca^{2+} event peak $[\text{Ca}^{2+}]$ ranged from 16.4 to 120 nM $[\text{Ca}^{2+}]$ across cells, averaging around 43 ± 3 nM $[\text{Ca}^{2+}]$.

The average relative area amplitude was 14.5 ± 0.8 nM increase in $[\text{Ca}^{2+}]$. 44% of the total Ca^{2+} events increased $[\text{Ca}^{2+}]$ by 10 to 15 nM, 22% of total events increased by 5 to 10nM $[\text{Ca}^{2+}]$ and 25% of total events increased by 15 to 25nM $[\text{Ca}^{2+}]$. The absolute average area amplitude ranged from 17.6 to 96.5 nM $[\text{Ca}^{2+}]$ across cells, averaging around 41 ± 2.5 nM $[\text{Ca}^{2+}]$.

B. Ca²⁺ event activity in relationship to ROI morphology

I further characterised the endogenous Ca²⁺ events in the astrocytes I investigated by considering the manually classified morphology (Fig 4.2.B) of the ROI where the events occurred.

First I considered the total active ROI recorded (Fig 4.2.A): 33 ROI of the 110 ROI analysed across 11 cells showed at least 1 event.

Overall active ROI (not taking into account the cell origin of the active ROI), 15 of the 33 active ROI recorded (45%) were classified as small secondary processes, the remaining active ROI were evenly distributed across large and periphery type morphology (Fig 4.2.B). I did not record any somatic events in these recordings.

Secondly, I established for each cell, the proportion of events in each of the three morphology categories tested. I counted the number of events across the three manually randomly selected ROI in each morphological category (large, small and peripheral processes) for each cell (n=11 active cells). I expressed this as total events per group as a proportion of the total events in the cell. To compare between cells, I divided the total counts by the total duration of the recording and expressed the values as events per minute.

Using this method, I aimed to establish if there was any preference in event occurrence in the cells I recorded from, for a particular morphological group (Table 4.1). I described a morphological preference when the proportion of events was higher in one morphological group than the others. Based on this definition of morphological preference, across the 11 cells tested, the events occurred preferentially in the small process group in 6 cells, 3 cells had equal proportion of Ca²⁺ events in 2 of the morphological categories and both large and peripheral process groups had 1 cell with a clear preference. However there was no significant difference in the average frequency of events recorded in each of these morphological categories (one-way analysis of variance: $p = 0.13$, $F = 2.2$; mean frequencies \pm standard error were 0.22 ± 0.02 , 0.34 ± 0.04 and 0.29 ± 0.06 events \times min⁻¹ in large, small and peripheral processes respectively).

| cell | Proportion of events per morphological category (% total events per cell) | | |
|------|--|-----------------|---------------------|
| | Large processes | Small processes | Periphery processes |
| 1 | 22.2 | 55.6 | 22.2 |
| 2 | 22.2 | 66.7 | 11.1 |
| 3 | 50 | 0 | 50 |
| 4 | 0 | 33.3 | 66.7 |
| 5 | 50 | 0 | 50 |
| 6 | 0 | 66.7 | 33.3 |
| 7 | 50 | 50 | 0 |
| 8 | 100 | 0 | 0 |
| 9 | 33.3 | 66.7 | 0 |
| 10 | 0 | 100 | 0 |
| 11 | 0 | 100 | 0 |

Table 4.1 Proportion of events per morphological category (n=11 cells)

The proportion of Ca²⁺ events is indicated for each cell (n=11), as the average number of events in 3 ROI per morphological group, divided by the total recording duration and expressed as a percentage of the total number of events recorded in all ROI.

If the cell displayed a clear higher proportion of events in one group (column), it is highlighted in bold.

C. Ca²⁺ event characteristics relationship with ROI resting [Ca²⁺]

Finally, I investigated the relationship between the endogenous Ca²⁺ events occurrence and characteristics, with resting [Ca²⁺] as illustrated in figure 4.4.A. I looked at the correlation between Ca²⁺ event characteristic and pre-event [Ca²⁺] in all 55 events recorded, regardless of the cell or ROI of origin.

i. Resting [Ca²⁺] distribution

In these recordings, the initial resting [Ca²⁺] and pre-event resting [Ca²⁺] estimated values ranged between 10 and 75 nM with most values being between 10 and 30nM across all ROIs (figure 4.4.B). Further discussion on the physiological relevance of these values and how they relate to previously published estimations of resting [Ca²⁺] is detailed in chapter 7.

The initial resting [Ca²⁺] was measured at the beginning of each recording for each ROI analysed (active or not) to estimate the range of resting [Ca²⁺] across ROIs and cells. Overall, most of the ROIs: 57 of the 144 ROIs analysed or 39.6% had a resting [Ca²⁺] between 20 and 30 nM. 14.6% ROI had a resting [Ca²⁺] between 10 and 20 nM and 22.9% of ROIs had a resting [Ca²⁺] between 30 and 40 nM.

The pre-event resting [Ca²⁺] was recorded immediately preceding each of the 55 Ca²⁺ events characterised. Most of the Ca²⁺ events occurred after pre-event resting [Ca²⁺] between 10 and 30 nM: 33% of events occurring after resting [Ca²⁺] between 10 and 20 nM and 47% of events occurring after resting [Ca²⁺] between 20 and 30 nM. However, this could be due to most ROIs, active or not, displaying resting [Ca²⁺] in that range: 50% of all ROIs recorded had initial resting [Ca²⁺] in the 15 to 30 nM range (72% of ROI initial resting [Ca²⁺] in 15 to 40 nM range).

The average initial resting [Ca²⁺] and pre-event resting [Ca²⁺] were similar across morphological sub categories described earlier (one-way analysis of variance suggest no significant differences across morphological group average initial resting [Ca²⁺]: F 1.9; p = 0.12) except for somatic resting [Ca²⁺] which tends to be lower than the rest of the cell (not significant using one-way ANOVA, figure 4.4.C). However, the somatic resting [Ca²⁺] estimation is more variable as it was measured only by one ROI in each cell whereas the other morphological groups were represented by three different ROIs across the cell for each morphological group.

ii. Ca²⁺ event characteristics and pre-event resting [Ca²⁺]

Figure 4.5 illustrates the relationship between Ca²⁺ event peak [Ca²⁺], amplitude, frequency and duration, with the resting [Ca²⁺] immediately preceding each event. All individual spontaneous Ca²⁺ events recorded are represented, regardless of their cell of origin. Spontaneous Ca²⁺ events that occurred in ROIs from astrocytes containing no other added Ca²⁺ or Ca²⁺ buffer are represented in grey in this figure.

Most of the recorded Ca²⁺ events occurred after similar pre-event resting [Ca²⁺] (\approx 20 to 25 nM) at which point their characteristics were similar. However, looking at the whole population of

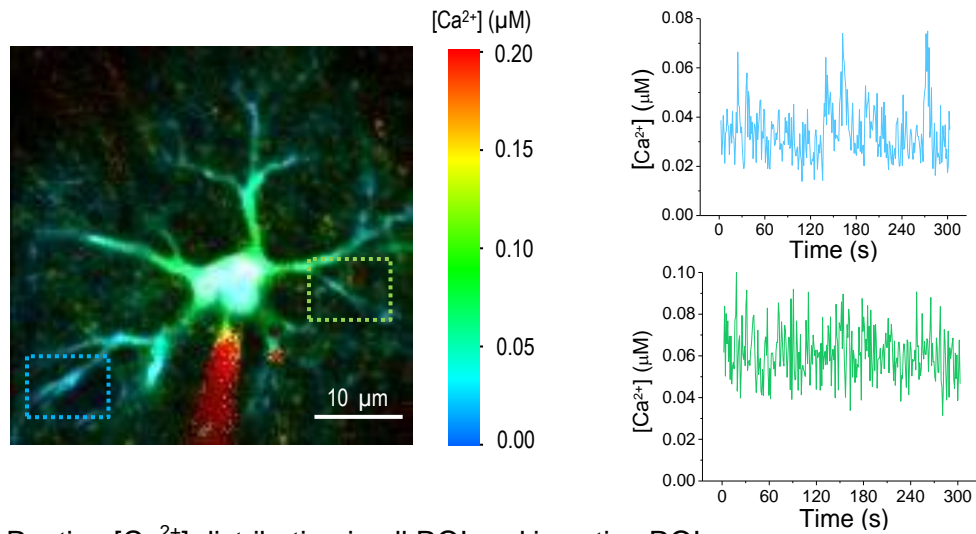
Ca²⁺ events recorded (55 events across 11 astrocytes), there was a potential positive correlation between resting [Ca²⁺] and event peak [Ca²⁺] as well as Ca²⁺ event amplitude (figure 4.5.A-B) (Spearman: 0.75, $p < 0.001$; 0.35, $p < 0.01$ for overall pre-event resting [Ca²⁺] correlations with Ca²⁺ event peak [Ca²⁺] or amplitude respectively). Indeed according to the R² value for a linear fit (adjusted for sample size), the variance in pre-event resting [Ca²⁺] could potentially explain 0.9 or 0.5 of the variance in spontaneous Ca²⁺ event peak [Ca²⁺] or amplitude respectively (figure 4.5.A-B) although further investigation would be necessary to establish a causal relationship (see discussion and following chapters).

This positive correlation was still present when considering only the peak [Ca²⁺] or amplitude of the 41 spontaneous Ca²⁺ events occurring only in astrocytes (n=5) containing no other added compounds (uncaged Ca²⁺ or Ca²⁺ buffers) other than the Ca²⁺ indicator OGB-2 (Spearman: 0.83, $p < 0.001$; 0.46, $p < 0.01$ for overall pre-event resting [Ca²⁺] correlations with peak [Ca²⁺] or amplitude respectively).

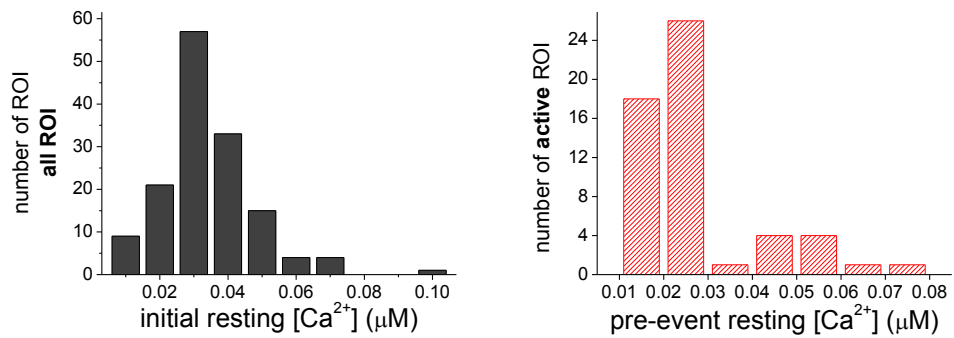
The frequency of Ca²⁺ events per ROI was less than 1 event per minute in all active ROIs and most of the Ca²⁺ events following pre-event resting [Ca²⁺] of ≈ 20 nM occurred at similar frequencies between 0.2 and 0.4 events per minute per ROI. However, the four extreme cases of higher and lowest frequency of Ca²⁺ events occurred in ROIs with respectively lower and higher resting [Ca²⁺] (figure 4.5.C). There was no significant correlation observed between the frequency of spontaneous Ca²⁺ events and the average pre-event resting [Ca²⁺] within each active ROI when considering all individual spontaneous Ca²⁺ events (figure 4.5.D; Spearman -0.15, $p = 0.40$). This was also the case when considering only individual spontaneous Ca²⁺ events from astrocytes containing no added Ca²⁺ or Ca²⁺ buffer other than the Ca²⁺ indicator OGB-2 (in grey in figure 4.5.D; Spearman -0.19, $p = 0.40$).

The Ca²⁺ event duration was quite variable for similar pre-event resting [Ca²⁺] of ≈ 20 nM. And although there were fewer Ca²⁺ events at other pre-event resting [Ca²⁺], these Ca²⁺ events were still variable in duration (figure 4.5.D). There was no significant correlation observed between the duration of a given spontaneous Ca²⁺ event and the pre-event resting [Ca²⁺] when considering all individual spontaneous Ca²⁺ events (figure 4.5.D; Spearman 0.20, $p = 0.15$). This was also the case when considering only individual spontaneous Ca²⁺ events from astrocytes containing no added Ca²⁺ or Ca²⁺ buffer other than the Ca²⁺ indicator OGB-2 (in grey in figure 4.5.D; Spearman 0.21, $p = 0.17$).

A. Example Ca^{2+} timelapse according to ROI resting $[\text{Ca}^{2+}]$



B. Resting $[\text{Ca}^{2+}]$ distribution in all ROI and in active ROI



C. Mean initial resting $[\text{Ca}^{2+}]_{(\pm\text{SEM})}$ per ROI morphology in all ROI and in active ROI

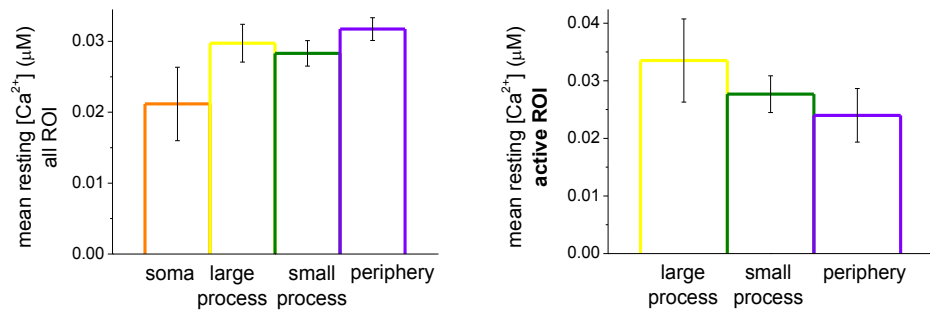


Figure 4.4 resting $[\text{Ca}^{2+}]$ distribution in patched astrocytes

A. Example cell: resting $[\text{Ca}^{2+}]$ distribution and example Ca^{2+} timelapse from 2 ROI

The first illustration shows the mean $[\text{Ca}^{2+}]$ per pixel as recorded through OGB2 fluorescence lifetime 90s timelapse imaging of an example astrocyte (scale bar $10\mu\text{m}$; colour scale: $0\text{-}200\text{nM}$ $[\text{Ca}^{2+}]$). The change in $[\text{Ca}^{2+}]$ (μM) over time (seconds) is shown for two similar size ROI with different resting $[\text{Ca}^{2+}]$: $\approx 35\text{nM}$ in blue (top graph) and $\approx 65\text{nM}$ in green (bottom graph). According to the criteria set in the methods section of this chapter, the blue trace shows some Ca^{2+} events whereas the green trace does not with the limitations due to the extensive noise.

B. Resting $[\text{Ca}^{2+}]$ distribution in all ROI and in all active ROI

The first graph (dark grey) shows the number of ROIs distributed across the range of resting $[\text{Ca}^{2+}]$ (μM) recorded in all 144 analysed ROI. The second graph (dark red) shows the same distributions but for the 33 active ROI only (ROI with at least one event).

C. Mean initial resting $[\text{Ca}^{2+}]_{(\pm\text{SEM})}$ per ROI morphology in all ROI and in all active ROI

These graphs illustrate the average resting $[\text{Ca}^{2+}] \pm \text{SEM}$ according to ROI morphology (soma in orange, large process in yellow, small process in green and periphery processes in violet). The first graph displays the resting $[\text{Ca}^{2+}]$ from all 144 ROI, the second graph displays the resting $[\text{Ca}^{2+}]$ from the 33 active ROI only.

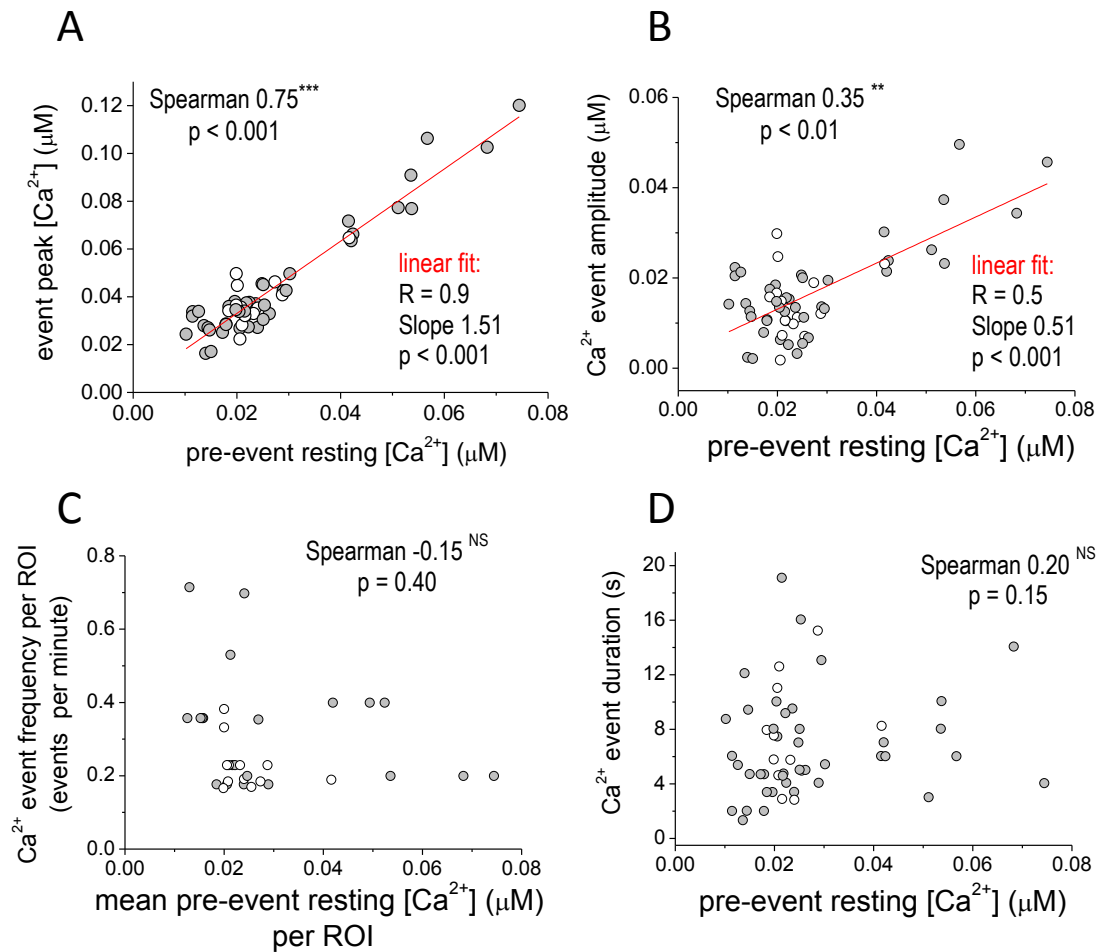


Figure 4.5 Relationship between resting $[Ca^{2+}]$ and spontaneous Ca^{2+} event

The characteristics of the 55 spontaneous Ca^{2+} events manually identified, recorded across 33 active ROI from 11 different astrocytes (11 acute hippocampal slices from 10 P21-25 male rats) using OGB-2 FLIM at near physiological temperature (32-34°C), were plotted against the pre-event resting $[Ca^{2+}]$ (μM). Spearman correlation coefficients and linear fits are calculated using all the spontaneous Ca^{2+} events recorded across all cells unless mentioned otherwise in the text. For illustration, the Ca^{2+} events occurring in astrocytes containing no additional Ca^{2+} or Ca^{2+} buffer are represented in grey. Ca^{2+} events occurring in astrocytes previously exposed to UV photolysis of caged or buffer (chapters 5, 6) are represented in white.

A: linear relationship between Ca^{2+} event peak $[Ca^{2+}]$ and pre event resting $[Ca^{2+}]$

The event peak $[Ca^{2+}]$ showed a positive linear fit (R^2 0.9, slope 1.51, $p < 0$) against pre-event resting $[Ca^{2+}]$, as displayed in panel A.

B: linear relationship between Ca^{2+} event amplitude and pre event resting $[Ca^{2+}]$

The event amplitude, relative to pre-event baseline $[Ca^{2+}]$, showed a positive linear fit (R^2 0.5, slope 0.51, $p = 7E^{-10}$) against pre-event resting $[Ca^{2+}]$, as displayed in panel B.

C: no linear relationship between frequency of spontaneous Ca^{2+} events and the active ROI average resting $[Ca^{2+}]$

The event frequency in each active ROI was relatively stable and not correlated with the average pre-event resting $[Ca^{2+}]$ in each ROI (Spearman -0.14; $p = 0.43$), as displayed in panel C.

D: no linear relationship between Ca^{2+} event duration and pre event resting $[Ca^{2+}]$

The event duration was quite variable for a given pre-event resting $[Ca^{2+}]$ and did not appear to be correlated with pre-event resting $[Ca^{2+}]$ in the case of the events recorded here (Spearman 0.20; $p = 0.15$), displayed in D.

DISCUSSION

A. Summary

In this chapter I have described that the endogenous Ca^{2+} activity in the astrocytes studied occurred in 30% of ROI (at least 1 Ca^{2+} event; 14 astrocytes). When spontaneous Ca^{2+} events did occur, their frequency of occurrence in that given ROI was on average 0.3 events per minute.

There did not seem to be any morphological preference for occurrence or frequency or duration or amplitude according to the morphology groups we identified.

Most ($\approx 40\%$) of the analysed ROI, active or not, had a resting $[\text{Ca}^{2+}]$ between 20 and 30nM. The active ROI resting $[\text{Ca}^{2+}]$ was not often above 30nM whereas the 23% of the total ROI had resting $[\text{Ca}^{2+}]$ between 30 and 40nM. However this could be due to the difference in number of ROI analysed: 144 total ROI and only 33 active ROI.

The duration of the Ca^{2+} events recorded was variable, between 1.5 and over 20 seconds long, but was not correlated with the pre-event resting $[\text{Ca}^{2+}]$.

The frequency of spontaneous Ca^{2+} events within a ROI did not correlate with the average pre-event resting $[\text{Ca}^{2+}]$ for the given ROI. The overall average frequency of spontaneous Ca^{2+} events within a given astrocyte (recorded across all ROI for a given cell) was also not found to correlate with the average initial resting $[\text{Ca}^{2+}]$ (Spearman -0.39; $p = 0.19$).

Both the spontaneous Ca^{2+} event peak $[\text{Ca}^{2+}]$ and amplitude showed a positive correlation with the pre-event resting $[\text{Ca}^{2+}]$ (figure 4.5.A-B). This could suggest that higher resting $[\text{Ca}^{2+}]$ may allow for more free Ca^{2+} availability giving rise to larger spontaneous Ca^{2+} events.

B. Larger spontaneous Ca^{2+} event amplitude was associated with higher pre-event resting $[\text{Ca}^{2+}]$

i. Possible mechanisms

The 55 Ca^{2+} events measured in total across all active ROIs from all recorded 11 cells displayed a significant ($p < 0.05$) positive correlation on average between the resting $[\text{Ca}^{2+}]$ immediately preceding the event and both the absolute peak $[\text{Ca}^{2+}]$ as well as the event amplitude. This was also the case when considering the 41 spontaneous Ca^{2+} events recorded in total across all active ROIs from 5 astrocytes containing no additional Ca^{2+} or Ca^{2+} buffer other than the Ca^{2+} indicator OGB-2.

It is important to note the possibility that these positive correlations could artificially arise during the sampling process. Indeed, these correlation plots (figure 4.5) represent all spontaneous Ca^{2+} events occurring across all ROIs from all astrocytes recorded, Therefore the differences and potential positive correlation observed could also reflect the variability across individual astrocytes, This and other limitations are discussed below, in section C. In this first section, I suggest and discuss what mechanisms could possibly explain this result if it were true.

- Resting $[Ca^{2+}]$ could enhance IP_3R2 dependent Ca^{2+} release

As suggested in chapter 1 and the introduction to this chapter, the sensitivity of IP_3R2 could be a potential explanation for this positive association of higher resting $[Ca^{2+}]$ with larger spontaneous event peak $[Ca^{2+}]$ and amplitude.

Some spontaneous Ca^{2+} events recorded in situ (Di Castro et al. 2011) and in vivo (Kanemaru et al. 2014) have been shown to rely on IP_3R dependent pathway for Ca^{2+} release from the endoplasmic reticulum into the astrocyte cytoplasm. The larger spontaneous Ca^{2+} events found to be associated with higher pre-event resting $[Ca^{2+}]$ could be simply explained by the Ca^{2+} sensitivity of IP_3R (reviewed in Foskett et al. 2007). Indeed, within the range of pre-event resting $[Ca^{2+}]$ measured in this chapter (≈ 15 to 80 nM), the IP_3R receptor open probability could be enhanced by cytosolic free Ca^{2+} which in turn would lead to larger influx of Ca^{2+} from the endoplasmic reticulum into the astrocyte cytosol, thus contributing to generate spontaneous Ca^{2+} events with larger amplitudes than at lower resting $[Ca^{2+}]$.

- Possible increased Ca^{2+} entry at higher resting $[Ca^{2+}]$

Additionally, some spontaneous Ca^{2+} events persist in recording in situ (Di Castro et al. 2011) and in vivo (Srinivasan et al. 2015; Kanemaru et al. 2014) from IP_3R2 disrupted animals suggesting IP_3R activation may not be the only mechanism underlying these spontaneous Ca^{2+} events. For example, astrocytes in culture have been shown to express transient receptor potential A1 (TRPA1) receptors that trigger astrocyte focal Ca^{2+} events upon exogenous agonist application. Although the endogenous mechanisms that may activate these receptors is not clear, upon activation these create non-selective cation channels which are thought to enable Ca^{2+} entry into astrocytes in culture (Shigetomi et al. 2012) and in astrocytes in the stratum radiatum area of acute hippocampal slices (Shigetomi et al. 2013b). These channels are also activated by intracellular $[Ca^{2+}]$ (Zurborg et al. 2007). Therefore, at higher resting $[Ca^{2+}]$, perhaps another potential mechanism by which astrocytes could trigger increased Ca^{2+} entry and thus larger Ca^{2+} events, could be through enhanced TRPA1 channel opening. However, Hausteiner et al. 2014 show that pharmacological inhibition of TRPA1 channels does not prevent the occurrence of spontaneous Ca^{2+} events in astrocytes in the stratum lucidum subregion of acute hippocampal slices.

- Saturation of endogenous Ca^{2+} buffers

Endogenous Ca^{2+} buffers also play an important role in Ca^{2+} signalling in general. Any substance that can bind Ca^{2+} could potentially buffer Ca^{2+} . The Ca^{2+} binding molecule concentration, its Ca^{2+} affinity (both in terms of $[Ca^{2+}]$ needed for buffer Ca^{2+} saturation and kinetics of Ca^{2+} binding process; approximated by K_D , K_{OFF} and K_{ON} for example) as well as its spatial location, diffusion or mobility within the cell determine the impact of these Ca^{2+} binding proteins on buffering Ca^{2+} influx during a Ca^{2+} event (reviewed in Gilibert 2012). At higher resting $[Ca^{2+}]$, Ca^{2+} buffers are more likely to be saturated in Ca^{2+} thus potentially leading to larger amplitudes of Ca^{2+} events as the event Ca^{2+} influx is less likely to be buffered. This mechanism could be a potential explanation underlying the positive correlation observed in this

chapter between astrocyte resting $[Ca^{2+}]$ and spontaneous Ca^{2+} events. Indeed, in neurons such a mechanism has been suggested to contribute to facilitation of synaptic transmission in neurons expressing high affinity Ca^{2+} buffers for example (Blatow et al. 2003) although internal stores are also likely to contribute to cytosolic Ca^{2+} buffering (Scott & Rusakov 2006).

However, Ca^{2+} binding proteins expression and Ca^{2+} buffers kinetics in astrocytes seem to be less documented than in neurons. Indeed, although calcium buffering has been shown to play a substantial role in the propagation of intercellular waves in cultured astrocytes (Z. Wang et al. 1997), to my knowledge, the buffering capacity of astrocytes is not known. On the one hand, the expression of buffers may differ across the heterogeneous astrocyte population. On the other hand, determining the buffering capacity in these cells may be challenging due to the fact that astrocytes do not exhibit action potentials or a store-independent, constant and defined Ca^{2+} influx. Indeed in neurons, where a given depolarisation may be well controlled, characterised and repeated, it has been possible to use this as a tool to estimate the effect of Ca^{2+} buffers when recording a Ca^{2+} event and thus extrapolate the Ca^{2+} buffering capacity of the cell investigated (for example Neher & Augustine 1992; Delvendahl et al. 2015).

The most documented Ca^{2+} binding protein in astrocytes is thought to be S100 β as its expression using immunohistochemistry is thought to be predominantly in astrocyte cytosol (Isobe et al. 1984). However, other than its roles on triggering a wide number of downstream effects once bound to Ca^{2+} , its role in Ca^{2+} buffering was suggested for when it is released by astrocytes into the extracellular space where it may have more impact on $[Ca^{2+}]$ as its affinity for Ca^{2+} is low (Morquette et al. 2015). Indeed, Morquette et al. 2015, using a calorimetry assay at 20°C and pH 7.4 of a recombinant S100 β protein, suggest its K_D for Ca^{2+} may be approximately 25 μ M. Other low affinity (K_D in low μ M range) Ca^{2+} binding proteins such as calmodulin and ATP (both may be present in astrocytes) are thought to play an important role in Ca^{2+} buffering in neurons due to their fast Ca^{2+} binding kinetics (Naraghi & Neher 1997; Meinrenken et al. 2002; Faas et al. 2011). However, due to their Ca^{2+} affinity in the low μ M range (\approx 2-6 μ M; Faas et al. 2011), none of these Ca^{2+} buffers are likely to be saturated at the resting $[Ca^{2+}]$ recorded here (in the range of 10 to 75 nM; minimum and maximum values in ROI from 5 astrocytes containing no additional Ca^{2+} or Ca^{2+} buffer other than OGB-2). However, the affinity could be modulated in the presence of other divalent ions such as magnesium or zinc. Indeed, S100 β was reported to enhance its affinity for Ca^{2+} in the presence of zinc (Baudier et al. 1986). Further studies of the distribution, concentration and binding kinetics in situ of these low affinity Ca^{2+} buffers in astrocytes could help determine their role in astrocyte Ca^{2+} buffering in these cells.

Neurons express a variety of high affinity Ca^{2+} buffers (Sloviter 1989) such as parvalbumin (K_D for Ca^{2+} \approx 51.4 nM; (Lee et al. 2000) which could play a role in the fast spiking phenotype of parvalbumin expressing interneurons. However their expression in astrocytes is not clear to my knowledge. Calbindin-D28k has a higher affinity for Ca^{2+} than these previously mentioned Ca^{2+} binding proteins (K_D \approx 300 nM; Nagerl et al. 2000). Calbindin-D28k was shown to be expressed in astrocytes but possibly only in reactive astrocytes following pathological conditions such as ischemia (Toyoshima et al. 1996).

Further investigation into the properties of endogenous astrocyte Ca^{2+} buffering would be required in order to establish if Ca^{2+} buffer saturation could be a mechanism that contributes to the positive correlation described between resting $[\text{Ca}^{2+}]$ and spontaneous Ca^{2+} event amplitude in this chapter. In the future, FLIM recordings and quantification of spontaneous Ca^{2+} events amplitude and resting $[\text{Ca}^{2+}]$ in astrocytes loaded with different concentrations of OGB Ca^{2+} indicators could perhaps indicate how much the added Ca^{2+} buffering contributes to the $[\text{Ca}^{2+}]$ estimates. Additionally, it could be interesting to see if this potential relationship between resting $[\text{Ca}^{2+}]$ and spontaneous Ca^{2+} events is still present in pathological conditions (such as in reactive astrocytes after ischemia, or perhaps in astrocytes in epileptic tissue) where perhaps astrocyte endogenous Ca^{2+} buffering capacity is altered.

- Internal store distribution could differ across ROIs or astrocytes

Furthermore, the distribution of internal stores, such as the endoplasmic reticulum, could also explain the positive correlation observed in this chapter between the given pre-event resting $[\text{Ca}^{2+}]$ and Ca^{2+} event amplitude or peak $[\text{Ca}^{2+}]$. This is further discussed in chapter 6.

In brief, simulations by Dr C. Henneberger based on an astrocyte model by Ullah et al 2006 (presented in chapter 6), suggest that the resting $[\text{Ca}^{2+}]$ as well as a simulated glutamate evoked event amplitude and peak $[\text{Ca}^{2+}]$ are all positively correlated with the ratio of endoplasmic reticulum to cytosol volume. Indeed, using electron microscopy Patrushev et al. 2013 suggest that endoplasmic reticulum and mitochondria are located in larger astrocytic processes presumably where spatial constraints are less than in the ultrathin perisynaptic astrocyte processes (see review Rusakov 2015). Although these nanoscale perisynaptic processes are beyond the optical diffraction limit of 2-photon microscopy perhaps it could be possible that similar spatial constraints could affect the distribution of internal stores across the visually identified astrocyte process morphology in this chapter.

There was no significant difference in initial resting $[\text{Ca}^{2+}]$ observed when considering all ROIs or only active ROIs taken from all astrocytes together (see figure 4.5). However, the amplitude of spontaneous Ca^{2+} events and the resting $[\text{Ca}^{2+}]$ recorded in astrocytes containing no additional Ca^{2+} or Ca^{2+} buffer other than the OGB-2 indicator ($n=5$) were both on average higher in large than in small or periphery astrocyte processes. The average \pm SEM resting $[\text{Ca}^{2+}]$ in active ROIs for these cells was 43.6 ± 11.4 , 27.9 ± 2.6 and 19.7 ± 3.5 nM across 5, 24 and 12 ROI visually classified as large, small and periphery processes respectively. The average \pm SEM spontaneous Ca^{2+} event amplitude was 24.6 ± 6.7 , 16.7 ± 2 and 14.5 ± 2.8 nM across 5, 24 and 12 ROI visually classified as large, small and periphery processes respectively.

Increasing the sample size of astrocytes recorded and/or the duration of recordings could perhaps help increase the number of active ROIs per morphological category which may reduce the standard error to the mean in particular in large process. However, ROIs were determined based on equal number of photons in order to reduce $[\text{Ca}^{2+}]$ estimation variability across ROIs.

As the larger processes are brighter than small processes, this visual morphological classification of ROI also results in ROI of different size: a given large process ROI covers less astrocyte area than periphery process ROI. More importantly, visual identification is likely to depend on the researcher and could bias the morphology classification. Perhaps another estimation of ROI morphology, such as estimating the volume fraction of a given ROI may be more appropriate in the future. This method uses the fluorescence of a Ca^{2+} independent morphological dye to estimate the size of the astrocyte structure in a given ROI based on the fluorescence of this indicator in a given ROI relative to a similar area ROI in the same focal plane taken from the soma of the astrocyte. The somatic ROI would be expected to show a reference fluorescence intensity where the totality of the ROI volume is occupied by the astrocyte (this method is used for example in Medvedev et al. 2014).

ii. Possible physiological relevance (see chapter 7)

The possible physiological relevance of larger astrocyte Ca^{2+} events is further discussed in chapter 7, particularly the impact on downstream astrocyte Ca^{2+} activated phenomena. For example, such as possibly reaching $[\text{Ca}^{2+}]$ thresholds thought to be necessary for Ca^{2+} dependent exocytosis of compounds in neurons (Augustine et al. 1991). Indeed, Ca^{2+} dependent exocytosis may also be a mechanism by which astrocyte Ca^{2+} signalling may shape synaptic transmission through gliotransmission for example (Jourdain et al. 2007; Bergersen et al. 2012). Therefore, similar $[\text{Ca}^{2+}]$ thresholds may also determine the possibility of gliotransmission through Ca^{2+} dependent exocytosis. If this were the case, then perhaps local areas of higher resting $[\text{Ca}^{2+}]$ may contribute to define subcompartments within astrocytes (reviewed in Rusakov et al. 2014) which could generate larger Ca^{2+} events and thus may be functionally more prone to Ca^{2+} dependent interactions with their neuronal, vasculature and extracellular environment.

iii. Further investigation

In order to assess the predictive role of pre-event resting $[\text{Ca}^{2+}]$ on determining the amplitude of spontaneous Ca^{2+} events in astrocytes in situ at near physiological temperature, it would be necessary to change the resting $[\text{Ca}^{2+}]$ for a given ROI and quantify the resulting change in Ca^{2+} event characteristics, should they occur.

However, in the case of the spontaneous astrocyte Ca^{2+} events, as recorded in this chapter, these spontaneous Ca^{2+} events were rare and when they did occur, it was infrequently in a given ROI. This sparsity of spontaneous Ca^{2+} events would render frequency comparisons after changing resting $[\text{Ca}^{2+}]$ too complex.

Indeed, it would be difficult to distinguish between no spontaneous Ca^{2+} events occurring because the resting $[\text{Ca}^{2+}]$ changed or because they are simply endogenously not frequent. We would need at least one Ca^{2+} event before and one after changing the resting $[\text{Ca}^{2+}]$ in a given

ROI to draw conclusions with regards to a causal relationship between resting $[Ca^{2+}]$ and spontaneous Ca^{2+} event characteristics. Furthermore, we do not know what triggers the spontaneous Ca^{2+} events recorded here. If different spontaneous Ca^{2+} events were triggered by different mechanisms then these differences could occlude or contaminate establishing a causal relationship between resting $[Ca^{2+}]$ and Ca^{2+} event amplitude in astrocytes in situ.

This led to investigating single evoked astrocyte Ca^{2+} events through pressure application of DHPG (an artificial metabotropic glutamate receptor agonist) as described in chapter 6. I would therefore be able to control the occurrence and trigger of an astrocyte Ca^{2+} event. This would allow us to investigate any changes in the characteristics of an evoked astrocyte Ca^{2+} event following modulation of the pre-event resting $[Ca^{2+}]$ (through UV photolysis of caged compounds, chapter 5).

C. Frequency of Ca^{2+} events detected and experimental limitations

i. Technical and analysis limitations may underestimate the frequency of astrocyte spontaneous Ca^{2+} events

The frequency of spontaneous Ca^{2+} events recorded in this chapter could be underestimated due to detection and analysis methods used. Indeed, I selected ROI across the cell and therefore may miss Ca^{2+} events occurring outside of these ROIs. ROIs were selected to equally represent each astrocyte, attempting to take into account possible differences in astrocyte morphology. ROI selection was also determined by the minimum number of photons required for $[Ca^{2+}]$ quantification using OGB-2 FLIM. Using the photon count ratio analysis method as opposed to the original fluorescence lifetime decay traces helps reduce the necessary amount of photons required for estimation of $[Ca^{2+}]$. Further analysis with smaller ROIs across the entire cell visible in the focal plane may increase the accuracy of estimation of the frequency of spontaneous Ca^{2+} events but would lose the information regarding the estimation of $[Ca^{2+}]$ due to insufficient photon collection.

Furthermore, the visual identification of Ca^{2+} events and poor signal to noise ratio may also underestimate the frequency of Ca^{2+} events occurring in the astrocytes recorded in this chapter. This could bias the detection in favour of larger spontaneous Ca^{2+} events as small Ca^{2+} events may be missed. OGB-2 has a slightly lower affinity for Ca^{2+} than OGB1 (K_D for $Ca^{2+} \approx 190$ and 580 nM for OGB-1 and OGB-2 respectively; as stated by Molecular Probes and measured by fluorescence intensity for increasing $[Ca^{2+}]$ in the absence of magnesium), which reduces the risk of saturating the dye at higher $[Ca^{2+}]$. Using OGB-2, we did not record saturating levels of Ca^{2+} thus reducing the risk of not detecting some of the Ca^{2+} events or curtailing the Ca^{2+} event amplitudes. Using dyes of better dynamic range could reduce the lack of detection of small Ca^{2+} events. Indeed, Fluo-4 is commonly used for studies of astrocyte Ca^{2+} signalling as it is brighter and has much better dynamic range than OGB dyes for example (at least 10 (up to 100) fold vs 3-5 fold difference in fluorescence intensity between minimal and saturation levels of $[Ca^{2+}]$ for Fluo-4 and OGB Ca^{2+} indicators respectively).

However, Fluo-4 lifetime is not sensitive to $[Ca^{2+}]$ and thus cannot be used for quantification with lifetime imaging method. Additionally, Ca^{2+} events could occur at a nanoscale level in smaller astrocyte processes surrounding the synapses which would not be detected as they could simply be below the optical diffraction limit for 2-photon excitation microscopy ($\approx 1 \mu\text{m}$; reviewed in Rusakov 2015).

The frame scan acquisition and signal to noise ratio in the recordings in this chapter would bias Ca^{2+} event detection towards Ca^{2+} events lasting more than 1 second. Hausteiner et al 2014 suggest that faster acquisition (using 3 minute recordings of repeated line scans acquired at 200 Hz) did not result in acquiring faster in situ astrocyte spontaneous Ca^{2+} events in their hands. Indeed the average Ca^{2+} events lasted ≈ 3 seconds regardless of the acquisition mode: in both fast line scan and slower frame scans. This suggests that the acquisition rate used in this thesis is appropriate in terms of time resolution for the detection of most astrocyte Ca^{2+} events as they may occur on second rather than millisecond timescale, at least when using 2-photon excitation microscopy timelapse Ca^{2+} imaging.

Increasing the acquisition rate could help detect more Ca^{2+} events but may also contribute to more photo stimulation: triggering Ca^{2+} increase by repeated laser excitation which could trigger photodamage or heat stimulation (as suggested for example in Kuga et al. 2011; Wang et al. 2006). Such Ca^{2+} events may not necessarily represent astrocyte Ca^{2+} events that would occur by endogenous triggers. However, as laser induced triggering of spontaneous Ca^{2+} activity may occur at higher excitation intensity than used in the recordings in this thesis, it is unlikely that laser excitation triggers the spontaneous Ca^{2+} events recorded here. Indeed, the 2-photon excitation laser intensity was kept below 10 mW as measured under the objective and is likely to be less intense at the cell as a function of the cell depth within the slice.

Finally, in some cases these timelapse recordings of spontaneous Ca^{2+} events were carried out in astrocytes previously exposed to UV photolysis of caged Ca^{2+} or Ca^{2+} buffer (see chapters 5 and 6). The number of spontaneous Ca^{2+} events recorded in those astrocytes (14 different spontaneous Ca^{2+} events in total across all ROI in 6 astrocytes; 2 astrocytes displayed no Ca^{2+} events in the recording) was less than in astrocytes containing no additional Ca^{2+} or Ca^{2+} buffer other than the OGB-2 Ca^{2+} indicator (41 different spontaneous Ca^{2+} events in total across all ROI in 5 astrocytes; 1 astrocyte displayed no Ca^{2+} events in the recording). This suggests that in astrocytes with added Ca^{2+} or Ca^{2+} buffer (respectively containing either 5 mM NPEGTA or 2.5 mM Diazo2, see chapter 5), the likelihood of spontaneously occurring Ca^{2+} events is reduced. This is consistent with previous reports that adding $> 5 - 10$ mM BAPTA or EGTA high affinity Ca^{2+} buffers greatly reduces Ca^{2+} activity in astrocytes (for example Di Castro et al. 2011; Navarrete et al. 2012). The impact of these added Ca^{2+} buffers in this thesis is further discussed in chapters 5, 6 and 7. However, the observed positive correlation between resting $[Ca^{2+}]$ and spontaneous Ca^{2+} events amplitude and peak $[Ca^{2+}]$ persists when considering Ca^{2+} events only in astrocytes containing no additional Ca^{2+} or Ca^{2+} buffer other than the OGB-2 Ca^{2+} indicator.

ii. Frequency of Ca²⁺ events is similar to bulk of previously reported values

The frequency of spontaneous, endogenous Ca²⁺ events in astrocytes is possibly around 1 event per minute per cell. In this chapter, the frequency of spontaneous Ca²⁺ events per minute was on average of 1.38 ± 0.3 per cell and 0.33 ± 0.04 per ROI as recorded in astrocytes containing no added Ca²⁺ or Ca²⁺ buffer other than the Ca²⁺ indicator OGB-2 (n= 5 astrocytes in 5 animals). Different experimental approaches (such as Ca²⁺ indicator used) and analysis (definition criteria for a Ca²⁺ event and location of the Ca²⁺ events within the astrocyte) contribute to the variability in estimating the frequency of these Ca²⁺ events in astrocytes.

- Spontaneous Ca²⁺ events occurred in astrocyte processes not soma

In P5-17 old rat thalamus acute slices using Fluo4 AM bulk loading, astrocytes were described as showing 0.5 Ca²⁺ events per 100 s per cell (Parri & Crunelli 2003).

Reeves et al. 2011 suggest that this bulk loading technique in situ could reduce the likelihood of detecting Ca²⁺ events in astrocyte processes which may explain how these older studies could report lower frequency of spontaneous events per cell than reported in this chapter. Indeed, we did not record any spontaneous Ca²⁺ events in the soma of the astrocytes in this chapter. This is consistent with astrocytes somatic Ca²⁺ events in situ shown to occur at frequency of 0.02 Ca²⁺ events per minute in hippocampus slices from 5-6 month adult mice using genetically encoded Ca²⁺ indicator Gcamp2 (Wu et al. 2014). Similarly, in vivo recordings of spontaneous astrocyte Ca²⁺ activity in the barrel cortex displayed a lack of activity in somatic ROI (only in 2 of 93 astrocytes) whereas the processes displayed more activity (34 Ca²⁺ events in total over 10 minute recordings in 93 astrocytes in 6 mice; Supplementary figures from Wang et al. 2006).

- Faster frequencies reported in more in depth analysis

However, in adult mouse dentate molecular layer hippocampal astrocytes in situ using Fluo-4 and faster scan rates, expanded Ca²⁺ have been shown to occur at 1.5 events per minute per process (Di Castro et al. 2011). A similar frequency has been suggested for Ca²⁺ events in vivo (Kanemaru et al. 2014). This is at a higher frequency than the 0.33 ± 0.04 events per minute per ROI reported here. As suggested above, this could be due to these studies using dyes with higher dynamic range than OGB-2 or smaller ROIs covering the entire cell processes which may lead us to underestimate the frequency of Ca²⁺ events in this thesis. However, Kuga et al. 2011 suggest that at low (<10 mW under the objective, as used in this thesis) excitation laser intensity, astrocytes in cortical networks in vivo express more 'glissandi' (regenerative Ca²⁺ waves that propagate across cells) than when using higher excitation laser intensity (10-30mW). They also suggest that these astrocytes expressing more 'glissandi' also show lower frequency of sporadic Ca²⁺ activity than in astrocytes with no 'glissandi', possibly associated with higher laser intensity. This could suggest that at low laser intensity used in this thesis, the frequency of spontaneous Ca²⁺ events would be less than in other studies using higher laser excitation intensity or more laser exposure (which could possibly happen during faster acquisition rates such as in Di Castro et al 2011 for example).

D. Conclusion

In this chapter we have identified and quantified spontaneous Ca^{2+} events recorded at near physiological temperature (32-34°C) in astrocyte processes in the stratum radiatum area of acute hippocampal slices of young adult rats. The frequencies of these Ca^{2+} events were similar to other frequencies reported in astrocytes and no specific Ca^{2+} event pattern was observed. Ca^{2+} oscillations, as in periodic spontaneous Ca^{2+} events, have been observed in astrocytes in culture (reviewed in Verkhratsky & Kettenmann 1996) and when considering global, predominantly somatic Ca^{2+} events in situ (for example Pasti et al. 1997; Nett et al. 2002). However in this chapter and as observed in other more recent studies using higher-resolution imaging techniques in situ and in vivo, spontaneous Ca^{2+} events recorded across the whole of the astrocyte (not only in the cell soma) do not necessarily exhibit such a periodic pattern (Di Castro et al. 2011; Kanemaru et al. 2014). These spontaneous Ca^{2+} events may perhaps be caused by stochastic fluctuations in resting $[\text{Ca}^{2+}]$ or by spontaneous release of synaptic vesicles by neighbouring neurons. Indeed, the application of bafilomycin to block such spontaneous vesicle release by neurons markedly reduced the number of spontaneous Ca^{2+} events (DiCastro et al. 2011).

The main result was that resting $[\text{Ca}^{2+}]$ and spontaneous Ca^{2+} event amplitude and peak $[\text{Ca}^{2+}]$ were positively correlated in our hands. This could be explained by increases in cytosolic $[\text{Ca}^{2+}]$ enhancing the open probability of $\text{IP}_3\text{R2}$ in the range of $[\text{Ca}^{2+}]$ we recorded and thus increasing release from the endoplasmic reticulum. The relative distribution of internal stores, such as the endoplasmic reticulum (see simulation in chapter 6, figure 6.15), compared to cytosol which may occur across different morphological structures or within different subcompartments of the astrocyte could also explain this positive correlation. Further investigation would be required to address if there is a causal relationship between resting $[\text{Ca}^{2+}]$ and Ca^{2+} event amplitude in these astrocytes.

Chapter5: MANIPULATING CALCIUM CONCENTRATIONS

INTRODUCTION

A. Objective

In order to test the causality of a role of resting calcium concentration in astrocyte calcium signalling, I need to be able to quantify and modify the intracellular resting calcium concentration whilst recording astrocytic calcium signalling (see discussion in chapter 4). This chapter describes the setup and use of ultraviolet (UV) uncaging of O-nitrophenyl-EGTA (NP-EGTA) or Diazo-2 to respectively increase or decrease resting $[Ca^{2+}]$ as recorded by OGB-2 fluorescence lifetime imaging in whole-cell patched astrocytes.

B. UV uncaging of NPEGTA or Diazo2

Flash photolysis allows the release of a previously-caged compound at a defined point in time and space, ie when and where the caged compound is exposed to UV light (300-380nm). Following exposure to UV light, the photoabsorbing 'cage' is submitted to a set of rapid dark reactions that unbinds cage and compound in order to release the compound for biological action (principle reviewed in Gurney 1987).

We used caged tetrapotassium cell impermeant calcium buffers to both decrease intracellular calcium using Diazo-2 and in other experiments, to increase calcium concentrations using (NP-EGTA). Indeed, upon UV excitation, the Diazo-2 dissociation constant (K_D) for Ca^{2+} is theoretically decreased from 2.2 μ M to 73 nM (Invitrogen, D-3034; see Lancaster & Batchelor 2000 for example in hippocampal neurons). Therefore, following sufficient photolysis, an increased amount of free cytosolic calcium should bind to Diazo-2 given that this compound now has a higher affinity for calcium thus reducing the resting calcium concentration.

NP-EGTA is widely used for calcium uncaging (Perea & Araque 2007 for example in astrocytes). It has a high affinity for calcium as a caged compound and upon UV excitation, it's K_D for Ca^{2+} is theoretically increased from 80 nM to >1 mM (Invitrogen, N-6802; reviewed in Ellis-Davies 2008). It can be loaded with calcium beforehand in order to increase the amount of calcium released after uncaging and not rely on calcium release from the cell.

C. UV LED setup

We setup and used a wide field UV exposure system using a high power UV light emitting diode (365 nm LED) coupled to an optical fibre. Indeed, LEDs have sufficient power (up to ≈ 50 mW at the tip of the fibre) to provide a cheaper alternative to a UV laser (Bernardinelli et al. 2005). Using an optical fibre to position the UV light exposure avoids the more complex parfocality issue with using two lasers: where one has to be sure both uncaging and imaging lasers are aligned in the same focal plane. Using a 2-photon laser at 720 nm for uncaging does have the benefit of avoiding as much UV light scattering but equally involves uncaging in a specific spot. The use of the optical fibre allows for UV exposure to the whole cell under investigation (Parpura & Haydon 1999), which is ideal when wanting to change the resting $[Ca^{2+}]$ in all of the structures of the patched astrocyte.

METHODS

A. UV uncaging setup

We set up the combination of a UV-LED and optical fibre that allows for the photolysis of caged compounds across the cell whilst imaging astrocytic calcium oscillations (Fig. 5.1.C).

i. UV light source

The source for UV light was the Thorlabs M365F1 high power LED which can generate up to 700mA UV light at 365nm (Fig. 5.1.A). LEDs do not emit coherent light therefore the coupling between the diode and the output has to be as efficient as possible in order to minimise loss of power. The Thorlabs LED achieve minimal loss of power by simply positioning the diode as close as possible to optical fibre input and coupling them as tightly as possible with SMA port (“butt- coupling technique”). The coupled fibre properties are also key to prevent power loss.

The light was guided from the LED to the recording chamber through a customised 1 m long, 1 mm diameter silica core, 0.39 numerical aperture optical fibre, *Thorlabs* FT1000EMT or FT1000UMT (Fig.5.1.C). These fibres are clad in a hard polymer (Technology Enhanced Clad Silica) and a Tefzel cover in order to prevent damage to the fibre core thus enhancing fibre flexibility with less risk of damage induced loss of output power. The fibre had a SMA port fitting on the end in contact with the LED so that the end of the fibre would be as tightly connected to the LED as possible. We chose a 1 mm diameter fibre as this large core diameter with a relatively high NA, to allow as much light as possible to enter the fibre input. Additionally, high-ethanol content fibre cores have less attenuation over distance for wavelengths below 400 nm. Finally, the output of the fibre was simply cleaved (removal of cladding and exposure of silica core) over approximately 1 cm.

ii. UV light control

- Positioning the optical fibre

The stripped end of the optical fibre was positioned above the area of interest in the recording chamber, ie the CA1 stratum radiatum area of the acute hippocampal slice. The fibre was carefully secured to a Scientifica micromanipulator with cable ties and a vice which then enabled control of the angle and position of the fibre (Fig.5.1.C). A constant low intensity UV light was used to check that the stratum radiatum area of interest was indeed potentially exposed to UV.

- Setting UV pulse parameters

The intensity, frequency and duration of the UV light pulse during uncaging protocols were controlled through a DC2100 LED driver with pulse modulation, Thorlabs (Fig. 5.1.B). This allowed to opt for either continuous or pulsed exposure. For the pulsed exposure, the duration of each pulse was set through a combination of the frequency and duty cycle. For example, a 50ms pulse was repeated every 50ms when the frequency was set for 10Hz and the duty cycle set for 50%. A further setting specified the number of pulses generated. I manually triggered the chosen cycle of pulses of UV excitation, although this driver can also be externally triggered by a simple TTL pulse (whose amplitude would determine the intensity of UV light and duration and repetition would set the UV pulse). The intensity of the UV light could range from 0 to 700mA for this particular 365nm LED. The power measured at the output, the cleaved end of the optical fibre, was measured using a power meter (Thorlabs) approximately centred and at a 5mm distance from the tip of the fibre.

At 100mA intensity, the approximate output power was measured as 6mW and 8mW for the EMT and UMT fibres respectively. At 500mA intensity, the approximate output power was measured as 33mW and 42mW for the EMT and UMT fibres respectively.

- Reducing UV mediated autofluorescence

For the acquisition of fluorescence lifetime, a custom made switch was added to the PicoQuant PMA Hybrid photon detector described previously in chapter 3. This enabled to bypass the automatic shutter built in to the detector, in order to be able to use UV light uncaging during FLIM acquisition. Indeed, UV light delivered to the brain slice triggers auto fluorescence emission over a wide range of wavelengths. The resulting drastic increase in photons would trigger the closure of the built in protective shutter to the detector. This added a few seconds to the unusable photon collection during UV exposure. This manually operated switch allowed to control this shutter. This reduced both the unusable time during UV exposure and the risk of photon saturation damage to the detector.

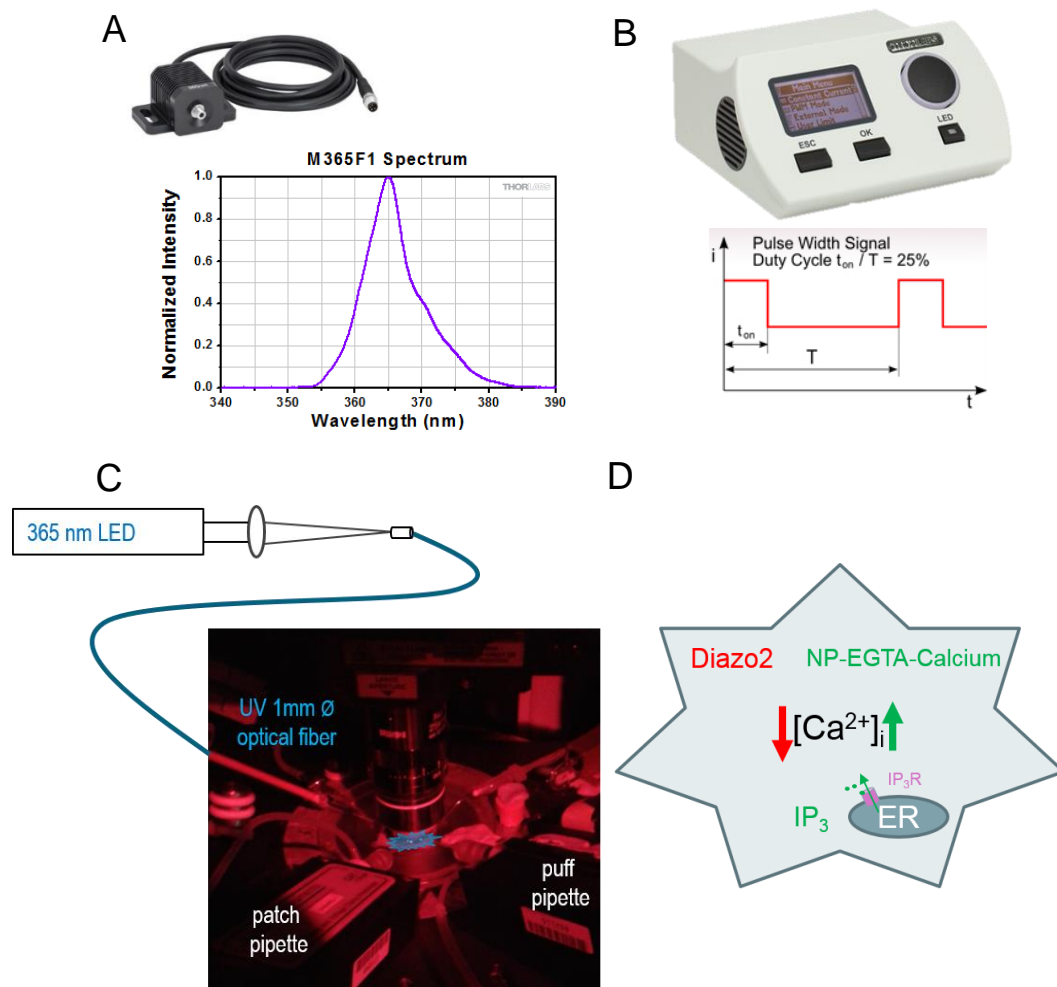


Fig. 5.1 UV LED uncaging of caged calcium or calcium buffers to modulate resting $[Ca^{2+}]$ in astrocytes, Setup.

A. High power UV LED, M 365F1 Thorlabs

We used the M 365F1 high power UV LED to supply up to emit up to 700mA UV light centred around 365nm.

B. LED driver with pulse modulation, DC2100 Thorlabs

The UV LED pulse was controlled with the DC2100 LED driver. The duration and intensity of UV exposure was controlled by setting the intensity, frequency, duty cycle and counts in the pulse width modulation mode.

C. Acute slice UV illumination configuration

The area under investigation in the acute slice preparation (CA1 stratum radiatum) is illuminated with UV light supplied by the high power UV LED (schematic) through a Thorlabs custom made 1mm diameter optical fibre, FT1000EMT/UMT. The cleaved end of the optical fibre is positioned very close to the objective with a Scientifica micro manipulator. This enables the most UV illumination (with as little as possible loss of UV through dispersion) without hindering the positioning of both puff and patch pipettes.

D. Caged calcium modulators

We used the following caged compounds: Diazo-2 tetrapotassium salt and O-nitrophenyl EGTA tetrapotassium salt (NP-EGTA), both supplied by Invitrogen, Life Technologies (respectively D-3034 and N-6802). Diazo-2 was used to reduce basal $[Ca^{2+}]_i$ as its K_d for Ca^{2+} decreases from 2.2 μ M to 73nM after UV flash photolysis. NP-EGTA was used to increase basal $[Ca^{2+}]_i$, its K_d for Ca^{2+} increases from 80nM to >1mM after UV flash photolysis. It can be preliminarily bound to Ca^{2+} in order to deliver Ca^{2+} after photolysis.

B. Protocol

i. Fluorescence lifetime recording of OGB-2 in Astrocytes

With the UV-LED set to constant and low intensity, the optical fibre was positioned so that the UV light would expose the stratum radiatum in P20-25 males Sprague-Dawley rat hippocampal slices as described above. Astrocytes were identified and loaded with a KMS internal solution through whole cell patch clamp as described in chapter 2, methods.

OGB-2 was added to all internal solutions at 200 μM for lifetime calcium imaging, as described in the FLIM section, chapter 3. 100 μM Alexa594 was added for intensity cell morphology identification, as described in chapter 2.

Using a continuous frame acquisition the resulting changes in OGB-2 lifetime were recorded over 300 frames or approximately 90s whilst the slices were perfused with ACSF at 32-34 $^{\circ}\text{C}$ (as described in chapter 2 and chapter 3, FLIM). The cells were all imaged using 25X Olympus objective with digital zoom at 6.4 resulting in a resolution of 0.310 $\mu\text{m}/\text{pixel}$. The 2-photon laser power was adjusted to be within 4-8mW at 800nm as measured under the objective and the dwell time was 4 $\mu\text{s}/\text{pixel}$. Cells were patched between 30 and 90 μm deep into the slice as a compromise between cell health (deeper cells less damaged by the slicing procedure) and UV light scattering (UV light scatters (Tyndall, Rayleigh, Raman effects) so deeper cells have less powerful exposure to UV light).

A few minutes after whole cell, allowing for dye diffusion and equilibration across the patched astrocyte, a single 90s/300 frame timelapse recording was started. The shutter to the photon detector was closed manually. The cell was then exposed to brief pulses of UV light with the setup explained above. The shutter to the photon detector was then reopened and a further 150 frames after UV exposure were recorded.

ii. Uncaging compounds

Three groups were devised based on internal solution composition: control, Diazo2 (Invitrogen, D3034) and NPEGTA (Invitrogen, N6802).

For the control group, a KMS/dyes-only internal was used to patch cells. Recordings were performed 20 minutes after whole-cell. The UV exposure through a FT1000EMT fibre was set for 10 pulses of 50ms at 10Hz using 600mA UV intensity.

For Diazo2 uncaging, 2.5mM of Diazo2 was added to the KMS/dyes based internal solution. 20 minutes after whole cell, the cell was exposed to 10 pulses of 50 ms at 10 Hz using 600 mA UV intensity, through a FT1000EMT fibre.

For NPEGTA uncaging, 5 mM NPEGTA and 3 mM CaCl_2 were added to the KMS/dyes based internal solution. 32 minutes after whole cell, the cell was exposed to 10 pulses of 50 ms at 10 Hz using 600 mA UV intensity, through a FT1000UMT fibre.

C. Data extraction and analysis

I analysed the lifetime traces acquired with the PicoQuant FLIM setup (cf chapter 3) using a custom made Matlab script provided by my supervisor, Dr Christian Henneberger. This enabled the calculation of the photon count ratio from the OGB-2 fluorescence lifetime traces recorded in each astrocyte. The $[Ca^{2+}]$ was estimated from the photon count ratio traces. The principles underlying the calculation of the photon count ratio and the ensuing estimation of $[Ca^{2+}]$ are described in chapter 3.

The following criteria, described below, were used for all cells across the three groups in order to enable as accurate as possible comparison across cells.

i. Regions of Interest

I used an automated arbitrary binning system to create rectangular regions of interest (ROIs) that would reflect the whole of the patched cell.

- Pixel binning

I binned the pixels in the acquired frame by groups of 16x16 pixels, creating a grid of rectangular ROIs across the frame (Fig.5.2.B) of $25 \mu m^2$. The number of pixels to bin, and thus ROI size, was selected in order to create ROIs containing enough photons for as accurate as possible estimation of the calcium from the lifetime photon count ratio (cf chapter 3). However, I also aimed to balance this with as accurate as possible reflection of the actual cell morphology. Indeed, binning more pixels would increase the likelihood of extracting an accurate estimation of the $[Ca^{2+}]$ in that ROI but also create larger ROIs. This would lessen the ROI's accurate reflexion of the cell morphology: sampling distinct processes as one ROI for example.

- Selection of representative ROIs

As stated above, ROIs were aimed at having enough photons in order to estimate $[Ca^{2+}]$ as accurately as possible and with similar variability in all cells. Additionally to pixel binning, an automatic cut off threshold was set for 2000 photons per ROI (Fig.5.2.B). Any ROI with less than 2000 photons was automatically discarded. This enabled discarding of ROIs with few photons such as ROIs outside of the given astrocyte territory (background or neighbouring astrocyte for example).

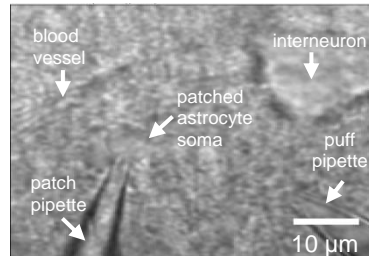
A further manual selection of ROI aimed to confirm that these automatically generated ROI were representative of the cell (Fig. 5.2.A-B). In most cases, the photon threshold enabled to remove all ROIs outside of the individual astrocyte's territory. However we found that, similarly to Zheng et al. 2015, that the patch pipette contributed at lot of photons (Fig 5.2).

In order to avoid any influence from these non-cell photons, all ROIs matching in total or in part the location of the patch or puff pipette were manually removed.

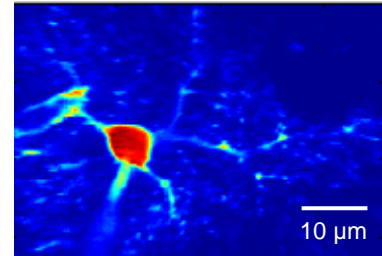
This was done by manually comparing the location of the pipettes in intensity picture to the ROI grid (Fig.5.2.A). One could also use the transmitted light image and a Z-projection of the Alexa594 intensity image to aid localisation of possibly pipette photons contaminated ROIs.


A. Cell visualisation

Cell visualisation 1:
DIC ZT projection



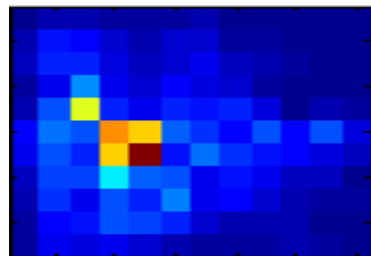
Cell visualisation 2:
OGB-2 intensity ZT projection





 OGB2 average intensity:
mean photon count per pixel

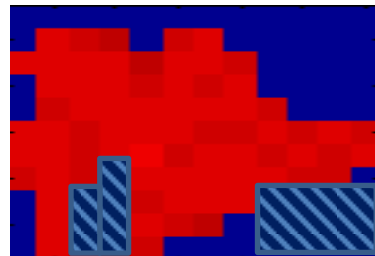
B. Regions of interest

ROI selection 1:
automated 16x16 pixel bins



 automatic bins of 16x16 pixels
 intensity: mean photon count per ROI

ROI selection 2:
automated photon cut-off
manual non-cell ROI removal






 ROI considered as cell
 ROI removed by photon cut-off
(not enough photons for accurate
[Ca²⁺] estimation)
 ROI removed manually
(non-cell photons)

Fig. 5.2 automatically defined Regions Of Interest (ROI)

A. Cell visualisation

The first illustration shows the neighbouring structures surrounding the patched astrocyte. In this case, the following items are distinguishable: patched astrocyte soma, patch pipette, puff pipette, neighbouring blood vessel and interneuron. Scale bar is 10μm. This helps identify structures not to include in regions of interest.

The second illustration shows the average OGB2 intensity in the same cell, same resolution. This enables visualisation of the patched astrocyte different morphological compartments which can help characterise regions of interest.

B. Creating regions of interest

The first illustration shows the automated created of regions of interest: each rectangle is a bin of 16x16 neighbouring pixels. The colours code for the average number of photons per ROI. The second illustration shows the selection of ROI considered to represent the cell (red). This selection is first done by setting an automatic cut-off for the minimum average number of photons per ROI (dark blue). The remaining ROI are subsequently manually compared to illustrations such as the above mentioned cell visualisations, in order to remove any ROI where photons may originate from non-cell structures.

ii. Quantifying the effect of UV photolysis of caged Ca^{2+} or Ca^{2+} buffer

I aimed to quantify the $[\text{Ca}^{2+}]$ before and after UV exposure in order to estimate the effect and extent of the manipulation of the patched astrocyte's resting $[\text{Ca}^{2+}]$ by this uncaging protocol. The average resting $[\text{Ca}^{2+}]$ was estimated by binning together 10 frames (3s on average) for each ROI. For each ROI, I extracted three average resting $[\text{Ca}^{2+}]$ time points: before/after UV exposure as well as before/after no UV exposure. Before UV exposure is the average of the 10 frames immediately preceding the closing of the shutter to the photon detector just before the UV exposure takes place. After UV exposure is the average of the 10 frames immediately after the opening of the shutter to the photon detector after the UV exposure has taken place. To estimate the variability of resting $[\text{Ca}^{2+}]$ over a similar time course without UV uncaging, the third time point was taken as the average of 10 frames before the "before UV exposure". A gap of the same time as was necessary for the closing and opening of the shutter during UV exposure, was taken into account between the before and after no UV average resting $[\text{Ca}^{2+}]$ time points (see Fig.5.3).

For each cell, the average for these three time points was taken over all ROI and shown in the figures 5.4-6. These resting $[\text{Ca}^{2+}]$ values for each cell were taken as both absolute Ca^{2+} values, ie the estimated $[\text{Ca}^{2+}]$ for each timepoint as well as relative, normalised values: ie the difference after either UV exposure or time only as a percentage of the resting $[\text{Ca}^{2+}]$ before either UV exposure or time only.

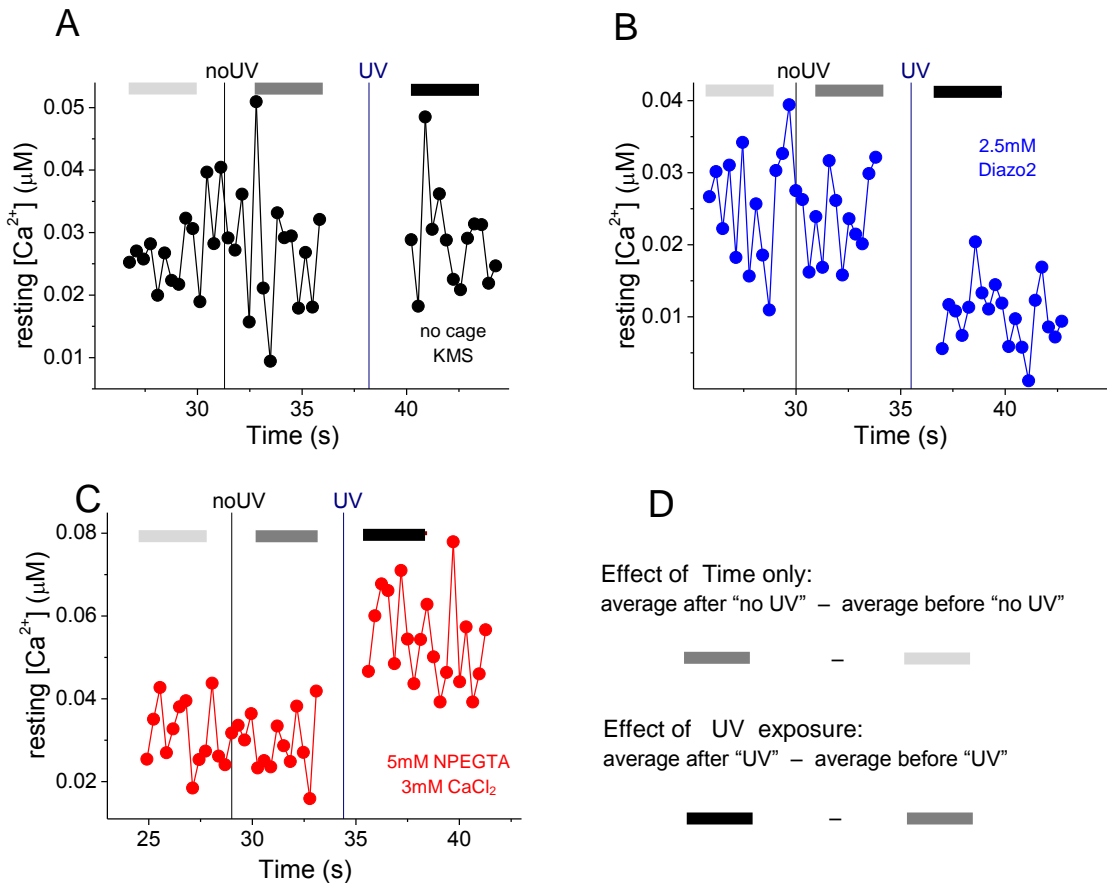


Fig. 5.3 Quantifying the effect of uncaging method

These 3 graphs illustrate the averaging process used to quantify the effect of uncaging on resting $[Ca^{2+}]$. The average effects per protocol group are presented in figures 5.4-6.

The graphs show the estimated resting $[Ca^{2+}]$ (μM) in 1 ROI from 1 cell over time (seconds) as recorded by continuous timelapse (≈ 3 frames/s) FLIM of OGB-2 in a whole-cell patched astrocyte in the CA1 stratum radiatum of an acute hippocampal P21-26 rat slice perfused with ACSF at 32-34°C. The vertical lines in all 3 graphs, represent the UV exposure in blue (UV) and a similar time period with no UV exposure in black (no UV). In all 3 graphs, the 3 horizontal lines represent the 10 $[Ca^{2+}]$ time points that were averaged to estimate resting $[Ca^{2+}]$ level before and after time only or UV exposure. For protection against detector saturation, a shutter on the PicoQuant TCSPC detector is manually closed before and opened after UV exposure (hence the lack of data points immediately surrounding UV exposure).

A: example trace, protocol and averaging in KMS-only containing astrocyte

Graph A, in black, shows the resting $[Ca^{2+}]$ for a ROI from a control cell containing no caged compounds. The averages (horizontal bars) were taken to show the effect of time and UV exposure only such as photodamage induced increases in resting $[Ca^{2+}]$. See application in figure 5.4.

B: example trace, protocol and averaging in KMS-Diazo2 containing astrocyte

Graph B, in blue, shows the resting $[Ca^{2+}]$ for a ROI from a Diazo2 containing cell. The averages (horizontal bars) were taken to show the effect of UV mediated release of Ca^{2+} buffer. See application in figure 5.5.

C: example trace, protocol and averaging in KMS-NPEGTA/ $CaCl_2$ containing astrocyte

Graph C, in red, shows the resting $[Ca^{2+}]$ for a ROI from a NPEGTA/ $CaCl_2$ containing cell. The averages (horizontal bars) were taken to show the effect of UV mediated release of Ca^{2+} . See application in figure 5.6.

D: differences in average resting $[Ca^{2+}]$ to quantify effect of time or UV exposure

The effects of time and UV exposure were measured as the difference in the average resting $[Ca^{2+}]$ before and after "no UV" or "UV" exposure respectively, as illustrated in D: In light grey, the average before no UV; in dark grey, the average before UV; in black the average after UV. See application in figures 5.4-6.

UNCAGING EFFECT ON ASTROCYTE [Ca²⁺]

To estimate the uncaging effect on astrocyte cytosolic [Ca²⁺], the resting [Ca²⁺] was quantified before and after either UV or no UV exposure as described above. Astrocyte resting [Ca²⁺] was decreased in the Diazo2 cells after UV exposure, illustrated in figure 5.5. UV exposure leads to an increase in astrocyte [Ca²⁺] in the NPEGTA cells, illustrated in figure 5.6. Finally, there was little effect of UV exposure only or time only in the control, no cage/KMS only cells, illustrated in figure 5.4.

A. KMS-only cells: quantifying UV exposure photodamage and non-uncaging related changes in astrocyte resting [Ca²⁺]

The effect of uncaging was tested in control cells containing no caged compounds in the internal solution, figure 5.4. The same protocol as for Diazo2-containing cells was applied. This enabled to test for potential side effects of these protocols such as photodamage from UV exposure or resting [Ca²⁺] modifications due to the presence of caged compounds in the internal solution in the Diazo2 and NPEGTA cells.

In the 3 cells recorded, the average resting [Ca²⁺] was 25 nM. There was an estimated average decrease in resting [Ca²⁺] of 1 nM after UV exposure. For these cells, this translates as an average 4.6% decrease in resting [Ca²⁺] after UV exposure.

Over a similar time period but without exposure to UV, the average resting [Ca²⁺] from these 3 cells increased by 0.8 nM or an average 4.2% increase in resting [Ca²⁺].

Uncaging Diazo2 or NPEGTA should therefore aim to change resting [Ca²⁺] by more than 5%.

B. Diazo2 cells: quantifying the uncaging related decrease in astrocyte resting [Ca²⁺]

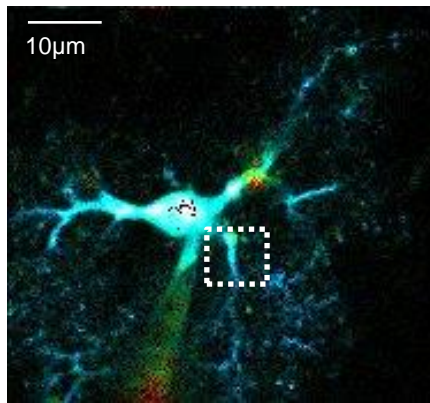
The uncaging in cells containing 2.5 mM Diazo2 in the internal solution decreased the astrocyte resting [Ca²⁺], figure 5.5. The same protocol as for KMS-only cells was applied.

In the 11 cells recorded, the overall collective average resting [Ca²⁺] was 46 nM. There was an estimated average decrease in resting [Ca²⁺] of 8nM after UV exposure. For these cells, this translates as an average 19.3% decrease in resting [Ca²⁺] after UV exposure.

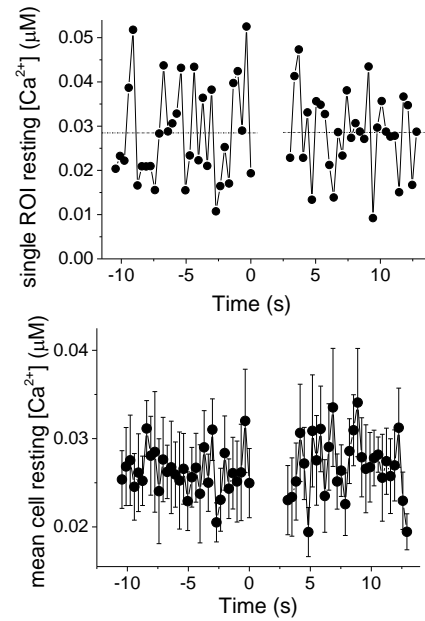
Over a similar time period but without exposure to UV, the average resting [Ca²⁺] from these 11 cells decreased by 0.6 nM or an average 1.2% increase in resting [Ca²⁺].

These results indicate that basal calcium levels in astrocytes can be reduced and that we have the dynamic range to detect basal astrocytic calcium levels.

A. Example KMS only cell



Mean $[Ca^{2+}]$ per pixel over 60s FLIM OGB2 recording. Selected ROI.



B. Average resting $[Ca^{2+}]$ across all ROI for each KMS only cell (n=3)

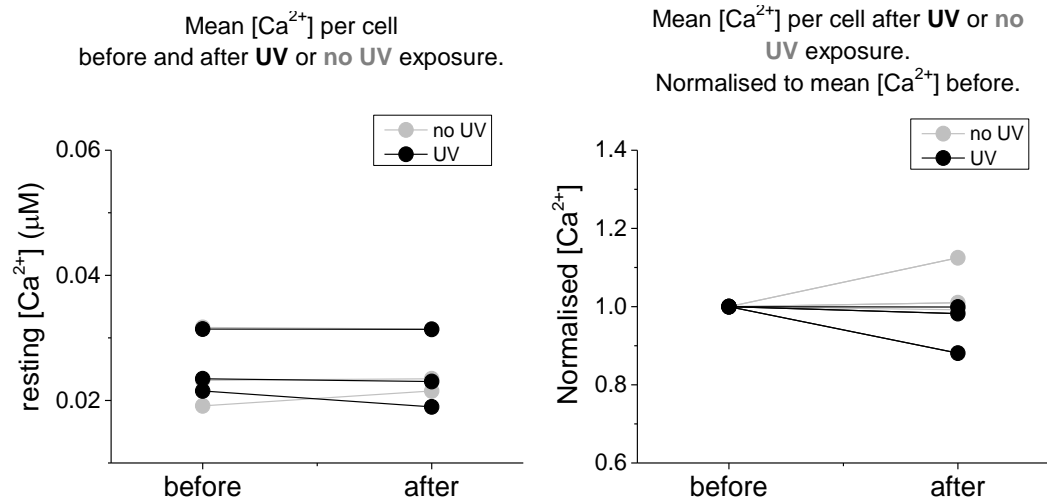


Fig. 5.4 UV LED effect on KMS-only, 'no cage' cells

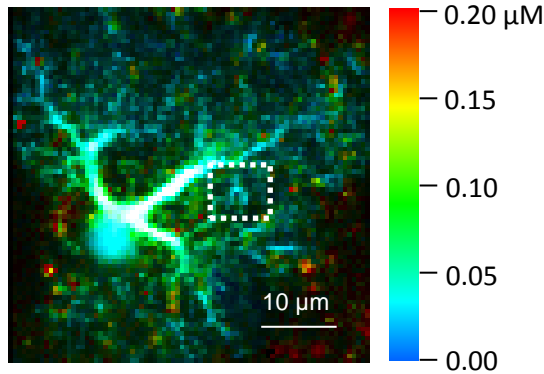
A. Example 2.5mM Diazo2 containing cell

The first illustration shows the mean $[Ca^{2+}]$ per pixel as estimated from OGB2 fluorescence lifetime 60s timelapse imaging of an example KMS-only astrocyte (scale bar 10 μ m; colour scale: 0-200nM $[Ca^{2+}]$). The change in $[Ca^{2+}]$ (μ M) over time (seconds) after uncaging at t=0s is shown for a single manually selected region of interest (white rectangle on cell map) and as the average of 10 manually selected representative ROI for that cell (mean \pm SEM, manual ROI selection as described in chapter 4).

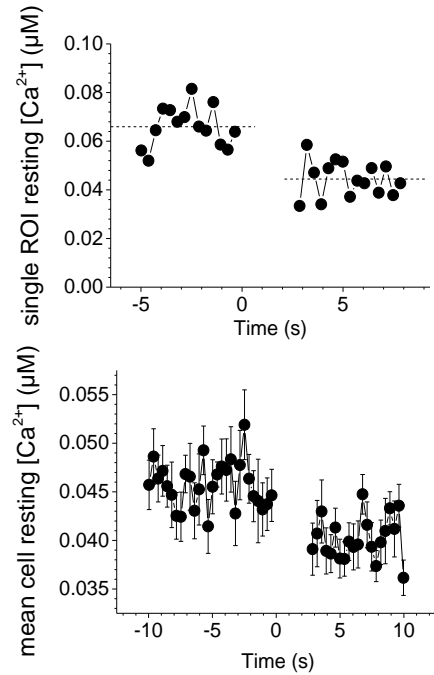
B. All 2.5mM Diazo2 containing cells

The first graph shows for each cell (n=3), the mean $[Ca^{2+}]$ (μ M) of all representative automatically selected ROI for each cell before and after UV exposure (black) or a similar time period with no UV exposure (grey). The method for determining these values is described in figure 5.3.D. The second graph shows the same changes in $[Ca^{2+}]$ but displayed as normalised values. For each cell, the mean $[Ca^{2+}]$ after either UV exposure (black) or a similar time period with no UV exposure (grey) is expressed as a percentage of the mean $[Ca^{2+}]$ before either protocol. The overall effect of UV light exposure is an overall average 4.6% decrease in baseline for these cells : 1nM $[Ca^{2+}]$ decrease. After no UV exposure, the overall average $[Ca^{2+}]$ increases by 0.8nM or 4.2% on average increase in baseline for these cells.

A. Example 2.5mM Diazo2 cell



Mean $[Ca^{2+}]$ per pixel over 300s FLIM OGB2 recording. Selected ROI.



B. Average resting $[Ca^{2+}]$ across all ROI for each KMS- 2.5mM Diazo2 cell (n=11)

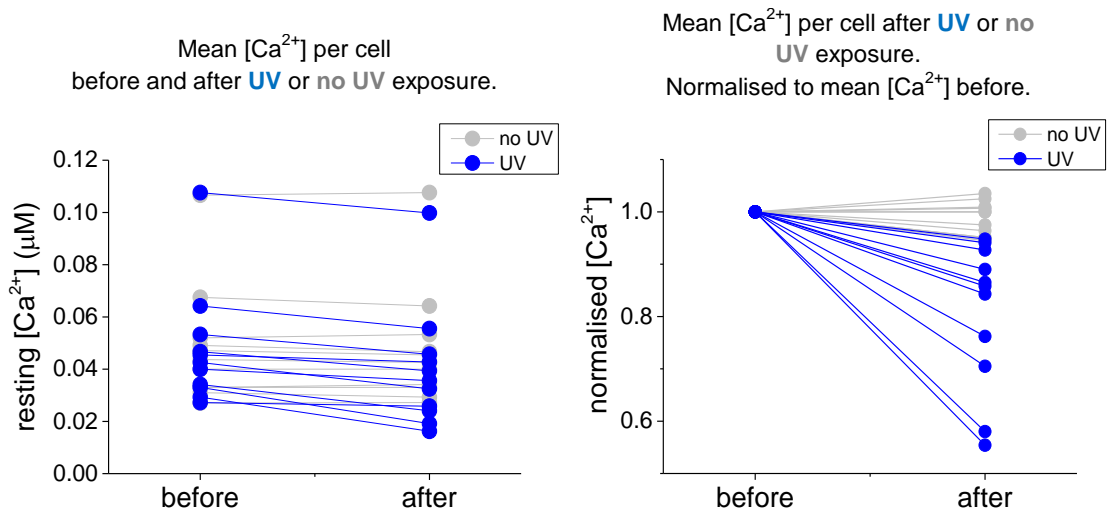


Fig. 5.5 UV LED uncaging of 2.5mM Diazo2 reduces resting $[Ca^{2+}]$ in patched astrocyte.

A. Example 2.5mM Diazo2 containing cell

The first illustration shows the mean $[Ca^{2+}]$ per pixel as estimated from OGB2 fluorescence lifetime 300s timelapse imaging of an example Diazo2-containing astrocyte (scale bar 10 μ m; colour scale: 0-200nM $[Ca^{2+}]$). The change in $[Ca^{2+}]$ (μ M) over time (seconds) after uncaging at t=0s is shown for a single manually selected region of interest (white rectangle on cell map) and as the average of all 10 manually selected representative ROI for that cell (mean \pm SEM, manual ROI selection as described in chapter 4).

B. All 2.5mM Diazo2 containing cells

The first graph shows for each cell (n=11), the mean $[Ca^{2+}]$ (μ M) of all automatically selected representative ROI for each cell before and after UV exposure (blue) or a similar time period with no UV exposure (grey). The method for determining these values is described in figure 5.3.D.

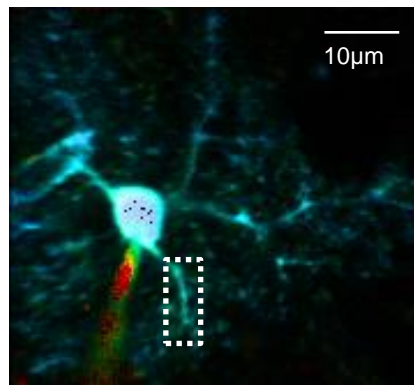
The second graph shows the same changes in $[Ca^{2+}]$ but displayed as normalised values. For each cell, the mean $[Ca^{2+}]$ after either UV exposure (blue) or a similar time period with no UV exposure (grey) is expressed as a percentage of the mean $[Ca^{2+}]$ before either protocol.

The overall effect of Diazo2 uncaging is an overall average 19.3% decrease in baseline or 8nM $[Ca^{2+}]$ decrease. After no UV exposure, the overall average $[Ca^{2+}]$ decreases by 0.6nM or a 1.2% on average decrease in baseline for these cells.

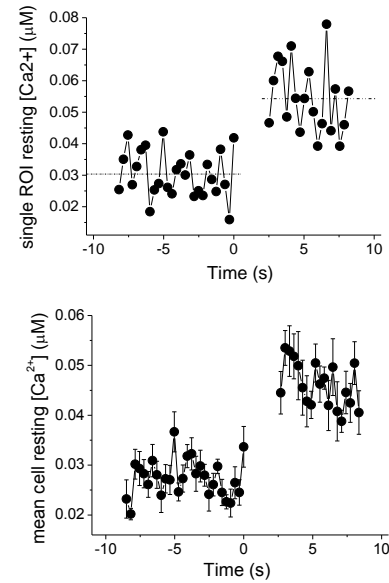
C. NPEGTA cells: quantifying the uncaging related increase in astrocyte resting $[Ca^{2+}]$

The uncaging in cells containing 5 mM NPEGTA/ 3 mM $CaCl_2$ in the internal solution increased the astrocyte resting $[Ca^{2+}]$, figure 5.6. The UV exposure protocol was slightly modified in order to increase the likelihood of increasing resting $[Ca^{2+}]$ to compensate for the possible decrease in resting $[Ca^{2+}]$ seen after UV exposure in control cells or that occurs even with time only in both Diazo2 and NPEGTA cells. Indeed a more efficient UV light conducting optical fibre was used, FT1000UMT as opposed to FT1000EMT for the other cells. The intensity of UV light was increased slightly from 600 mW in Diazo2/KMS-only cells to 690 mW for NPEGTA cells. The duration, frequency and number of light pulses were the same in all groups. In the 8 cells recorded, the average resting $[Ca^{2+}]$ was 30 nM. There was an estimated average increase in resting $[Ca^{2+}]$ of 12.7 nM after UV exposure. For these cells, this translates as an average 46% increase in resting $[Ca^{2+}]$ after UV exposure. Over a similar time period without exposure to UV, the average resting $[Ca^{2+}]$ from these 8 cells decreased by 1nM or an average 3.1% decrease in resting $[Ca^{2+}]$.

A. Example 5mM NPEGTA / 3mM CaCl₂ cell



Mean [Ca²⁺] per pixel over 90s FLIM OGB2 recording. Selected ROI.



B. Average resting [Ca²⁺] across all ROI for each 5mM NPEGTA/3mM CaCl₂ cell (n=8)

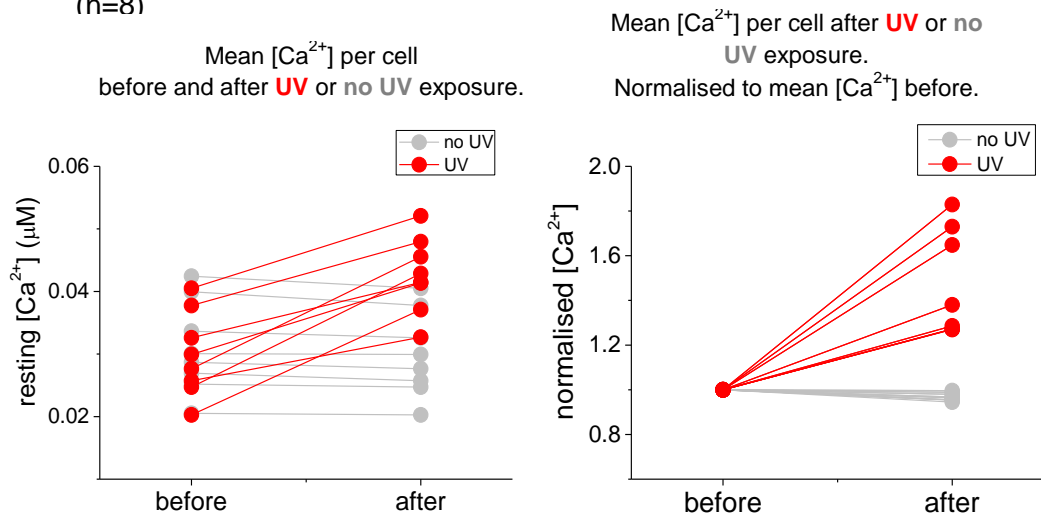


Fig. 5.6 UV LED uncaging of 5mM NP-EGTA/3mM CaCl₂ increases resting [Ca²⁺] in patched astrocyte.

A. Example 2.5mM Diazo2 containing cell

The first illustration shows the mean [Ca²⁺] per pixel as estimated from OGB2 fluorescence lifetime 90s timelapse imaging of an example NPEGTA-containing astrocyte (scale bar 10μm; colour scale: 0-200nM [Ca²⁺]). The change in [Ca²⁺] (μM) over time (seconds) after uncaging is shown for a single manually selected region of interest (white rectangle on cell map) and as the average of all manually selected representative ROI for that cell (mean ±SEM, manual ROI selection as described in chapter 4).

B. All 2.5mM Diazo2 containing cells

The first graph shows for each cell (n=8), the mean [Ca²⁺] (μM) of all representative ROI for each cell before and after UV exposure (red) or a similar time period with no UV exposure (grey). The method for determining these values is described in figure 5.3.D.

The second graph shows the same changes in [Ca²⁺] but displayed as normalised values. For each cell, the mean [Ca²⁺] after either UV exposure (red) or a similar time period with no UV exposure (grey) is expressed as a percentage of the mean [Ca²⁺] before either protocol.

The overall effect of NPEGTA/CaCl₂ uncaging is an overall average 46% increase in baseline or 12.7nM [Ca²⁺] increase. After no UV exposure, the overall average [Ca²⁺] decreases by 1nM, a 3.1% on average decrease in baseline for these cells.

DISCUSSION

A. Summary

In this chapter I illustrate how I have successfully setup a UV LED uncaging system to quantifiably manipulate astrocyte resting $[Ca^{2+}]$. Indeed, uncaging Diazo2 led to a decrease in resting $[Ca^{2+}]$ and uncaging NPEGTA/ $CaCl_2$ enabled the increase of resting $[Ca^{2+}]$. This enabled to control when and how resting $[Ca^{2+}]$ change in order to test if this has any effect on astrocyte calcium signalling as will be discussed in the next chapters.

B. UV exposure adjustments

Optimising the UV power at the actual cell for optimal uncaging effectiveness is key to the success and extent of the manipulation of the resting $[Ca^{2+}]$. We investigated some options in order to try to get the most efficient setup.

i. Improving the coupling between UV LED and optical fibre to increase the output power at slice

We first used a UVLED couple to an optical fibre custom made for us by Rapp-Opto. They seem to use the same “butt-coupling technique” as Thorlabs: creating a LED holder that would position fibre input and diode as tightly together as possible. However, the output power at the end of the custom made optical fibre they provided was maximum 2mW. Thorlabs equip their LED holder with a heat dissipating casing and use an SMA port to couple the fibre to the diode. Perhaps their LEDs are simply more powerful. Regardless, we settled for the Thorlabs setup as it provides more power at the output in our hands (up to 50mW).

The second issue was selecting the optimal optical fibre. We initially used 200 μm core fibres; by simply increasing the core diameter to 1000 μm we increased the output power by X%.

Finally, we realised later on that the OH levels in the core of the fibre affected attenuation of UV light. Switching from the FT1000EMT to the FT1000UMT fibres increased the output power by approximately 25% in our hands. As both fibres were only 1m long, despite the attenuation of UV light in the FT100EMT, we were still able to uncage Diazo2 sufficiently to decrease astrocyte resting $[Ca^{2+}]$. Using the extra 25% power gained from the more UV suitable FT1000UMT fibre, we were able to compensate for the time related decrease in resting $[Ca^{2+}]$ and uncage NPEGTA/ $CaCl_2$ sufficiently to see an increase in astrocyte resting $[Ca^{2+}]$.

ii. UV exposure optimisation

Because of UV light scattering, it is difficult to estimate how efficient the uncaging will be in the patched astrocyte in an acute hippocampal slice. We tried different UV exposure protocols to optimise the uncaging efficiency in situ without increasing the UV exposure induced photodamage. For example, in the case of Diazo2, cells were exposed to 50ms instead of 10ms pulses which seemed to increase the decrease in resting $[Ca^{2+}]$ by $\approx 10\%$.

C. Caged compound concentrations

We aimed to increase the likelihood of changing resting $[Ca^{2+}]$ by UV uncaging whilst limiting the effect of the caged compound pre-UV exposure on resting $[Ca^{2+}]$. Additionally to optimising the UV photolysis, we explored different caged compound concentrations. Diazo2 has not been commonly used in astrocytes before. In Perea & Araque 2007, they used 5 mM NPEGTA without previously loading Ca^{2+} . Therefore we started using 5 mM concentrations for both caged compounds. As we still saw an effect with 2.5 mM Diazo2 we stuck with this concentration. For NPEGTA, we tested 300 μ M concentration which showed no increase in $[Ca^{2+}]$ after photolysis. The combination of 5 mM NPEGTA and 3 mM $CaCl_2$ did show an increase in $[Ca^{2+}]$ after UV exposure. We tried other combinations in order to maximise this increase in $[Ca^{2+}]$ but they did not show any advantages. Increasing the preloading of NPEGTA with $CaCl_2$ from 3 to 4.5 mM not only did not show an increase the effect of photolysis in the few cells tested but also made it harder to patch astrocytes.

The potential adverse effect of using these Ca^{2+} buffers on resting $[Ca^{2+}]$ as well as their impact on Ca^{2+} signalling in astrocytes is discussed in chapter 7.

D. Conclusion

In this chapter 5, I present the method UV photolysis of Diazo2 or NP-EGTA/ $CaCl_2$ which I successfully set up and used to respectively decrease or increase the resting $[Ca^{2+}]$ (and simultaneously the Ca^{2+} buffering capacity) across individual whole-cell patched clamped astrocytes in situ.

I optimised both the UV photolysis (in terms of setup, intensity and pulse protocol) and the concentration of caged compound. The final protocols used were established in order to reach a compromise between effectively modifying the resting $[Ca^{2+}]$ whilst recording the astrocyte Ca^{2+} signalling using 2-photon excitation FLIM and attempting to minimise the potential disruption of Ca^{2+} signalling by the addition of exogenous Ca^{2+} buffers.

Chapter 6: ASTROCYTE CALCIUM EVENTS EVOKED BY ACTIVATION OF METABOTROPIC GLUTAMATE RECEPTORS

INTRODUCTION

A. Objective

The aim was to quantify Ca^{2+} responses in whole-cell patch clamped astrocytes to the pressure application of a group I metabotropic glutamate receptor (mGluR) agonist. I tested the relationship of this response to the astrocyte average resting $[\text{Ca}^{2+}]$ immediately prior to this pressure application and ensuing astrocyte Ca^{2+} response (Ca^{2+} response within 1s of agonist application, see methods below). I first quantified the resting $[\text{Ca}^{2+}]$ and response $[\text{Ca}^{2+}]$ using the photon count ratio method of FLIM for OGB-2 as described in chapter 3. I then used the UV uncaging of NPEGTA/ Ca^{2+} or Diazo2 to respectively increase or decrease the resting $[\text{Ca}^{2+}]$ (as described in chapter 5) and quantify the resulting change in the response to the pressure application of the mGluR agonist.

B. DHPG activation of group I mGluRs in astrocytes

Metabotropic glutamate receptors are coupled to G-proteins. When the ligand, which endogenously is the excitatory neurotransmitter glutamate, binds to the receptor orthosteric ligand binding domain, it induces a conformational change which ultimately triggers the activation of these g-proteins (Kunishima et al. 2000). There are at least eight mGluR subtypes which are classified into three different groups based on many characteristics such as sequence homology or the mechanisms underlying the transduction of their signal (reviewed in Nakanishi 1992). Indeed, group I mGluRs are associated with phospholipase C through their coupling to G-proteins subtype q/11. Their activation thus triggers a signaling cascade that leads to an increase in intracellular IP_3 and diacylglycerol. This increase in IP_3 activates receptors on the endoplasmic reticulum to trigger a cytosolic Ca^{2+} increase via Ca^{2+} release by the internal stores.

Astrocytes express mGluRs and specifically group I mGluR5 (Schools & Kimelberg 1999). However, recent studies have suggested that the expression of mGluR5 is developmentally regulated in astrocytes: mGluR5 expression may be reduced in astrocytes from adult animals (> 3 weeks old; Sun et al. 2013). This suggests that the age of the preparation could be an important consideration when studying astrocytic Ca^{2+} signals relying on group I mGluR activation.

Exogenous glutamate application was found to evoke Ca^{2+} events in cultured in adult astrocyte (Cornell-Bell et al. 1990a; Charles et al. 1991). Astrocyte Ca^{2+} events can also be triggered in acute slice preparations of the hippocampus for example, where stimulation of CA3 Schaffer collaterals to trigger endogenous pathways also leads to astrocyte cytosolic Ca^{2+} increases (Porter & Mccarthy 1996; Henneberger et al. 2010).

Porter & Mccarthy 1996 suggested that these evoked astrocyte Ca^{2+} events in situ could be generated in response to glutamate released by the stimulation of CA3 pyramidal neuron Schaffer collaterals. Indeed they suggested that these evoked astrocyte Ca^{2+} events in young rat hippocampal slices (10-13 days postnatal) were reduced after exposure to a general group I/II mGluR antagonist. More recently, Tang et al. 2015 suggest that group I mGluR agonist application, such as DHPG, mimics Schaffer collateral stimulation evoked Ca^{2+} events astrocyte processes from the stratum radiatum of acute hippocampal slices (2-3 month old mice). Although other pathways are also likely to be involved (such as ATP through P2 purinergic receptors for example; Tang et al. 2015), glutamate activation of group I mGluRs could be an endogenous mechanism to evoke Ca^{2+} events in astrocytes in situ in both young and adult rats (though mGluR5 and mGluR1 respectively; Porter & Mccarthy 1996; Sun et al. 2013; Tang et al. 2015). Therefore, despite differences in the pattern of expression of the subtypes of group I mGluRs, group I mGluR activation overall is an endogenous mechanism by which stratum radiatum astrocytes sense synaptic activity in situ, at the CA3 to CA1 synapse in the hippocampus.

(s)-3,5-dihydroxyphenylglycine (DHPG) is a selective agonist of group I mGluR (mGluR1 and mGluR5; Schoepp et al. 1994). It has been commonly used to trigger Ca^{2+} release in astrocytes (Parri & Crunelli 2003; Wu et al. 2014; Tang et al. 2015). I used a pressure application of DHPG to trigger Ca^{2+} release from internal stores through selective activation of group1 mGluRs at a given timepoint and in the vicinity of an individual whole-cell patch clamped astrocyte in the stratum radiatum area of young adult (21-25 postnatal days old rats) hippocampal acute slices. This method should evoke astrocyte Ca^{2+} events through a similar mechanism by which these cells could sense synaptic activity in situ as described above. The main focus of this thesis was to investigate the role of resting $[\text{Ca}^{2+}]$ in astrocyte signaling. To that effect, we found a positive correlation between the resting $[\text{Ca}^{2+}]$ and spontaneous Ca^{2+} event peak $[\text{Ca}^{2+}]$ and amplitude in individual ROIs taken from astrocytes in situ in chapter 4. In order to test the causality of this relationship, we aimed to quantify the changes in astrocyte Ca^{2+} event amplitude following changes in astrocyte resting $[\text{Ca}^{2+}]$ as mediated by UV photolysis of caged Ca^{2+} or Ca^{2+} buffers (chapter 5). However in order to test this, we would require at least one Ca^{2+} event both before and after changing the resting $[\text{Ca}^{2+}]$. This would be unlikely if we did these experiments with spontaneous astrocyte Ca^{2+} events due to their frequency as discussed in chapter 4. This can be circumvented by evoking astrocyte Ca^{2+} events, as described in this chapter, where we can trigger a Ca^{2+} event both before and after changing the astrocyte resting $[\text{Ca}^{2+}]$. Furthermore, DHPG activation of group I mGluRs is linked to IP_3R mediated Ca^{2+} release as described above.

IP₃Rs are thought to play a role in the mechanisms that can generate spontaneous (Di Castro et al. 2011; Kanemaru et al. 2014) and evoked (Tang et al. 2015) astrocyte Ca²⁺ signaling.

As suggested in chapters 1 and 4, IP₃R2 sensitivity to resting [Ca²⁺] could be a mechanism by which astrocyte resting [Ca²⁺] could modulate astrocyte Ca²⁺ events at the resting [Ca²⁺] recorded in our hands in chapter 4.

In this chapter, we therefore aim to establish the relationship between astrocyte resting [Ca²⁺] and DHPG-pressure application evoked Ca²⁺ events.

METHODS

This section describes the acquisition and analysis of OGB-2 fluorescence lifetime in whole cell patched astrocytes (as described in chapters 2-3) during pressure application of DHPG (described below). In some cases this was done before and after UV uncaging of Ca²⁺ or Ca²⁺ buffer to change resting [Ca²⁺] as described in chapter 5.

A. Acquisition

i. Recording protocol

For each of the cells described in this chapter, I applied two pressure applications of DHPG whilst recording OGB-2 fluorescence lifetime timelapse images of whole-cell patched astrocytes in the CA1 area stratum radiatum of acute hippocampal slices from male P21-26 rats.

300 frame timelapse images (\approx 90 s) were recorded at near physiological temperatures (32-34°C), 20-30 minutes after whole cell configuration of the patched astrocyte (as described in chapter 2). For each cell, a first recording was made at this time with a single pressure application of DHPG at frame 150 (DHPG-p1), after 45 seconds resting recording. A second identical recording with a second pressure application of DHPG (DHPG-p2) was done 90 s after the end of the first recording.

In NPEGTA or Diazo2 containing astrocytes (but not in KMS-only astrocytes), UV uncaging of Ca²⁺ or Ca²⁺-buffer respectively, was achieved through a UV pulse (as described in chapter 4) at the 100th frame (prior to the pressure application of DHPG) of this second recording. Therefore the characteristics of DHPG-p1 will be referred to as 'before', i.e. prior to UV-mediated (NPEGTA or Diazo2 cells) or time (KMS-only) change of resting [Ca²⁺] whereas the characteristics of DHPG-p2 will be referred to as 'after' this change in resting [Ca²⁺].

ii. Pressure application

DHPG (Tocris, 0805) was dissolved in dH₂O at a stock concentration of 30 mM. This stock was stored in a freezer for up to 6 months at -20°C in airtight 20 µL aliquots.

A freshly thawed aliquot was used for each experimental day to make up the solution that would be pressure-applied onto the cells (puff solution). This puff solution contained 300 µM DHPG and 3 µM Alexa Fluor 647. The stock solutions were dissolved to these final concentrations in freshly made and oxygenated ACSF on each experimental day.

I applied the puff solution onto the patched astrocyte through a borosilicate glass pipette (puff pipette) similar to the pipette used for whole cell patch clamp (patch pipette, described in chapter 2). However, I modified the pipette tip opening to a slightly larger diameter than that used for patching as this enabled a more diffuse spread of the puff solution for a given pressure and reduced risk of blockage (final puff pipette resistance ≈1 MΩ). I also increased the tapering of the puff pipette to minimise disruption whilst positioning the puff pipette through the tissue as I could not apply positive pressure during this process.

The puff pipette was filled with ≈12 µL of puff solution and mounted into a ISO-S-1.5g (G23 Instruments) pipette holder connected to the PV830 pneumatic picopump (World Precision Instruments; see figure 5.1 for recording configuration illustration).

The pneumatic picopump was set to manual trigger mode meaning that the solution in the pipette is kept on hold until activation of the trigger. The 'hold' configuration enables not expose the tissue to DHPG and prevent ACSF from entering the puff pipette so as not to dilute the puff solution.

The position of the puff pipette was controlled by a PatchStar Scientifica micromanipulator.

Once I had selected the astrocyte that I would aim to record from, I lowered the puff pipette to rest approximately 50µm above the slice and positioned it far enough from the cell so as not to obstruct the path of the patch pipette.

2-3 minutes after achieving whole cell patch clamp of the given astrocyte, I proceeded to position the puff pipette close to the patched astrocyte. I first applied a 200 ms pressure application above the tissue and away from the slice to remove any obstruction that may have accumulated in the tip of the puff pipette. I then moved the puff pipette through the tissue at an angle in order not to cause too much tissue damage or movement. I monitored the position of both patch and puff pipettes with the transmitted light in order to adjust for any movements. Whilst placing the puff pipette tip approximately 20 µm from the patched astrocyte soma, I monitored the quality of the patch by checking for any changes in access resistance or resting membrane potential displayed by the seal test in the voltage clamp mode of Clampex software. Final position adjustments were made if necessary immediately prior to recording but both pipettes were not moved once acquisition started. During the pressure application, I could monitor the success of the release of puff solution from the puff pipette by visualising a concomitant brief cloud of Alexa 647 fluorescence (lasting < 1 s before being washed away by the perfusion) using the Olympus PMT with appropriate filters for Alexa 647 fluorescence.

B. ROI selection

I used an automated method to generate ROIs and then selected ROIs that matched the location of the patched astrocyte. This process is described in chapter 5, specifically figure 5.2. Briefly, rectangular ROIs were automatically created by bins of 16x16 pixels ($25 \mu\text{m}^2$). Each ROI had to have at least 1500 photons to ensure equivalent variability in $[\text{Ca}^{2+}]$ estimation across ROIs. If there were too few photons (for example when recording from cells deeper in the tissue), 2 consecutive frames were binned together (1 point per 600ms instead of 300ms).

ROIs were discarded if they did not appear to contain only photons from the patched cell (figure 5.2). ROIs were also removed from analysis if their photon count was less than 1500 photons (photon cut-off point); typically in ROIs outside of the astrocyte territory (these ROIs had fewer photons than cell containing ROIs).

A further manual ROI selection step enabled the removal of ROIs containing photons from pipettes or from other cells. This was done by visually comparing the ROI location with both transmitted light and Alexa 594 fluorescence images to identify the relative positions of pipettes and other cells for example.

C. DHPG mediated Ca^{2+} response and resting $[\text{Ca}^{2+}]$ analysis

i. Quantifying DHPG-puff Ca^{2+} response and resting $[\text{Ca}^{2+}]$

The time of occurrence and success of the pressure application was visually confirmed by the presence of a cloud of Alexa Fluor 647 fluorescence intensity (figure 6.1.A). I started measuring the DHPG-pressure application (DHPG-p) astrocyte Ca^{2+} response from 3 frames after the pressure application frame.

The Ca^{2+} response to a single DHPG-pressure application was quantified by two parameters in this chapter: response peak $[\text{Ca}^{2+}]$ and amplitude (figure 5.1.B). For each OGB-2 fluorescence lifetime recording, I calculated the photon count ratio and estimated the equivalent $[\text{Ca}^{2+}]$ (principles are described in chapter 3) using Matlab scripts provided by Dr C. Henneberger.

In this chapter I considered the initial portion of the Ca^{2+} response to DHPG-pressure application: I estimated the $[\text{Ca}^{2+}]$ over the average of the first 10 frames (2.7 - 3 seconds) of the DHPG-pressure application Ca^{2+} response for each astrocyte.

The peak $[\text{Ca}^{2+}]$ was taken as the absolute $[\text{Ca}^{2+}]$ estimated over the average of these first 10 frames of DHPG-p response. The response amplitude was taken as this estimated peak $[\text{Ca}^{2+}]$ subtracted by the average estimated resting $[\text{Ca}^{2+}]$ prior to the pressure application (pre-event resting $[\text{Ca}^{2+}]$).

The pre-event resting $[\text{Ca}^{2+}]$ was estimated from the average of 10 frames immediately preceding the pressure application frame.

Pre-event resting $[\text{Ca}^{2+}]$, response peak $[\text{Ca}^{2+}]$ and amplitude were quantified for both the 1st and 2nd pressure applications, for each ROI in each cell.

ii. DHPG pressure applications 1 and 2: before and after changing the resting $[Ca^{2+}]$

Each ROI in each cell was exposed to two single DHPG-pressure applications: one applied before and one after manipulating the astrocyte resting $[Ca^{2+}]$.

Therefore the change in pre-event $[Ca^{2+}]$ was calculated as the absolute difference in $[Ca^{2+}]$ between the pre-event resting $[Ca^{2+}]$ before the 2nd and 1st pressure application of DHPG ('after - before'). Similarly, the change in response peak $[Ca^{2+}]$ or amplitude were calculated as the absolute difference in $[Ca^{2+}]$ between the peak $[Ca^{2+}]$ or amplitude of the response to the 2nd and 1st pressure application of DHPG ('after - before').

These changes were measured in all ROIs in the three cell groups based on internal solution composition (KMS-only, KMS-Diazo2 and KMS-NPEGTA/ $CaCl_2$). These groups were expected to show the following changes in pre-event resting $[Ca^{2+}]$: no change, decrease and increase respectively (see chapter 5). All ROIs for each cell in a given internal solution composition group did not necessarily show a similar change in pre-event resting $[Ca^{2+}]$. I used arbitrarily defined criteria to qualify the change in resting $[Ca^{2+}]$ for each ROI according to the absolute difference in pre-event resting $[Ca^{2+}]$ between the 2nd and 1st DHPG pressure application. An increase in resting $[Ca^{2+}]$ was described for absolute $[Ca^{2+}]$ changes larger than + 6 nM. A decrease in resting $[Ca^{2+}]$ was described for absolute $[Ca^{2+}]$ decreases of more than -6 nM. Finally, no change in resting $[Ca^{2+}]$ was described if the absolute difference in $[Ca^{2+}]$ was within ± 6 nM.

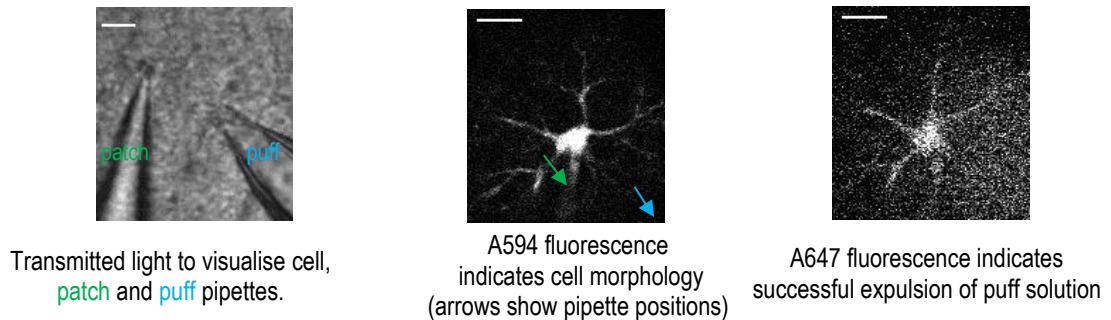
iii. Statistical analysis

Correlation analysis was used to determine if the pre-event resting $[Ca^{2+}]$ was associated with the DHPG-pressure application mediated Ca^{2+} response (as described by response peak $[Ca^{2+}]$ and amplitude). The peak $[Ca^{2+}]$ or the amplitude of the response to DHPG-pressure application was plotted against the pre-event resting $[Ca^{2+}]$ for each ROI in a given cell for a given single DHPG-pressure application. The correlation coefficient was calculated using Origin Pro.9 software and the correlation coefficient (Spearman rho and Kendall tau) as well as its significance (the p value for 95% confidence interval) is given for each plot.

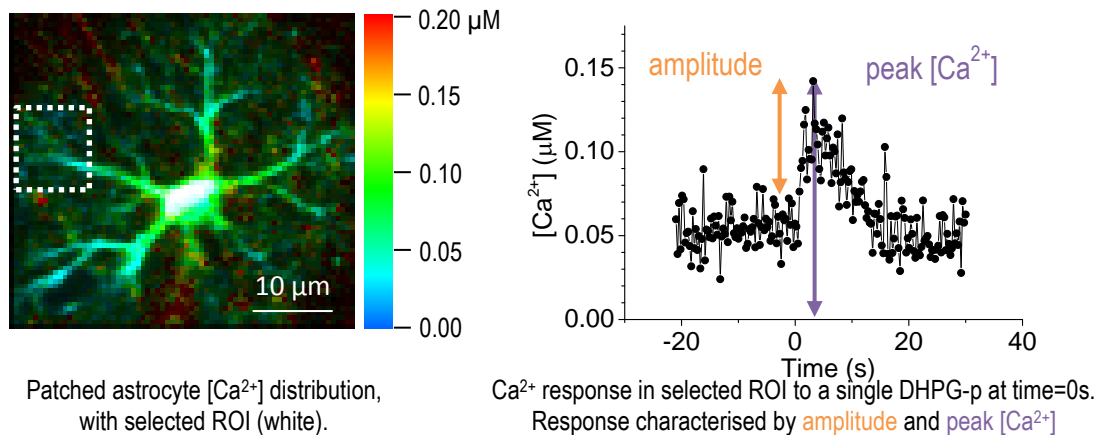
A paired t-test was used to compare the mean absolute values of the characteristics of the Ca^{2+} response to DHPG-pressure applications before and after changing the resting $[Ca^{2+}]$. The p values indicate how significantly the reported change in the Ca^{2+} response mean values was different from 0 (i.e. Ca^{2+} responses to 1st and 2nd DHPG pressure application are equal). When comparing the relative change for these characteristics ('after' normalized to 'before'), a single population t-test was used. The p values indicate how significantly the reported mean relative change in Ca^{2+} response was different from 1 (i.e. Ca^{2+} responses are equal').

One-way ANOVA was performed in Origin Pro9 software to analyse the difference in mean peak $[Ca^{2+}]$ or amplitude changes between groups of ROIs qualitatively defined by their change in resting $[Ca^{2+}]$ between the two DHPG applications ('same', 'increase', 'decrease'; figures 6.12-14). If the ANOVA was significant, a Tukey post-hoc test was carried out to identify which groups contributed to this difference in group means. Mean values were described as mean \pm standard error (SEM; figure 6.2) or mean \pm standard deviation (SD; figures 6.5-6).

A. 300 μ M DHPG-pressure application method illustration



B. Example Ca^{2+} response to single DHPG-pressure application



C. Example further characterisation of DHPG-pressure application response

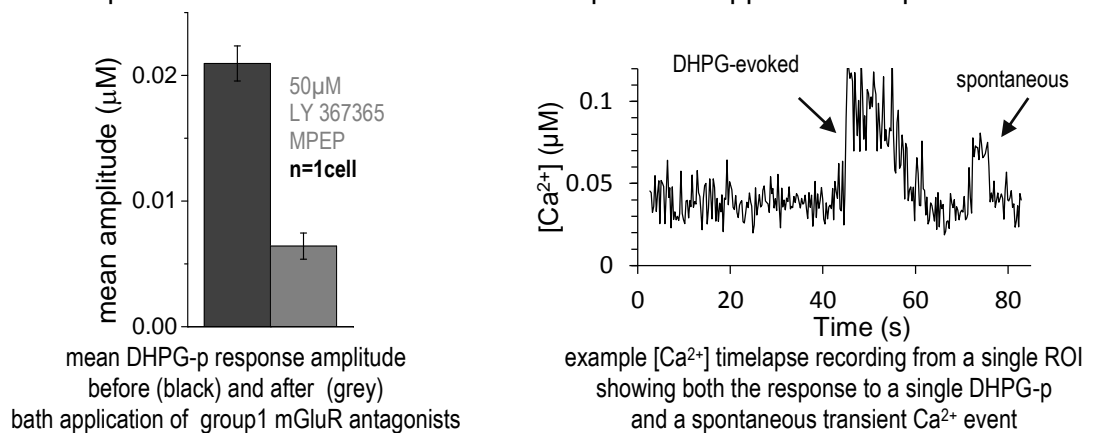


Figure 6.1 DHPG-pressure application (DHPG-p) evoked Ca^{2+} response in patched astrocyte method illustration.

A. Example Ca^{2+} response to a DHPG-p

After achieving whole cell patch clamp configuration, the puff pipette (blue) was positioned near the patched astrocyte (A_1). A594 fluorescence was used to indicate both morphology of the patched cell as well as any change in focal plane during recording (A_2). A647 fluorescence was used to monitor the success of expulsion of puff solution when triggering a pressure application (A_3). Scale bars 10 μm .

B. Example Ca^{2+} response to a single DHPG-p

This example trace (B_2) shows the Ca^{2+} response from a single ROI (B_1) to a single DHPG-p. The parameters used to characterise this response in this chapter are the peak $[\text{Ca}^{2+}]$ (purple) and the amplitude (orange) of the response.

C. Example further characterisation of DHPG-p response

The bar graph shows a 73% reduction in the average Ca^{2+} response amplitude (average \pm SEM across all ROI in one cell) after 50 μM application of group I mGluR antagonists (grey). This is an illustration only as was **only done in one cell**.

In a few occasions (2-3 ROI in 4 out of 17 cells analysed), a spontaneous transient increase would occur either before or after the DHPG-p. In these cases, the amplitude of these events was smaller than the DHPG-evoked response (illustrated in C_2).

RESULTS

A. DHPG-evoked Ca^{2+} response and resting $[\text{Ca}^{2+}]$

For each cell, the average \pm SEM pre-event resting $[\text{Ca}^{2+}]$, peak $[\text{Ca}^{2+}]$ and amplitude of the DHPG-p response was measured across all recorded ROI. These average response characteristics were plotted against the average pre-event resting $[\text{Ca}^{2+}]$ for each cell in figure 6.2.

i. Correlations tested across all ROIs

Overall the cells measured, the response peak $[\text{Ca}^{2+}]$ was positively correlated to the resting $[\text{Ca}^{2+}]$ measured across the cells as displayed by a significant positive correlation coefficient (figure 6.2.A; Spearman 0.8, $p < 0.001$).

The average DHPG-puff response amplitude did not follow a linear relationship with the average resting $[\text{Ca}^{2+}]$ measured across the cells (figure 6.2.C). Indeed, although these displayed a weak positive correlation trend, this was not significant (Spearman 0.21, $p = 0.31$). When considering spontaneous Ca^{2+} events in chapter 4, we considered only active ROIs: displaying at least 1 spontaneous Ca^{2+} event. In this chapter, when considering all ROIs, we do not distinguish between ROIs that did actually show a response to the DHPG pressure application and ROIs that did not. This could explain why we do not see a correlation between resting $[\text{Ca}^{2+}]$ and DHPG-evoked Ca^{2+} event amplitude in figure 6.2.C.

ii. Exclusion of non-responsive ROIs

However, we then considered the mean characteristics across only DHPG-responsive ROI for each cell (figure 6.2.B, D). Indeed, non-responsive ROI could bias the correlations as they may not be able to generate a response to a DHPG-p irrespective of their resting $[\text{Ca}^{2+}]$. These non-responsive ROI could perhaps not have the necessary constituents such as lack of mGluR or IP_3R in order to respond to this DHPG-p (see review in Rusakov et al. 2014). These ROIs could alternatively simply not be exposed to the DHPG in this given pressure application (illustration in figure 6.1.A3) although this seems unlikely due to the concentration of DHPG and proximity of the application to the astrocyte under investigation. In this chapter, we therefore excluded ROIs that could possibly be non-responsive to the DHPG-pressure application by using an arbitrarily defined minimum Ca^{2+} response amplitude of +6 nM to the DHPG-pressure application. Therefore, all references to DHPG-responsive ROIs represent only ROIs where the DHPG-evoked Ca^{2+} event amplitude was larger than +6 nM; references to all ROIs represent all ROIs irrespective of their response or lack of response to DHPG-pressure application.

iii. Correlations tested across DHPG-responsive ROIs

When considering the mean peak $[\text{Ca}^{2+}]$ and amplitude of the Ca^{2+} response to DHPG-pressure application across all these DHPG-responsive ROIs (see above) for each astrocyte, we found a significant positive correlation of both these parameters with the pre-event mean resting $[\text{Ca}^{2+}]$ (figure 6.2.B,D).

The positive correlation was slightly stronger between the mean peak $[Ca^{2+}]$ and mean resting $[Ca^{2+}]$ (Spearman 0.86, $p < 0.001$) than when considering all ROIs (including non-responsive ROIs; figure 6.2.B vs 6.2.A). In the case of the mean amplitude, considering only DHPG-responsive ROIs revealed a significant positive correlation (Spearman 0.41, $p < 0.05$) which was not present when considering all ROIs. In the case of these average parameters when considering only DHPG-responsive ROIs across all cells, these positive correlations with the mean pre-event resting $[Ca^{2+}]$ are similar to what was found in the case of spontaneously occurring Ca^{2+} events in chapter 4 (figure 4.5.A-B). It could be possible that ROIs with higher resting $[Ca^{2+}]$ would have enhanced IP_3R_2 opening (reviewed in Foskett 2007) that would therefore allow more IP_3R -mediated Ca^{2+} release from the endoplasmic reticulum for a given DHPG stimulation thus generating larger evoked Ca^{2+} events compared to Ca^{2+} events evoked at lower resting $[Ca^{2+}]$ (see chapter 4, 6 and 7 for further discussion).

iv. DHPG-response across individual ROI

As stated above, it is possible that each individual ROI may have distinctive receptor expression, different proportions of internal stores relative to cytosol or different exposure to DHPG. Therefore we also considered whether or not the significant positive correlation between DHPG-pressure application Ca^{2+} response characteristics and pre-event resting $[Ca^{2+}]$ could be due to averaging over all ROIs per cell. We tested these correlations by plotting all the individual ROIs irrespectively of their cell of origin (figure 6.3). Once again, we first looked at all the ROIs from all cells in figure 6.3.A,C. We found a significant positive correlation (Spearman 0.66, $p < 0.001$) between the peak $[Ca^{2+}]$ of the response to a given single DHPG-pressure application and the pre-event resting $[Ca^{2+}]$ in individual ROI across all ROIs from all cells (figure 6.3.A). The amplitude of this Ca^{2+} response however showed no correlation with the pre-event resting $[Ca^{2+}]$ (Spearman -0.02, $p = 0.30$; figure 6.3.C).

However, when looking at all the DHPG-responsive ROIs across all cells (figure 6.3.B, D), both the peak $[Ca^{2+}]$ and amplitude of the response to a single DHPG-p show a significant positive correlation with the pre-event resting $[Ca^{2+}]$ (respectively: Spearman 0.71, $p < 0.001$; Spearman 0.09, $p < 0.01$). The positive correlation with pre-event resting $[Ca^{2+}]$ was much weaker for the amplitude than for the peak $[Ca^{2+}]$ of the response to DHPG-pressure application. This is similar to what was found for spontaneous Ca^{2+} events in chapter 4.

Using all information from all cells regardless of experimental protocol group enables to increase the range of resting $[Ca^{2+}]$ recorded which in turns helps determine correlations with this resting $[Ca^{2+}]$ parameter. However, these positive correlations were comparable to those found for spontaneous Ca^{2+} events even when considering only DHPG-responsive ROIs from KMS-only cells. Indeed these cells contain no additional Ca^{2+} or Ca^{2+} buffer other than OGB-2 which could impact these correlations when considering all 3 groups together(see discussion). In these KMS-only cells (361 DHPG-responsive ROIs from 7 cells), the positive correlation was observed between peak $[Ca^{2+}]$ and pre-event resting $[Ca^{2+}]$ (Spearman 0.81, $p < 0.001$) as well as between amplitude and pre-event resting $[Ca^{2+}]$ (Spearman 0.30, $p < 0.001$).

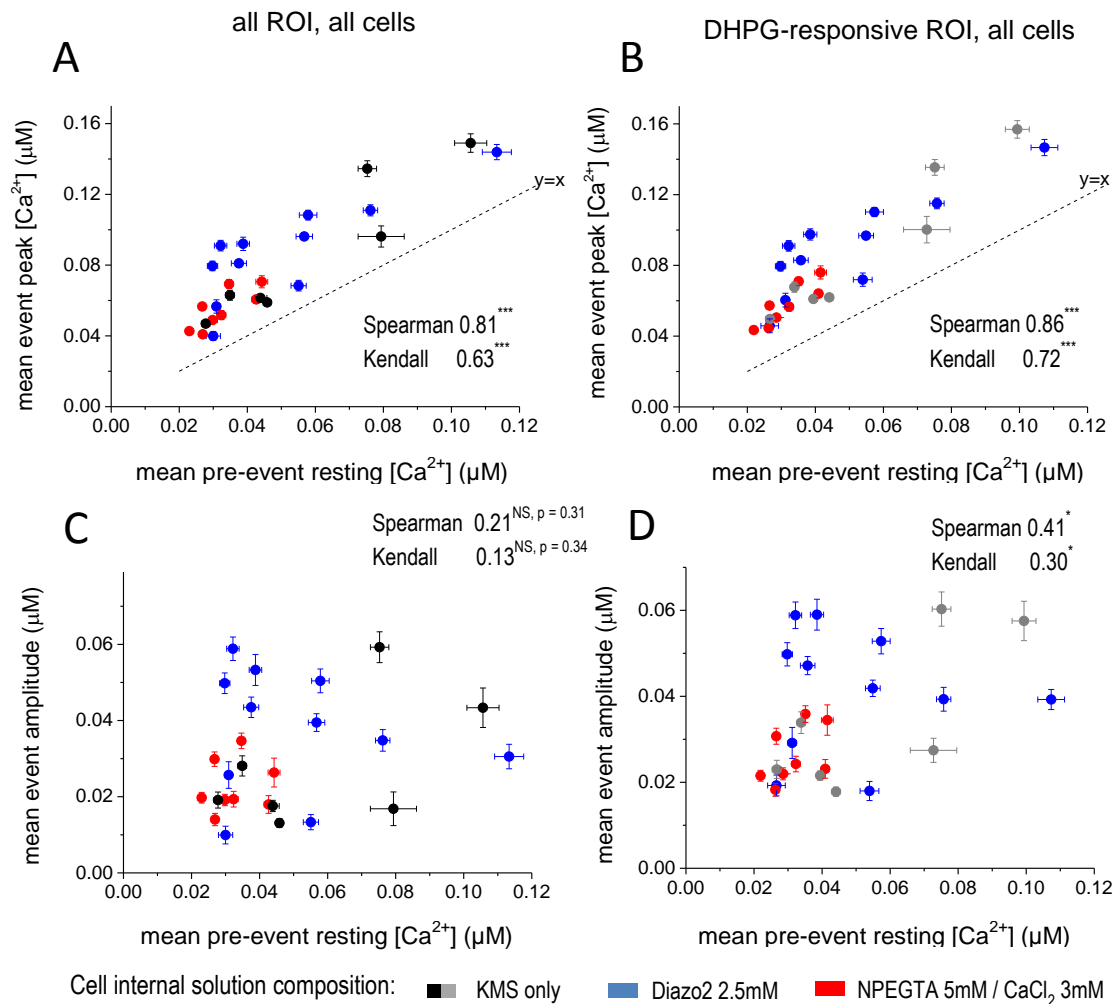


Figure 6.2 mean response to a single DHPG-p vs pre-event resting [Ca²⁺] in each cell

Each cell is represented by a single point (average [Ca²⁺] in µM ±SEM error bars). The colour represents the internal solution composition of the patched astrocyte considered: KMS-only (grey; 7cells), KMS+2.5mM Diazo2 (blue; 11 cells), KMS+ 5mM NPEGTA/3mM CaCl₂ (red; 8 cells). The values were taken for a single DHPG puff, none of the cells were exposed to UV (none of the caged compounds were yet uncaged in the cells represented here). The significance of the correlation indicated by Spearman and Kendall values is: NS p > 0.05, * p < 0.05, *** p < 0.001.

A: mean event peak [Ca²⁺] is positively correlated with the mean resting [Ca²⁺], averages across all ROI For all recorded astrocytes, the peak [Ca²⁺] (see 6.1.A and 4.2.A) of the response to a single DHPG-puff was averaged across all the automatically created ROI (see 5.2) recorded for each cell. This was plotted against the similarly averaged resting [Ca²⁺] for each cell.

B: mean event peak [Ca²⁺] is positively correlated with the mean resting [Ca²⁺], averages across all DHPG-responsive ROI For all recorded astrocytes, the peak [Ca²⁺] of the response to a single DHPG-puff was averaged across all the arbitrarily defined DHPG-responsive ROI (if amplitude > 6nM) automatically created ROI recorded for each cell. This was plotted against the similarly averaged resting [Ca²⁺] for each cell.

A significant positive correlation was seen between the mean peak [Ca²⁺] and mean resting [Ca²⁺] of each cell when considering all recorded cells. This correlation was stronger when considering only the responsive ROI (B). The black dotted line represents y=x to indicate how far the mean peak [Ca²⁺] is from the mean baseline [Ca²⁺] (ie: if y=x, there was no response to DHPG-puff).

C: mean event amplitude is not correlated with the mean resting [Ca²⁺], averages across all ROI For all recorded astrocytes, the amplitude of the response to a single DHPG-puff was averaged across all ROI for each cell. This was plotted against the similarly averaged resting [Ca²⁺] for each cell.

D: mean event amplitude is positively correlated with the mean resting [Ca²⁺], averages across all DHPG-responsive ROI For all recorded astrocytes, the amplitude of the response to a single DHPG-puff was averaged across all DHPG-responsive ROI (if amplitude > 6nM) for each cell. This was plotted against the similarly averaged resting [Ca²⁺] for each cell.

A non-significant positive trend was seen between amplitude and baseline [Ca²⁺] across the cells recorded (C). However, a weak positive correlation was found when considering the mean amplitude and baseline [Ca²⁺] in DHPG-responsive ROI only (D).

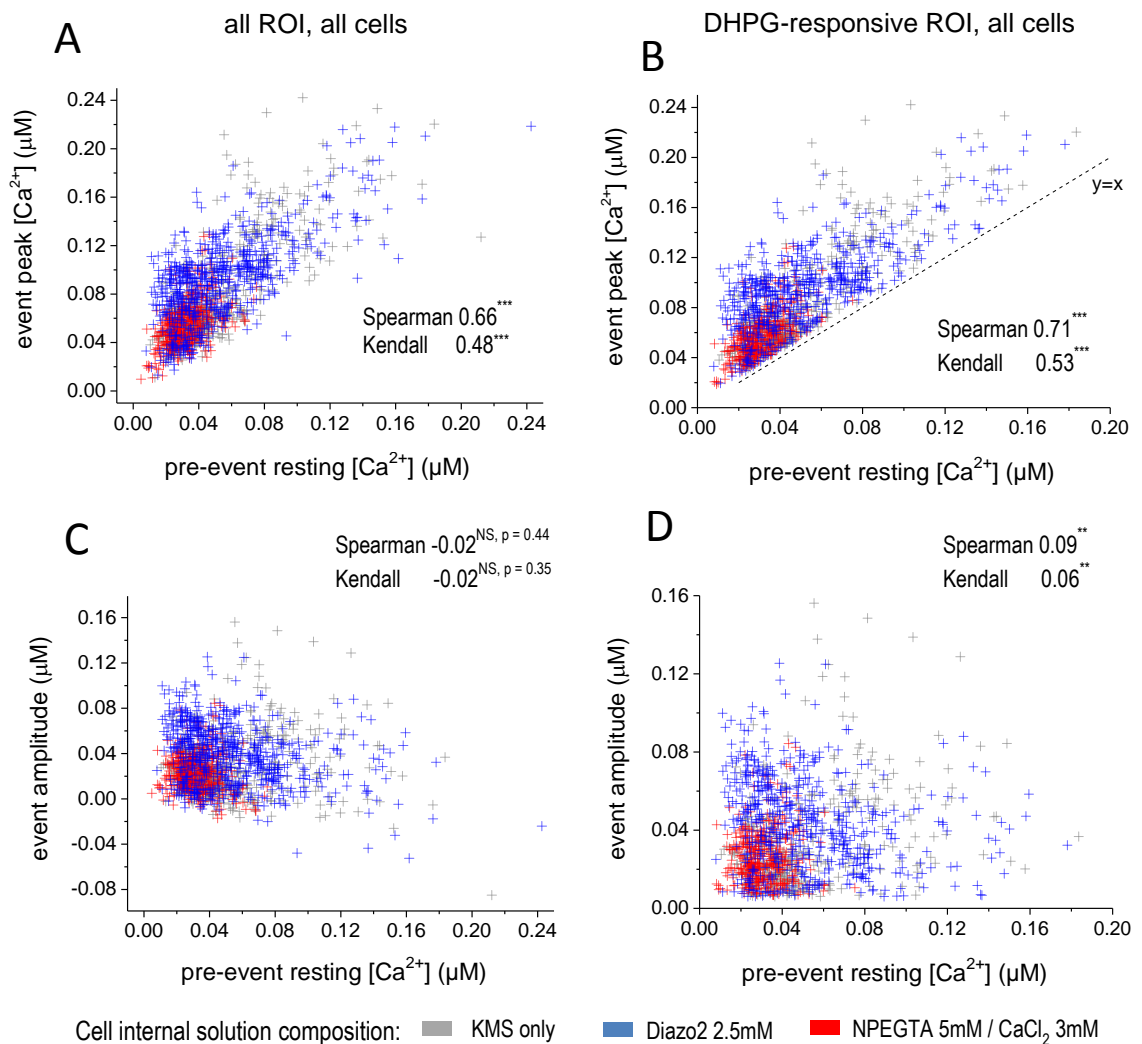


Figure 6.3 Response to a single DHPG-p vs pre-event resting $[Ca^{2+}]$ in each ROI

For all graphs: each ROI from all cells is represented by a single point. The colour represents the internal solution composition of the patched astrocyte considered: KMS-only (grey; 7 cells), KMS+2.5mM Diazo2 (blue; 11 cells), KMS+ 5mM NPEGTA/3mM $CaCl_2$ (red; 8 cells). The values were taken for a single DHPG-p, none of the cells were exposed to UV (none of the caged compounds were yet uncaged in the cells represented here). Spearman and Kendall correlation values are given for all ROI irrespective of the cell of origin. Star indicates significance of the correlation: NS $p > 0.05$, ** $p < 0.01$, *** $p < 0.001$.

A: event peak $[Ca^{2+}]$ is positively correlated with pre-event resting $[Ca^{2+}]$, considering all ROI from all cells The peak $[Ca^{2+}]$ of the response to a single DHPG-p is represented as a function of the pre-event resting $[Ca^{2+}]$ for each ROI, from all cells.

B: event peak $[Ca^{2+}]$ is positively correlated with pre-event resting $[Ca^{2+}]$, considering all DHPG-responsive ROI from all cells The peak $[Ca^{2+}]$ of the response to a single DHPG-p is represented as a function of the pre-event resting $[Ca^{2+}]$ for each DHPG-responsive ROI (amplitude $> 6nM$), from all cells.

In both graph A and B, the peak $[Ca^{2+}]$ is significantly correlated to the pre-event resting $[Ca^{2+}]$. The correlation is stronger when considering only DHPG-responsive ROI (graph B). In graph B, the black dotted line represents $y=x$ to indicate how far the peak $[Ca^{2+}]$ is from the pre-event resting $[Ca^{2+}]$ (ie: if $y=x$, there was no response to DHPG-p).

C: event amplitude is not correlated with pre-event resting $[Ca^{2+}]$, considering all ROI from all cells The amplitude of the response to a single DHPG-p is plotted as a function of the pre-event resting $[Ca^{2+}]$ for each ROI, from all cells.

D: event amplitude is positively correlated with pre-event resting $[Ca^{2+}]$, considering all DHPG-responsive ROI from all cells The amplitude of the response to a single DHPG-p is plotted as a function of the pre-event resting $[Ca^{2+}]$ for each DHPG-responsive ROI (amplitude $> 6nM$), from all cells.

The DHPG-p response amplitude shows a non-significant negative correlation with the pre-event resting $[Ca^{2+}]$ when considering all ROI (graph C) but there is a significant mild positive correlation when considering only DHPG-responsive ROI (graph D).

B. Mean cell DHPG-evoked Ca^{2+} response after changing the resting $[\text{Ca}^{2+}]$

i. Aim

The peak $[\text{Ca}^{2+}]$ and amplitude of the response to a given DHPG-pressure application show a positive correlation with the pre-event resting $[\text{Ca}^{2+}]$ similar to that seen in the case of spontaneous Ca^{2+} events (chapter 4). However, because we can control the time of occurrence in the case of DHPG-pressure application evoked Ca^{2+} events, we were able to manipulate the pre-event resting $[\text{Ca}^{2+}]$ (as described in chapter 5) to test its effect on DHPG-evoked Ca^{2+} event peak $[\text{Ca}^{2+}]$ and amplitude.

In the next figures, we will consider three groups of recordings determined by the internal solution composition of the cells recorded. I first recorded any changes in the characteristics of the Ca^{2+} response to a 1st and 2nd DHPG-pressure application (no UV exposure) in KMS-only cells (grey, $n = 7$; figures 6.4, 6.7, 6.12) to control for the stability of the astrocyte Ca^{2+} response to DHPG. Next, we aimed to test the effect of respectively increasing or decreasing the pre-event resting $[\text{Ca}^{2+}]$ on astrocyte Ca^{2+} response to DHPG-pressure application. I recorded the changes to these DHPG-evoked Ca^{2+} events before and after UV exposure in NPEGTA/ CaCl_2 containing cells (red, $n = 8$; figures 6.5, 6.8, 6.13) and in Diazo2 containing cells (blue, $n = 11$; figures 6.6, 6.9, 6.14). Only DHPG-responsive ROIs (arbitrarily defined as ROIs where the Ca^{2+} response amplitude to the first DHPG-pressure application was larger than + 6 nM) were considered in figures 6.4, 6.5 and 6.6.

ii. Stability of Ca^{2+} response to repeated DHPG pressure applications (KMS-only cells)

In these astrocytes, we quantified the changes in the response to a 1st and 2nd single DHPG-pressure application. These cells contained no caged compound and were not exposed to UV photolysis. However, the pre-event resting $[\text{Ca}^{2+}]$ did significantly drop by 7.7nM on average overall the 7 cells recorded, between the 1st and 2nd (≈ 3 minutes after the 1st DHPG-pressure application) exposure to a DHPG-pressure application (paired t-test: $t = -3.0$, $p < 0.05$, 7 cells; figure 6.4.A). This could be due to further equilibration over time of the cytosol with the internal patch solution containing OGB-2, as it could act as Ca^{2+} buffer (see discussion, chapters 4,6,7). The peak $[\text{Ca}^{2+}]$ also significantly decreased by 9.8 nM on average overall the 7 cells recorded (paired t-test: $t = -2.7$, $p < 0.05$, 7 cells; figure 6.4.B).

The amplitude however, decreased by only 2 nM on average which was not significant in these cells (paired t-test: $t = -1.2$, $p > 0.05$, 7 cells; figure 6.4.C).

We then considered the mean relative values for these characteristics expressed as a factor of the mean values for the first DHPG-p ('after/before'; figure 6.4.D). The overall significance of the mean relative decrease for each parameter was similar although stronger (t-test: hypothesis that the mean= 1).

KMS-only, n=7 cells

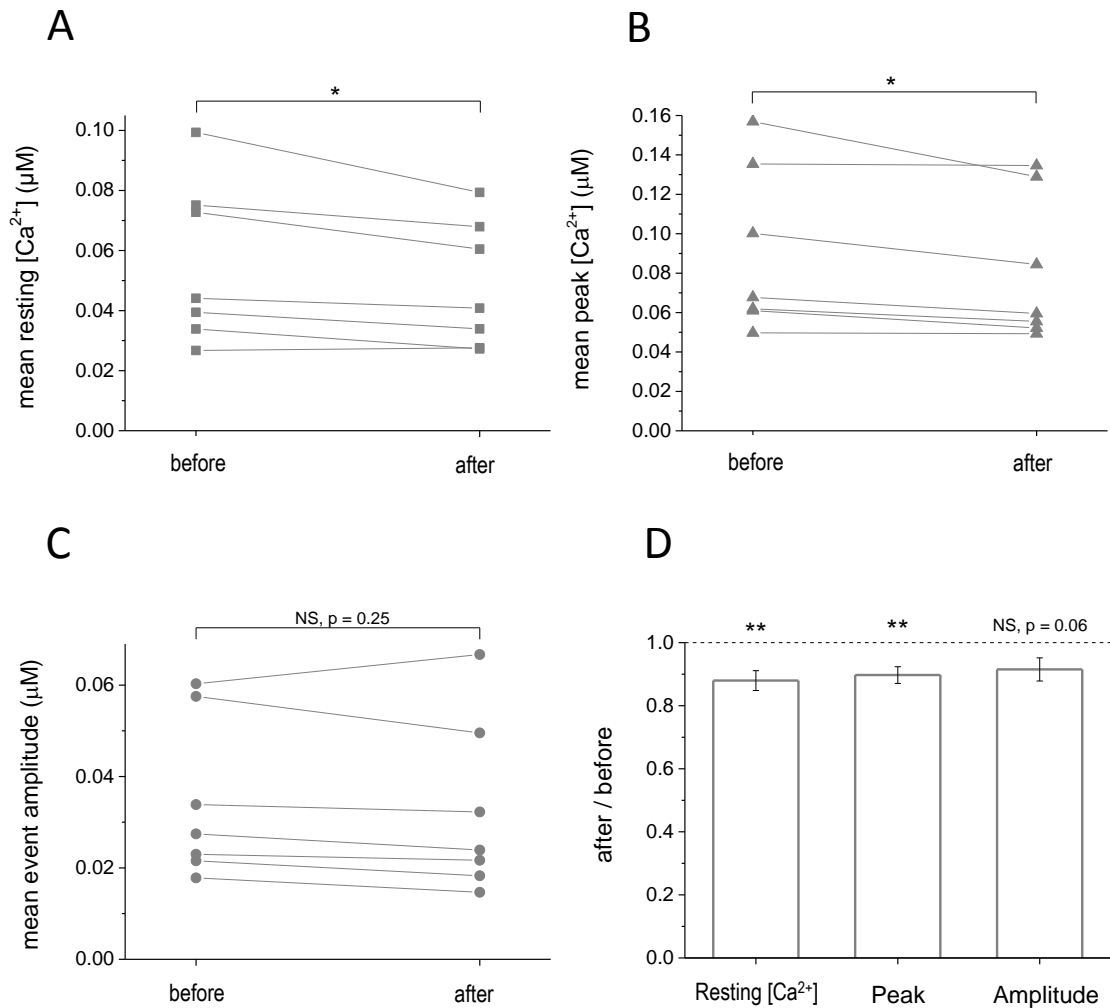


Figure 6.4 mean response to DHPG-p before and after time in KMS-only cells

We first tested the stability of the astrocyte Ca^{2+} response to a given DHPG pressure application within individual astrocytes. A 1st DHPG pressure application ('before') was applied between 17 and 22 minutes after achieving whole-cell patch clamp of the given astrocyte. A 2nd DHPG pressure application ('after') was applied approximately 3 minutes after the first DHPG application in all cells. The values indicate the mean $[\text{Ca}^{2+}]$ across all DHPG-responsive ROIs for each cell containing KMS-only internal solution (n=7 cells, no UV exposure; graphs A, B and C). For graphs A, B and C, significance is indicated as a result of a paired t-test (hypothesis: characteristic after – characteristic before = 0): NS $p > 0.05$; * $p < 0.05$.

A: Absolute changes in resting $[\text{Ca}^{2+}]$

After ≈ 3 minutes and no UV exposure, the mean absolute resting $[\text{Ca}^{2+}]$ significantly decreases ($p < 0.05$) as recorded immediately prior to the 1st and 2nd DHPG-pressure applications.

B: Absolute changes in DHPG-evoked Ca^{2+} response peak $[\text{Ca}^{2+}]$

The mean absolute peak $[\text{Ca}^{2+}]$ of the Ca^{2+} response to a single DHPG pressure application significantly decrease ($p < 0.05$) between the 1st and 2nd DHPG pressure applications.

C: Absolute changes in DHPG-evoked Ca^{2+} response amplitude

The mean absolute DHPG pressure application evoked Ca^{2+} response amplitude does not significantly decrease ($p=0.25$) between the 1st and 2nd DHPG pressure applications.

D: relative changes in the Ca^{2+} response to DHPG pressure application

The values in graph D represent the characteristics of the Ca^{2+} response to the 2nd DHPG-application relative to the characteristics for the first DHPG-application ('after/ before'). For each characteristic, the average relative value \pm SEM across all cells is plotted in bar graph D. The significance of the average relative characteristic across all KMS-only cells (n=7) is quantified by a single population t-test (Hypothesis: mean relative characteristic in all cells = 1), NS $p > 0.05$, ** $p < 0.01$.

iii. Effect of Ca^{2+} uncaging: NPEGTA/ CaCl_2 cells

In these cells, we quantified the changes in the response to a single DHPG-pressure application before and after UV photolysis of 5 mM NPEGTA and 3 mM CaCl_2 containing astrocytes. As described in chapter 5, this method leads to a significant increase in resting $[\text{Ca}^{2+}]$. Indeed the pre-event resting $[\text{Ca}^{2+}]$ significantly increased by 6.9 nM on average overall the 8 cells recorded, between the 1st and 2nd exposure to a DHPG-pressure application, after Ca^{2+} uncaging (paired t-test: $t = 7.3$, $p < 0.001$, 8 cells; figure 6.5.A). This method of increasing $[\text{Ca}^{2+}]$ involves use of millimolar concentration of NPEGTA which may in itself change the Ca^{2+} response to DHPG-pressure application through change in Ca^{2+} buffering capacity of the cell (see discussion, chapters 4,6,7).

The peak $[\text{Ca}^{2+}]$ was not significantly altered after Ca^{2+} uncaging and increased by only 0.6 nM on average overall the 8 cells recorded (paired t-test: $t = 0.5$, $p > 0.05$, 8 cells; figure 6.5.B).

The amplitude however, significantly decreased by 6.3 nM on average after Ca^{2+} uncaging in these cells (paired t-test: $t = -4$, $p < 0.01$, 8 cells; figure 6.5.C).

We then considered the mean relative values for these characteristics expressed as a factor of the mean values for the first DHPG-pressure application, before uncaging Ca^{2+} ('after/before'; figure 6.5.D). The overall significance of the mean relative change for each parameter was similar although stronger (single population t-tests).

iv. Effect of Ca^{2+} buffer uncaging: Diazo2 cells

In these cells, we quantified the changes in the response to a single DHPG-pressure application before and after UV photolysis of 2.5 mM Diazo2 containing astrocytes. As described in chapter 5, this method leads to a significant decrease in resting $[\text{Ca}^{2+}]$. Indeed the pre-event resting $[\text{Ca}^{2+}]$ significantly decreased by 8.9 nM on average overall the 11 cells recorded, between the 1st and 2nd exposure to a DHPG-pressure application, after Ca^{2+} buffer uncaging (paired t-test: $t = -3.8$, $p < 0.01$, 11 cells; figure 6.6.A). This method of decreasing $[\text{Ca}^{2+}]$ involves use of millimolar concentrations of Diazo2 which may in itself change the Ca^{2+} response to the DHPG-pressure application through increase in Ca^{2+} buffering capacity of the cell upon photolysis (see discussion, chapters 4,6,7).

The peak $[\text{Ca}^{2+}]$ significantly decreased after Ca^{2+} buffer uncaging, with a 22.6 nM decrease on average overall the 11 cells recorded (paired t-test: $t = -5.2$, $p < 0.001$, 11 cells; figure 6.6.B).

The amplitude also significantly decreased by 13.6 nM on average after Ca^{2+} buffer uncaging in these cells (paired t-test: $t = -4.5$, $p < 0.01$, 11 cells; figure 6.6.C).

We then considered the mean relative values for these characteristics expressed as a factor of the mean values for the first DHPG-p ('after/before'; figure 6.6.D). The overall significance of the mean relative decrease for each parameter was similar to the paired-testes described above (t-test: hypothesis that the mean = 1, response characteristic after decrease in resting $[\text{Ca}^{2+}]$ = characteristic before).

KMS-NPEGTA/CaCl₂, n=8 cells

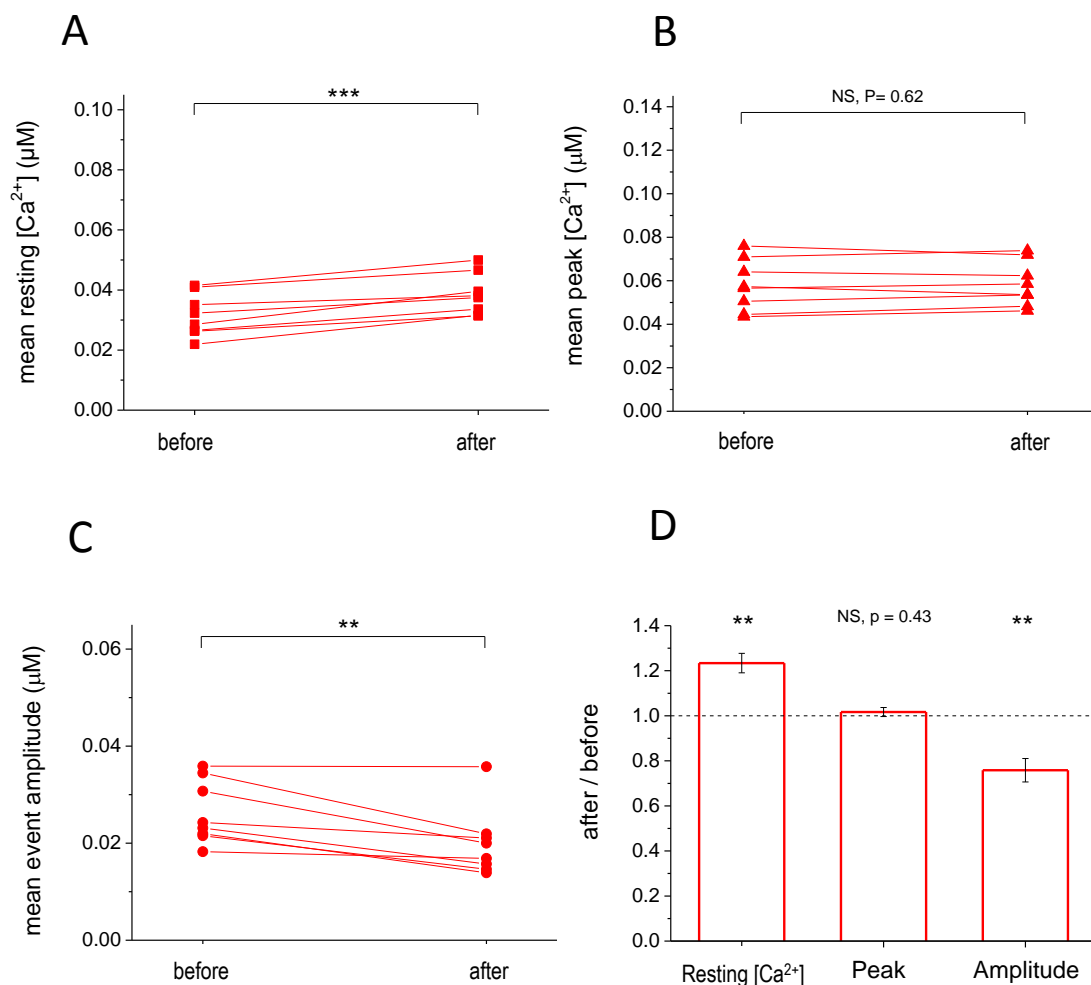


Figure 6.5 mean response to DHPG-p before and after Ca²⁺ uncaging in NPEGTA cells

In these cells we tested the effect of changing resting [Ca²⁺] through Ca²⁺ uncaging on the astrocyte Ca²⁺ response to a DHPG pressure application. Each astrocyte was exposed to UV uncaging of Ca²⁺ (NPEGTA/CaCl₂) between a 1st and 2nd DHPG pressure application. The values indicate the mean [Ca²⁺] across all DHPG-responsive ROIs for each cell containing KMS-NPEGTA/CaCl₂ internal solution (n=8 cells; graphs A, B and C). In graphs A, B and C, statistical significance is indicated as a result of a paired t-test (hypothesis: characteristic after –characteristic before = 0): NS p > 0.05, * p < 0.05, ** p < 0.01, *** p < 0.001.

A: Absolute changes in resting [Ca²⁺] before and after Ca²⁺ uncaging

The mean absolute resting [Ca²⁺] recorded prior to DHPG pressure application significantly increased after Ca²⁺ uncaging (p < 0.001).

B: Absolute changes in response peak [Ca²⁺] before and after Ca²⁺ uncaging

The mean absolute peak [Ca²⁺] of the response to DHPG pressure applications is not significantly (p=0.62) altered after Ca²⁺ uncaging.

C: Absolute changes in response amplitude before and after Ca²⁺ uncaging

The mean absolute amplitude of the Ca²⁺ response to DHPG pressure applications is significantly decreased (p < 0.01) after Ca²⁺ uncaging.

D: Relative changes in [Ca²⁺] between the 1st and 2nd DHPG applications

The values in graph D represent the characteristics for the second DHPG-p relative to the characteristics for the first DHPG-p (after Ca²⁺ uncaging (after) relative to before uncaging (before)). For each characteristic, the average relative value ±SEM across all cells is plotted in bar graph D. The significance of the average relative characteristic across all KMS-Diazo2 cells (n=11) is quantified by a single population t-test (Hypothesis: mean characteristic in all cells = 1), NS p > 0.05, ** p < 0.01.

KMS-Diazo2, n=11 cells

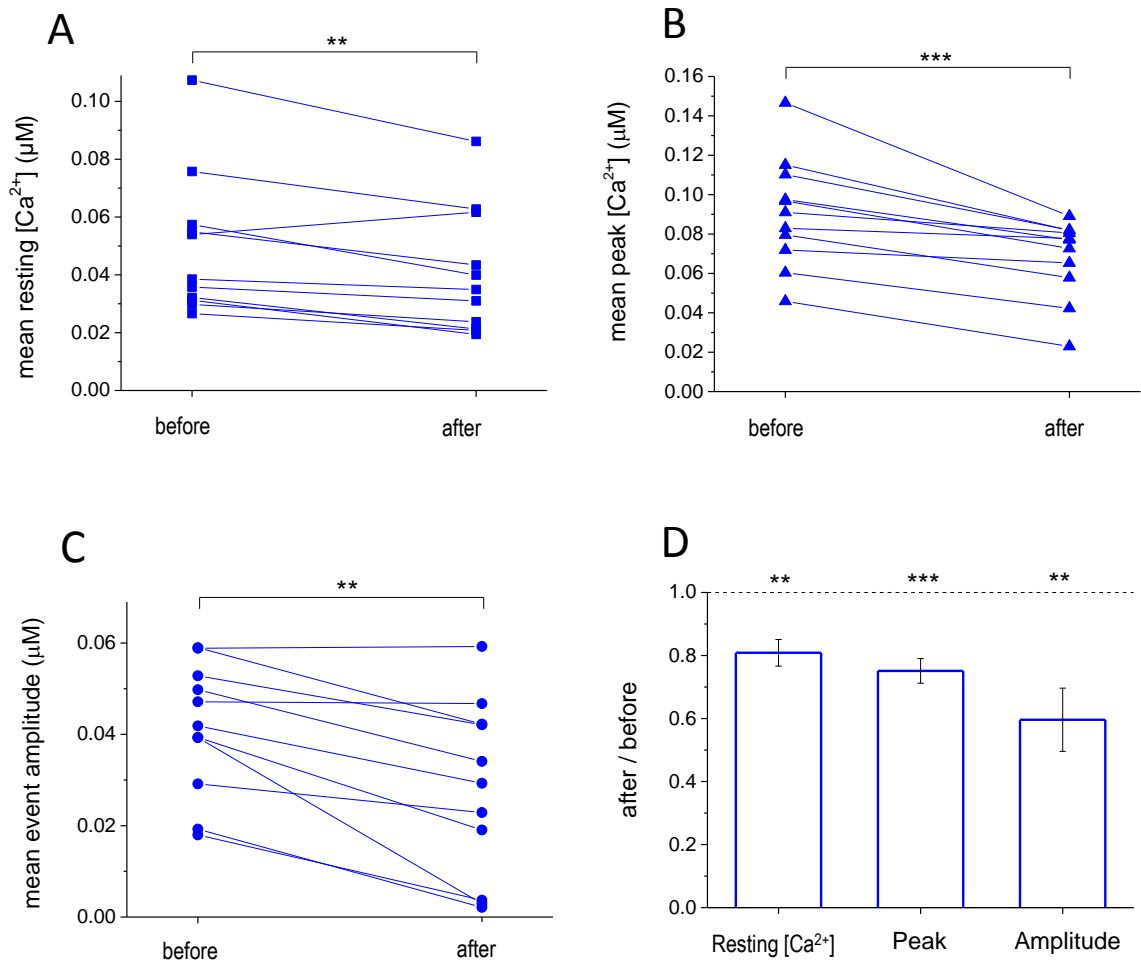


Figure 6.6 mean response to DHPG-p before and after Ca^{2+} buffer uncaging in Diazo2 cells.

In these astrocytes, we recorded the changes in the response to a given DHPG pressure application after UV uncaging of a Ca^{2+} buffer (to decrease resting $[\text{Ca}^{2+}]$). Each cell was exposed to UV uncaging of a Ca^{2+} buffer (Diazo2) between the 1st and 2nd DHPG pressure applications. The values indicate the mean $[\text{Ca}^{2+}]$ across all DHPG-responsive ROI for each cell containing KMS-Diazo2 internal solution (n=11 cells; graphs A, B and C). In graphs A, B and C, statistical significance is indicated as a result of a paired t-test (hypothesis: characteristic in puff 2 –characteristic in puff 1 = 0): NS $p > 0.05$, * $p < 0.05$, ** $p < 0.01$, *** $p < 0.001$.

A: Absolute changes in resting $[\text{Ca}^{2+}]$ after Ca^{2+} buffer uncaging

The mean absolute resting $[\text{Ca}^{2+}]$ recorded prior to a given DHPG pressure application was significantly ($p < 0.01$) decreased after Ca^{2+} buffer uncaging.

B: Absolute changes in response peak $[\text{Ca}^{2+}]$ after Ca^{2+} buffer uncaging

The mean absolute peak $[\text{Ca}^{2+}]$ of the Ca^{2+} response to a given DHPG pressure application was significantly ($p < 0.001$) decreased after Ca^{2+} buffer uncaging.

C: Absolute changes in response amplitude after Ca^{2+} buffer uncaging

The mean absolute amplitude of the response to a given DHPG pressure application was significantly decreased ($p < 0.01$) after Ca^{2+} buffer uncaging.

D: Relative changes in Ca^{2+} response to DHPG after Ca^{2+} buffer uncaging

The values in graph D represent the characteristics for the second DHPG-p relative to the characteristics for the first DHPG-p (after Ca^{2+} buffer uncaging (after) relative to before uncaging (before)). For each characteristic, the average relative value \pm SEM across all cells is plotted in bar graph D. The significance of the average relative characteristic across all KMS-Diazo2 cells (n=11) is quantified by a single population t-test (Hypothesis: mean characteristic in all cells = 1), ** $p < 0.01$, *** $p < 0.001$.

C. DHPG-evoked Ca^{2+} response after changing the resting $[\text{Ca}^{2+}]$: individual ROIs

i. Aim

As stated at the beginning of this chapter all ROIs within an individual astrocyte may not respond similarly to a given DHPG-pressure application. Additionally, individual ROIs within a given astrocyte may not all respond to manipulating the pre-event resting $[\text{Ca}^{2+}]$ (differences in diffusion of the caged compound or amount of UV exposure within a given astrocyte for example). This could mean that averaging the response across all ROIs for each cell (as done above, figures 6.4-6) may obscure or alter the effects of changing the resting $[\text{Ca}^{2+}]$ on astrocyte response to DHPG-pressure application. We therefore considered any changes in the characteristics of the Ca^{2+} response to DHPG-pressure application within individual ROIs across all cells for each group (figures 6.7 to 6.14).

In the following section, figures 6.7-10, we therefore tested for correlations between the change in pre-event resting $[\text{Ca}^{2+}]$ and the change in DHPG-evoked Ca^{2+} response peak $[\text{Ca}^{2+}]$ or amplitude within each individual ROI. As previously described, we also made the distinction between considering all ROIs from all cells or only DHPG-responsive ROIs from all cells.

ii. DHPG response peak $[\text{Ca}^{2+}]$ after changing the pre-event resting $[\text{Ca}^{2+}]$ in individual ROIs

Panels A and B (respectively all ROI and DHPG-responsive ROI only) in figures 6.7, 6.9 and 6.10 (not 6.8 for NPEGTA cells) show a significant positive correlation between the change of response peak $[\text{Ca}^{2+}]$ and the change in pre-event $[\text{Ca}^{2+}]$ in the individual ROI considered. This negative correlation is slightly stronger when considering only DHPG-responsive ROI (figures 6.7 to 6.10, panel D).

However, in the case of NPEGTA/ CaCl_2 containing astrocytes, the change in peak $[\text{Ca}^{2+}]$ did not significantly correlate with the change in resting $[\text{Ca}^{2+}]$ after Ca^{2+} uncaging (Spearman 0.08, $p > 0.05$; figure 6.8.A-B). This is consistent with the observation that the relative increase in mean peak $[\text{Ca}^{2+}]$ per cell after Ca^{2+} uncaging, was also not significant (figure 6.5.D).

It is possible that the presence of 5mM NPEGTA changes the Ca^{2+} buffering capacity of the cell which could mask a possible positive correlation with resting $[\text{Ca}^{2+}]$. Indeed, the UV photolysis of NPEGTA may not be complete, in which case increase in peak $[\text{Ca}^{2+}]$ could be curtailed by the presence of additional Ca^{2+} buffer, independently of the change in resting $[\text{Ca}^{2+}]$.

iii. DHPG response amplitude after changing the pre-event resting $[\text{Ca}^{2+}]$ in individual ROIs

The most consistent result, within all three cell groups, was a negative correlation between change of resting $[\text{Ca}^{2+}]$ and the change in response amplitude. Panels C and D (respectively: all ROIs and only DHPG-responsive ROIs) in figures 6.7 to 6.10 show a significant negative correlation between the change of response amplitude and the change in pre-event $[\text{Ca}^{2+}]$ in

the individual ROI considered. This negative correlation is slightly weaker when considering only DHPG-responsive ROI (figures 6.7 to 6.10, panel D).

iv. Equilibration of Ca^{2+} stores and cytosol: possible qualitative explanation

In order to potentially explain the correlations observed between the change in DHPG response and the change in resting $[\text{Ca}^{2+}]$ in individual ROIs, we tested the predicted changes of these parameters in a simple Ca^{2+} equilibration model for a given compartment of interest (figure 6.11). This model makes the assumption that the DHPG pressure application is sufficient to activate enough IP_3 for the concentration to equilibrate across the endoplasmic reticulum and the cytosol. This simulation does not take into account the extrusion mechanisms (endoplasmic reticulum SERCA pumps, $\text{Na}^+/\text{Ca}^{2+}$ exchanger in the cell membrane and mitochondria; reviewed in Verkhratsky et al. 2012) that could be activated and reduce the likelihood of a long-lasting equilibration of $[\text{Ca}^{2+}]$ across these two compartments.

This model takes into account the distribution of Ca^{2+} within a given subcellular compartment of interest. The respective volumes of cytosol and endoplasmic reticulum fractions of the given subcellular compartment of interest are V_C and V_{ER} . The $[\text{Ca}^{2+}]$ within these two volumes of a given compartment are $[\text{Ca}^{2+}]_C$ and $[\text{Ca}^{2+}]_{ER}$. Therefore the total amount of Ca^{2+} in the given compartment can be described as $n_{Ca} = V_C \times [\text{Ca}^{2+}]_C + V_{ER} \times [\text{Ca}^{2+}]_{ER}$.

If Ca^{2+} equilibrates over both cytosol and ER volumes of a given ROI after a given DHPG-pressure application, then the total $[\text{Ca}^{2+}]$ of the DHPG-evoked response recorded for this given ROI: $[\text{Ca}^{2+}]_P = n_{Ca} / (V_C + V_{ER}) = (V_C \times [\text{Ca}^{2+}]_C + V_{ER} \times [\text{Ca}^{2+}]_{ER}) / (V_C + V_{ER})$.

Dr C. Henneberger applied this prediction for given values of $V_{ER} = 0.15$, $V_C = 0.85$, $[\text{Ca}^{2+}]_{ER} = 1.0 \mu\text{M}$. The $[\text{Ca}^{2+}]_C$ was randomly chosen as $0.6 \pm 0.2 \mu\text{M}$ (mean \pm SD).

The resulting plots of estimated peak $[\text{Ca}^{2+}]$ and amplitude of a possible DHPG-pressure application as a function of resting $[\text{Ca}^{2+}]$, predicted for these chosen parameter values should the Ca^{2+} equilibrate across both cytosol and ER volumes of a given compartment, are plotted in figure 6.11.A-B.

This model shows that the peak $[\text{Ca}^{2+}]$ increases when the resting $[\text{Ca}^{2+}]$ increases (figure 6.11.A) whereas the amplitude of the response decreases when the resting $[\text{Ca}^{2+}]$ increases (figure 6.11.B).

Consequently, a positive correlation can be found when plotting the change of peak $[\text{Ca}^{2+}]$ against the change of resting $[\text{Ca}^{2+}]$ (figure 6.11.C). In contrast, the change of amplitude is negatively correlated with the resting $[\text{Ca}^{2+}]$ (figure 6.11.D). These correlations found for predicted changes in DHPG-evoked response and changes in resting $[\text{Ca}^{2+}]$ in this model for equilibration over cytosol and ER volumes of a given compartment qualitatively match the correlations previously described in this section (cf figure 6.10). Therefore it is possible that the positive correlation of change of peak $[\text{Ca}^{2+}]$ of the response to DHPG and the negative correlation of change of response amplitude with the change of resting $[\text{Ca}^{2+}]$ can be qualitatively explained by a equilibration of the DHPG- resulting Ca^{2+} across the cytosol and ER volumes of the given compartment of interest.

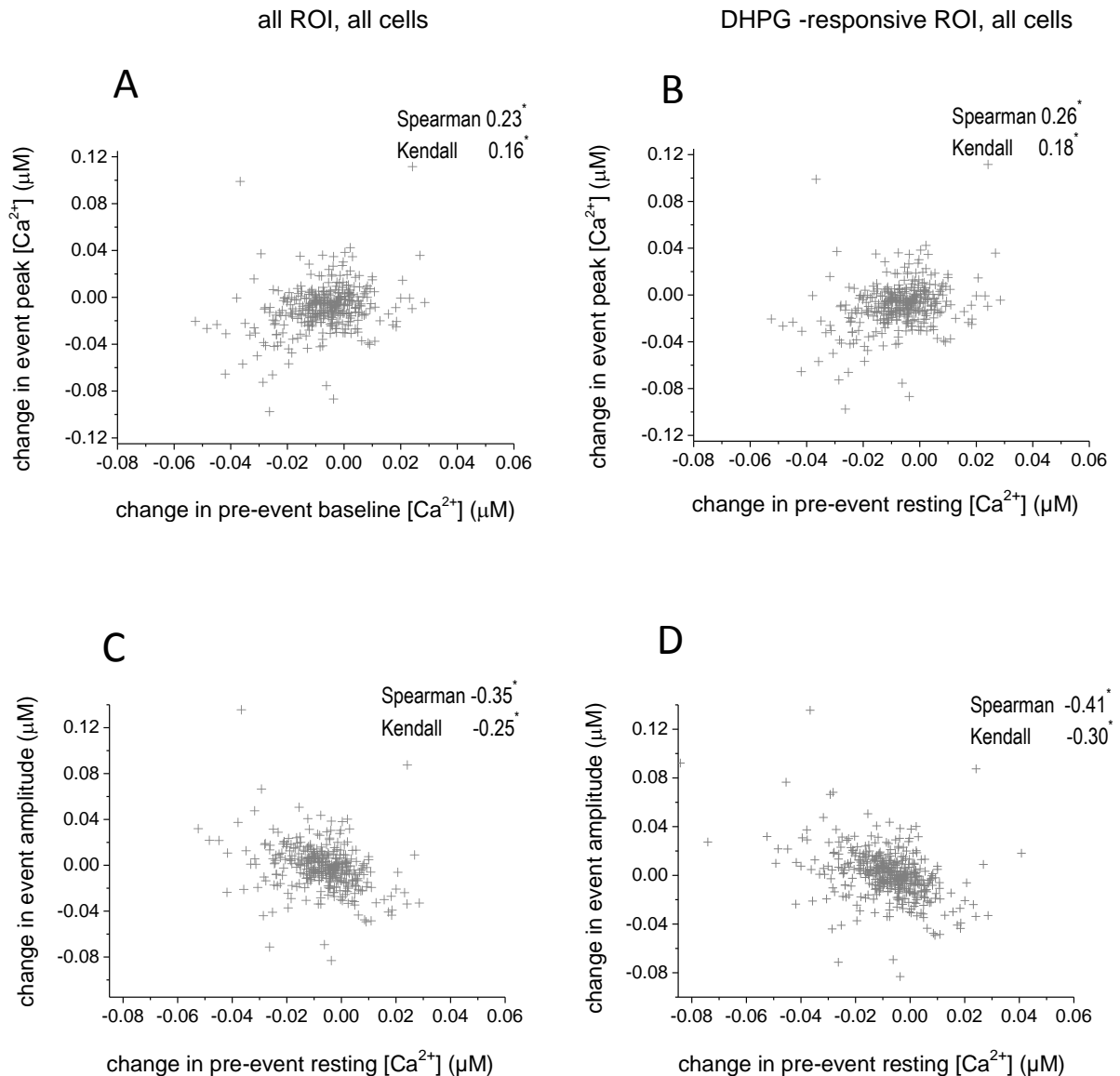


Figure 6.7 change in DHPG-puff response vs change in resting $[Ca^{2+}]$

for all ROI from cells with no uncaging (KMS-only, no UV exposure)

The difference in the response to DHPG-p (DHPG-p2 – DHPG-p1) is given for each ROI (change in $[Ca^{2+}]$, μM) as a function of the change in pre-event resting $[Ca^{2+}]$ for that given ROI. These graphs represent all ROI (graphs A and C) and all responsive ROI (response amplitude larger than 6nM; graphs B and D) from all KMS-only containing cells (grey, n=7 cells). Change in response peak $[Ca^{2+}]$ is plotted in A and B, change in response amplitude is plotted in C and D. Spearman and Kendall correlation coefficients are given for each graph: * $p < 0.001$.

The change in DHPG-peak $[Ca^{2+}]$ response is significantly positively correlated with the change in pre-event baseline $[Ca^{2+}]$ (graphs A and B). This correlation is stronger when considering only DHPG-responsive ROI (graph B).

The change in DHPG-response amplitude is significantly correlated with the change in pre-event baseline $[Ca^{2+}]$ (graphs C and D). This correlation is slightly weaker when considering only DHPG-responsive ROI (graph D).

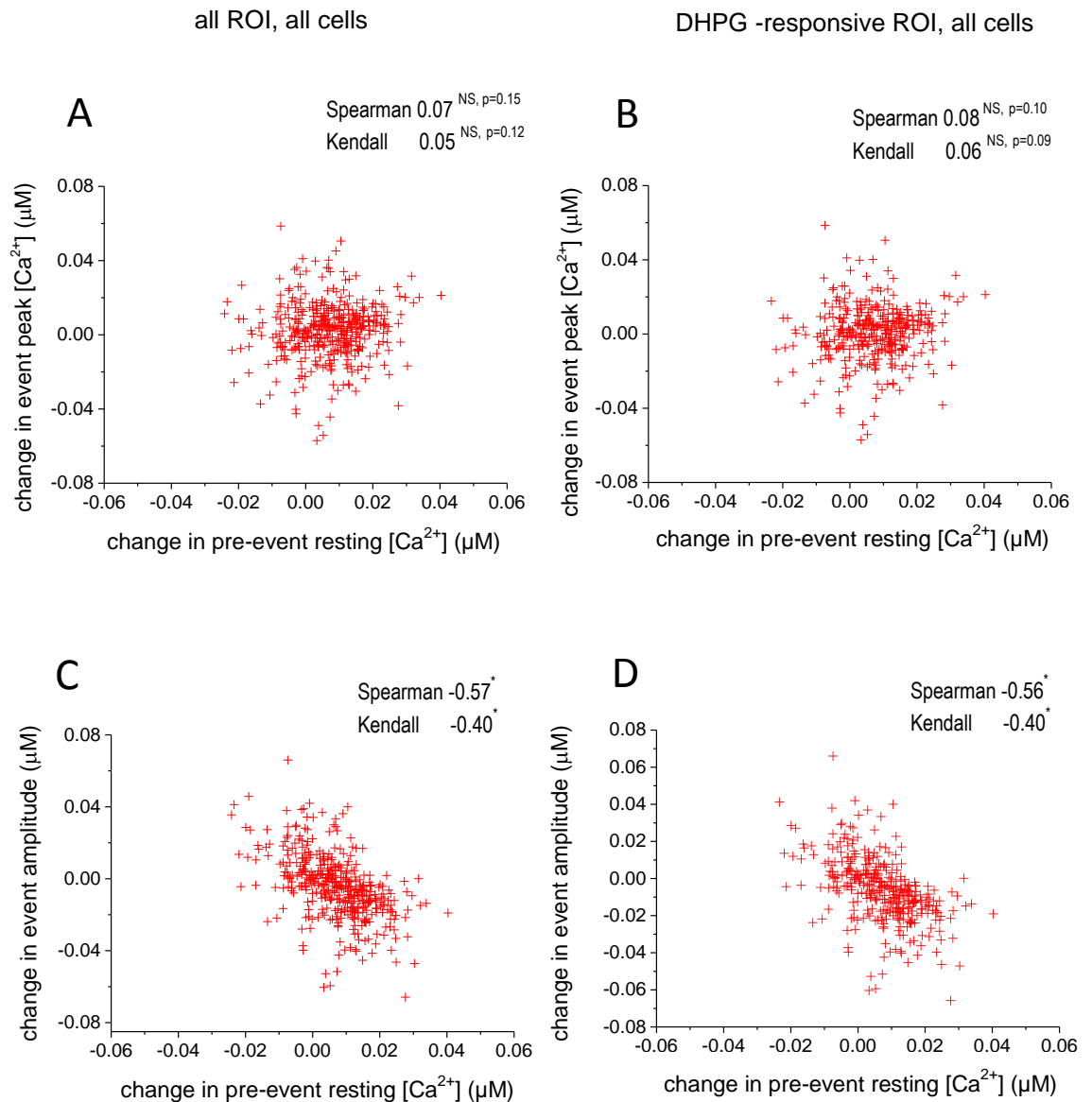


**Figure 6.8 change in DHPG-p response vs change in resting $[Ca^{2+}]$
for all ROI from cells with Ca^{2+} uncaging (NPEGTA/ $CaCl_2$)**

The difference in the response to DHPG-p (DHPG-p2 – DHPG-p1) is given for each ROI (change in $[Ca^{2+}]$, μM) as a function of the change in pre-event resting $[Ca^{2+}]$ for that given ROI. These graphs represent all ROI (graphs A and C) and all responsive ROI (response amplitude larger than 6nM; graphs B and D) from all cells exposed to UV uncaging of Ca^{2+} (red = cells contain NPEGTA/ $CaCl_2$; n=8 cells). Change in response peak $[Ca^{2+}]$ is plotted in A and B, change in response amplitude is plotted in C and D. Spearman and Kendall correlation coefficients are given for each graph: NS $p > 0.05$, * $p < 0.001$.

The change in DHPG-peak $[Ca^{2+}]$ response is not significantly correlated with the change in pre-event resting $[Ca^{2+}]$ (non-significant slight positive trend, graphs A and B).

The change in in DHPG-response amplitude is significantly correlated with the change in pre-event resting $[Ca^{2+}]$ (graphs C and D). This correlation is slightly weaker when considering only DHPG-responsive ROI (graph D).

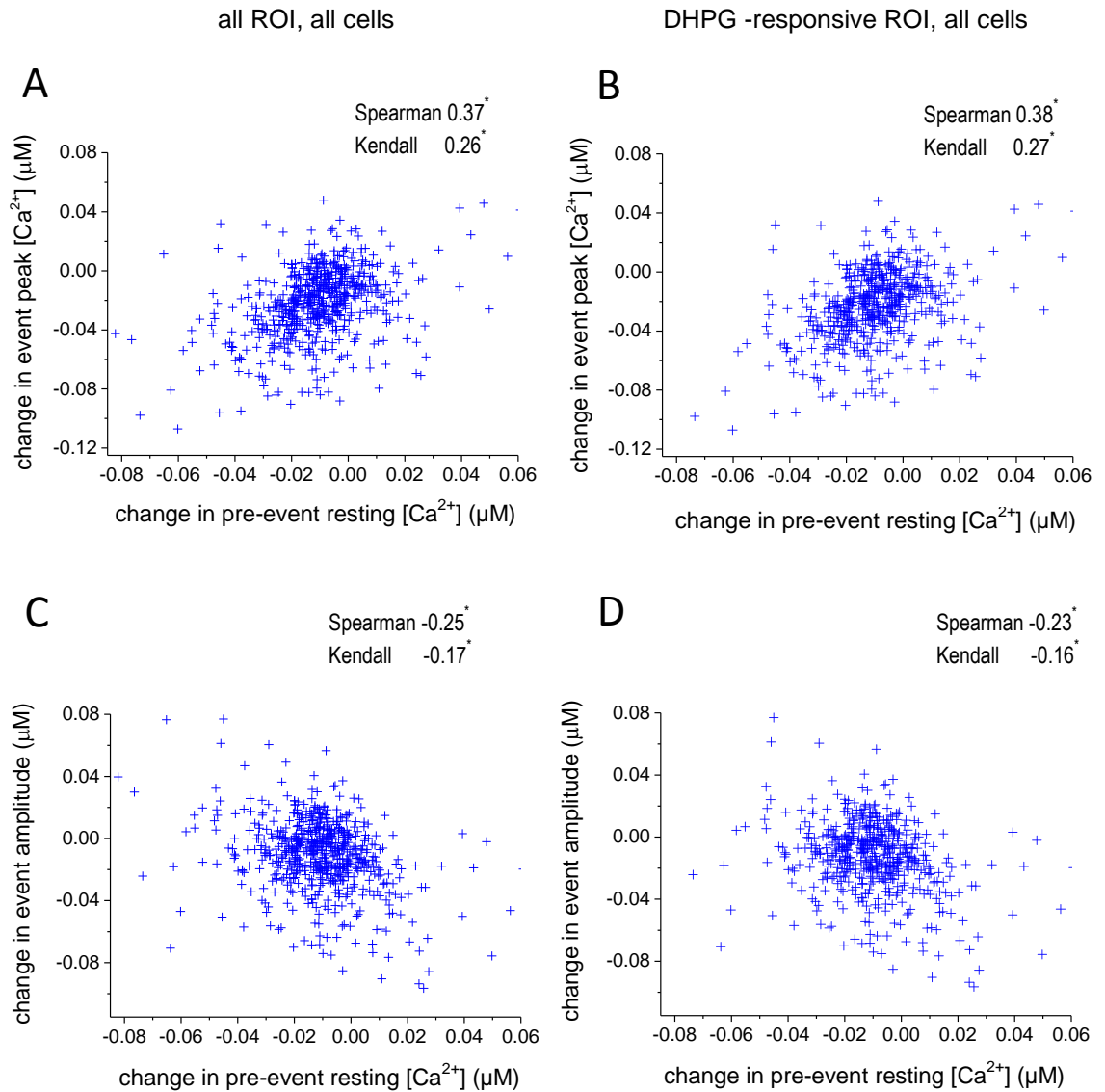


**Figure 6.9 change in DHPG-p response vs change in resting $[Ca^{2+}]$
for all ROI from cells with Ca^{2+} -buffer uncaging (Diazo2)**

The difference in the response to DHPG-p (DHPG-p2 – DHPG-p1) is given for each ROI (change in $[Ca^{2+}]$, μM) as a function of the change in pre-event resting $[Ca^{2+}]$ for that given ROI. These graphs represent all ROI (graphs A and C) and all responsive ROI (response amplitude larger than 6nM; graphs B and D) from all cells exposed to UV uncaging of Ca^{2+} -buffer (blue= cells contain Diazo2, n=11 cells). Change in response peak $[Ca^{2+}]$ is plotted in A and B, change in response amplitude is plotted in C and D. Spearman and Kendall correlation coefficients are given for each graph: * $p < 0.001$.

The change in DHPG-peak $[Ca^{2+}]$ response is significantly positively correlated with the change in pre-event resting $[Ca^{2+}]$ (graphs A and B). This correlation is stronger when considering only DHPG-responsive ROI (graph B).

The change in in DHPG-response amplitude is significantly correlated with the change in pre-event resting $[Ca^{2+}]$ (graphs C and D). This correlation is slightly weaker when considering only DHPG-responsive ROI (graph D).

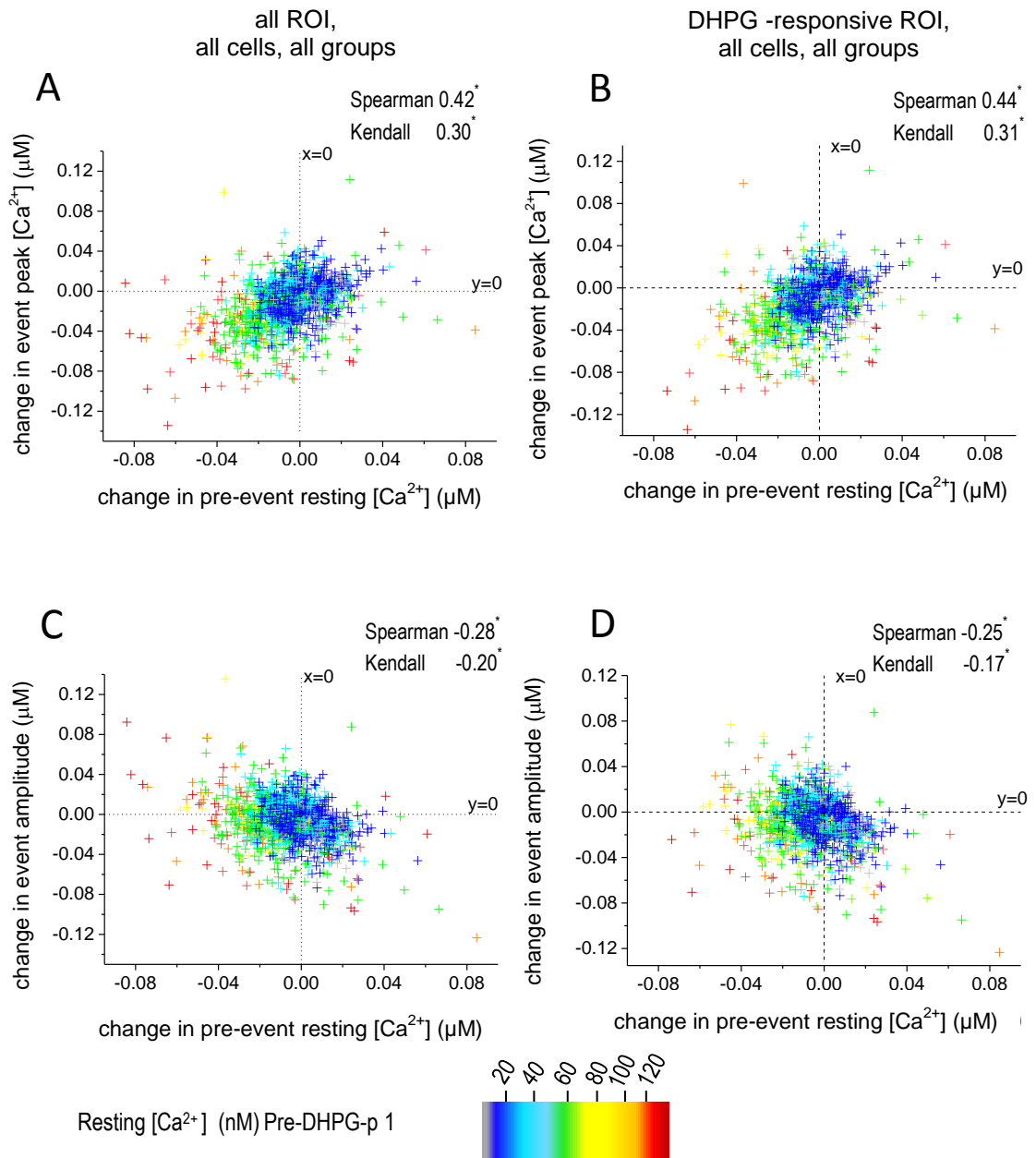


Figure 6.10 change in DHPG-p response vs change in resting $[Ca^{2+}]$ for all ROI

The difference in the response to DHPG-p (DHPG-p2 – DHPG-p1) is given for each ROI (change in $[Ca^{2+}]$, μM) as a function of the change in pre-event resting $[Ca^{2+}]$ for that given ROI. The colour reflects the pre-event 1 resting $[Ca^{2+}]$ (in nM; before DHPG-p 1) for each ROI as indicated by the colour scale. Change in response peak $[Ca^{2+}]$ is plotted in A and B, change in response is plotted in C and D.

All ROI from all cells are represented in graphs A and C. All DHPG-responsive ROI (amplitude larger than 6nM) are represented in graphs B and D.

The dashed lines indicate x or $y = 0 \mu M$, no absolute change in parameter. Spearman and Kendall correlation coefficients are given for each graph: * $p < 0.001$.

The change in DHPG-peak $[Ca^{2+}]$ response is significantly positively correlated with the change in pre-event resting $[Ca^{2+}]$ (graphs A and B). This correlation is stronger when considering only DHPG-responsive ROI (graph B).

The change in in DHPG-response amplitude is significantly correlated with the change in pre-event resting $[Ca^{2+}]$ (graphs C and D). This correlation is slightly weaker when considering only DHPG-responsive ROI (graph D).

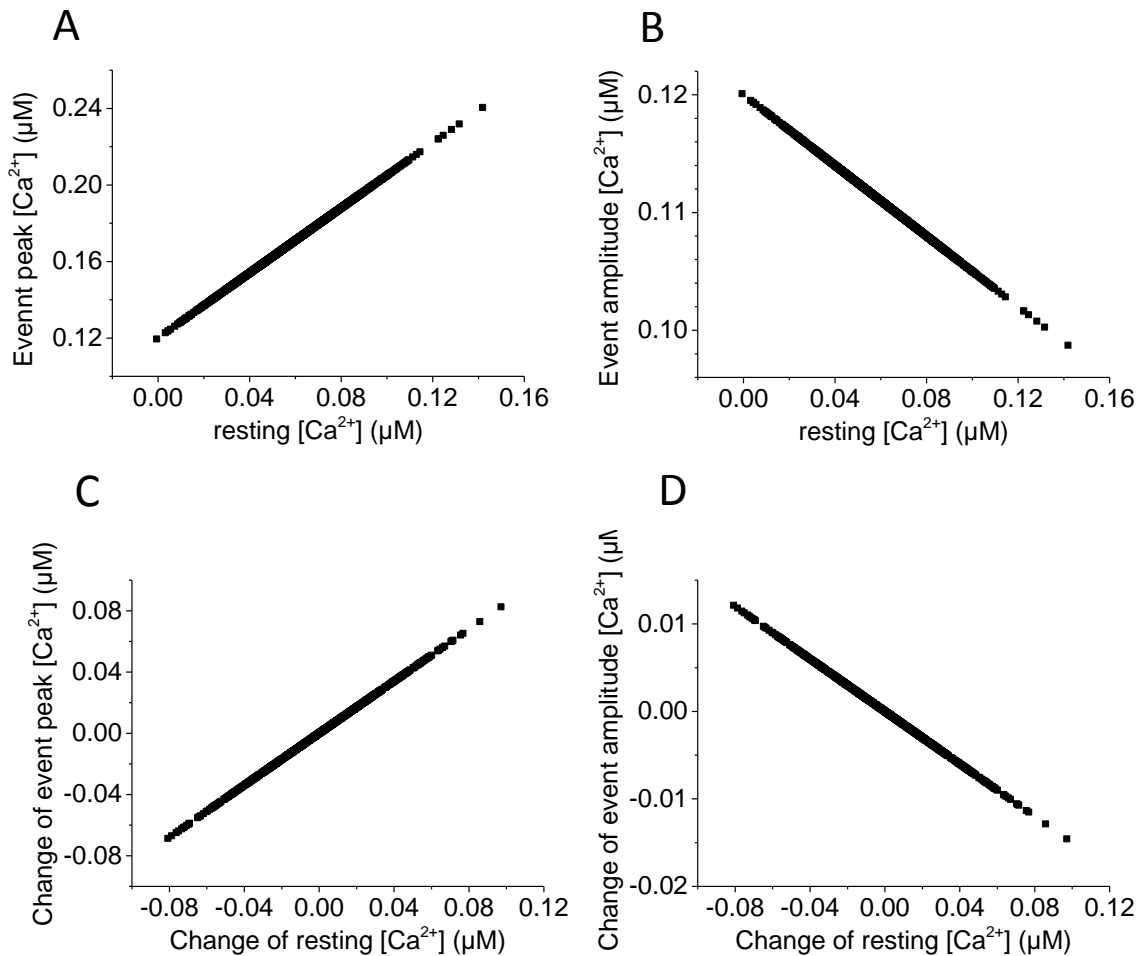


Figure 6.11 Equilibration of Ca^{2+} stores and cytosol qualitatively explains correlations between change of resting $[\text{Ca}^{2+}]$ and response peak $[\text{Ca}^{2+}]$ or amplitude

Simulation by Dr C. Henneberger

For a given single compartment, V_C refers to the volume occupied by the cytosol and $[\text{Ca}^{2+}]_C$ refers to the Ca^{2+} concentration in this cytosolic volume of the compartment. Similarly, V_{ER} refers to the volume of the given compartment that is occupied by the endoplasmic reticulum (ER) and $[\text{Ca}^{2+}]_{ER}$ refers to the Ca^{2+} concentration in this ER volume of the compartment. Therefore, the total amount of Ca^{2+} in that compartment (n_{Ca}) can be expressed as $n_{Ca} = V_C \times [\text{Ca}^{2+}]_C + V_{ER} \times [\text{Ca}^{2+}]_{ER}$.

If Ca^{2+} equilibrates over both compartments after DHPG-p, then the DHPG response $[\text{Ca}^{2+}]_P = n_{Ca} / (V_C + V_{ER}) = (V_C \times [\text{Ca}^{2+}]_C + V_{ER} \times [\text{Ca}^{2+}]_{ER}) / (V_C + V_{ER})$.

In this figure, $V_{ER} = 0.15$, $V_C = 0.85$, $[\text{Ca}^{2+}]_{ER} = 1.0 \mu\text{M}$. $[\text{Ca}^{2+}]_C$ was randomly chosen as $0.6 \pm 0.2 \mu\text{M}$ (mean \pm SD).

A: Simulation event peak $[\text{Ca}^{2+}]$ increases with increasing resting $[\text{Ca}^{2+}]$ for the given simulation cytosol and ER volumes

B: Simulation event amplitude increases with increasing resting $[\text{Ca}^{2+}]$ for the given simulation cytosol and ER volumes

Peak $[\text{Ca}^{2+}]$ increases with increasing resting $[\text{Ca}^{2+}]$ (panel A) while the response amplitude is decreased (panel B).

C: Simulation change in event peak $[\text{Ca}^{2+}]$ increases with increasing change in resting $[\text{Ca}^{2+}]$ for the given simulation cytosol and ER volumes

D: Simulation change in event amplitude increases with increasing change in resting $[\text{Ca}^{2+}]$ for the given simulation cytosol and ER volumes

As a consequence of A, the change of peak $[\text{Ca}^{2+}]$ shows a positive correlation with the change of resting $[\text{Ca}^{2+}]$ (panel C). In contrast, the change of amplitude is negatively correlated with the resting $[\text{Ca}^{2+}]$ (panel D).

Thus, a single Ca^{2+} equilibration model can qualitatively account for the correlations observed in experimental data.

v. Further qualitative analysis confirms these correlations between change of response to DHPG and change of resting $[Ca^{2+}]$ in individual ROIs.

The distribution and average (\pm SD in graphs) response peak $[Ca^{2+}]$ and amplitude according to arbitrarily defined qualitative changes in resting $[Ca^{2+}]$ groups ('same', 'decrease', 'increase'; described below) was plotted for all DHPG-responsive ROI from all cells within the three experimental protocol groups (figures 6.12-14). These plots displayed significant differences between the mean changes in both response peak $[Ca^{2+}]$ and amplitude between the relevant different qualitative 'change in resting $[Ca^{2+}]$ ' groups.

These qualitative differences were consistent with the correlations observed in figures 6.7-9. This further analysis lends support to the possible positive correlation between the change in response peak $[Ca^{2+}]$ and the change in resting $[Ca^{2+}]$, as well as the negative correlation between the change in response amplitude and the change in resting $[Ca^{2+}]$ recorded in these DHPG-responsive individual ROIs (as described in figures 6.7-11).

The change in resting $[Ca^{2+}]$ groups were defined according to the absolute difference in $[Ca^{2+}]$ between the resting $[Ca^{2+}]$ recorded before the 2nd and 1st DHPG pressure application ('after' - 'before' manipulating the resting $[Ca^{2+}]$). Three groups were defined: no change or less than ± 6 nM ('same'), decrease by more than -6 nM ('decrease') and increase by more than +6 nM ('increase'). A one-way ANOVA was performed to identify any differences across these 'change in resting $[Ca^{2+}]$ ' defined groups. If significant, a post-hoc Tukey means comparison test was used to identify the significant differences between 'change in resting $[Ca^{2+}]$ ' determined groups of ROI. Significant differences in mean values are represented by lines in figures 6.12-14.

In DHPG-responsive ROIs from KMS-only containing astrocytes (figure 6.12), the mean change in peak $[Ca^{2+}]$ was significantly decreased (mean difference \pm SEM: -7.8 ± 2.3 nM) in ROIs where the resting $[Ca^{2+}]$ decreased compared to the mean change in peak $[Ca^{2+}]$ in ROI where the resting $[Ca^{2+}]$ only changed within ± 6 nM ('decrease' vs 'same', Tukey: $q = 4.8$, $p < 0.01$; figure 6.12.A). This is consistent with the positive correlation seen between change in resting $[Ca^{2+}]$ and change response peak $[Ca^{2+}]$ in figure 6.7.B.

The mean change in amplitude significantly increased (mean difference \pm SEM: $+7.2 \pm 2.3$ nM) in ROIs where the resting $[Ca^{2+}]$ decreased compared to the mean change in peak $[Ca^{2+}]$ in ROIs where the resting $[Ca^{2+}]$ only changed within ± 6 nM ('decrease' vs 'same', Tukey: $q = 4.4$, $p < 0.01$). The opposite occurred between the mean amplitude change in ROIs where the resting $[Ca^{2+}]$ increased compared to the mean change in peak $[Ca^{2+}]$ in ROIs where the resting $[Ca^{2+}]$ only changed within ± 6 nM ('increase' vs 'same', mean difference \pm SEM: -12.8 ± 4 nM, Tukey: $q = 4.6$, $p < 0.01$; figure 6.12.B). This is consistent with the negative correlation observed between change in resting $[Ca^{2+}]$ and change in response amplitude in figure 6.7.D.

In DHPG-responsive ROIs from NPEGTA/CaCl₂ containing astrocytes (figure 6.13), the mean change in peak [Ca²⁺] was not significantly different across the different 'change in resting [Ca²⁺]' groups (one way ANOVA, F= 1.8, p=0.15; figure 6.13.A). This is consistent with the lack of correlation observed between change in resting [Ca²⁺] and change in response peak [Ca²⁺] (figure 6.8.B). The mean change in response amplitude was significantly decreased (mean difference ±SEM: -14.1 ±1.9 nM) in ROIs where the resting [Ca²⁺] increased compared to the mean change in amplitude in ROIs where the resting [Ca²⁺] only changed within ±6 nM ('increase' vs 'same', Tukey: q=10.5, p < 0.001; figure 6.13.B). This is consistent with the negative correlation observed between the change in amplitude and the change in resting [Ca²⁺] in figure 6.8.D.

In DHPG-responsive ROIs from Diazo2 containing astrocytes (figure 6.14), the mean change in peak [Ca²⁺] was significantly decreased (mean difference ±SEM: -13.7 ± 2.4 nM) in ROIs where the resting [Ca²⁺] decreased by more than -6 nM compared to the mean change in amplitude in ROIs where the resting [Ca²⁺] only changed within ±6 nM ('decrease' vs 'same', Tukey: q= 8.2, p < 0.001; figure 6.14.A). This is consistent with the observed positive correlation between the change in peak [Ca²⁺] and the change in resting [Ca²⁺] in figure 6.9.B.

The mean change in amplitude significantly increases (mean difference ±SEM: +27.6 ± 3.1 nM) in ROIs where the resting [Ca²⁺] decreased by more than 6 nM compared to the mean change in amplitude in ROIs where the resting [Ca²⁺] increased by more than +6 nM ('decrease' vs 'increase', Tukey: q= 12.7, p < 0.001; figure 6.14.B). This is consistent with the observed negative correlation between the change in amplitude and the change in resting [Ca²⁺] in figure 6.9.D.

However, the mean change in amplitude does not significantly increase (mean difference ±SEM: +4.3 ± 2.6 nM) in ROIs where the resting [Ca²⁺] decreased by more than 6 nM compared to the mean change in amplitude in ROIs where the resting [Ca²⁺] only changed within ±6 nM ('decrease' vs 'same', Tukey: q= 2.6, p = 0.25; figure 6.14.B). This is also seen in figure 6.9.D. Indeed, in these Diazo2 containing cells, it seems that decreasing the resting [Ca²⁺] further than -6 nM slightly reduces the decrease in amplitude but not significantly. The negative correlation observed in 6.9.D seems to be due mostly to the large decrease in amplitude seen in the ROIs where the resting [Ca²⁺] increased by more than +6 nM (figure 6.14.B).

Overall, this further qualitative analysis does seem to corroborate the observed positive correlations between peak [Ca²⁺] and change in resting [Ca²⁺] or negative correlations between change in response amplitude and change in resting [Ca²⁺]. However, it does highlight some of the limitations which are further discussed below and in the discussion sections of chapters 4 and 7. Indeed, the use of caged- Ca²⁺ buffers implicates different Ca²⁺ buffering capacity across cells which limits comparisons across cells in the three different experimental groups (KMS, NPEGTA and Diazo2). Yet distinguishing the effect of changing the resting [Ca²⁺] within these experimental groups would require more equal number of ROIs within each qualitative resting [Ca²⁺] group. Perhaps localised uncaging protocols could help in the future.

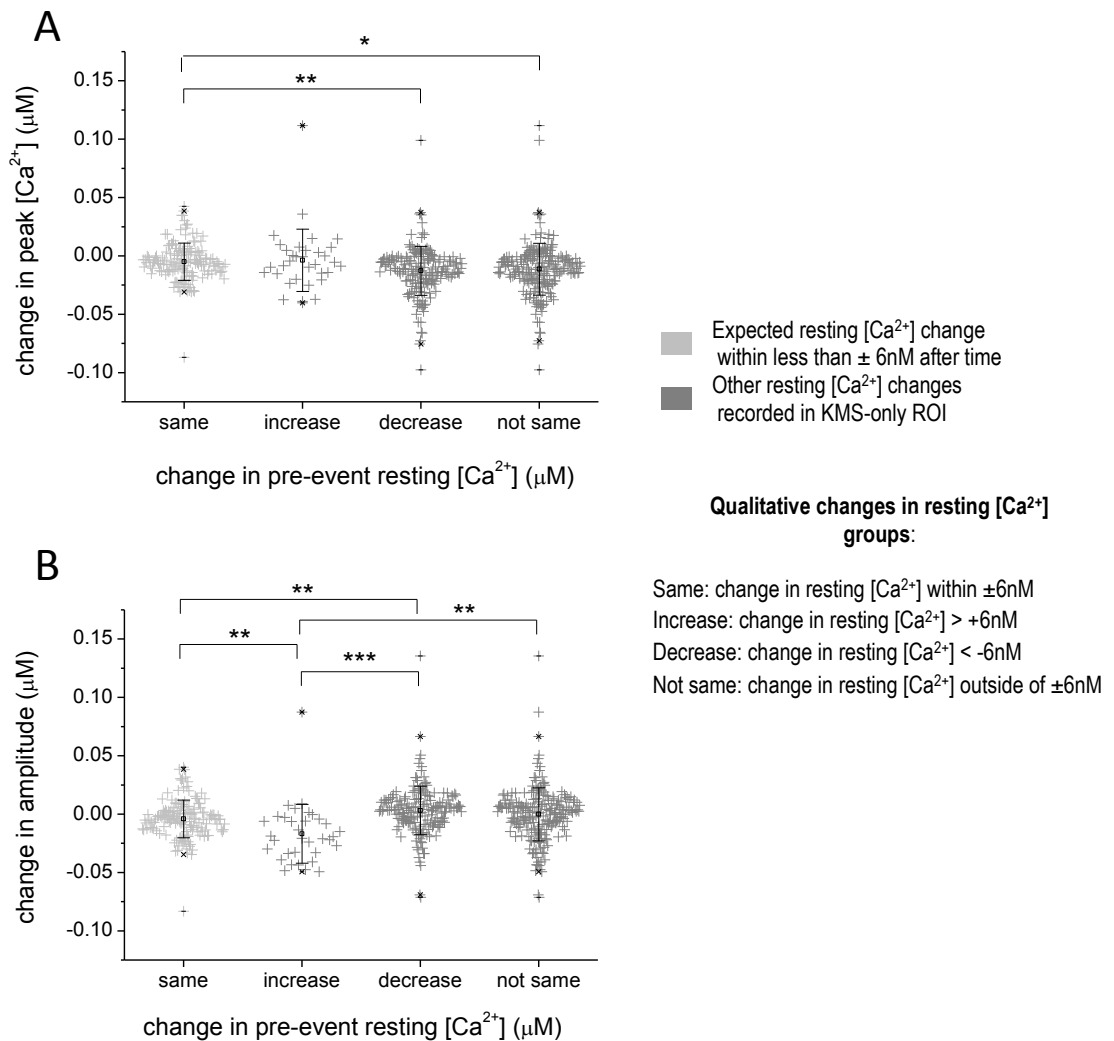


Figure 6.12 change in DHPG-p response in all DHPG-responsive ROI according to qualitative change in resting $[Ca^{2+}]$ groups in KMS-only ROI.

These distribution plots show the change in response peak $[Ca^{2+}]$ (μM , graph A) and in response amplitude ($[Ca^{2+}]$, μM , graph B) after time only, for all DHPG-responsive ROI according to qualitative change in resting $[Ca^{2+}]$ groups.

The squares indicate the average change in DHPG-p response with \pm standard deviation bars. ROI were classified into 4 arbitrarily defined groups based on the qualitative change in resting $[Ca^{2+}]$ recorded between DHPG-p 1 and 2. If the ROI resting $[Ca^{2+}]$ changed by less than $\pm 6nM$ then it was considered as 'no change/same'. If the ROI resting $[Ca^{2+}]$ increased by more than $6nM$, the ROI was considered as part of the 'increase' group. If the ROI resting $[Ca^{2+}]$ decreased by more than $-6nM$, the ROI was considered as part of the 'decrease' group. Finally, the last group represents all ROI where the baseline changed differently to the expected experimental protocol. For KMS-only cells, this includes all ROI that displayed a change in resting $[Ca^{2+}]$ outside of the $6nM$ range and they are represented in the 'not same' group.

A one way ANOVA was performed across groups and when a significant difference was found, a post hoc Tukey test was used to identify groups with significantly different means. These significant differences are indicated by horizontal brackets, stars indicate significance (* $p < 0.05$, ** $p < 0.01$, *** $p < 0.001$).

The mean peak $[Ca^{2+}]$ response is significantly decreased when the resting $[Ca^{2+}]$ changes by more than $\pm 6nM$ (graph A, * $p < 0.05$).
The mean amplitude does not significantly change when the resting $[Ca^{2+}]$ changes by more than $+6nM$ (graph B, NS $p > 0.05$).

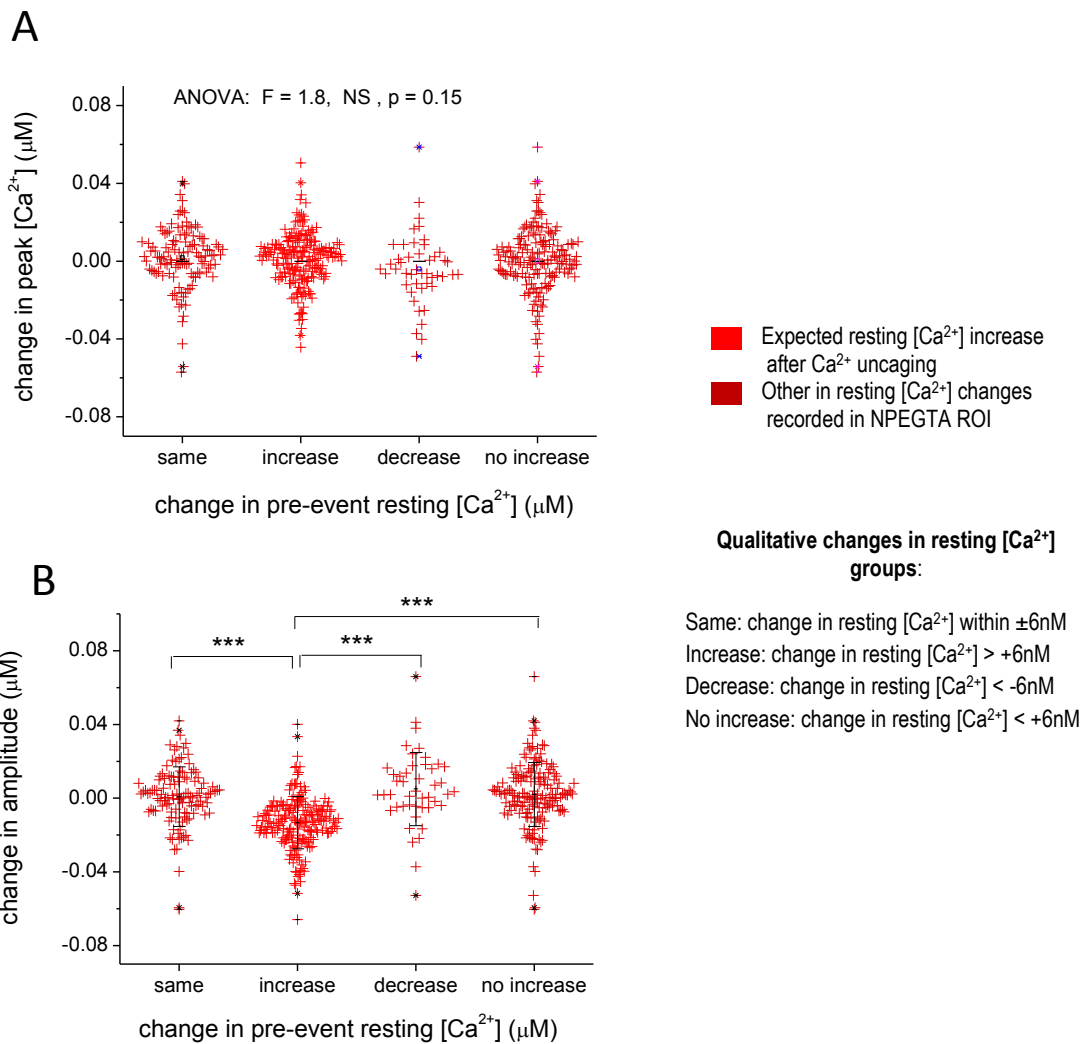


Figure 6.13 change in DHPG-puff response in all DHPG-responsive ROI according to qualitative change in resting $[Ca^{2+}]$ in ROI with Ca^{2+} uncaging (NPEGTA/ $CaCl_2$).

These distribution plots show the change in response peak $[Ca^{2+}]$ (μM , graph A) and in response amplitude ($[Ca^{2+}]$, μM , graph B) between before and after Ca^{2+} uncaging, for all DHPG-responsive ROI according to qualitative change in resting $[Ca^{2+}]$ groups.

The squares indicate the average change in DHPG-p response with \pm standard deviation bars. ROI were classified into 4 arbitrarily defined groups based on the qualitative change in resting $[Ca^{2+}]$ recorded between DHPG-p 1 and 2. If the ROI resting $[Ca^{2+}]$ changed by less than $\pm 6nM$ then it was considered as 'no change/same'. If the ROI resting $[Ca^{2+}]$ increased by more than $6nM$, the ROI was considered as part of the 'increase' group. If the ROI resting $[Ca^{2+}]$ decreased by more than $-6nM$, the ROI was considered as part of the 'decrease' group. Finally, the last group represents all ROI where the baseline changed differently to the expected experimental protocol. For NPEGTA cells, this includes all ROI that displayed a change in resting $[Ca^{2+}]$ of less than $+6nM$ and they are represented in the 'no increase' group.

A one way ANOVA was performed across groups and when a significant difference was found, a post hoc Tukey test was used to identify groups with significantly different means. These significant differences are indicated by horizontal brackets, stars indicate significance (* $p < 0.05$, ** $p < 0.01$, *** $p < 0.001$).

The mean peak $[Ca^{2+}]$ response is not significantly altered by the change in resting $[Ca^{2+}]$ (graph A, ANOVA NS $p > 0.05$).

The mean amplitude is significantly decreased when the resting $[Ca^{2+}]$ increases by more than $6nM$ (graph B, *** $p < 0.001$).

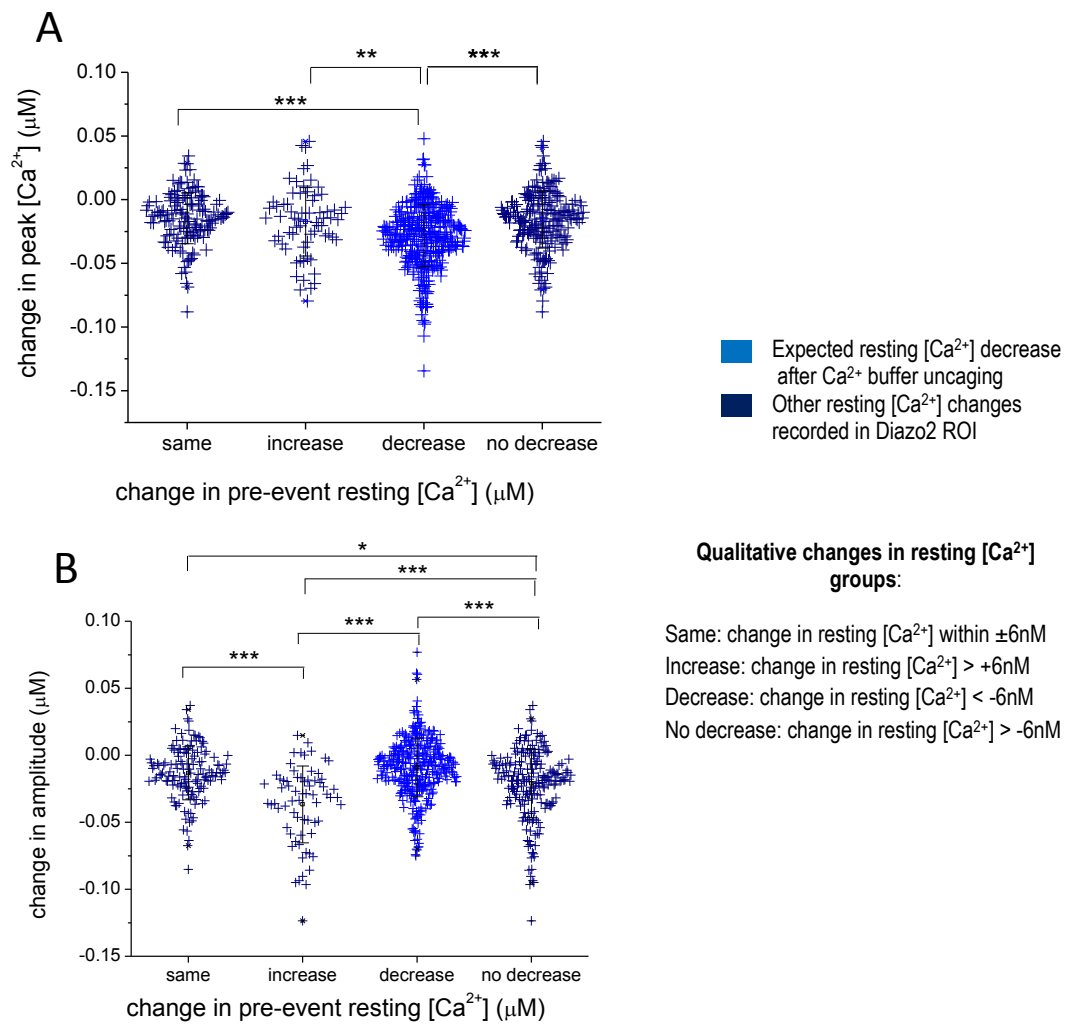


Figure 6.14 change in DHPG-p response in all DHPG-responsive ROI according to qualitative change in resting $[Ca^{2+}]$, in ROI with Ca^{2+} buffer uncaging (Diaz2).

These distribution plots show the change in response peak $[Ca^{2+}]$ (μM , graph A) and in response amplitude ($[Ca^{2+}]$, μM , graph B) between before and after Ca^{2+} buffer uncaging, for all DHPG-responsive ROI according to qualitative change in resting $[Ca^{2+}]$ groups.

The squares indicate the average change in DHPG-p response with \pm standard deviation bars.

ROI were classified into 4 arbitrarily defined groups based on the qualitative change in resting $[Ca^{2+}]$ recorded between DHPG-p 1 and 2. If the ROI resting $[Ca^{2+}]$ changed by less than $\pm 6nM$ then it was considered as 'no change/same'. If the ROI resting $[Ca^{2+}]$ increased by more than $6nM$, the ROI was considered as part of the 'increase' group. If the ROI resting $[Ca^{2+}]$ decreased by more than $-6nM$, the ROI was considered as part of the 'decrease' group. Finally, the last group represents all ROI where the baseline changed differently to the expected experimental protocol. For Diaz2 cells, this includes all ROI that displayed a change in resting $[Ca^{2+}]$ of more than $-6nM$ and they are represented in the 'no decrease' group.

A one way ANOVA was performed across groups and when a significant difference was found, a post hoc Tukey test was used to identify groups with significantly different means. These significant differences are indicated by horizontal brackets, stars indicate significance (* $p < 0.05$, ** $p < 0.01$, *** $p < 0.001$).

The mean amplitude is significantly increased when the resting $[Ca^{2+}]$ decreases by more than $6nM$, but it does not increase significantly further than when the resting $[Ca^{2+}]$ doesn't change by $\pm 6nM$ (graph B, NS $p > 0.05$, *** $p < 0.001$).

D. Ratio of endoplasmic reticulum to cytosol in an astrocyte model

Ullah et al. 2006 defined a model for the dynamic estimation of cytosolic $[Ca^{2+}]$ in astrocytes. In their model, Ullah et al. took into account the IP_3R mediated Ca^{2+} flux from the ER into the cytosol, Ca^{2+} influx from the extracellular space into the cytosol, active uptake of Ca^{2+} from the cytosol into the ER and Ca^{2+} extrusion. These parameters were not taken into account in the previous simple simulation in figure 6.11. Using this model, we investigated the impact of the ratio of endoplasmic reticulum (ER) to cytosol volumes on both resting $[Ca^{2+}]$ and the response to a single evoked glutamate stimulation in figure 6.15. We performed this simulation in order to test the possibility that differences in the distribution of ER could explain the differences in resting $[Ca^{2+}]$ and Ca^{2+} response peak $[Ca^{2+}]$ and amplitude to a given single DHPG pressure application observed across different individual ROIs or astrocytes (figures 4.5.A,B; 6.2-3).

Ullah et al. 2006's model for astrocyte cytosolic $[Ca^{2+}]$ was adapted by Dr C. Henneberger with the following settings: initial $[Ca^{2+}]$ of $4\ \mu M$ and $0.1\ \mu M$ for the ER and cytosol volumes respectively, the initial $[IP_3]$ was fixed. After 30 seconds, a single evoked Ca^{2+} event was triggered by increasing external glutamate concentration from 0 to $100\ \mu M$ for 1 second (figure 6.15.A). Four increasing ratios of ER to cytosol volumes were tested: 0.1, 0.2, 0.3 and 0.4 (respectively in pink, purple, grey and black; figure 6.15.A). The resulting pre-event resting $[Ca^{2+}]$ (figure 6.15.B), response peak $[Ca^{2+}]$ (figure 6.15.C) and response amplitude (figure 6.15.D) all increased when the ratio of ER to cytosol increased from 0.1 to 0.4.

This suggests that in this astrocyte model, the volume occupied by endoplasmic reticulum is positively correlated with the resting $[Ca^{2+}]$ and thus also the evoked response peak $[Ca^{2+}]$ and amplitude. These results are similar to the positive correlations seen between pre-event resting $[Ca^{2+}]$ and DHPG-evoked response peak $[Ca^{2+}]$ and amplitude (figures 6.2-3). Therefore it could be possible that these correlations may be explained by differences in average total ratio of ER to cytosol volumes across different astrocytes for figure 6.2 as well as local ER to cytosol volume ratios in individual ROI in figure 6.3.B,D.

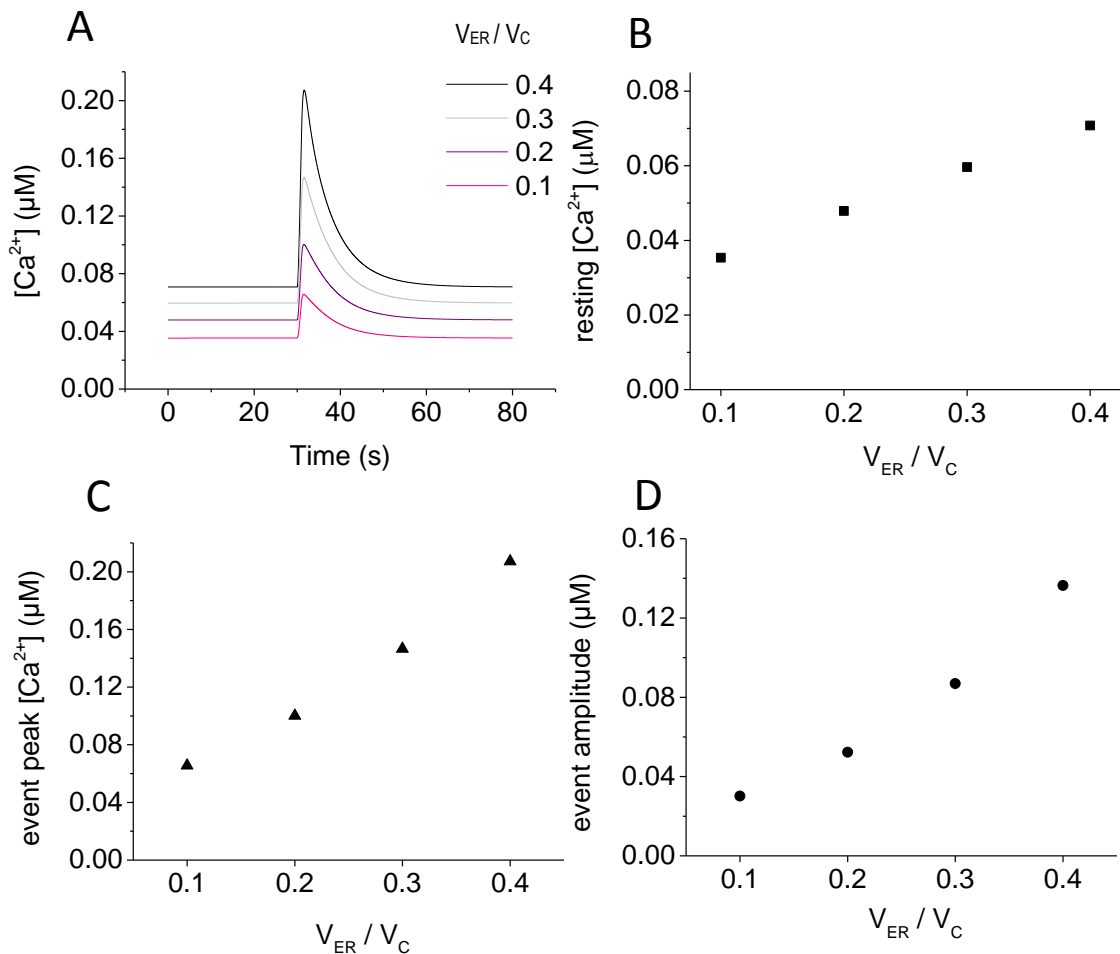


Figure 6.15 The ratio of endoplasmic reticulum (ER) to cytosol volumes determines resting $[Ca^{2+}]$ and event peak $[Ca^{2+}]$ and amplitude in an astrocyte model.

Simulation by Dr C. Henneberger

A: Simulation of glutamate evoked Ca^{2+} event for different set ratios of ER to cytosol volumes

The ratio of ER volume to cytosol volume (V_{ER}/V_C) was set to 0.1, 0.2, 0.3 or 0.4. Using an astrocyte model adapted by Dr Christian Henneberger from Ullah et al. 2006, the effect of altering these ratios on $[Ca^{2+}]$ was tested on a modelled evoked Ca^{2+} event (panel A).

The initial $[Ca^{2+}]$ conditions in these volumes for this adapted model were: $[Ca^{2+}]_{ER} = 4 \mu M$, $[Ca^{2+}]_{cytosol} = 0.1 \mu M$. The initial IP_3 concentration was fixed. The model was allowed to equilibrate for 120 seconds. After 30 seconds, an event was evoked by raising the ambient glutamate concentration from 0 to 100 μM , for 1 second.

B: Resulting resting $[Ca^{2+}]$ increases with simulation of increase in the ratio of ER to cytosol volume

Simulation of effect on resting $[Ca^{2+}]$ as a result of equilibration of C.H. model with initially fixed $[IP_3]$, cytosol and ER $[Ca^{2+}]$, for four different ratios of ER to cytosol volumes.

C: The peak $[Ca^{2+}]$ of the simulated glutamate evoked event increases with simulation of increase in the ratio of ER to cytosol volume

Simulation of effect on evoked Ca^{2+} event peak $[Ca^{2+}]$ as a result of equilibration of C.H. model with initially fixed $[IP_3]$, cytosol and ER $[Ca^{2+}]$, for four different ratios of ER to cytosol volumes.

D: The amplitude of the simulated glutamate evoked event increases with simulation of increase in the ratio of ER to cytosol volume

Simulation of effect on resting $[Ca^{2+}]$ as a result of equilibration of C.H. model with initially fixed $[IP_3]$, cytosol and ER $[Ca^{2+}]$, for four different ratios of ER to cytosol volumes.

The pre-event resting $[Ca^{2+}]$ (panel B), the event peak $[Ca^{2+}]$ (panel C) and the event amplitude (panel D) were all increased with the increase in V_{ER}/V_C .

DISCUSSION

A. Peak $[Ca^{2+}]$ and amplitude astrocyte Ca^{2+} response to a given DHPG-application are positively correlated to the resting $[Ca^{2+}]$

The experiments discussed in this chapter show a positive correlation between resting $[Ca^{2+}]$ and both the peak $[Ca^{2+}]$ and amplitude of the astrocyte Ca^{2+} response to a given single, local, cell-wide, 200 ms pressure application of 300 μ M group I mGluR agonist, DHPG. This correlation is present when considering all individual DHPG-responsive ROIs or their average values per cell (figures 6.2-3). This suggests that this particular protocol does not lead cells to reach a particular $[Ca^{2+}]$ ceiling level.

Recording larger response peak $[Ca^{2+}]$ at higher resting $[Ca^{2+}]$ could be simply explained by the fact that the peak $[Ca^{2+}]$ reflects total $[Ca^{2+}]$ (the sum of the event amplitude and the resting $[Ca^{2+}]$). Therefore an increase in resting $[Ca^{2+}]$ would lead to an increase in response peak $[Ca^{2+}]$.

As discussed in chapters 1, 4 and the introduction to this chapter, IP_3R2 is thought to mediate group I mGluRs evoked Ca^{2+} events in rodent astrocytes. In turn, cytosolic $[Ca^{2+}]$ is thought to modulate IP_3R2 by enhancing rodent IP_3R2 mediated Ca^{2+} release from the endoplasmic reticulum for resting $[Ca^{2+}]$ of ≈ 10 up to 200 nM. At higher resting $[Ca^{2+}]$, above ≈ 200 nM, IP_3R2 mediated Ca^{2+} release from the endoplasmic reticulum is reduced, resulting in a bell shaped modulation of IP_3R2 mediated Ca^{2+} release from the endoplasmic reticulum by resting $[Ca^{2+}]$ (resting $[Ca^{2+}]$ affects IP_3Rs IP_3 affinity in a bell shaped fashion; see review Foskett et al. 2007). The resting $[Ca^{2+}]$ recorded in this thesis were in the 15 to 190 nM range which could suggest that perhaps in these astrocytes, the cytosolic resting $[Ca^{2+}]$ recorded were not high enough to see a negative impact on IP_3R2 mediated Ca^{2+} release from the endoplasmic reticulum. This could be an explanation for the recording of larger Ca^{2+} responses in response to DHPG pressure application in astrocytes or individual ROIs recorded at higher resting $[Ca^{2+}]$, leading to the positive correlations between resting $[Ca^{2+}]$ and DHPG-evoked Ca^{2+} event peak $[Ca^{2+}]$ or amplitude observed in this chapter (when considering overall response per astrocyte or individual DHPG-responsive ROIs). Indeed, the DHPG-evoked Ca^{2+} response amplitudes recorded in these experiments were positively correlated to resting $[Ca^{2+}]$ only when considering DHPG responsive ROIs (as individual ROIs or the averages across cells). Indeed, when considering all ROIs, a bias may be introduced by ROIs which may be unable to respond to a DHPG-pressure application irrespectively of their resting $[Ca^{2+}]$. These non-responsive ROIs could be due to lack of exposure to the DHPG-pressure application as well as lack of group I mGluRs or internal stores for example. Including these ROIs could mask the potential relationship of DHPG-pressure application Ca^{2+} response with resting $[Ca^{2+}]$.

B. The change in response amplitude is negatively correlated to the change in resting $[Ca^{2+}]$ in individual ROI

To test the role of resting $[Ca^{2+}]$ on this astrocyte Ca^{2+} response to DHPG-pressure application, I used UV uncaging of NPEGTA and Diazo2 to respectively increase and decrease the resting $[Ca^{2+}]$ (as described in chapter 5). I quantified the change in peak $[Ca^{2+}]$ and amplitude within individual ROIs in all cells between the response to a 1st and 2nd DHPG pressure application, respectively before and after maintaining or changing the resting $[Ca^{2+}]$. I found a negative correlation between the change in DHPG-evoked Ca^{2+} response amplitude and the change in resting $[Ca^{2+}]$ in all ROIs in all conditions. Overall there was a positive correlation between the change in peak $[Ca^{2+}]$ response and the change in resting $[Ca^{2+}]$. However, the change in response peak $[Ca^{2+}]$ did not correlate with the change in resting $[Ca^{2+}]$ in cells containing NPEGTA.

i. Individual ROIs

We next considered individual ROIs as opposed to the mean cell-wide changes in response to the pressure application of DHPG. Indeed, individual ROIs may differ in their exposure to DHPG or potential mechanical effect of the pressure application as well as effectiveness in UV photolysis of caged Ca^{2+} or Ca^{2+} buffer. Alongside these possible technical differences, physiological specificities (ratio of ER to cytosol, expression of mGluRs for example) of a given astrocyte subcellular compartment may also be reflected in differences across different ROIs.

Indeed, due in part to the development and broader use of higher resolution Ca^{2+} imaging techniques, recent astrocyte Ca^{2+} signalling studies have focused on the study of local Ca^{2+} events and potential subcellular compartments as opposed to the cell-wide slow general Ca^{2+} elevations in earlier studies. Astrocyte Ca^{2+} events can be confined to small areas of a given astrocyte or expand throughout a process, not necessarily resulting in a cell wide somatic Ca^{2+} event (Di Castro et al. 2011). Local glutamate uncaging was found to evoke such localised Ca^{2+} events in astrocytes yet the ability to respond to this local stimulation varied with the astrocyte process investigated (Panatier et al. 2011). Further studies, using cytosol-soluble genetically encoded Ca^{2+} indicators, contributed evidence to the possibility of regional Ca^{2+} hotspots in astrocytes in acute brain slices (Shigetomi et al. 2013). However, in order to collect sufficient photons for $[Ca^{2+}]$ estimations, the ROIs used in this thesis cover larger areas than the small microdomains where these focal Ca^{2+} events are thought to occur.

In the future, perhaps it could be of interest to use 2-photon excitation to locally photolyse caged-glutamate according to FLIM-determined resting $[Ca^{2+}]$ astrocyte subcompartments in order to refine the contribution of resting $[Ca^{2+}]$ to astrocyte ability to respond to such evoked stimulation.

ii. Possible mechanisms

In order to explain the observed negative correlation between the change in amplitude of the Ca^{2+} response to DHPG-evoked this chapter, we suggested the possibility that the application of DHPG could perhaps be sufficient to generate enough IP_3 for the equilibration of $[\text{Ca}^{2+}]_i$ s across the endoplasmic reticulum and cytosolic volumes of a given ROI. Indeed, a simple simulation based on this assumption qualitatively reflected the observed correlations found between changes in peak $[\text{Ca}^{2+}]_i$ or amplitude of the Ca^{2+} response to DHPG and changes in resting $[\text{Ca}^{2+}]_i$ within a given ROI (figure 6.11).

However, this simple model (contrary to figure 6.15) does not take into account the mechanisms that are thought to regulate cytosolic and endoplasmic reticulum $[\text{Ca}^{2+}]_i$. Indeed $\text{Na}^+/\text{Ca}^{2+}$ exchangers enable Ca^{2+} extrusion into the extracellular space or into mitochondria to prevent cytosolic $[\text{Ca}^{2+}]_i$ increases. The $[\text{Ca}^{2+}]_i$ in the endoplasmic reticulum is replenished through active transport (SERCA pumps) but store operated Ca^{2+} entry is also thought to occur in astrocytes (although the mechanisms are not fully characterised in situ; reviewed in Verkhratsky & Parpura 2014). The kinetics of these mechanisms would have to be further investigated in order to determine if the DHPG evoked IP_3 release is sufficient to suggest equilibration of $[\text{Ca}^{2+}]_i$ across endoplasmic reticulum and cytosol compartments within a given astrocyte ROI.

As discussed in chapter 4, endogenous Ca^{2+} buffers also play a role in Ca^{2+} signalling. Some binding proteins possess multiple binding sites. For example, Calmodulin is thought to have two Ca^{2+} binding sites at different affinities for Ca^{2+} (Faas et al. 2011); S100 proteins are thought to form dimers of α or β subunits which could affect their Ca^{2+} affinity or its modulation (Baudier et al. 1986). In some cases, such as for Ca^{2+} binding protein calretinin which has four different Ca^{2+} binding sites, the rate of binding is non-linear: when one site is bound to Ca^{2+} , the Ca^{2+} binding rate for the other sites increases. Faas et al. 2007 suggested that when cytosolic $[\text{Ca}^{2+}]_i$ increases, the overall Ca^{2+} binding rate of calretinin would increase in a non-linear fashion. These studies are done in neurons. If such a cooperative Ca^{2+} binding mechanism applied to endogenous Ca^{2+} buffers in astrocytes then perhaps this would suggest that at higher resting $[\text{Ca}^{2+}]_i$, there could be enhanced cytosolic Ca^{2+} buffering and thus lower DHPG-evoked Ca^{2+} response amplitudes than at lower resting $[\text{Ca}^{2+}]_i$ ROIs. However, in the case of calretinin this mechanism is thought to occur at changes in resting $[\text{Ca}^{2+}]_i$ from a μM to mM range, whereas in this chapter changes in resting $[\text{Ca}^{2+}]_i$ are smaller and in the nM range. It would be therefore necessary to determine more precisely what the endogenous Ca^{2+} buffers are in these astrocytes and their Ca^{2+} binding kinetics. This difference in range of resting $[\text{Ca}^{2+}]_i$ could also be due to masking the endogenous Ca^{2+} buffering capacity through adding of high affinity buffers or caged compounds as discussed below and in chapter 7.

C. Methodology limitations

i. DHPG pressure application caveats

In order to confirm that the astrocyte Ca^{2+} response to the DHPG pressure application protocol I used was mediated by group I mGluRs, I tested the DHPG-puff Ca^{2+} response that I measured across all ROIs in one cell (Figure 6.1.C) against application of 50 μM group I mGluR antagonists. LY 367 385 (Tocris, 1237) is an mGluR1 antagonist which has an IC_{50} of 8.8 μM . MPEP (Tocris, 1212) is an mGluR5 antagonist, with an IC_{50} of 36 nM. In the presence of 1 μM TTX, I applied 3 DHPG-pressure applications (at 3 minute intervals) to a whole-cell patch clamped astrocyte in situ containing a KMS-only based internal solution and OGB-2. I then added the antagonists in the ACSF perfusing the astrocyte. 10 minutes after bath application of these antagonists, I applied 3 more DHPG-pressure applications. The average of the Ca^{2+} responses to the 3 DHPG-pressure applications before and after mGluR1 and 5 antagonists' application are shown in figure 6.1.C₁. Across the whole astrocyte, I recorded an average 75% decrease in Ca^{2+} response when blocking mGluR1/5. Earlier astrocyte studies have used trans-ACPD ((\pm)-1-Aminocyclopentane-trans-1,3-di carboxylic acid; an agonist of group I and II mGluRs) to induce astrocyte Ca^{2+} elevations and therefore blocked these using a general group I/II mGluR antagonist MCPG (Pasti et al. 1997; Nett et al. 2002). More recently, Tang et al. 2015 applied DHPG and found that this did induce astrocyte Ca^{2+} events in adult mice slice preparations, similar to those triggered by their Schaffer collateral stimulation protocol. They also applied MCPG, in separate experiments, and found that Schaffer collateral evoked astrocyte Ca^{2+} events were reduced in part but not in total, consistently with lack of mGluR5 in these older astrocytes (Sun et al. 2013).

Although I would have to repeat this protocol, this recording, alongside what is suggested in the literature, suggest that the astrocyte Ca^{2+} response to this DHPG-pressure application protocol is mostly due to its agonist activation role of mGluR1/5, in this preparation of young adult rat hippocampal slices.

It is possible that some of the Ca^{2+} response could be due to mechanical activation which also triggers astrocyte Ca^{2+} events (Cornell-bell et al. 1990a; Charles et al. 1991). Although we did not poke the astrocyte with the 'puff' pipette, it was positioned in the vicinity of the astrocyte territory. More physiological approaches have been used to understand evoked Ca^{2+} signalling in astrocytes, specifically in the context of neuronal-astrocytic interactions. Indeed, it could be possible in the future to use FLIM to quantify resting $[\text{Ca}^{2+}]$ and evoked Ca^{2+} events in astrocytes following electrophysiological depolarisation of CA1 neurons or LTP protocols (Henneberger et al., 2010). Alternative evocation of astrocyte Ca^{2+} events without risking mechanical activation has been suggested by using optogenetics to selectively activate calcium permeable channel rhodopsin expressed in nearby CA1 neurons (Bernardinelli et al. 2011).

ii. Caged compounds are Ca²⁺ buffers

UV-uncaging and use of caged-Ca²⁺ buffers could affect the original resting [Ca²⁺] or Ca²⁺ response itself. These additional Ca²⁺ buffers could potentially mask any relationship between resting [Ca²⁺] and DHPG-evoked Ca²⁺ response in astrocytes. In this chapter, this may indeed explain the lack of correlation between change in response peak [Ca²⁺] and change in resting [Ca²⁺] in NPEGTA containing astrocytes (figures 6.5,8). These cells also seem to record lower and perhaps less variable resting [Ca²⁺] than could be possibly recorded in KMS-only cells for example (figures 6.2-3; average \pm SEM cell resting [Ca²⁺] per group is: 59 ± 11 ; 51 ± 8 and 33 ± 3 nM for KMS-only (n=7), Diazo2 (n=11) and NPEGTA (n=8) astrocyte groups respectively. This difference in means is not significant according to a one-way ANOVA $F= 2.7$; $p= 0.09$).

Even in cells with KMS-only internal solution, 200 μ M of OGB-2 (a Ca²⁺ buffer itself) is used in these experiments. Despite the benefits of being indicator concentration independent, FLIM measurements still require enough photons to enable an accurate estimation of the [Ca²⁺] (see chapter 3, figure 3.6). Therefore reducing the concentration of OGB-2 used to lessen the effect of added Ca²⁺ buffer would weaken the estimation of [Ca²⁺] due to lack of photons. Currently, OGB dyes are the principal Ca²⁺ indicators whose fluorescence lifetime is also sensitive to [Ca²⁺] in a suitable range for astrocyte physiology. However these dyes have a lower quantum efficiency than Fluo-4 for example (a given excitation and [Ca²⁺] will generate less photons than Fluo4 dyes for example). This can be remedied by longer acquisitions which are suitable for measuring astrocyte resting [Ca²⁺] but not transient fast Ca²⁺ activity in the hundreds of milliseconds range. The photon count ratio method used in this thesis enables us to reduce the impact of these limitations whilst still providing quantitative estimation of [Ca²⁺].

Previous research has tried to identify the role of Ca²⁺ buffers in impeding or restricting spontaneous Ca²⁺ events in astrocytes. Indeed, using different concentrations of Fluo4-AM (1, 5 and 20 μ M) to artificially increase the astrocyte Ca²⁺ buffering capacity, it was shown that both the frequency and number of astrocytes displaying Ca²⁺ spontaneous activity were reduced (but not the amplitude or the capacity to generate Ca²⁺ events, Parri & Crunelli 2003). Similar findings were shown by direct application of different concentrations of the Ca²⁺ chelator BAPTA, in cultured astrocytes (Z. Wang et al. 1997). These methods are not well suited for quantitative approach to astrocyte [Ca²⁺] (see chapter 3 for intensity versus lifetime comparisons). Bulk loading using (acetyloxy)methyl-ester conjugated indicators (AM dyes) approach leads to no quantitative control over how much dye has been taken up in the cells (calibration issues) or where it could be taken up (cytosolic or inside internal stores). Furthermore, this technique in situ leads to poor spatial resolution in situ (restricted to soma; Reeves et al. 2011). Gaining a better understanding of the endogenous Ca²⁺ buffering capacity of a given astrocyte and the intracellular distribution and diffusion of these Ca²⁺ buffers within astrocyte subcellular compartments would help resolve this issue. In the meantime, perhaps more physiological protocols to alter resting [Ca²⁺] could help clarify its role in predicting the capacity of a given astrocyte sub-cellular compartment to respond to evoked stimulation.

D. Conclusion and remarks/perspectives

Overall, two main observations were described in this chapter 6 with regards to the relationship between pre-event resting $[Ca^{2+}]$ and the peak or amplitude of Ca^{2+} events in response to group I mGluR activation through the pressure application of DHPG. On the one hand, a positive correlation was observed between resting $[Ca^{2+}]$ and the peak or amplitude (weaker correlation) of the evoked Ca^{2+} event when considering recordings across different ROIs (figures 6.2-3). On the other hand, when considering changes of resting $[Ca^{2+}]$ induced within a given individual ROI (figures 6.7-11), a negative correlation was observed between the change in resting $[Ca^{2+}]$ and the change in amplitude of the evoked Ca^{2+} event in that ROI.

This first observation indicates that resting $[Ca^{2+}]$ is heterogeneous between different ROIs which is in line with the observations of a heterogeneous landscape of nM resting $[Ca^{2+}]$ in astroglia recently shown using FLIM of OGB-1 (Zheng et al. 2015). This heterogeneous pre-event resting $[Ca^{2+}]$ is observed to be positively correlated with the Ca^{2+} event peak $[Ca^{2+}]$ or amplitude (also observed for spontaneous Ca^{2+} events recorded in chapter 4) in this chapter 6. This alludes to the possibility that, for a given ROI at high resting $[Ca^{2+}]$, any dependent mechanism (such as metabolism, gliotransmission or vasculature control for example) may be more pronounced in this particular ROI. Thus this observation represents further experimental evidence for the potential specialisation of astrocyte subcompartments (reviewed in Rusakov et al. 2014). In this chapter we suggest, through a modified model of astrocyte signalling (figure 6.15), that a heterogeneous resting $[Ca^{2+}]$ across different ROIs could reflect differences in the relative distribution of ER to cytosol volumes within these ROIs. In the future, we could investigate this hypothesis by staining for the ER in astrocyte ROIs. This might be done either concomitantly with the recording of astrocyte Ca^{2+} signalling through the use of fluorescently labelled thapsigargin for example or as through post-hoc immunocytochemistry (using specific ER-targeted antibodies).

The second observation in this chapter 6 was a negative correlation of resting $[Ca^{2+}]$ and amplitude but not peak. A simple equilibration of the $[Ca^{2+}]$ across the ER and cytosol volumes qualitatively reproduces the correlations observed between the changes in evoked Ca^{2+} event amplitude and the manipulation of resting $[Ca^{2+}]$ within individual ROIs (figure 6.11). The dependence of the Ca^{2+} event amplitude and peak on the resting $[Ca^{2+}]$ concentration suggests that, within a given ROI, the previous history of Ca^{2+} concentrations could influence the amplitude of a Ca^{2+} response in that particular ROI. The physiological consequences of this observation would depend on the Ca^{2+} sensitivity of a downstream Ca^{2+} -dependent mechanisms. For example, Ca^{2+} dependent release from an astrocyte could depend on the Ca^{2+} concentration according to a power law (as is the case in neurons Schneggenburger & Neher 2000). In that case, an increase of the peak $[Ca^{2+}]$ could be more important to the release of transmitter from the astrocyte than the reduced amplitude of the Ca^{2+} event. However, little is known about the quantitative relationship between Ca^{2+} and, for instance, Ca^{2+} dependent release from astrocytes. See chapter 7 for further discussion.

Chapter 7: GENERAL DISCUSSION

The principal focus of this thesis was to investigate if resting $[Ca^{2+}]$ is a strong modulator of astrocyte Ca^{2+} events in situ. I therefore used FLIM of OGB-2 to quantify resting $[Ca^{2+}]$ and Ca^{2+} events (chapter 3) in whole-cell patched astrocytes in situ (chapter 2). I found that low resting $[Ca^{2+}]$ were associated with smaller amplitudes of both spontaneous and evoked astrocyte Ca^{2+} events when considering recordings across all cells (chapters 4 and 6). I next used UV-photolysis to increase or decrease resting $[Ca^{2+}]$ (chapter 5) and quantified the changes in the amplitude of glutamate metabotropic receptor agonist DHPG-pressure application evoked Ca^{2+} events (chapter 6). I found that within individual regions of interest, an increase in resting $[Ca^{2+}]$ was associated with lower amplitude of the evoked Ca^{2+} event.

These experiments and results are summarised and discussed in this chapter. I will also present how the resting $[Ca^{2+}]$ and Ca^{2+} events recorded in this thesis relate to previously published values and finally, I will discuss, through the example of Ca^{2+} dependent exocytosis, what could be the physiological impact of modulating Ca^{2+} event amplitude for Ca^{2+} dependent gliotransmission.

During my PhD, I also contributed to a project on the pre-synaptic active zone scaffolding protein Bassoon. As this is a different project, this work constitutes an annex to this thesis and is therefore not included as a main chapter. Our results suggest that the interaction of Bassoon and RIM-binding protein contribute to selectively anchor and position voltage-gated Ca^{2+} channel subtype 2.1 to the presynaptic active zone for synaptic transmission, as measured through extracellular field recordings of excitatory post synaptic potentials, at the CA3 Schaffer collateral to CA1 pyramidal neuron synapse in acute hippocampal slices. These experiments and results are presented and discussed in the attached annex.

Summary

A. Higher pre-event resting $[Ca^{2+}]$ may be associated with larger amplitudes of Ca^{2+} events.

I next investigated the potential relationship between the resting $[Ca^{2+}]$ and both the evoked and endogenous Ca^{2+} activity in these astrocytes. I found that the amplitudes of spontaneous Ca^{2+} transients positively correlate with the $[Ca^{2+}]$ immediately before the Ca^{2+} event (chapter 4). This was also the case for DHPG-evoked Ca^{2+} events when different cells or regions of interest of the same cell were compared (chapter 6). The well-established increase of IP_3R open probability with increased cytosolic $[Ca^{2+}]$, at least within the 10 to 200 nM $[Ca^{2+}]$ for IP_3R2 which is thought to be expressed in rodent astrocytes in situ (Foskett et al. 2007), can explain this observation.

These receptors are thought to play an important role in generating Ca^{2+} release from the endoplasmic reticulum for the integration of neuronal activity by astrocyte Ca^{2+} signalling. Therefore astrocytes, or individual astrocytic subcompartments, with higher resting $[\text{Ca}^{2+}]$ (within a 10-200 nM range) could enhance astrocyte Ca^{2+} signalling through larger Ca^{2+} event peak $[\text{Ca}^{2+}]$ and amplitudes as Ca^{2+} release by endoplasmic reticulum is increased for these resting $[\text{Ca}^{2+}]$. Additionally, simulations of glutamate-evoked Ca^{2+} response in an astrocyte model designed by Dr C. Henneberger based on Ullah et al. 2006, suggest that these positive correlations between Ca^{2+} event amplitude and resting $[\text{Ca}^{2+}]$ could also be explained by increases in the volume occupied by endoplasmic reticulum in relation to cytosol (simulation in chapter 6). However there are limitations to these observed correlations as other factors (such as endogenous buffering capacity or technical differences in UV or DHPG exposure for example) may also affect the Ca^{2+} event amplitudes in individual ROIs. To test this relationship between resting $[\text{Ca}^{2+}]$ and Ca^{2+} event amplitude we artificially manipulated the resting $[\text{Ca}^{2+}]$ as described below.

B. Within a ROI, increasing resting $[\text{Ca}^{2+}]$ decreases the amplitude of evoked Ca^{2+} events.

We next used cell-wide UV-photolysis of either caged EGTA/ Ca^{2+} or, in separate experiments, Diazo-2, loaded into the astrocyte to respectively increase or decrease the resting $[\text{Ca}^{2+}]$ in order to test its relationship with DHPG-evoked Ca^{2+} events. We quantified the changes in $[\text{Ca}^{2+}]$ within given astrocyte ROIs in order to control for technical or cellular characteristics, other than resting $[\text{Ca}^{2+}]$ changes, that may also impact DHPG-evoked Ca^{2+} event such as a given region's exposure to DHPG or its expression levels of mGluRs for example.

In contrast to the previously described positive association between resting $[\text{Ca}^{2+}]$ and spontaneous or DHPG-evoked Ca^{2+} events across all astrocytes recorded, UV-photolysis mediated increases in resting $[\text{Ca}^{2+}]$ within a single astrocyte region were associated with lower amplitudes of DHPG-evoked Ca^{2+} transients (chapter 6). DHPG-induced equilibration of cytosol and store $[\text{Ca}^{2+}]$ could be a potential qualitative explanation for this effect (simulation in chapter 6; figure 6.11) although further investigation taking into account Ca^{2+} extrusion and replenishment mechanisms in order to test if this equilibration could occur endogenously.

Resting $[Ca^{2+}]$ variability in astrocytes

Having established a potential relationship between resting $[Ca^{2+}]$ and spontaneous or DHPG-evoked astrocyte Ca^{2+} events, I will discuss here how to put the astrocyte resting $[Ca^{2+}]$ estimated in this thesis into physiological perspective. Here I will describe what are the resting $[Ca^{2+}]$ recorded in the astrocytes in this thesis and how they relate to previously reported estimations of astrocyte resting $[Ca^{2+}]$. This should help evaluate how physiologically relevant the astrocyte resting $[Ca^{2+}]$ estimations in this thesis could be as well as possible previous reports of physiological changes in resting $[Ca^{2+}]$.

A. Astrocyte resting $[Ca^{2+}]$ recorded in this thesis

I will first describe the resting $[Ca^{2+}]$ estimated in my hands using OGB-2 FLIM in whole-cell patch clamped astrocytes in situ in relation to similar recordings I performed in gap-junction coupled cells as well as OGB-1 FLIM of astrocytes in-vivo preparations.

i. Resting $[Ca^{2+}]$ in whole-cell patch clamped astrocytes

The average resting $[Ca^{2+}]$ was 58 nM with a standard deviation of 28 nM and standard error to the mean of 11 nM. This is the mean resting $[Ca^{2+}]$ recorded across 7 different astrocytes (7 different acute slices from 5 different animals) loaded with 200 μ M OGB-2 KMS internal solution only (chapters 2-3). The minimum mean resting $[Ca^{2+}]$ recorded was 28 nM whereas the maximum mean resting $[Ca^{2+}]$ recorded was 100 nM.

Within a given cell, the standard deviation of the average resting $[Ca^{2+}]$ recorded across individual ROIs seemed to be related to the average resting $[Ca^{2+}]$ of the given cell. Indeed, the 4 cells recorded with total average resting $[Ca^{2+}]$ of 28-50 nM, had standard deviations of 9 to 15 nM across the ROIs within each cell. The standard deviations was of 30-38 nM across individual ROI within each of the 3 cells recorded with total average resting $[Ca^{2+}]$ of 75-100 nM. Although this is a small sample, it is in line with OGB-1 FLIM recordings by Zheng et al. 2015 suggesting the possibility of resting $[Ca^{2+}]$ heterogeneity across different astrocytes. Indeed, Zheng et al. 2015 suggest two groups of astrocytes based on their overall average resting $[Ca^{2+}]$ recorded in situ and in vivo. In their recordings in situ, astrocytes had resting $[Ca^{2+}]$ either below 80-90 nM or above this range.

ii. Resting $[Ca^{2+}]$ in gap-junction coupled astrocytes

Whole-cell patch clamp by definition changes the internal solution composition of the cell under investigation though both mechanical stimulation with the patch pipette (for example mechanical stimulation of astrocytes creates Ca^{2+} events Cornell-Bell et al. 1990a) and dialysis of the internal molecular composition of the cell with the artificial solution provided through the patch pipette (Christoffersen & Skibsted 1975). Estimating the resting $[Ca^{2+}]$ in gap-junction coupled astrocytes could indicate resting $[Ca^{2+}]$ without some of these potential effects of patch-clamp

technique. Indeed astrocytes are thought to form gap-junctions between neighbouring astrocytes which are permeable to small molecules (Giaume et al. 1991; Giaume & McCarthy 1996). Although OGB dyes have a large molecular weight (≈ 1500 kDa), they are permeable to gap-junctions. Given enough time, the OGB dyes can diffuse from a whole-cell patch clamped astrocyte into neighbouring gap-junction coupled astrocytes.

One of the main advantages of FLIM is that the lifetime acquisition is independent of the indicator concentration in the area of interest (see chapter 3). Therefore even with little OGB concentrations, providing there is enough dye to generate sufficient photons, it is possible to gain quantitative insight into the resting $[Ca^{2+}]$ of these neighbouring astrocytes. This may give indications of astrocyte resting $[Ca^{2+}]$ without some of the patch-clamp related potential disruptions.

In this thesis I recorded the somatic resting $[Ca^{2+}]$ and the resting $[Ca^{2+}]$ in the main large process of gap-junction coupled astrocytes. These were recorded approximately one hour after whole cell patch clamp configuration of the patched astrocyte. At this point, enough OGB-2 had reached nearby astrocytes in order to generate sufficient photons for FLIM recordings. I recorded similar continuous timelapse recordings as were done in chapter 4. These astrocytes were within 20-50 μ m away from the patched astrocyte as astrocytes close to the patched astrocyte would be the first neighbouring astrocytes to be more likely to load with OGB-2. I recorded from 5 of these coupled astrocytes in 2 different slices from 2 different animals on two different experimental days. In order to maintain similar number of photons per ROI as when estimating $[Ca^{2+}]$ from the patched cell, I had to bin 6 frames together due to the very few photons in these gap-junction coupled cells. I found that the average resting $[Ca^{2+}]$ (mean \pm SEM, 5 cells, 2-3 ROI per cell, 2 animals) in these cells was 48 ± 5.4 nM. The average somatic resting $[Ca^{2+}]$ was 34 ± 4.8 nM whereas the average resting $[Ca^{2+}]$ in the large main process was 64.7 ± 5.4 nM. These resting $[Ca^{2+}]$ values seem to be similar to those recorded in whole cell patch clamped astrocytes. The two patched astrocytes from the two slices where these gap-junction astrocytes were recorded had estimated somatic $[Ca^{2+}]$ of ≈ 25 nM and in large main processes $[Ca^{2+}]$ were $\approx 35 - 60$ nM. The $[Ca^{2+}]$ gradient in these OGB-2 FLIM recorded examples in my hands seem to be similar (processes at higher $[Ca^{2+}]$ than soma $[Ca^{2+}]$) in the whole-cell patched astrocyte and the neighbouring gap-junction coupled astrocytes where there may be less disruption (from patch pipette etc). However, OGB-2 is a large molecule (1600 Da) and thus doesn't diffuse very far across the network of gap-junction coupled astrocytes (at least in sufficient quantities for FLIM and thus $[Ca^{2+}]$ estimations). Using FLIM of OGB-1 (1114 Da), Zheng et al. 2015, were able to estimate $[Ca^{2+}]$ in more and a little further away gap-junction coupled astrocytes were they also found that somatic $[Ca^{2+}]$ were lower than in the astrocyte large processes.

Taken together, these examples would contribute to validate the resting $[Ca^{2+}]$ estimations in the whole-cell patched astrocytes used in this thesis.

iii. Resting $[Ca^{2+}]$ in astrocytes in vivo

During my thesis, I also contributed, alongside Drs K. Zheng and J. Reynolds, to the design of experiments to record astrocyte and neuronal resting $[Ca^{2+}]$ in vivo using FLIM recordings of OGB1-AM bulk loaded cells (Zheng et al. 2015). Dr J. Reynolds performed the surgery and in vivo acute bulk loading of OGB1-AM into neurons and astrocytes in the somatosensory cortex of urethane-anaesthetised p25-30 male rats; whereas Dr K. Zheng carried out most FLIM recordings and analysis. I wanted to use this opportunity to preliminary investigate the relationship between spontaneous Ca^{2+} activity and resting $[Ca^{2+}]$ in these in-vivo models.

I recorded OGB-1 FLIM (using similar recording setup as described in chapter 3: MaiTai 800nm 2-photon excitation, PicoQuant TCSPC system and Olympus FV10000 adapted for in-vivo preparation) of 5 minutes continuous frame scans of 3 astrocytes in two different animals of this in-vivo preparation. The respective average resting $[Ca^{2+}]$ overall ROI recorded in each of these cells was of 60, 85 and 55 nM respectively. These were similar to the average resting $[Ca^{2+}]$ recorded in vivo by Dr K. Zheng (Zheng et al. 2015). Despite being acquired from astrocytes in a different model, different brain structure, using different lifetime analysis and acquisition techniques, these values of astrocyte average resting $[Ca^{2+}]$ are similar to those recorded with OGB-2 FLIM in KMS-only whole-cell patched astrocytes in acute hippocampal slices in this thesis (as described above).

Overall, the average resting $[Ca^{2+}]$ we recorded in gap-junction coupled astrocytes or in-vivo are similar to those recorded in whole-cell patch clamped astrocytes. This contributes to validate the whole-cell patch clamp method used in this thesis to record and estimate overall astrocyte resting $[Ca^{2+}]$ as a reasonable approach to understand resting $[Ca^{2+}]$ in astrocyte physiology.

B. Previously reported astrocyte resting $[Ca^{2+}]$

i. Reported astrocyte resting $[Ca^{2+}]$

Earlier studies used ratiometric fluorescence intensity measurements of the Ca^{2+} indicator fura-2 to quantify the resting $[Ca^{2+}]$ in cortical astrocyte cultures from embryonic (Grimaldi et al. 2001) or P 1 - 2 (Floyd et al. 2005) rat pups. These studies reported resting $[Ca^{2+}]$ of less than 100 nM (≈ 60 nM, but not very clear). Another study, in hippocampal astrocyte cultures from P1-2 rats, used both a ratiometric fura-2 based calibration and a bulk loading of Fluo-3-AM fluorescence intensity with added Ca^{2+} ionophore based calibration (similar to what is described in chapter 3 for the Ca^{2+} indicator Fluo-4 and the Ca^{2+} ionophore Ionomycin), to estimate resting $[Ca^{2+}]$ in these cells at 87 nM on average (Parpura & Haydon 2000). Once again, using different quantification methods and a different model, these estimated astrocyte resting $[Ca^{2+}]$ are within the same range (20-100 nM) although higher on average (≈ 80 nM as opposed to ≈ 60 nM) to those described in this thesis (see above).

These studies were done in astrocytes that are very different morphologically (more 2-dimensional) from astrocytes in situ or in vivo, prepared at younger developmental stage than the astrocytes recorded in this thesis, developed and prepared with less preservation of the local environment and interactions as in situ or in vivo. These studies would suggest that astrocytes may maintain resting $[Ca^{2+}]$ within the range of $[Ca^{2+}]$ recorded here (20-100 nM) regardless of these parameters. However more recently, also using Fura-2, Shigetomi et al. 2008 find resting $[Ca^{2+}]$ in the 50 nM range when considering astrocytes in situ (stratum radiatum of hippocampal slices) whereas in co-cultured astrocytes Shigetomi et al. 2012 report $[Ca^{2+}]$ in the 100 nM range.

In vivo, a study used FLIM of OGB1 in cortical astrocytes from 3month old mice and quantified their resting $[Ca^{2+}]$ at 81 ± 3 nM (Kuchibhotla et al. 2009). Although in vivo studies preserve the structure and interactions of these astrocytes, it is vital to be able to monitor the animal's physiological well-being (which could be less immediately discernible if an animal is under anaesthesia and artificially ventilated and can be overcome through regular monitoring of blood sample oxygenation for example). Indeed, a repeated 5 minute timelapse recording of OGB1 (repeated exposure to 2-photon laser) in a single astrocyte raised the resting $[Ca^{2+}]$ by an average of ≈ 15 nM (from ≈ 80 to ≈ 100 nM) in one case of the cells I recorded using OGB-1 FLIM as described above. Resting $[Ca^{2+}]$ measured in more accessible and better dye-loaded cells (less deep in the tissue, close to injection sites) may also be more susceptible to damage from craniotomy as well as photodamage (Kuga et al. 2011; Wang et al. 2006).

It may be more relevant in the future to quantify astrocyte $[Ca^{2+}]$ in freely moving in vivo animal models for perhaps more qualitative physiological insight into the astrocyte resting $[Ca^{2+}]$ recorded. Indeed, Thrane et al. 2012 found that regularly used anaesthetics (ketamine, isoflurane and urethane) to sedate animals during in vivo recordings from anaesthetised animals, depressed spontaneous and (agonists or whisker stimulation) evoked Ca^{2+} events in cortical astrocytes in awake mice. These Ca^{2+} events were reduced 10-fold in overall frequency and ≈ 30 % reduction in average Ca^{2+} event amplitude following anaesthetic application and generally reversible after anaesthetic removal. These astrocyte Ca^{2+} events were also found to rely on IP_3R2 . If our reports of a relationship between astrocyte resting $[Ca^{2+}]$ and event peak $[Ca^{2+}]$ are true, then these differences in Ca^{2+} event amplitude could suggest that resting $[Ca^{2+}]$ may also be different in these awake animal models.

ii. Physiological changes in astrocyte resting $[Ca^{2+}]$

As with other cell-types, cell damage or unhealthy tissue are commonly associated with increased resting $[Ca^{2+}]$ in astrocytes. Indeed, astrocyte average resting $[Ca^{2+}]$ was reported to increase from less than 100 nM to 500 nM or up to 1500 nM, after and as a function of the severity of mechanical stretch injury (Rzagalinski et al. 1998). Once again, this early study used the ratiometric indicator fura-2 in cultured rat astrocytes. This model may therefore not well reflect likely pathophysiological conditions.

Perhaps a more plausible reflection of the impact of pathology on astrocyte resting $[Ca^{2+}]$ was found in cortical astrocytes from an in-vivo rodent model of Alzheimer's disease using FLIM of OGB-1 bulk loaded cells. Indeed, mutant mice expressing the human precursor to β -amyloid in neurons (APP/PS1) develop increased β -amyloid production leading to plaques.

The astrocyte resting $[Ca^{2+}]$ was recorded as 149 ± 6 nM in these mice models of Alzheimer's disease whereas it was only 81 ± 3 nM in wild-type mice (Kuchibhotla et al. 2009).

Outside of disease models, it has also been suggested that the resting $[Ca^{2+}]$ rises slightly (as recorded by an increase in relative Fluo4 fluorescence intensity), immediately preceding the occurrence of an astrocyte Ca^{2+} event (Parri & Crunelli 2003).

Within a given astrocyte, the subcellular composition may give rise to local compartments of different resting $[Ca^{2+}]$. As suggested by simulations (figure 6.15), the relative distribution of endoplasmic reticulum within a given astrocyte compartment could be positively correlated with the resting $[Ca^{2+}]$ in that particular ROI. ER is suggested to be absent from the nanoscopic perisynaptic astrocyte processes due to spatial constraints (Patrushev et al. 2013). Mitochondria also play an important role in compartmentalising astrocyte Ca^{2+} (Boitier et al. 1999). The distribution of these internal Ca^{2+} stores, possibly reflected by astrocyte morphology, may explain the variability of the resting $[Ca^{2+}]$ recorded across different ROI within a given astrocyte as suggested at the beginning of this chapter and described by heterogeneous recordings of OGB-1 FLIM within astrocytes compartments (Zheng et al. 2015) or using genetically encoded indicators (Shigetomi et al. 2013).

Physiological relevance of the observed evoked or spontaneous astrocyte Ca^{2+} event amplitudes

A. Comparing changes in $[Ca^{2+}]$ and changes in Ca^{2+} indicator fluorescence intensity (F/F_0)

One of the issues across the field of astrocyte Ca^{2+} signalling investigations could be a lack of coherence across the methods used to acquire, evoke and evaluate these astrocytic Ca^{2+} events. In order to compare the recorded $[Ca^{2+}]$ of events in this thesis with Ca^{2+} events recorded using Fluo-4 fluorescence intensity, we estimated the equivalent F/F_0 fluorescence intensity ratios (event fluorescence/resting fluorescence) for the estimated $[Ca^{2+}]$ recorded here.

i. Estimation of 'Fluo-4 equivalent F/F_0 ' from OGB-2 FLIM $[Ca^{2+}]$

The fluorescence intensity of a Ca^{2+} indicator F is equal to the Ca^{2+} bound indicator concentration $[BCa^{2+}]$ times an unknown factor a , such as: $F = a [BCa^{2+}]$. Using the dissociation equation for a given indicator: $K_d = [Ca^{2+}][B] / [BCa^{2+}]$ where $[Ca^{2+}]$ and $[B]$ represent the concentrations of unbound (free) c and Ca^{2+} indicator, respectively. Finally, the total indicator concentration $[B]_{TOTAL}$ is the sum of bound indicator and free indicator: $[B]_{TOTAL} = [BCa^{2+}] + [B]$.

This enables to extract the unknown $[BCa^{2+}]$ and replace it with values that can be experimentally quantified: $[BCa^{2+}] = [B]_{TOTAL} * [Ca^{2+}] / K_d + [Ca^{2+}]$.

Using this equation for both F and F_0 , we can estimate F/F_0 as: $F/F_0 = [Ca^{2+}] * (K_d + [Ca^{2+}]_0) / (K_d + [Ca^{2+}]) * [Ca^{2+}]_0$ where values are the Ca^{2+} estimations for a given Ca^{2+} event unless indicated by $_0$ which refers to values for resting pre-event Ca^{2+} values.

Using this approach, we calculated the estimated equivalent F/F_0 for Fluo-4 (K_d 345nM) for the mean DHPG response peak $[Ca^{2+}]$ and pre-event resting $[Ca^{2+}]$ quantified for each cell in chapter 6. On average, these mean evoked events $[Ca^{2+}]$ could be estimated as an "equivalent Fluo4 F/F_0 " of 1.7 ± 0.06 (mean \pm SEM, 26 cells). Similarly, the average DHPG-evoked Ca^{2+} event amplitude in these astrocytes was estimated as a mean $86 \% \pm 0.07$ increase ($\Delta F/F_0 = [(F-F_0) / F_0] * 100$).

ii. Comparison with previously reported Fluo-4 $\Delta F/F_0$ recordings of astrocyte Ca^{2+} events

On average, Fluo-4 fluorescence intensity recorded astrocyte Ca^{2+} events in situ and in vivo have been reported to be of similar amplitude to this estimation of average $\Delta F/F_0$ for the DHPG-evoked Ca^{2+} events in this thesis.

Spontaneous Ca^{2+} events recorded with Fluo-4 in astrocytes in situ (acute slice preparations) have been on average Fluo-4 $\Delta F/F_0$ of 80 - 114 % (Parri & Crunelli 2003; Panatier et al. 2011; Shigetomi et al. 2013).

In situ, localised focal spontaneous astrocyte Ca^{2+} events were shown to be of 3-fold lower amplitude to larger expanded spontaneous Ca^{2+} events (Di Castro et al. 2011) suggesting that differences in amplitude recorded in Fluo-4 $\Delta F/F_0$ could also be due to differences in types of Ca^{2+} events. Indeed Ca^{2+} events in astrocyte processes in hippocampus slices were recorded as on average Fluo-4 $\Delta F/F_0$ of 92 or 82 % (respectively in Panatier et al. 2011; Shigetomi et al. 2013) whereas in the same astrocytes, somatic Ca^{2+} events were on average Fluo-4 $\Delta F/F_0$ of 110 % (Fluo4 AM hippocampus slices (Shigetomi et al. 2013)). The Ca^{2+} events recorded in this thesis occurred perhaps more in astrocyte processes than larger somatic events (as suggested for the spontaneous Ca^{2+} events recorded in chapter 4, where no Ca^{2+} events were recorded in the soma).

However, evoked Ca^{2+} events may be reported as slightly higher amplitude on average Fluo-4 $\Delta F/F_0 \approx 100 - 160 \%$ (Wang et al. 2006; Panatier et al. 2011) possibly due to differences in stimulation protocols. For example on average, whisker stimulation triggers Ca^{2+} events of $\Delta F/F_0$ $100 \pm 20 \%$ in barrel cortex astrocytes in-vivo whereas local mGluR agonist tACPD iontophoresis application trigger $\Delta F/F_0$ $142 \pm 11 \%$ in similar astrocytes (Wang et al. 2006). In situ, single pulse stimulation of presynaptic neuronal elements designed to mimic basal neuronal activity trigger Ca^{2+} events of on average $\Delta F/F_0$ $128 \pm 20 \%$ in hippocampal astrocytes (Panatier et al. 2011).

There are also limitations to these comparisons across studies as even if using the same indicator (such as Fluo-4 in these examples), the estimations could differ in the way the amplitude of a Ca^{2+} event is recorded: background correction or not, event amplitude relative to noise for example. The properties of the Ca^{2+} indicator used are likely to play important role on the properties of the Ca^{2+} events detected (reviewed in Volterra et al. 2014). For example, in acute hippocampal slices Fluo-4-AM bulk loaded astrocytes displayed Ca^{2+} events of 25 % lower amplitude than Ca^{2+} events recorded in astrocytes expressing genetically encoded Ca^{2+} indicator (Shigetomi et al. 2013).

As the Ca^{2+} events recorded in this thesis are comparable to some extent to previously reported astrocyte Ca^{2+} events, we will next discuss the potential physiological role of these astrocyte Ca^{2+} events as well as the limitations of the estimation of these Ca^{2+} events.

B. Possible consequences of increased astrocyte event peak $[\text{Ca}^{2+}]$ through the example of astrocyte Ca^{2+} dependent vesicular release

In chapters 4 and 6, we found that both endogenous and evoked Ca^{2+} event peak $[\text{Ca}^{2+}]$ and amplitudes were larger in ROI with higher resting $[\text{Ca}^{2+}]$. Increasing the $[\text{Ca}^{2+}]$ of the Ca^{2+} event may imply reaching thresholds or increasing Ca^{2+} -dependent vesicular release. Thus resting $[\text{Ca}^{2+}]$ could affect the likelihood and extent of neuro-active compounds release, such as glutamate or D-serine, which is thought to be one aspect of Ca^{2+} -dependent gliotransmission.

i. Ca^{2+} dependent exocytosis in neurons

In neurons, an action potential at the nerve terminal will trigger the release of a localised transient Ca^{2+} increase at the presynaptic active zone which in turn induces synaptic vesicle exocytosis. This enables fast Ca^{2+} dependent release of neuronal transmitters into the synaptic cleft which initiate synaptic transmission through binding onto postsynaptic receptors. The Ca^{2+} dependence of this mechanism was originally determined by Katz & Miledi 1967. Spontaneous exocytosis in neurons may also be Ca^{2+} dependent (Xu et al. 2009).

This Ca^{2+} regulation of vesicle release implies Ca^{2+} sensors at the presynaptic active zone. Synaptotagmins are membrane trafficking proteins that can be found in synaptic vesicles or in plasma membrane of presynaptic nerve terminals. They are thought to play a key role as Ca^{2+} sensors for Ca^{2+} dependent vesicular release (reviewed in Südhof 2012b). Different Synaptotagmins (1 to 15 subtypes, not all Ca^{2+} dependent) may have different sensitivity to Ca^{2+} due to differences in atomic structure of the Ca^{2+} binding domain (Poser et al. 1997; Dai et al. 2004). Therefore identifying the Ca^{2+} sensor (such as synaptotagmin subtype) to identify its respective Ca^{2+} affinity and specific location within the presynaptic active zone could help understand the quantitative role of Ca^{2+} for Ca^{2+} dependent vesicular release.

Giant synapse models such as the squid giant axon or the calyx of held in rodents allow for more detailed quantitative investigation of the local $[Ca^{2+}]$ trigger at the presynaptic active zone. Indeed, in these synapses it has been thought that local $[Ca^{2+}]$ should reach larger than 100 μM to initiate vesicular release (Augustine et al. 1991). Since then, further studies have tried to refine the quantitative role of Ca^{2+} at the active zone. In particular, models taking into account fixed endogenous buffers or diffusible buffers (such as ATP) suggest that increases in local buffering capacity will negatively impact Ca^{2+} -dependent vesicular release. More specifically, the Ca^{2+} affinity and diffusion capacity of buffers are key to determining the $[Ca^{2+}]$ at the active zone (Adler et al. 1991; reviewed in Meinrenken et al. 2003).

These studies suggest that the specific structures such as Ca^{2+} sensor subtype and the local endogenous Ca^{2+} buffers (and how well these may be reflected by the experimental techniques used) are key to determining the quantitative role of Ca^{2+} in vesicular release.

ii. Ca^{2+} dependent exocytosis in astrocytes

- astrocytes exhibit functional Ca^{2+} dependent exocytosis

Astrocytes have been found to show functional components for vesicular Ca^{2+} dependent exocytosis. Indeed immunogold cytochemistry on ultrathin adult rat hippocampal slices for electron microscopy has revealed D-serine or glutamate containing vesicles in astrocyte processes (Bergersen et al. 2012; Bezzi et al. 2004). Astrocytes have also been shown to express synaptotagmins and has been suggested that synaptotagmin 4 is critical for glutamate release of glutamate by astrocytes (Zhang et al. 2004). These studies give structural evidence to support Ca^{2+} dependent vesicular release as a mediator of gliotransmission (Kreft et al. 2004). Indeed both Ca^{2+} dependent release of glutamate (Marchaland et al. 2008) and D-serine (Henneberger et al. 2010) by astrocytes are thought to play a role in synaptic plasticity.

Furthermore, astrocyte vesicular release of ATP and D-serine was directly recorded using extracellular biosensors in acute neocortical slices and largely decreased in astrocytes of disrupted vesicular release (astrocyte specific dn-SNARE animals; Rasooli-Nejad et al. 2014). Using neuronal 'sniffer patches' as indicators of neuronal (Lalo) as well as LTP protocols in slices, Rassoli et al. contribute to further evidence for astrocyte vesicular released compounds (specifically ATP) could be sensed by neurons (through P2X receptors) and affect synaptic plasticity.

- astrocytes, relative to neurons, may require lower $[Ca^{2+}]$ for Ca^{2+} dependent exocytosis

In addition, astrocytes have been shown to express the molecular components that underlie vesicular exocytosis. Indeed, astrocytes in culture were found to express the components for vesicle docking prior to exocytosis such as the SNARE proteins: synaptobrevin, syntaxin and cellubrevin (Parpura et al. 1995) as well as an astrocyte equivalent of the neuronal SNAP25, SNAP 23 (Hepp et al. 1999). These components were shown to be functional as fluorescent tagged vesicle associated glutamate transporter allowed for dynamic imaging of vesicle exocytosis following metabotropic activation of astrocytes in culture (Bezzi et al. 2004).

Interestingly, the suggestion that SNAP23 is the main SNAP isoform expressed in astrocytes, both in culture (Hepp et al. 1999) and in situ (Schubert et al. 2011), could provide a possible molecular basis for low $[Ca^{2+}]$ mediated vesicular release. Indeed, the expression of SNAP25, in specific neurons endogenously lacking this isoform, lowers the Ca^{2+} responsiveness in these cells whereas the expression of SNAP23 does not affect it (Verderio et al. 2004). In PC12 cells, it was suggested that one of the molecular differences between these two SNAP isoforms could be that they do not bind to the same subtypes of synaptotagmins. Indeed, (Chieriegatti et al. 2004) find that SNAP23 binds with synaptotagmin 7 (a high affinity Ca^{2+} sensor) in these cells whereas in neurons, SNAP25 is thought to bind to synaptotagmin 1 (a lower affinity Ca^{2+} sensor; see previous section on exocytosis in neurons). As astrocytes also predominantly express SNAP23, perhaps this specific molecular interaction with high affinity Ca^{2+} sensors could also be found in astrocytes as speculated by Schubert et al. 2011 (in their discussion). This could provide a possible mechanism by which only submicromolar $[Ca^{2+}]$ would be required for the docking/fusion of vesicles in astrocytes, consistent with nanomolar $[Ca^{2+}]$ recorded in this thesis and previously published.

Indeed in functional terms, in astrocyte and neuronal rat co-cultures, increases in Fluo-3 $\Delta F/F_0$ of $196 \pm 33\%$ (triggered by UV uncaging of NPEGTA-AM) were sufficient to induce substantial glutamatergic slow inward currents in neighbouring neurons (Parpura & Haydon 2000). As previously described, this study attempted to quantify this change in $[Ca^{2+}]$ (both through intensity measures of saturating $[Ca^{2+}]$ and ratiometric dye fura-2). They found that evoked increases in cultured astrocytic $[Ca^{2+}]$ from 84 to 140nM were sufficient to generate these currents in neighbouring co-cultured neurons.

These Ca^{2+} increases are similar to those recorded for the Ca^{2+} events in the astrocytes or astrocyte ROI of higher pre-event resting $[Ca^{2+}]$ in hippocampal slices in chapters 4 and 6 of this thesis. This could suggest that the Ca^{2+} events recorded in this thesis for ROIs of higher pre-event resting $[Ca^{2+}]$ may be of enough magnitude of Ca^{2+} to potentially lead to gliotransmission possibly through Ca^{2+} dependent exocytosis. If peak Ca^{2+} event $[Ca^{2+}]$ are positively associated with higher resting $[Ca^{2+}]$ as suggested in this thesis, perhaps local areas of different resting $[Ca^{2+}]$ could similarly indicate the likelihood of sufficient $[Ca^{2+}]$ to trigger Ca^{2+} dependent gliotransmission for example.

iii. Other astrocyte Ca^{2+} dependent impacts

As suggested in Hamilton & Attwell 2010, there are many mechanisms other than exocytosis by which astrocyte Ca^{2+} may impact neuronal activity. However, although also Ca^{2+} dependent, it is not as clear how different Ca^{2+} sensitivity may affect these pathways. Shigetomi et al. 2012 have suggested a mechanism where lower $[Ca^{2+}]$ (both through inhibition of TRAP1 channels or application of 13 mM BAPTA) reduces the astrocyte membrane expression of GABA transporter GAT-3.

This in turn, increases the [GABA] in the extracellular space (as less GABA can be taken up by astrocytes). At these extracellular higher GABA concentrations, there could be an increase in sensitisation of high affinity GABA_A receptors on interneurons. This is how they suggest that an astrocyte resting [Ca²⁺] dependent decrease in astrocytic GABA uptake leads to the observation of a reduced inhibitory postsynaptic current amplitude in interneurons. However, increased astrocyte [Ca²⁺] (suggesting increase in membrane GAT-3 expression) did not affect the amplitude of these inhibitory post synaptic currents. Although it may not be the case in this study, this still suggests another means by which differences in astrocyte [Ca²⁺] might contribute to the cell's local ability to alter the expression of channels or transporters at their plasma membrane.

Additionally, astrocyte Ca²⁺ signalling is implicated in the regulation of local vasculature tone (Otsu et al. 2015; Dunn et al. 2013). Using Fluo-4 saturation after application of the Ca²⁺ ionophore Ionomycin (see chapter 3) to estimate [Ca²⁺], Dunn et al. 2013 suggest that the astrocyte Ca²⁺ events in processes surrounding blood vessels (endfeet) reach ≈ 150 nM in order to generate 11 % vasodilation. They hypothesise that higher [Ca²⁺] are required for vasoconstriction. Perhaps the resting [Ca²⁺] level in these specific astrocyte compartments could determine the vasculature tone through contributing to set astrocyte Ca²⁺ events amplitude in these astrocyte endfeet.

C. Discrepancy in quantitative [Ca²⁺] recorded in astrocytes and neurons for Ca²⁺ dependent vesicular release.

The order of magnitude of event [Ca²⁺] recorded here are much lower (nM) than those suggested for fast neurotransmitter release in neurons where high [Ca²⁺] (μM range; 100μM in giant squid, Augustine et al. 1991) micro or nano-domains are thought to lead to Ca²⁺ dependent vesicle release (reviewed in Schneggenburger & Neher 2005).

i. Limitations of the estimation of [Ca²⁺] in this thesis

As with the recordings in this thesis, these quantitative nM [Ca²⁺] measurements need to be interpreted with caution. Indeed, adding artificial Ca²⁺ buffering through added Ca²⁺ indicator and caged Ca²⁺ buffers is likely to reduce Ca²⁺ to possibly levels below threshold for Ca²⁺ dependent vesicle release. Specifically diffusible buffers (such as the water soluble compounds used in this thesis) have been thought to further reduce the likelihood of Ca²⁺ dependent release in neuronal models (Meinrenken et al. 2003).

Whole cell patch clamp in itself may thus also affect the endogenous Ca²⁺ buffers through wash out of endogenous molecules despite the replacement of ATP for example in the internal patch solution.

The effect of additional Ca^{2+} buffers is commonly studied in neurons (see annex for further discussion) ever since the original experiment of direct injection of BAPTA at the presynaptic terminal in the giant squid reduced neurotransmitter release. The extent of the reduction seemed to increase with the speed of binding kinetics of the buffer injected (EGTA had less effect than BAPTA; Adler et al. 1991). In astrocytes in hippocampal slices, high concentrations of BAPTA severely decreased astrocyte Ca^{2+} dependent aspects of synaptic transmission in CA1 pyramidal neurons by abolishing evoked Ca^{2+} events. Indeed, loading astrocytes with 20mM BAPTA prevented the increase in frequency and amplitude of miniature inhibitory postsynaptic currents in the neighbouring CA1 pyramidal cells that had been seen following stimulation (Kang et al. 1998). Similarly, loading astrocytes with 40mM BAPTA resulted in a loss of LTP at the CA3-CA1 synapse that occurred following stimulation of hippocampal cholinergic pathways (Navarrete et al. 2012).

These quenching effects of Ca^{2+} buffers on astrocyte Ca^{2+} signalling (and the resulting inhibition of possible astrocyte Ca^{2+} events dependent aspects of synaptic transmission) occurred at larger concentrations than were used in the Diazo2 and NPEGTA containing cells in chapters 5 and 6. However, much smaller concentrations of these buffers (200 μM OGB1, 0.45mM EGTA, 0.14mM CaCl_2) were used to clamp astrocytes at resting $[\text{Ca}^{2+}]$ of 50-80nM. This significantly reduced the rate of Ca^{2+} events in these astrocytes and was sufficient to inhibit both endocannabinoid mediated spike timing dependent depression (Min & Nevian 2012) and long term potentiation (Henneberger et al. 2010).

Additionally, the Ca^{2+} indicator concentration itself (even in μM concentrations) may impact astrocyte Ca^{2+} dynamics (as discussed in chapter 6; Z. Wang et al. 1997; Parri & Crunelli 2003). The resting $[\text{Ca}^{2+}]$ recorded in the presence of a Ca^{2+} indicator is different to the endogenous cytoplasmic free $[\text{Ca}^{2+}]$ in the absence of a Ca^{2+} indicator. Early studies suggest using the ratiometric indicator fura 2 at 400 μM results in strong attenuation of the $[\text{Ca}^{2+}]$ estimation in bovine chromaffin cells (Neher & Augustine 1992). In astrocytes in culture increasing the concentration of fura 2 (fura 2-AM, for bulk loading) from 1 to 20 μM also impacted the velocity and spread of Ca^{2+} waves (Z. Wang et al. 1997).

Since then many studies in neurons, at large synapse structures such as mossy fibre boutons in the hippocampus (Scott & Rusakov 2006) or the cerebellum (Delvendahl et al. 2015) have used patch clamp loading of different Ca^{2+} indicator dyes with different Ca^{2+} affinity or different concentrations of the same Ca^{2+} indicator in combination with modelling to estimate local endogenous buffering capacity of the synapse. Recording resting $[\text{Ca}^{2+}]$ using different concentrations of OGB-2 or caged Ca^{2+} buffers may help estimate how much the resting $[\text{Ca}^{2+}]$ recorded in this thesis are affected by the addition of the Ca^{2+} indicator OGB-2 or caged Ca^{2+} buffers respectively.

Furthermore, averaging the $[\text{Ca}^{2+}]$ estimation in time and space may well underestimate the actual $[\text{Ca}^{2+}]$ in a given astrocyte or astrocyte subcompartment.

Indeed, as discussed above and in chapter 6, Ca^{2+} microdomains, through local differences in the ratios of internal stores or vesicles or endogenous buffers, may determine the possibility of Ca^{2+} dependent vesicular release. Therefore general and random ROI may not match the location of these microdomains: averaging of very high (microdomain) and very low (surrounding cytosol) $[\text{Ca}^{2+}]$ would lead to lower quantitative estimations of the astrocyte resting $[\text{Ca}^{2+}]$ for the given ROI. Additionally, these microdomains could dissipate before Ca^{2+} can be bound by the Ca^{2+} indicator. As discussed in chapter 6, selection of ROI through morphology criteria for example may help reduce this impact of averaging on the quantitative estimation of resting $[\text{Ca}^{2+}]$. However a more morphological means of selecting ROI may be to the detriment of temporal characteristics of Ca^{2+} events as sufficient photons are required for estimation of $[\text{Ca}^{2+}]$ which could be difficult in smaller astrocyte processes. This could be key if the relationship between ER distribution and morphology (as in spatial limitation) exists and the resulting volume of ER to cytosol does indeed contribute to setting the resting $[\text{Ca}^{2+}]$ and thus the amplitude of response.

ii. Astrocyte $[\text{Ca}^{2+}]$ requirements for Ca^{2+} dependent release could be different

Alternatively, the Ca^{2+} dependent release may function differently in astrocytes. For example, perhaps astrocytes have higher Ca^{2+} sensitivity sensors for Ca^{2+} dependent vesicular release. For example, despite being necessary for glutamate release in astrocytes, synaptotagmin 4 may not necessarily bind Ca^{2+} as X-ray crystallography of rat synaptotagmin 4 suggest its structural properties are possibly incompatible with Ca^{2+} binding (Dai et al. 2004). This could suggest alternative Ca^{2+} sensors might be involved in astrocytes or in different astrocyte subgroups. Indeed, in the previously mentioned study, Parpura & Haydon 2000 found that graded raises in Ca^{2+} in astrocyte cultures triggered graded currents in neighbouring co-cultured neurons in some but not all cultured astrocyte-neurons groups investigated. Some synaptotagmins are thought to have higher Ca^{2+} affinity for example (Sugita et al. 2002), perhaps ratios of different Ca^{2+} sensitivity sensors could be distributed differently in astrocytes relative to neurons as well as across different astrocytes.

However, a lot of these studies of Ca^{2+} affinity were done in large synapse structures such as the calyx of Held or in PC12 cell lines which do not resemble the small perisynaptic processes of astrocytes. Finally, whilst neuronal Ca^{2+} buffers are well documented, there is as of yet less molecular knowledge of the endogenous Ca^{2+} buffers distribution, affinity and regulation in astrocytes. This could reveal further properties to explain how or if astrocyte Ca^{2+} dependent vesicle exocytosis, for example, may be different to that in neurons.

Finally, the correlations observed may not hold or could be altered in more physiological models of astrocyte Ca^{2+} signalling. If regions of higher resting $[\text{Ca}^{2+}]$ enable the generation of larger DHPG-evoked or endogenous Ca^{2+} events, then perhaps these regions could propagate an intracellular Ca^{2+} wave at higher velocity through Ca^{2+} -dependent increase of Ca^{2+} -release from

stores. Mice subjected to forebrain engraftment of Human glial progenitor cells developed human-like astrocytes where UV-photolysis evoked intracellular Ca^{2+} waves propagated 3-fold faster than in the endogenous murine astrocytes. This faster spread of Ca^{2+} events seemed to enhance both synaptic plasticity (LTP) and learning (as assessed by fear conditioning, Barnes maze navigation and novel object recognition behavioural tests; Han et al. 2013). These human cortical protoplasmic astrocytes are 2.6 fold larger in diameter than their rodent counterparts (Oberheim et al. 2009) and remain somewhat larger in the previously mentioned engraftment study. Perhaps this could allow for different morphological distribution of internal stores.

CONCLUSIONS AND PERSPECTIVES

In this thesis I was able to quantify resting and event $[\text{Ca}^{2+}]$ using FLIM of OGB-2 in astrocytes of acute hippocampal slices. I found positive correlations between resting $[\text{Ca}^{2+}]$ and peak $[\text{Ca}^{2+}]$ and amplitude of both spontaneous and Ca^{2+} events evoked by group I mGluR activation recorded across different ROIs in these cells. A recent study in the laboratory has identified heterogeneous distribution of resting $[\text{Ca}^{2+}]$ within similar astrocytes using FLIM of OGB-1 (Zheng et al, 2015). This is consistent with recent findings that suggest astrocyte Ca^{2+} signalling properties are heterogeneous within individual astrocytes in situ (Di Castro et al. 2011; Panatier et al. 2011) and in vivo (Kanemaru et al. 2014). This first observation could lend further support the concept of subcellular compartment specialisation in astrocytes (reviewed in Rusakov et al. 2014).

In this thesis, we investigated the role of resting $[\text{Ca}^{2+}]$ in astrocyte signalling. We used FLIM of OGB-2 to quantify $[\text{Ca}^{2+}]$ in whole-cell patched astrocytes in hippocampal slices using a photon-count ratio method. We observed that lower resting $[\text{Ca}^{2+}]$ were associated with smaller spontaneous or evoked Ca^{2+} events (as characterised by event peak $[\text{Ca}^{2+}]$ and amplitude) in astrocytes in hippocampal slices when considering different individual ROIs or the average evoked Ca^{2+} event across cells. To test the causality of these correlations, we used UV photolysis of caged Ca^{2+} or Ca^{2+} buffer to manipulate the resting $[\text{Ca}^{2+}]$ and test its relationship with evoked astrocyte Ca^{2+} events. Within a given individual ROI, the change in evoked Ca^{2+} response amplitude was negatively correlated with the changes in resting $[\text{Ca}^{2+}]$.

The results discussed in this thesis therefore suggest the possibility of a functional impact of astrocyte resting $[\text{Ca}^{2+}]$ heterogeneity on astrocyte Ca^{2+} signalling through its influence on endogenous and DHPG-evoked astrocyte Ca^{2+} event peak $[\text{Ca}^{2+}]$ or amplitude.

In order to identify the mechanisms and functional implications of these results, we would need to investigate how these downstream physiological Ca^{2+} dependent functions could be altered. One approach would be to systematically modify the intracellular Ca^{2+} buffering capacity through the use of additional buffers (such as in chapters 5, 6). In addition, optogenetic methods could help to generate a more defined and localized Ca^{2+} source within an astrocyte compared to DHPG application.

Furthermore, resting $[Ca^{2+}]$ maps within astrocytes, refined through further physiological molecular studies of astrocyte Ca^{2+} buffer dynamics, could perhaps predict local Ca^{2+} dependent roles of astrocytes or astrocyte subcompartments on local environment within the brain. Indeed Ca^{2+} is thought to mediate a plethora of astrocyte interactions such as with local vasculature and neurons (see chapter 1). In particular, the modulation of Ca^{2+} event amplitude could potentially impact neurotransmission through differences in modulation of astrocyte Ca^{2+} dependent exocytosis (as discussed above) of neurotransmitters or modulators such as D-serine for example, which may in turn fine tune synaptic transmission or plasticity.

As demonstrated in this thesis, FLIM can be successfully used as a tool for a quantitative approach to investigating Ca^{2+} events in astrocytes in order to refine our understanding of astrocyte function in the brain. Refining the investigation into astrocyte Ca^{2+} signalling could help resolve some of the controversies, in particular with regards to Ca^{2+} mediated gliotransmission.

In conclusion, the main point of this thesis was to quantitatively investigate a basic mechanism of astrocyte Ca^{2+} signalling. We have raised the observation that the resting $[Ca^{2+}]$ can contribute to determining the amplitude and peak $[Ca^{2+}]$ of a Ca^{2+} event and thus alters Ca^{2+} signalling in subcompartments of astrocytes.

ANNEX:

Bassoon-RPB interaction regulates $Ca_v1.2$ synaptic transmission recorded in acute hippocampal slice field recordings.

INTRODUCTION

A. Objective:

Additionally to the main focus of my PhD on astrocyte signalling in the CA1 region of the hippocampus, I allotted some of my PhD time to further understand the role of calcium in neurotransmission in the hippocampus. Indeed, I had the opportunity to perform extracellular field-recording experiments to help an ongoing collaboration project between my supervisors and Dr Anna Fejtova in Magdeburg.

The project wanted to identify the role of the active zone scaffolding protein Bassoon and its interaction with RIM-binding proteins (RBP; RIM: Rab-3 Interacting Molecule) in synaptic transmission. Specifically, the project wanted to identify if this interaction (Bassoon-RBP) could explain the differential recruitment of voltage-gated calcium channels (Ca_v) to the pre-synaptic active zone.

The data I collected contributed to 2 of the figures in the resulting publication by the journal *Neuron* (Davydova, 2014; figure 5.F-H, figure 7.D and supplementary figure S6.C). In this chapter, I will describe and discuss in detail the methods used and results gathered from the experiments I performed. Any work, used for explanation purposes, that was not carried out by myself will be explicitly mentioned as such.

My role was to experimentally record synaptic transmission with extracellular field recordings evoked by stimulation at the CA3-Schaffer-collaterals and recorded in the stratum radiatum of the CA1 area in acute hippocampal rodent slices. I used pharmacological inhibition of either $Ca_v2.1$ (P/Q-type) or $Ca_v2.2$ (N-type) and measured the impact of interfering with Bassoon on this measurement of synaptic transmission. I used specific peptides designed by Magdeburg group to block Bassoon interaction with RBP and in other experiments I used hippocampal slices from Bassoon knockout animals.

In this introduction I will describe the key role of Ca^{2+} in synaptic transmission (as recorded in this chapter) at the CA3 to CA1 synapses in the hippocampus. A more detailed description of the hippocampus physiological functions can be found in the introduction to chapter 2.

B. Brief overview of the Hippocampus anatomy

Four sub-regions, named cornu-ammonis 1 to 4, can be distinguished in the hippocampus based on the position and morphology of their neurons. These regions are referred to as CA1, 2, 3 and 4. Additionally to playing a key functional role in learning and memory formation (see chapter 2), the hippocampus has a lamellar structure: fibres arising from the subdivisions of the hippocampal formation run parallel to each other, transversely to the longitudinal axis of the hippocampus. Indeed a stimulus to the entorhinal cortex leads to successive activation of the perforant path, the mossy fibres, the Schaffer collaterals and finally the alvear fibres of CA1. This original observation in the rabbit hippocampus led to the development of the lamellar hypothesis (Andersen et al. 1971), which proposes that neurones in the different hippocampal sub-regions within a single transverse band or lamella may act as a functional unit in the hippocampus. The essence of this tri-synaptic circuit (illustrated in figure A.1) still holds true though may be refined by more recent investigations into the intricacies of the hippocampus organisation (reviewed in Sloviter & Lømo 2012). This principally unidirectional property of the hippocampal network has allowed this circuit to be studied in great detail in in-vitro slices. Indeed, as the hippocampus cells are organised and orientated similarly, both large synaptic currents can be evoked through the ease of access to the stimulation of many innervating axons and the summation of the responses can be recorded extracellularly. This principal underlies the extracellular field recordings method used in this chapter.

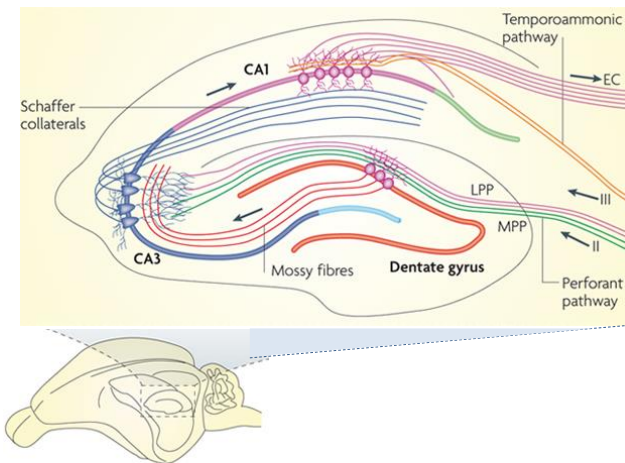


Figure A.1 the tri synaptic hippocampal network

This illustration shows the hippocampal circuitry in a slice of the hippocampus taken as suggested by the whole brain schematic below (adapted from Deng et al. 2010).

The hippocampal network is principally unidirectional. The excitatory tri synaptic pathway is illustrated by arrows: entorhinal cortex (EC) → dentate gyrus → CA3 → CA1 → EC.

The layer II/IV neurons of the entorhinal cortex project onto the dentate gyrus and CA3 via the perforant pathway (split into lateral and medial, LPP and MPP). CA1 also receive direct input from the EC layer III/V (temporoammonic pathway). CA3 neurons receive input from the dentate gyrus through mossy fibres. CA3 neurons project onto CA1 through their Schaffer collaterals (the Associational Commissural Pathway is not represented here, CA3 to contralateral hippocampus). CA1 neurons in turn are the main output of the hippocampus and project back into the EC (via the subiculum, not shown).

C. Extracellular field recordings of CA3 to CA1 synaptic transmission

The basic circuit of the hippocampus consists of a feed-forward synaptic circuit between its sub-regions. In this chapter, I aim to record synaptic transmission at the glutamatergic excitatory synapse from CA3 to CA1 pyramidal neurons. This is the last synapse within the sub-regions of the hippocampus, after which CA1 projections go to the subiculum and entorhinal cortex which are the main structures to which the hippocampus outputs information. I stimulated the Schaffer collaterals of the CA3 region pyramidal cells to evoke synaptic transmission onto the apical dendrites of CA1 pyramidal cells which are found in the CA1 stratum radiatum. An extracellular electrode positioned in the stratum radiatum of CA1 enables the recording of these large evoked currents as field-excitatory post synaptic potentials (fEPSP).

Indeed, post synaptic potentials recorded extracellularly reflect the changes in current sinks and sources after synaptic transmission. When recording in stratum radiatum, extracellular sodium and calcium ions enter the CA1 dendrites after post-synaptic activation of their receptors. This 'current sink' relative to the extracellular pipette results in recording a negative amplitude current after evoking synaptic transmission or post-synaptic potential. Similarly, the fibre volley recorded reflects the summation of the action potentials triggered during the stimulation of axons (CA3 Schaffer-collaterals in this case). Positioning the recording electrode in the stratum radiatum allows us to record only the post-synaptic potentials (CA1 dendrites response to CA3 axon stimulation) and minimise the contamination by population spikes (the current source generated by action potentials in the postsynaptic CA1 axons in response to CA1 dendritic activation by CA3 axon stimulation).

A wide variety of interneurons are present in this area of the hippocampus, additionally to the glutamatergic pyramidal CA3 and CA1 neurons. Most of these, but not all, are inhibitory interneurons as they are found to release γ -aminobutyric acid (GABA) upon stimulation (reviewed in Freund & Buzsáki 1996). As we are using extracellular (field) recordings of the overall stimulation of CA3 Schaffer-collaterals, in this chapter we blocked any activation of the GABA-A receptor through application of its specific antagonist picrotoxin. This enabled to maximise the amplitude and probability of recording glutamatergic EPSPs through these extracellular recordings.

D. Ca^{2+} , Ca_v s and synaptic transmission

In this chapter I focus on the voltage-dependent Ca^{2+} channels (Ca_v s) contribution to synaptic transmission, recorded as described above, at the CA3 to CA1 synapse.

i. The role of Ca^{2+} and Ca_v s in synaptic transmission

Ca^{2+} influx into the pre-synaptic terminal is the critical determinant of transmitter release at chemical synapses (Katz & Miledi 1967). Indeed, Ca^{2+} determines both the fusion with presynaptic membrane and the exocytosis of synaptic vesicles which leads to the release of neurotransmitters into the synaptic cleft for synaptic transmission onto the postsynaptic neuron (Ca^{2+} dependent vesicle exocytosis is further discussed in chapter 7).

Action potential evoked neurotransmitter release is mediated through depolarisation of the presynaptic terminal which activates CaVs. Upon activation, these channels allow Ca^{2+} entry from the higher $[\text{Ca}^{2+}]$ in extracellular medium into the relatively low intracellular $[\text{Ca}^{2+}]$ in the presynaptic terminal creating local high $[\text{Ca}^{2+}]$ microdomains in the presynaptic terminal. Therefore CaVs contribute to determining the local presynaptic $[\text{Ca}^{2+}]$. Studies in the rat calyx of held, a giant synapse in the brainstem, enabled to further identify the key role of these Ca^{2+} channels at the presynaptic active zone. Indeed, the recruitment of synaptic vesicles to presynaptic sites where CaVs cluster has been shown to be critical in enabling the generation of local $[\text{Ca}^{2+}]$ transients of sufficient amplitude required for rapid release of synaptic vesicles for synaptic transmission in the rat calyx of held (Wadel et al. 2007).

The density of CaVs at the presynaptic active zones as measured through cell-attached current and capacitance recordings at the calyx was found to vary from 5 to 218 (average 42). These differences in CaV density seem to lead to differences in vesicle release probability which therefore also determined short term facilitation or depression (Sheng et al. 2012).

Taken together these studies suggest that the density and position of CaVs at the presynaptic active zone may play a key role in fine tuning synaptic transmission as well as short term synaptic plasticity (reviewed in Catterall & Few 2008). Understanding the structures that enable the recruitment of these CaVs to the active zone should help understand the mechanisms that may help determine the efficacy of synaptic transmission.

ii. Voltage-gated Ca^{2+} channels in the hippocampus

This collaboration project investigated the structural mechanisms that enable the recruitment of these Ca_v s to the presynaptic active zone. Specifically, we investigated the differential recruitment of $\text{Ca}_v2.1$ and $\text{Ca}_v2.2$ at the hippocampal CA3-CA1 synapse.

Application of the pharmacological inhibitors used in this chapter (agatoxin and conotoxin) at the CA3 to CA1 synapse (in guinea-pig acute hippocampal slices) helped identify $\text{Ca}_v2.1$ and $\text{Ca}_v2.2$ as the main Ca_v s contributing to presynaptic sources of Ca^{2+} influx at this synapse (Wu & Saggau 1994). These Ca_v s mediate P/Q and N type currents respectively. The action potential relief of G-protein mediated inhibition of CaVs is different for these 2 subtypes. Indeed in chromaffin model cells, endogenous $\text{Ca}_v2.1$ exhibited larger relief of voltage dependent inhibition than $\text{Ca}_v2.2$ for a given stimulation (Currie & Fox 2002). Differences between these two subtypes suggest that their relative distribution at synapses could have functional implications for synaptic transmission (reviewed in Reid et al. 2003). The variability in the proportion of $\text{Ca}_v2.1$ or $\text{Ca}_v2.2$ contributing to exocytosis was confirmed across individual synapses yet there was not thought to be any association between a given Ca_v distribution and synaptic efficacy (Ariel et al. 2013). However at a particular given synapse, the change in relative contribution of a given Ca_v subtype is thought to be a possible mechanism to underlie synaptic plasticity in the hippocampus. Indeed, the contribution of $\text{Ca}_v2.2$ to exocytosis at the perforant path to CA1 synapse is enhanced during LTP (Ahmed & Siegelbaum 2009).

iii. Presynaptic active zone structure

In this collaboration project, the Magdeburg group focused on identifying the possible differences in interactions of structural components in the presynaptic active zone with these two subtypes of Ca_vs in order to explain differential recruitment of CaV2.1 and CaV2.2 to the active zone. Indeed, some structural components of the presynaptic active zone have been shown to control the quantity and position of CaVs at the synapse, particularly through the interaction between active zone structural components Rab3-interacting molecule (RIM) and RIM-binding protein (RBP) with the subunits of CaVs.

CaVs are formed of a Ca permeable pore, subunit $\alpha 1$, and auxiliary subunits β and $\alpha 2\delta$. $\alpha 2\delta$ is thought to contribute to the abundance of CaVs at the active zone via anchoring CaVs to the presynaptic membrane (demonstrated in tsA-cells, Davies et al. 2010) but may also play a role in the efficiency of CaVs mediated Ca²⁺ dependant probability of synaptic vesicle exocytosis in hippocampal neuronal cultures (Hoppa et al. 2012).

RIM interacts with GTP-complexed Rab3 (Y. Wang et al. 1997). Rab3 are small proteins which associate with synaptic vesicles when they are bound to GTP (guanosine tri phosphate). This RIM/Rab3 interaction is thought to help regulate the fusion of docked synaptic vesicles and the presynaptic membrane for exocytosis (Y. Wang et al. 1997). RIM deletion in RIM knock out mice also reduces the docking of vesicles to the active zone relative to control mice, at the calyx of Held (Han et al. 2011).

RIM is thought to regulate CaVs density at the presynaptic active zone as identified through RIM knockouts in drosophila (Graf et al. 2012) and in mice (Han 2011, Kaeser 2011). Indeed, in neuronal cultures where RIM was deleted, the reduced presynaptic [Ca²⁺] and abnormal CaV location were rescued through direct interaction of RIM PDZ domains and CaV subunit (Kaeser 2011). Additionally, RIM-binding proteins also interact with CaVs and thus thought to contribute to physically link synaptic vesicles (via RIM/Rab3GTP) to the high presynaptic [Ca²⁺] domains (surrounding CaVs) necessary for Ca²⁺ dependent exocytosis (via synaptotagmin Ca²⁺ sensors). This interaction between RBP and the pore-forming subunit of CaVs was demonstrated in PC12 cells (Hibino et al. 2002). More recently, RBPs were found to be essential for exocytotic neurotransmitter as knock out of the drosophila RBP impaired CaV position and [Ca²⁺] at the presynaptic active zone as well as reduce synaptic release probability (Liu et al. 2011).

These disruptions of CaV subunits (Hoppa et al. 2012) or RIM (Han et al. 2011; Kaeser et al. 2011) both reduce presynaptic [Ca²⁺] through reduction of CaVs at the presynaptic active zone. However the relative contribution of P/Q and N type currents does not seem to be altered (no compensation of one current type relative to the other) suggesting these interactions equally occur across both CaV subtypes 2.1 and 2.2. Therefore these RIM/RBP/CaV interactions alone cannot explain the differential recruitment of these two CaV subtypes to the presynaptic active zone during fine tuning of synaptic transmission.

iv. Bassoon is a large structural component of the presynaptic active zone which is also thought to be involved in regulating synaptic transmission.

Contrary to some of the other structural components of the active zone (such as RIM), Bassoon is thought to be specific to vertebrates. In mouse hippocampal neuronal cultures, Bassoon was found to be highly concentrated at the active zone, colocalise with synaptic vesicle proteins and thought to be tightly associated with the components of the cytoskeleton. It is therefore thought to be involved in cytomatrix organisation at the presynaptic active zone (Dieck et al. 1998).

Bassoon is thought to play a regulatory role in central nervous system excitatory synaptic transmission. Indeed in Bassoon knock out mice lacking the central part of the protein, the disruption of Bassoon has been shown to reduce synaptic transmission as recorded through fEPSPs and EPSCs in CA1 pyramidal neurons of hippocampal slices. Further molecular investigations in hippocampal neuronal cultures in these mice revealed that a fraction of these glutamatergic active zones displayed synaptic vesicles but these were unable to fuse rendering these synapses inactive (Altrock et al. 2003). Spontaneous EPSC recordings at the cerebellar mossy fibre to granule cell synapse in Bassoon null mutant mice ($Bsn^{-/-}$) were not impaired relative to wildtype (WT) littermates. However in $Bsn^{-/-}$, these synapses exhibited depression and slower recovery from depression at high frequency stimulations due to halved rate of vesicle reloading relative to WT (Hallermann et al. 2010). These studies respectively reveal a possible regulatory role of Bassoon at hippocampal excitatory synapses through contributions to the enhancement of synaptic vesicle fusion and to the speed of recruitment of these vesicles to the active zone.

In this project, Davydova et al. used a quantitative in vitro binding assay to isolate the physical interaction between Bassoon and RBP in hippocampal neuronal cultures. This Bassoon-RBP interaction enables the localisation of the CaV2.1 subtype at the synapse but does not affect the CaV2.2 localisation as shown by co-immuno-precipitation and immunocytochemistry in hippocampal neuronal cultures. They used $Bsn^{-/-}$ animals or acute interference with the Bassoon binding site to RBP to show that the disruption of this interaction (Bassoon and RBP) leads to a failure to position specifically the CaV2.1 subtype at the synapse.

Figure A.2, adapted from Davydova et al, illustrates the (simplified) interactions between these previously described structural components of the presynaptic active zone, CaV2.1 and synaptic vesicles as suggested by these studies.

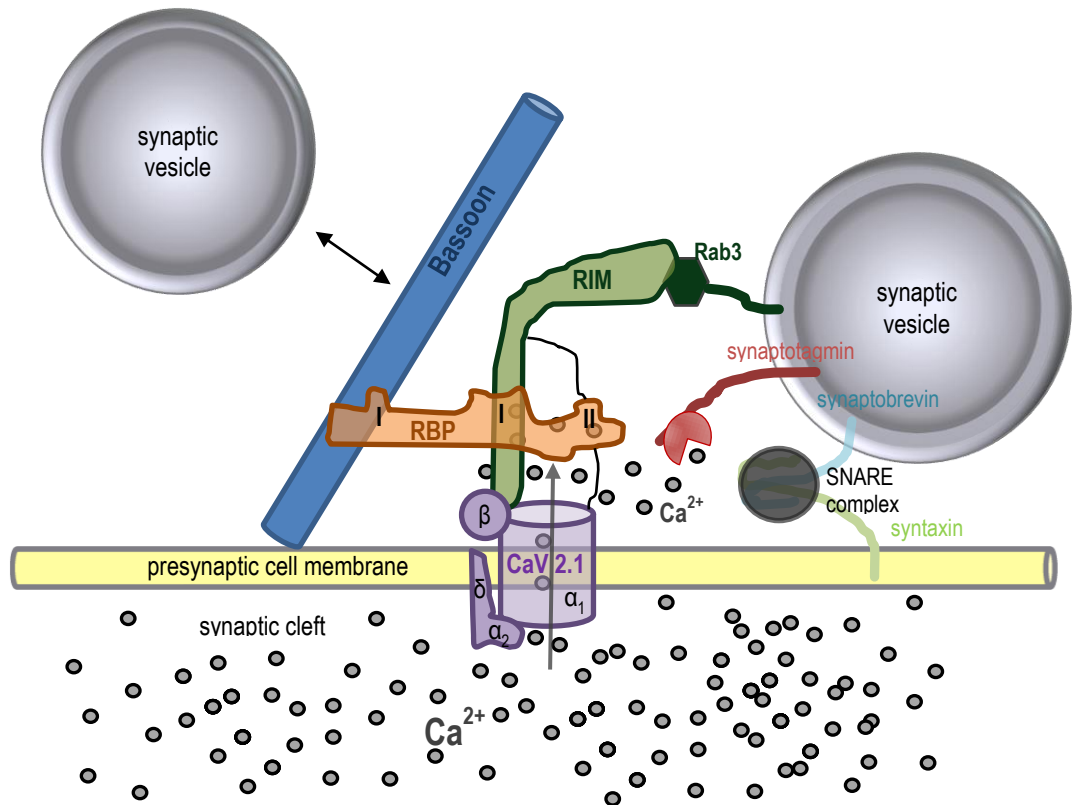


Figure A.2 simplified interactions at the presynaptic active zone

This illustration shows simplified interactions between CaV (purple) and structural active zone components Bassoon (blue), RIM (green) and RBP (orange) which form a multiprotein complex around RBP that may enable the spatial and functional coupling of multiple steps of Ca^{2+} dependent vesicular release (adapted from Davydova et al. 2014; Sudhof 2012a).

Bassoon is a structural component of the presynaptic active zone which may regulate synaptic transmission by facilitating the recruitment of synaptic vesicles to areas of high presynaptic $[\text{Ca}^{2+}]$ mediated by CaVs. Indeed the Bassoon is thought to interact with CaV2.1 through coupling with RBP. In turn RBP also tethers synaptic vesicles through its interaction with RIM which can bind to Rab3/GTP complex on synaptic vesicles. This whole process enables Ca^{2+} sensors on the synaptic vesicle (such as synaptotagmin, red) to increase the possibility of binding Ca^{2+} . In turn this facilitates Ca^{2+} dependent fusion of synaptic vesicles to the presynaptic cell membrane through SNARE complex.

This study investigated the role of the Bassoon-RBP interaction on the relative contribution to synaptic transmission at the CA3 to CA1 synapse in acute hippocampal slices.

METHODS

In this collaboration, my role was to determine the impact on synaptic transmission in the CA3 to CA1 synapse, of the failure to position CaV2.1 at the presynaptic active zone through the disruption of the interaction between Bassoon and RBP.

A. Acute hippocampal slice preparation

i. Animals used.

The peptides experiments were done on acute hippocampal slices from 21-26 day old Sprague Dawley rats, in compliance with the UK regulations for animal welfare implemented at the Institute Of Neurology, UCL.

Other experiments were done in acute hippocampal slices obtained from 6 to 8 week old homozygous Bassoon null mutant (*Bsn*^{-/-}) mice where the whole gene was trapped and thus prevented from expression (as described in Hallermann et al. 2010) and their wildtype littermates (WT), in compliance with the German regulations for animal welfare implemented at the Institute for Cellular Neuroscience, Bonn University. Genotype for each mouse used was confirmed by the Magdeburg institute through analysis of sample tissue (tail clippings).

ii. Slice preparation

Hippocampal slices were prepared in ice-cold oxygenated slicing solution, set to recover for 15 minutes in 34°C oxygenated slicing solution and then transferred to ACSF for recovery prior to recordings. This procedure and solutions are fully described in chapter 2.

For peptide experiments (Sprague-Dawley slices), the slices were transferred from the slicing solution to oxygenated ACSF containing 5 µM of either TAT-WT or TAT-RBM peptides provided by Magdeburg. Slices were incubated with these peptides at 34°C for 1 hour and then stored at room temperature until recordings.

For experiments using *Bsn*^{-/-} and WT mice slices, no peptides were added to ACSF. The slices were transferred from slicing solution to ACSF and stored at room temperature until recordings.

B. Recording protocol

i. Experimental groups

For all recordings, a cut was made between CA3 and CA1 (figure A.3.A) to prevent recurring activity. Slices were then transferred to a submersion-type recording chamber and superfused at 33-35°C with ACSF containing no TAT peptides. 50 µM picrotoxin and 100 µM D-APV (Tocris) were added to the ACSF as specific antagonists of respectively GABA-A and NMDA receptors.

In all peptide and *Bsn*^{-/-} experiments, three experimental groups were devised based on the pharmacological inhibition of Ca_vs. Control recordings were made from slices exposed to ACSF containing no further toxins than those described above (PTX/APV). In the two other groups, either 500 nM ω-conotoxin GVIA or ω-agatoxin IVA (Abcam Biochemicals) was added to ACSF to respectively block Ca_v2.2 or Ca_v2.1.

For a given experimental day, one animal was used to collect as many slices as possible. The slices for each animal were equally divided between each group to at least aim to record equally from each animal (control, conotoxin, agatoxin, TAT-WT and TAT-RBM). Slices were transferred to the submersion chamber and exposed to one of the three ACSF solutions for at least 15 minutes before recordings started. All solutions were continuously bubbled with 95% O₂ / 5% CO₂.

ii. Field recordings

Field excitatory postsynaptic potentials (fEPSPs) were recorded using a standard borosilicate glass pipette (slightly larger diameter than used for patch) filled with ACSF placed in the middle of the *stratum radiatum* of the CA1 region (figure A.3.A).

Synaptic responses were evoked by orthodromic stimulation (100 μs, 25-150 μA, constant throughout a day of experiments) of Schaffer collaterals using a bipolar concentric stimulation electrode (Royem Scientific) connected to a constant voltage isolator stimulation unit (Digitimer model DS3). The stimulation electrode was placed in the *stratum radiatum* >200 μm away from the recording electrode. Field responses were evoked every 30 seconds.

iii. fEPSP analysis

The amplitude of the fibre volley and the fEPSP slope (illustrated in figure A.3.B) of a minimum of 10 responses per slice were determined and averaged in PClamp analysis software. The average slope was then normalized to the fibre volley to compensate for variations in stimulation efficiency between slices and experimental days.

Fiber volleys were not affected by peptide incubations or Bassoon knockout ($P > 0.2$ all groups). Single population and unpaired two-population Student's t-tests were used as appropriate.

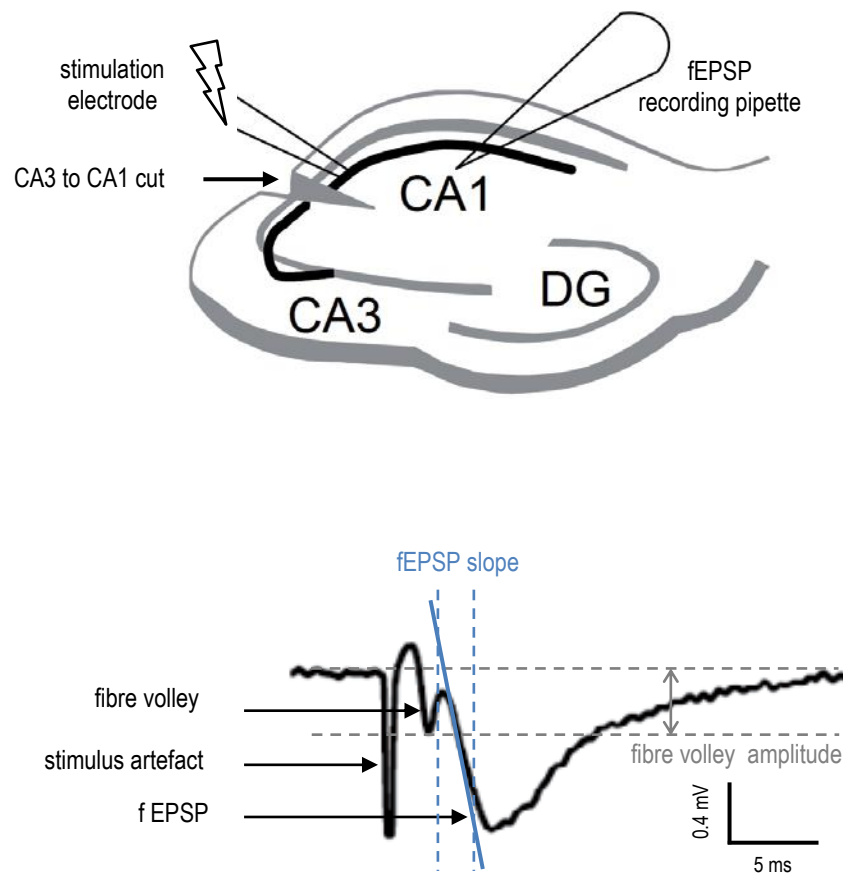


Figure A.3 recording fEPSPs in acute hippocampal slices

A. fEPSP recording method illustration

Acute hippocampal slices were prepared from Sprague-Dawley rats or *Bsn^{-/-}* and WT littermate mice. Prior to recording, a cut was made between CA3 and CA1 (arrow). The field EPSP recording pipette (borosilicate glass) was filled with ACSF and positioned in the stratum radiatum of the CA1 region. The stimulation electrode (concentric bipolar electrode, Royem Scientific) to evoke EPSPs through stimulation of CA3 Schaffer collaterals, was positioned in the CA1 stratum radiatum, closer to CA3 and at least 200 μm away from the recording electrode. The pyramidal cell body layer is represented in thick grey line. CA1 and CA3 stand for the respective *Cornu Ammonis* pyramidal cell areas of the hippocampus. DG stands for the dentate gyrus hippocampal area: cell bodies of granular cells are represented in grey line.

B. fEPSP analysis illustration

This illustration of the mean fEPSP recorded (over 10 recordings for 1 slice) illustrates the components acquired: stimulus artefact, fibre volley and fEPSP. The slope (blue) was calculated from the initial until the end point during which the fEPSP was linear (ie before peak). The fibre volley amplitude (grey) was measured for each recording. The average fEPSP slope of at least 10 recordings per slice was normalised to the average fiber volley amplitude to compensate for variations in stimulation efficiency between slices and experimental days. The scale bars indicate amplitude (mV) and recording duration (ms).

RESULTS

A. Acute interference with Bassoon-RBP interaction weakens evoked synaptic transmission reliant on Cav2.1 at the CA3 Schaffer-collaterals to CA1 synapses.

I used specific peptides designed by Magdeburg group to test the role of the Bassoon PXXP motif interaction with RBPs in synaptic transmission.

Peptides were synthesised to mimic either the RBP-binding site on Bassoon sequence (RTLPSPP, amino acids 2,880–2,899; TAT-WT) or a 3 amino acid mutation in the RBP-binding site (RTLPSPP → ATLASPA; TAT-RBM).

These peptides were TAT-conjugated: a TAT sequence was inserted in the N-terminus of the peptide to ensure effective membrane permeability (Dietz & Bähr 2005).

They were used in a competition assay: incubating with TAT-WT should sequester the endogenous Bassoon binding site on endogenous RBPs, thus preventing or greatly obscuring the endogenous functional interaction between Bassoon and RBP. The TAT-RBM peptide is used as a control against any TAT-peptide incubation effect on synaptic transmission unrelated to Bassoon-RBP interaction. Indeed, this mutation renders the RBP-binding site non-functional.

These peptides were tested for specificity in neuronal cultures by the Magdeburg group and TAT-WT induced similar disruption to CaV2.1 synaptic location as was seen in cultures from Bsn^{-/-} animals.

I evoked fEPSP by Schaffer collateral stimulation and recorded them in the stratum radiatum of the CA1 area in acute hippocampal slices prepared from young adult Sprague-Dawley rats.

The average fEPSP slope (normalised to the fibre volley amplitude) of at least 10 fEPSP recordings per slice was measured in slices incubated for 1 hour at 34°C with 5 µM of either TAT-RBM or TAT-WT peptides. In each peptide incubation group, fEPSPs were recorded in slices perfused with ACSF only (control), ACSF + 500 nM ω-conotoxin GVIA (conotoxin) or ACSF + 500 nM ω-agatoxin IVA (agatoxin). Example mean fEPSP recording traces are shown in figure A.4.A.

In the three groups (control, conotoxin and agatoxin), the average fEPSP slope for slices incubated with the TAT-WT peptide was expressed as a percentage of the similarly quantified average fEPSP slope recorded in slices incubated with the TAT-RBM control peptide (figure A.4.B).

In the control slices (ACSF only), a significant reduction of fEPSP slopes was observed in slices incubated with TAT-WT relative to control slices incubated with TAT-RBM peptide. Indeed, these TAT-WT control slices had fEPSP slopes of only 48.1% ± 11.8% of TAT-RBM control slices (n = 8 slices, p = 0.0032, figure A.2.B).

In slices from the conotoxin group, synaptic transmission was expected to be majorly mediated through Ca_v2.1 as conotoxin incubation enables specific pharmacological inhibition of Ca_v2.2 (Dutar et al. 1989). A significant reduction in fEPSP slopes was observed in conotoxin slices incubated with TAT-WT relative to conotoxin slices incubated with TAT-RBM peptide. Indeed, these TAT-WT conotoxin slices had fEPSP slopes of only 45.2% ± 5.8% of TAT-RBM conotoxin slices (n = 11 slices, p < 0.001, figure A.4.B). This reduction in TAT-WT relative to TAT-RBM fEPSP slope was comparable to that observed in the control group.

In slices from the agatoxin group, synaptic transmission was expected to be majorly mediated through Ca_v2.2 as agatoxin incubation enables specific pharmacological inhibition of Ca_v2.1 (Mintz et al. 1992). A non-significant (n=5 slices, p =0.51) slight reduction in fEPSP slopes was observed in agatoxin slices incubated with TAT-WT relative to agatoxin slices incubated with TAT-RBM peptide. These TAT-WT agatoxin slices had fEPSP slopes of 45.2% ± 5.8% of TAT-RBM agatoxin slices (figure A.4.B). This slight reduction in fEPSP slope was significantly less than the reduction observed in conotoxin slices (p= 0.025, figure A.4.B).

Overall, these experiments suggest that synaptic transmission (as measured through fEPSP, in CA1 stratum radiatum of acute hippocampal slices) relying on Ca influx mediated through Ca_v2.1 (identified in conotoxin group) but not through Ca_v2.2 (identified in agatoxin group) is affected by the TAT-WT peptide specific interference with Bassoon-RBP interaction. This is in line with the experiments performed by the Magdeburg group in neuronal cultures.

These experiments contribute to assessing the functional role of the Bassoon-RBP interaction mediated synaptic localisation of Ca_v2.1 that was shown in the Magdeburg group experiments (Davydova et al. 2014; figures 1-5).

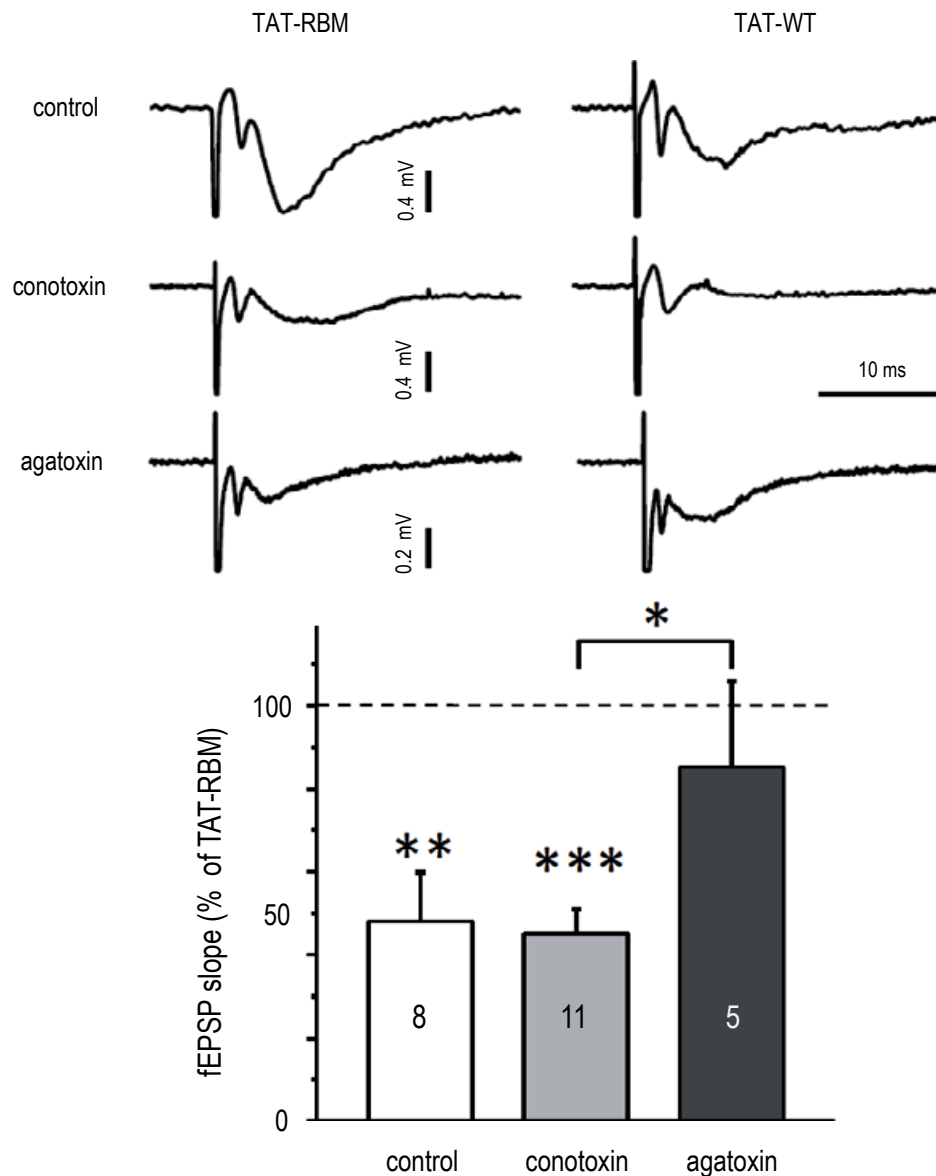


Figure A.4 acute interference with Bassoon-RBP interaction weakens synaptic transmission

A. Sample traces from Sprague Dawley rat slices incubated with TAT-RBM or TAT-WT peptides
fEPSPs were evoked by Schaffer collateral stimulation and recorded from the stratum radiatum of the CA1 region in acute hippocampal slices. Sample average fEPSP traces from slices incubated with TAT-RBM (left column) or TAT-WT (right column) peptides. Within each of these peptide incubation groups, the slices were divided across 3 different recording protocols: ACSF only (no Ca_v inhibitors; control), ACSF and 500nM ω -conotoxin GVIA ($Ca_v2.2$ inhibitor; conotoxin) or ACSF and 500nM ω -agatoxin IVA ($Ca_v2.1$ inhibitor; agatoxin). Amplitude (mV) represented by vertical scale bars and time (ms) represented by horizontal scale bar.

B. fEPSP slope in TAT-WT slices as a percentage of the slope in TAT-RBM slices

Mean fEPSP slopes are represented (+SEM) for each experimental recording protocols: control (white), conotoxin (light grey) and agatoxin (dark grey). TAT-WT incubated slices fEPSP slope values for each experimental group are expressed as a percentage of the slope values recorded in the TAT-RBM (control peptide) incubated slices.

fEPSPs were significantly reduced upon TAT-WT incubation without Ca_v inhibitors (control). They were comparably significantly reduced in synaptic transmission mediated by $Ca_v2.1$ (conotoxin). There was no significant reduction with TAT-WT incubation in slices were transmission relied primarily on $Ca_v2.2$ (agatoxin).

Stars represent the significance of this reduction in fEPSP slope after TAT-WT incubation relative to the fEPSP slope in TAT-RBM slices (100%, dotted line) for both control and conotoxin groups. For agatoxin, the star represents the significant difference in fEPSP reduction between conotoxin and agatoxin TAT-WT slices. ***p < 0.001; **p < 0.01; *p < 0.05; n.s. = p > 0.05.

Values in bars indicate number of slices analysed

B. Synaptic Transmission Relies More on Ca_v2.2 upon Bassoon Deletion

I evoked fEPSP by Schaffer collateral stimulation and recorded them in the stratum radiatum of the CA1 area in acute hippocampal slices prepared from Bassoon knock-out animals (Bsn^{-/-}) or from their wild-type (WT) littermates.

Slices prepared from each animal were divided across three recording protocol groups based on the presence of Ca_v inhibitors in the ACSF perfusing the slice during fEPSP recordings. Control slices were perfused with ACSF containing no Ca_v inhibitors. Conotoxin slices were perfused with ACSF and 500nM ω-conotoxin GVIA (specific Ca_v2.2 inhibitor). Agatoxin slices were perfused with ACSF and 500nM ω-agatoxin IVA (specific Ca_v2.1 inhibitor in nM range).

Sample fEPSP traces in all three groups are shown for slices prepared from WT or Bsn^{-/-} mice in figure A.5.A.

I measured the average fEPSP slope in agatoxin or conotoxin slices and normalised this value to the average fEPSP slope in control slices recorded for the same animal on the same day (dotted line, figure A.5.B).

In fEPSP recordings in conotoxin treated slices, the fEPSP slope (relative to same day control slices) was significantly decreased in slices prepared from Bsn^{-/-} mice relative to WT littermates. Indeed the ω-conotoxin GVIA-resistant, Ca_v2.1 mediated synaptic transmission recorded normalised fEPSP slopes of 0.60 ± 0.14 in WT slices versus 0.17 ± 0.05 in Bsn^{-/-} slices (n = 5 versus 5, p = 0.035; figure A.5.B).

On the hand, the relative fEPSP slope recorded in agatoxin treated slices was significantly increased in slices prepared from Bsn^{-/-} mice relative to WT littermates. Indeed the ω-agatoxin IVA-resistant, Ca_v2.2 mediated synaptic transmission recorded normalised fEPSP slopes of 0.25 ± 0.05 in WT slices versus 0.71 ± 0.12 in Bsn^{-/-} slices (n = 11 versus n = 10, p = 0.003; figure A.5.B).

These results suggest that the contribution of Ca_v2.2 to synaptic transmission recorded by fEPSP in acute hippocampal mice slices is enhanced in slices prepared from Bsn^{-/-} mice compared to their WT littermates.

These results contribute to the hypothesis that Bassoon plays an important role in controlling the contribution of Ca_v2.1 to synaptic transmission as measured by fEPSP recordings at the CA3 Schaffer collaterals to CA1 synapses. These results also suggest that evoked synaptic transmission at these synapses can be recovered in Bsn^{-/-} animals through a possible enhanced recruitment of Ca_v2.2 contribution.

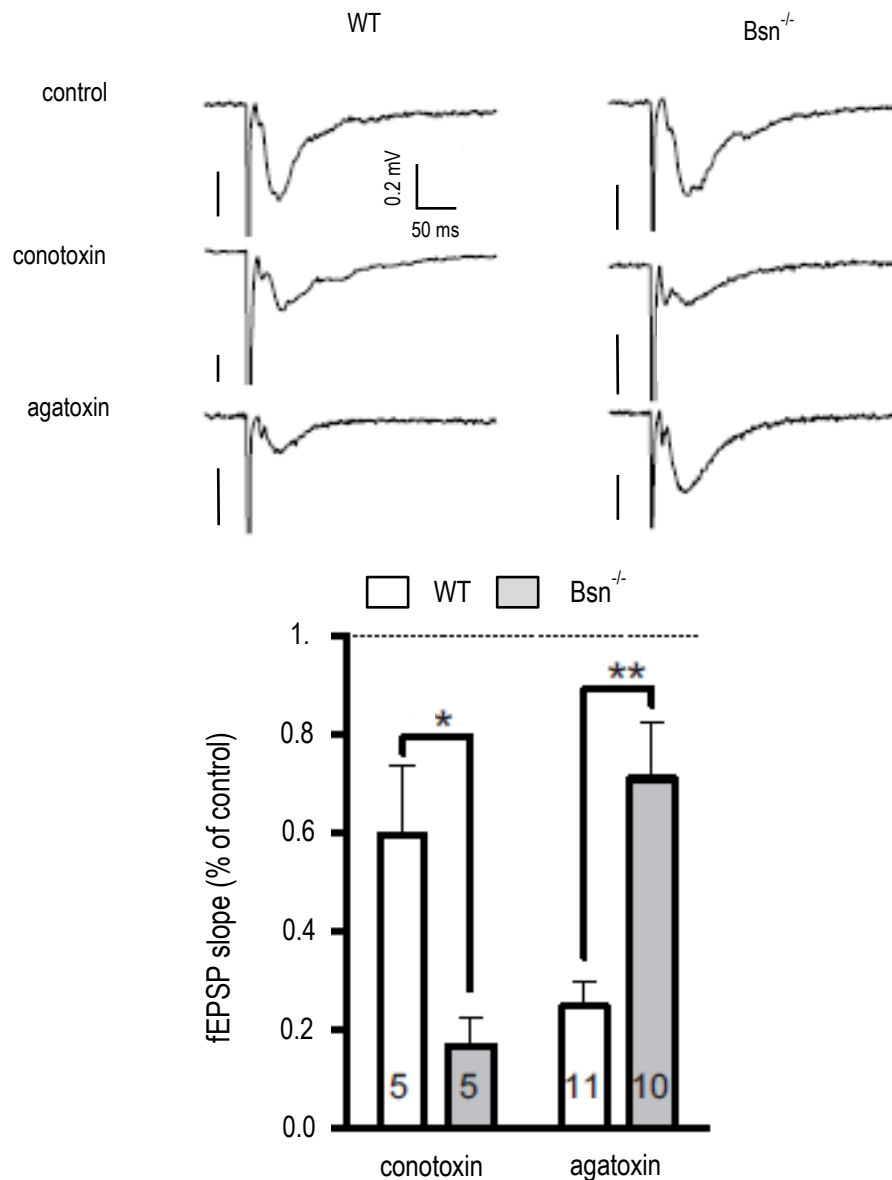


Figure A.5 synaptic transmission relies more on Ca_v2.2 in slices from Bsn^{-/-} mice

A. Sample traces in slices from Bsn^{-/-} mice and their WT littermates.

fEPSPs were evoked by Schaffer collateral stimulation and recorded from the stratum radiatum of the CA1 region in acute hippocampal slices. Sample average fEPSP traces from hippocampal slices prepared from WT littermates (left column) or Bsn^{-/-} (right column) mice. Within each of these WT or Bsn^{-/-} groups, the slices were divided across 3 different recording protocols: ACSF only (no Cav inhibitors; control), ACSF and 500nM ω-conotoxin GVIA (Ca_v2.2 inhibitor; conotoxin) or ACSF and 500nM ω-agatoxin IVA (Ca_v2.1 inhibitor; agatoxin). Amplitude (mV) represented by vertical scale bars and time (ms) represented by horizontal scale bar.

B. fEPSP slope in WT or Bsn^{-/-} slices as a percentage of fEPSP recorded in control ACSF

Mean fEPSP slopes (+SEM) are represented for WT (white) and Bsn^{-/-} (grey) slices when acquired in conotoxin or agatoxin recordings. For each experimental group, fEPSP slopes are given as a percentage of the fEPSP slope measured in slices from the same animal exposed to ACSF only (control) recorded on the same day (1.0, dotted line). The values in the bars indicate the number of slices analysed. The relative to control fEPSP slopes in slices from Bsn^{-/-} mice (grey) were significantly reduced in conotoxin treated slices but were increased in agatoxin treated slices compared to slices from WT littermates (white). This could suggest a decrease in Ca_v2.1 contribution and an enhanced contribution of Ca_v2.2 to synaptic transmission in bassoon knockout mice. Stars represent the significant difference between WT and Bsn^{-/-} slices in conotoxin and in agatoxin recordings: **p < 0.01, *p < 0.05.

DISCUSSION

A. Summary

In this project, the Magdeburg group show that the presynaptic scaffolding protein Bassoon localizes specifically Ca_v2.1 to active zones via molecular interaction with the RIM-binding proteins (RBPs) (Davydova, 2014).

In this chapter I have described my contribution to this project. I measured the effect of interference with Bassoon on evoked synaptic transmission, as recorded at the CA3 to CA1 synapse through an extracellular electrode in the stratum radiatum of CA1 in acute hippocampal slices. I pharmacologically isolated synaptic transmission mediated mainly by Ca_v2.1 only or, in other experiments, mainly by Ca_v2.2.

Using specific peptides to acutely compete with the Bassoon-RBP interaction, I measured a decrease in synaptic transmission that was matched in slices reliant on Ca_v2.1 but not Ca_v2.2 mediated presynaptic Ca²⁺ influx.

In acute hippocampal slices from Bassoon knock out mice (Bsn^{-/-}), I also measured a weaker Ca_v2.1 driven synaptic transmission, which seemed to be compensated for by a larger contribution of Ca_v2.2 dependant transmission. Indeed the specific contribution of Ca_v2.1 and Ca_v2.2 to synaptic transmission seemed to be reversed in Bsn^{-/-} relative to their WT littermates. Alongside the experiments by the Magdeburg group to identify the specific interaction site between Bassoon and RBP, show Bassoon dependent synaptic localisation of Ca_v2.1 and its impact on vesicular release, my fEPSP experiments comfort the hypothesis that Bassoon is a major regulator of the molecular composition of the presynaptic neurotransmitter release sites. Bassoon appears to impact on synaptic transmission through the specific recruitment of Ca_v2.1 but not Ca_v2.2 to the presynaptic active zone.

B. The contribution of CaV2.2 to synaptic transmission is increased in Bsn^{-/-} mice, compensating for reduced CaV2.1 contribution in these animals.

In slices from Bsn^{-/-} animals, synaptic transmission at the CA3-CA1 synapse was predominantly reliant on CaV2.2 (figure A.5). This suggests that in the absence of Bassoon, compensatory replacement of CaV2.1 by CaV2.2 is possible at this synapse. This is consistent with previously reported compensation. Indeed, in CaV2.1 knock out mice, strong functional compensation was measured as the EPSC (excitatory postsynaptic currents) recorded at the calyx of Held synapse were approximately two thirds of the magnitude of EPSCs recorded in WT mice. CaV2.2 was thought to mediate this compensation by replacement at this synapse of the lack of CaV2.1 in these mice (Inchauspe et al. 2004).

More recently, the relative contribution to EPSCs was pharmacologically dissociated for N or P/Q type currents whilst having overexpressed either CaV2.2 or CaV2.1 in cultured hippocampal neurons. This study identified that overexpressing CaV2.2 could lead to competitively displacing the relative contribution to synaptic transmission from predominately CaV2.1 to CaV2.2. The opposite was not true: overexpression of CaV2.1 did not lead to higher contribution of CaV2.1 relative to CaV2.2 to synaptic transmission. These findings lead to the possibility of two different CaV slots at the presynaptic active zone: CaV2.1 preferring slots (but accepting both CaV2.1 and CaV2.2) and CaV2.2 exclusive slots (rejecting CaV2.2) (Cao & Tsien 2010). Therefore the CaV2.2 compensation found in our hands in Bsn^{-/-} (figure A.5) would contribute to the suggestion that Bassoon could selectively specify only CaV2.1 preferring slots (Davydova et al. 2014). In contrast, RIM and auxiliary subunits of CaVs would associate with either type of CaV slot.

C. Functional relevance of the Bassoon-mediated specific recruitment of CaV2.1 for synaptic transmission

In contrast to interference with interactions of other components of the presynaptic active zone equally affecting both CaV2.1 and CaV2.2 (for example Han et al. 2011), this project seems to show that Bassoon mediates specific recruitment of Cav2.1 only to synaptic sites. Indeed, the selective disruption of Bassoon and RBM reduces synaptic transmission and this reduction is of similar magnitude in slices reliant on CaV2.1 whereas pharmacologically isolated transmission reliant on CaV2.2 does not show a reduction of such magnitude (figure A.4). Perhaps this Bassoon-RBM interaction mediated recruitment of CaV2.1 could give a structural basis to the differences in CaV2.1 and CaV2.2 mediated synaptic transmission. Indeed, CaV2.1 mediated presynaptic Ca²⁺ influx is more susceptible to facilitation at the calyx of Held (Inchauspe et al. 2004). CaV2.2 on the other hand is more susceptible to neuromodulation by opioids (Bourinet et al. 1996) through its associated G-protein inhibition (Currie & Fox 2002). Bassoon could therefore potentially contribute to set the capacity of a given synapse to finetune synaptic transmission through determining the CaV2.1 preferring slots at the presynaptic active zone.

The relative contribution of these 2 CaV subtypes can change at different synapses (Iwasaki et al. 2000) and during development (Scholz & Miller 1995), generally through how much the contribution of CaV2.1 relative to CaV2.2 is enhanced. It would be interesting perhaps to study the molecular interactions of Bassoon-RBM-CaV2.1 at different developmental stages to see if they match such changes in CaV2.1 contribution to synaptic transmission. The increased contribution of CaV2.2 may underlie some aspects of long term synaptic plasticity (Ahmed & Siegelbaum 2009). Therefore it could be interesting to determine the molecular changes in interactions at the active zone during synaptic plasticity and if Bassoon plays any role in these changes of relative contribution.

Finally, additionally to reduced synaptic transmission at CA1 pyramidal neurons, genetically interfering with Bassoon enhanced the propensity to undergo epileptic seizures in these mice as is also common in other mutations of synaptic proteins (Altrock et al. 2003). This was also observed in the homozygous $Bsn^{-/-}$ mice used in this chapter which underwent severe seizures often leading to death as these animals grew older. If possible, perhaps selective genetic disruption of Bassoon-RBM binding site could be a means to investigate if the interactions between Bassoon and CaV2.1 reported in (Davydova et al. 2014) have a functional impact in changes of synaptic transmission during neurological pathology such as in epilepsy.

REFERENCES

- Adler, E., Augustine, J., Duffy, N. & Charlton, P., 1991. Alien Intracellular Calcium Chelators Attenuate Release at the Squid Giant Synapse. *The Journal of Neuroscience*, 11(6), pp.1496–1507.
- Agronskaia, a V, Tertoolen, L. & Gerritsen, H.C., 2004. Fast fluorescence lifetime imaging of calcium in living cells. *Journal of biomedical optics*, 9(6), pp.1230–1237.
- Agulhon, C., Fiacco, T. a. & McCarthy, K.D., 2010. Hippocampal short- and long-term plasticity are not modulated by astrocyte Ca²⁺ signaling. *Science (New York, N.Y.)*, 327(March), pp.1250–1254.
- Agulhon, C., Petravicz, J., McMullen, A.B., Sweger, E.J., Minton, S.K., Taves, S.R., Casper, K.B., Fiacco, T. a. & McCarthy, K.D., 2008. What Is the Role of Astrocyte Calcium in Neurophysiology? *Neuron*, 59, pp.932–946.
- Ahmed, M.S. & Siegelbaum, S. a., 2009. Recruitment of N-Type Ca²⁺ Channels during LTP Enhances Low Release Efficacy of Hippocampal CA1 Perforant Path Synapses. *Neuron*, 63(3), pp.372–385.
- Akerboom, J., Chen, T.-W., Wardill, T.J., Tian, L., Marvin, J.S., Mutlu, S., Calderon, N.C., Esposti, F., Borghuis, B.G., Sun, X.R., Gordus, a., Orger, M.B., Portugues, R., Engert, F., Macklin, J.J., Filosa, a., Aggarwal, a., Kerr, R. a., Takagi, R., Kracun, S., Shigetomi, E., Khakh, B.S., Baier, H., Lagnado, L., Wang, S.S.-H., Bargmann, C.I., Kimmel, B.E., Jayaraman, V., Svoboda, K., Kim, D.S., Schreiter, E.R. & Looger, L.L., 2012. Optimization of a GCaMP Calcium Indicator for Neural Activity Imaging. *Journal of Neuroscience*, 32(40), pp.13819–13840.
- Allaman, I., Belanger, M. & Magistretti, P.J., 2011. Astrocyte – neuron metabolic relationships : for better and for worse. *Trends in Neurosciences*, 34(2), pp.76–87.
- Altrock, W.D., Dieck, S., Sokolov, M., Meyer, A.C., Sigler, A., Brakebusch, C., Richter, K., Boeckers, T.M., Potschka, H., Brandt, C., Lo, W., Dresbach, T., Hempelmann, A., Hassan, H., Balschun, D., Frey, J.U., Brandsta, J.H., Garner, C.C., Rosenmund, C. & Gundelfinger, E.D., 2003. Functional Inactivation of a Fraction of Excitatory Synapses in Mice Deficient for the Active Zone Protein Bassoon. *Neuron*, 37, pp.787–800.
- Andersen, P., Bliss, T.V.P. & Skrede, K.K., 1971. Lamellar organization of hippocampal excitatory pathways. *Experimental Brain Research*, 13(2), pp.222–238.
- Anderson, C.M. & Swanson, R. a., 2000. Astrocyte glutamate transport: Review of properties, regulation, and physiological functions. *Glia*, 32(March), pp.1–14.
- Araque, A., Li, N., Doyle, R.T. & Haydon, P.G., 2000. SNARE Protein-Dependent Glutamate Release from Astrocytes. *The Journal of neuroscience*, 20(2), pp.666–673.
- Araque, A., Martin, E.D., Perea, G., Arellano, J.I. & Buno, W., 2002. Synaptically Released Acetylcholine Evokes Ca²⁺ Elevations in Astrocytes in Hippocampal Slices. *The Journal of neuroscience*, 22(7), pp.2443–2450.
- Araque, A., Parpura, V., Sanzgiri, R.P. & Haydon, P.G., 1999. Tripartite synapses : glia , the unacknowledged partner. *Trends in Neurosciences*, 22(5), pp.208–214.
- Ariel, P., Hoppa, M.B. & Ryan, T. a., 2013. Intrinsic variability in Pv, RRP size, Ca²⁺ channel repertoire, and presynaptic potentiation in individual synaptic boutons. *Frontiers in Synaptic Neuroscience*, 5(JAN), pp.1–18.

- Augustine, G.J., Adler, E.M. & Charlton, P., 1991. The Calcium Signal for Transmitter Secretion from Presynaptic Nerve Terminals. *Annals of the New York Academy of Sciences*, 635, pp.365–381.
- Baudier, J., Glasser, N. & Gerard, D., 1986. Ions Binding to S100 Proteins. Calcium and Zinc-binding properties of bovine brain S100aa, S100ab and S100bb protein: Zinc regulates Calcium binding on S100bb protein. *the journal of biological chemistry*, 261(18), pp.8192–8203.
- Benninger, C., Kadis, J. & Prince, D., 1980. Extracellular calcium and potassium changes in hippocampal slices. *Brain Research*, 187, pp.165–182.
- Bergersen, L.H., Morland, C., Ormel, L., Rinholm, J.E., Larsson, M., Wold, J.F.H., Røe, a. T., Stranna, a., Santello, M., Bouvier, D., Ottersen, O.P., Volterra, a. & Gundersen, V., 2012. Immunogold detection of L-glutamate and D-serine in small synaptic-like microvesicles in adult hippocampal astrocytes. *Cerebral Cortex*, 22(July), pp.1690–1697.
- Bergles, D.E. & Jahr, C.E., 1997. Synaptic activation of glutamate transporters in hippocampal astrocytes. *Neuron*, 19, pp.1297–1308.
- Bernardinelli, Y., Haeberli, C. & Chatton, J.Y., 2005. Flash photolysis using a light emitting diode: An efficient, compact, and affordable solution. *Cell Calcium*, 37, pp.565–572.
- Bernardinelli, Y., Muller, D. & Nikonenko, I., 2014. Astrocyte-Synapse Structural Plasticity. *Neural Pasticity*.
- Bernardinelli, Y., Salmon, C., Jones, E. V, Farmer, W.T., Stellwagen, D. & Murai, K.K., 2011. Astrocytes display complex and localized calcium responses to single-neuron stimulation in the hippocampus. *The Journal of neuroscience : the official journal of the Society for Neuroscience*, 31(24), pp.8905–8919.
- Berridge, M.J., 1993. Inositol trisphosphate and calcium signalling. *Nature*, 361, pp.315–325.
- Bezprozvanny, I., Watras, J. & Ehrlich, B.E., 1991. Bell-shaped calcium-response curves of Ins(1,4,5)P₃- and calcium-gated channels from endoplasmic reticulum of cerebellum. *Nature*, 351, pp.751–754.
- Bezzi, P., Gundersen, V., Galbete, J.L., Seifert, G., Steinhäuser, C., Pilati, E. & Volterra, A., 2004. Astrocytes contain a vesicular compartment that is competent for regulated exocytosis of glutamate. *Nature neuroscience*, 7(6), pp.613–620.
- Biglami, A. & Dahl, D., 1974. Astrocyte specific protein and radial glia in the cerebral cortex of the newborn rat. *Nature*, 252, pp.55–56.
- Blatow, M., Caputi, A., Burnashev, N., Monyer, H. & Rozov, A., 2003. Ca²⁺ Buffer Saturation Underlies Paired Pulse Facilitation in Calbindin-D28k-Containing Terminals. *Neuron*, 38, pp.79–88.
- Bliss, T.V.P. & Collingridge, G.L., 1993. A synaptic model of memory: long-term potentiation in the hippocampus. *Nature*, 361(1), pp.31–39.
- Bliss, T.V.P. & Collingridge, G.L., 2013. Expression of NMDA receptor-dependent LTP in the hippocampus: bridging the divide. *Molecular brain*, 6(5).
- Bliss, T.V.P. & Lomo, T., 1973. Long lasting potentiation of synaptic transmission in the dentate area of the anaesthetized rabbit following stimulation of the perforant path. *journal of physiology*, 232, pp.331–356.
- Boitano, S., Dirksen, E.R. & Sanderson, M.J., 1992. Intercellular Propagation of Calcium Waves Mediated by Inositol Trisphosphate. *Science*, 258, pp.292–295.

- Boitier, E., Rea, R. & Duchen, M., 1999. Modulation of the propagation of intracellular calcium waves by mitochondria in rat cortical astrocytes. *Journal of cell biology*, 145(4), pp.795–808.
- Bourinet, E., Soong, T.W.A.H., Stea, A. & Snutch, T.P., 1996. Determinants of the G protein-dependent opioid modulation of neuronal calcium channels. *PNAS*, 93(February), pp.1486–1491.
- Bushong, E. a, Martone, M.E., Jones, Y.Z. & Ellisman, M.H., 2002. Protoplasmic astrocytes in CA1 stratum radiatum occupy separate anatomical domains. *The Journal of neuroscience : the official journal of the Society for Neuroscience*, 22(1), pp.183–192.
- Cao, Y. & Tsien, R.W., 2010. Different Relationship of N- and P/Q-Type Ca²⁺ Channels to Channel-Interacting Slots in Controlling Neurotransmission at Cultured Hippocampal Synapses. *The Journal of Neuroscience*, 30(13), pp.4536–4546.
- Di Castro, M.A., Chuquet, J., Liaudet, N., Bhaukaurally, K., Santello, M., Bouvier, D., Tiret, P. & Volterra, A., 2011. Local Ca²⁺ detection and modulation of synaptic release by astrocytes. *Nature Neuroscience*, 14(10), pp.1276–1284.
- Catterall, W. a. & Few, A.P., 2008. Calcium Channel Regulation and Presynaptic Plasticity. *Neuron*, 59(6), pp.882–901.
- Charles, A.C., Merrill, J.E., Dirksen, E.R. & Sanderson, M.J., 1991. Intercellular Signaling in Glial Cells : Calcium Waves and Oscillations in Response to Mechanical Stimulation and G lutamate. *Neuron*, 6, pp.983–992.
- Chieriegatti, E., Chicka, M., Chapman, E. & Baldini, G., 2004. SNAP-23 functions in Docking/Fusion of Granules at Low Ca²⁺. *Molecular biology of the cell*, 15(April), pp.1918–1930.
- Christoffersen, G.R.J. & Skibsted, L.H., 1975. Calcium ion activity in physiological salt solutions : influence of anions substituted for chloride. *Comp. Biochem. Physiol.*, 52(A), pp.317–322.
- Condorelli, D., Mudo, G., Trovato-Salinaro, A., Mirone, M., Amato, G. & Belluardo, N., 2002. Connexin-30 mRNA is Up-regulated in Astrocytes and Expressed in Apoptotic Neuronal Cells of Rat Brain Following Kainate-Induced Seizures. *molecular and cellular neuroscience*, 21, pp.94–113.
- Cornell-Bell, a. H., Finkbeiner, S.M., Cooper, M.S. & Smith, S.J., 1990. Glutamate induces calcium waves in cultured astrocytes: long-range glial signaling. *Science (New York, N. Y.)*, 247(4941), pp.470–473.
- Cornell-Bell, a. H., Thomas, P.G. & Smith, S.J., 1990. The Excitatory Neurotransmitter Glutamate Causes Filopodia Formation in Cultured Hippocampal Astrocytes. *Glia*, 3, pp.322–334.
- Crunelli, V., Carmignoto, G. & Steinhäuser, C., 2015. Novel astrocyte targets : New Avenues for the Therapeutic Treatment of Epilepsy. *The Neuroscientist*, 21(1), pp.62–83.
- Currie, K.P.M. & Fox, A.P., 2002. Differential facilitation of N- and P/Q-type calcium channels during trains of action potential-like waveforms. *The Journal of physiology*, 539(2), pp.419–431.
- Dai, H., Shin, O., Machius, M., Tomchick, D.R., Südhof, T.C. & Rizo, J., 2004. Structural basis for the evolutionary inactivation of Ca²⁺ binding to synaptotagmin 4. *Nature structural and molecular biology*, 11(9), pp.844–849.

- Dakin, K., Zhao, Y. & Li, W.-H., 2005. LAMP, a new imaging assay of gap junctional communication unveils that Ca²⁺ influx inhibits cell coupling. *Nature methods*, 2(1), pp.55–62.
- Danbolt, N.C., Storm-Mathisen, J. & Kanner, B.I., 1992. An [Na⁺ + K⁺]coupled L-glutamate transporter purified from rat brain is located in glial cell processes. *Neuroscience*, 51(2), pp.295–310.
- Dani, J.W., Chernjavsky, a. & Smith, S.J., 1992. Neuronal activity triggers calcium waves in hippocampal astrocyte networks. *Neuron*, 8, pp.429–440.
- Davies, A., Kadurin, I., Alvarez-laviada, A., Douglas, L., Nieto-rostro, M., Bauer, C.S., Pratt, W.S. & Dolphin, A.C., 2010. The $\alpha 2 \delta$ subunits of voltage-gated calcium channels form GPI-anchored proteins, a posttranslational modification essential for function. *PNAS*, 107(4), pp.1654–1659.
- Davydova, D., Marini, C., King, C., Klueva, J., Bischof, F., Romorini, S., Montenegro-Venegas, C., Heine, M., Schneider, R., Schröder, M.S., Altmann, W.D., Henneberger, C., Rusakov, D. a., Gundelfinger, E.D. & Fejtova, A., 2014. Bassoon specifically controls presynaptic P/Q-type Ca²⁺ channels via RIM-binding protein. *Neuron*, 82, pp.181–194.
- Delvendahl, I., Jablonski, L., Baade, C., Matveev, V., Neher, E. & Hallermann, S., 2015. Reduced endogenous Ca²⁺ buffering speeds active zone Ca²⁺ signaling. *PNAS*, pp.E3075–3084.
- Deng, W., Aimone, J.B. & Gage, F.H., 2010. New neurons and new memories: how does adult hippocampal neurogenesis affect learning and memory? *Nature Reviews Neuroscience*, 11(March), pp.339–350.
- Derouiche, A. & Frotscher, M., 1991. Astroglial processes around identified glutamatergic synapses contain glutamine synthetase: evidence for transmitter degradation. *Brain Research*, 552, pp.346–350.
- Dieck, S., Sanmartí-vila, L., Langnaese, K., Richter, K., Kindler, S., Soyke, A., Wex, H., Smalla, K., Kämpf, U., Fränzer, J., Stumm, M., Garner, C.C. & Gundelfinger, E.D., 1998. Bassoon, a Novel Zinc-finger CAG/Glutamine-repeat Protein Selectively Localized at the Active Zone of Presynaptic Nerve Terminals. *the journal of cell biology*, 142(2), pp.499–509.
- Dietz, G.P.H. & Bähr, M., 2005. Peptide-enhanced cellular internalization of proteins in neuroscience. *Brain Research Bulletin*, 68(1-2), pp.103–114.
- Dunn, K.M., Hill-eubanks, D.C., Liedtke, W.B. & Nelson, M.T., 2013. TRPV4 channels stimulate Ca²⁺ induced Ca²⁺ release in astrocytic endfeet and amplify neurovascular coupling responses. *PNAS*, 110(15), pp.6157–6162.
- Dutar, P., Rascol, O. & Lamour, Y., 1989. omega-Conotoxin GVIA blocks synaptic transmission in the CA1 field of the hippocampus. *European Journal of Pharmacology*, 174(2-3), pp.261–266.
- Ellis-Davies, G.C.R., 2008. Neurobiology with caged calcium. *Chemical Reviews*, 108, pp.1603–1613.
- Faas, G.C., Raghavachari, S., Lisman, J.E. & Mody, I., 2011. Calmodulin as a direct detector of Ca²⁺ signals. *Nature neuroscience*, 14(3), pp.301–304.
- Faas, G.C., Schwaller, B., Vergara, J.L. & Mody, I., 2007. Resolving the fast kinetics of cooperative binding: Ca²⁺ buffering by calretinin. *PLoS Biology*, 5(11), pp.2646–2660.
- Fiacco, T.A., Agulhon, C., Taves, S.R., Petravicz, J., Casper, K.B., Dong, X., Chen, J. & McCarthy, K.D., 2007. Selective Stimulation of Astrocyte Calcium In Situ Does Not Affect Neuronal Excitatory Synaptic Activity. *Neuron*, 54, pp.611–626.

- Floyd, C.L., Gorin, F. a. & Lyeth, B.G., 2005. Mechanical strain injury increases intracellular sodium and reverses Na⁺/Ca²⁺ exchange in cortical astrocytes. *Glia*, 51(1), pp.35–46.
- Foskett, J.K., White, C., Cheung, K. & Mak, D.D., 2007. Inositol Trisphosphate Receptor Ca²⁺ Release Channels. *Physiological Reviews*, 87, pp.593–658.
- Francis, D., Stergiopoulos, K., Ek-Vitorín, J.F., Cao, F.L., Taffet, S.M. & Delmar, M., 1999. Connexin diversity and gap junction regulation by pHi. *Developmental genetics*, 24(July 1998), pp.123–136.
- Freund, T.F. & Buzsáki, G., 1996. Interneurons of the hippocampus. *Hippocampus*, 6(4), pp.347–470.
- Giaume, C., Fromaget, C., Aoumari, A.E., Cordier, J., Glowinski, J. & Gros, D., 1991. Gap Junctions in cultured astrocytes : single-channel currents and characterization of channel-forming protein. *Neuron*, 6(1), pp.133–143.
- Giaume, C. & McCarthy, K.D., 1996. Control of gap-junctional communication in astrocytic networks. *Trends in Neurosciences*, 19, pp.319–325.
- Giaume, C. & Venance, L., 1998. Intercellular calcium signalling and Gap Junctional Communication in Astrocytes. *Glia*, 24, pp.50–64.
- Gilbert, J.A., 2012. Chapter 20: Cytoplasmic calcium buffering. In *Calcium Signalling. Advances in Experimental Medicine and Biology*. pp. 483–498.
- Graf, E., Valakh, V., Wright, C., Wu, C., Liu, Z., Zhang, Y. & DiAntonio, A., 2012. RIM promotes calcium channel accumulation at active zones of the drosophila neuromuscular junction. *The Journal of Neuroscience*, 32(47), pp.16586–16596.
- Grimaldi, M., Atzori, M., Ray, P. & Alkon, D.L., 2001. Mobilization of calcium from intracellular stores, potentiation of neurotransmitter-induced calcium transients, and capacitative calcium entry by 4-aminopyridine. *The Journal of neuroscience*, 21(9), pp.3135–3143.
- Grynkiewicz, G., Poenie, M. & Tsien, R., 1985. A new generation of calcium indicators with greatly improved fluorescence properties. *Journal of Biological Chemistry*, 260(6), pp.3440–3450.
- Gurney, A.M., 1987. Flash photolysis of caged compounds. *Microelectrode Techniques: The Plymouth Workshop Handbook*, pp.389–406.
- Guthrie, P.B., Knappenberger, J., Segal, M., Bennett, M.V.L., Charles, A.C. & Kater, S.B., 1999. ATP Released from Astrocytes Mediates Glial Calcium Waves. *The Journal of neuroscience*, 19(2), pp.520–528.
- Haber, M., Zhou, L. & Murai, K.K., 2006. Cooperative Astrocyte and Dendritic Spine Dynamics at Hippocampal Excitatory Synapses. *the journalof neuroscience*, 26(35), pp.8881–8891.
- Halassa, M.M., Fellin, T., Takano, H., Dong, J. & Haydon, P.G., 2007. Synaptic Islands Defined by the Territory of a Single Astrocyte. *Journal of Neuroscience*, 27(24), pp.6473–6477.
- Halassa, M.M., Florian, C., Fellin, T., Munoz, J.R., Abel, T., Haydon, P.G. & Frank, M.G., 2009. Astrocytic modulation of sleep homeostasis and cognitive consequence of sleep loss. *Neuron*, 61(2), pp.213–219.
- Hallermann, S., Fejtova, A., Schmidt, H., Weyhersmüller, A., Silver, R.A., Gundelfinger, E.D. & Eilers, J., 2010. Bassoon speeds vesicle reloading at a central excitatory synapse. *Neuron*, 68(4), pp.710–723.
- Hamilton, N.B. & Attwell, D., 2010. Do astrocytes really exocytose neurotransmitters? *Nature reviews. Neuroscience*, 11(4), pp.227–238.

- Han, X., Chen, M., Wang, F., Windrem, M., Wang, S., Shanz, S., Xu, Q., Oberheim, N.A., Bekar, L., Betstadt, S., Silva, A.J., Takano, T., Goldman, S. a. & Nedergaard, M., 2013. Forebrain engraftment by human glial progenitor cells enhances synaptic plasticity and learning in adult mice. *Cell Stem Cell*, 12(3), pp.342–353.
- Han, Y., Kaeser, P., Sudhof, T. & Schneggenburger, R., 2011. RIM Determines Ca²⁺ Channel Density and Vesicle Docking at the Presynaptic Active Zone. *Neuron*, 69, pp.304–316.
- Haustein, M.D., Kracun, S., Lu, X., Shih, T., Jackson-Weaver, O., Tong, X., Xu, J., Yang, X.W., O'Dell, T.J., Marvin, J.S., Ellisman, M.H., Bushong, E.A., Looger, L.L. & Khakh, B.S., 2014. Conditions and constraints for astrocyte calcium signaling in the hippocampal mossy fiber pathway. *Neuron*, 82(2), pp.413–429.
- Heinemann, U., Gabriel, S., Jauch, R., Schulze, K., Kivi, a, Eilers, a, Kovacs, R. & Lehmann, T.N., 2000. Alterations of glial cell function in temporal lobe epilepsy. *Epilepsia*, 41 Suppl 6(10), pp.S185–S189.
- Heja, L., Brabas, P., Nyitrai, G., Kekesi, K.A., Lasztozci, B., Toke, O., Tarkanyi, G., Madsen, K., Schousboe, A., Dobolyi, A., Palkovits, M. & Kardos, J., 2009. Glutamate Uptake Triggers Transporter-Mediated GABA Release from Astrocytes. *PLoS ONE*, 4(9), p.e7153.
- Henneberger, C., Papouin, T., Oliet, S.H.R. & Rusakov, D. a, 2010. Long-term potentiation depends on release of D-serine from astrocytes. *Nature*, 463(January), pp.232–236.
- Hepp, R., Perraut, M., Chasserot-golaz, S., Galli, T., Aunis, D., Langley, K. & Grant, N.J., 1999. Cultured Glial Cells Express the SNAP-25 Analogue SNAP-23. *Glia*, 27, pp.181–187.
- Hibino, H., Pironkova, R., Onwumere, O., Vologodskaia, M., Hudspeth, A.J. & Lesage, F., 2002. RIM Binding Proteins (RBPs) Couple Rab3-Interacting Molecules (RIMs) to Voltage-Gated Ca²⁺ Channels. *Neuron*, 34, pp.411–423.
- Hirase, H., Qian, L., Bartho, P. & Buzsáki, G., 2004. Calcium Dynamics of Cortical Astrocytic Networks In Vivo. *PLoS Biology*, 2(4), pp.494–499.
- Holtzclaw, L.A., Pandhit, S., Bare, D.A.N.J., Mignery, G.A. & Russell, J.T., 2002. Astrocytes in Adult Rat Brain Express Type 2 Inositol 1,4,5-Triphosphate Receptors. *Glia*, 39, pp.69–84.
- Hoppa, M.B., Lana, B., Margas, W., Dolphin, A.C. & Ryan, T.A., 2012. $\alpha 2\delta$ expression sets presynaptic calcium channel abundance and release probability. *Nature*, 486(7401), pp.122–125.
- Houades, V., Koulakoff, A., Ezan, P., Seif, I. & Giaume, C., 2008. Gap Junction-Mediated Astrocytic Networks in the Mouse Barrel Cortex. *The Journal of Neuroscience*, 28(20), pp.5207–5217.
- Huang, Y.H., Sinha, S.R., Tanaka, K., Rothstein, J.D. & Bergles, D.E., 2004. Astrocyte Glutamate transporters regulate metabotropic Glutamate Receptor-Mediated Excitation of Hippocampal Interneurons. *The Journal of Neuroscience*, 24(19), pp.4551–4559.
- Inchauspe, C., Martini, F.J., Forsythe, I.D. & Uchitel, O.D., 2004. Functional Compensation of P/Q by N-Type Channels Blocks Short-Term Plasticity at the Calyx of Held Presynaptic Terminal. *The Journal of Neuroscience*, 24(46), pp.10379–10383.

- Isobe, T., Takahashi, K. & Okuyama, T., 1984. SIOOa0 (aa) Protein Is Present in Neurons of the Central and Peripheral Nervous System. *Journal of Neurochemistry*, 43(5), pp.1494–1496.
- Iwasaki, S., Momiyama, A., Uchitel, O.D. & Takahashi, T., 2000. Developmental Changes in Calcium Channel Types Mediating Central Synaptic Transmission. *The Journal of Neuroscience*, 20(1), pp.59–65.
- Jahn, K. & Hille, C., 2014. Asante Calcium Green and Asante Calcium Red--novel calcium indicators for two-photon fluorescence lifetime imaging. *PloS one*, 9(8), p.e105334.
- Jalonen, T., Margraf, R., Wielt, D., Charniga, C., Linne, M. & Kimelberg, H.K., 1997. Serotonin induces inward potassium and calcium currents in rat cortical astrocytes. *Brain Research*, 758, pp.69–82.
- Jessen, K.R., 2004. Glial cells. *The International Journal of Biochemistry & Cell Biology*, 36(10), pp.1861–1867.
- Jourdain, P., Bergersen, L.H., Bhaukaurally, K., Bezzi, P., Santello, M., Domercq, M., Matute, C., Tonello, F., Gundersen, V. & Volterra, A., 2007. Glutamate exocytosis from astrocytes controls synaptic strength. *Nature neuroscience*, 10(3), pp.331–339.
- Kaesler, P.S., Deng, L., Wang, Y., Dulubova, I., Liu, X., Rizo, J. & Su, T.C., 2011. RIM Proteins Tether Ca²⁺ Channels to Presynaptic Active Zones via a Direct PDZ-Domain Interaction. *Cell*, 144, pp.282–295.
- Kanemaru, K., Sekiya, H., Xu, M., Satoh, K., Kitajima, N., Yoshida, K., Okubo, Y., Sasaki, T., Moritoh, S., Hasuwa, H., Mimura, M., Horikawa, K., Matsui, K., Nagai, T., Iino, M. & Tanaka, K.F., 2014. In Vivo Visualization of Subtle, Transient, and Local Activity of Astrocytes Using an Ultrasensitive Ca²⁺ Indicator. *CellReports*, 8, pp.311–318.
- Kang, J., Jiang, L., Goldman, S.A. & Nedergaard, M., 1998. Astrocyte-mediated potentiation of inhibitory synaptic transmission. *Nature neuroscience*, 1(8), pp.683–692.
- Kang, J., Kang, N., Lovatt, D., Torres, A., Zhao, Z., Lin, J. & Nedergaard, M., 2008. Cx43 hemichannels are permeable to ATP. *The Journal of neuroscience*, 28(18), pp.4702–4711.
- Katona, G., Szalay, G., Maák, P., Kaszás, A., Veress, M., Hillier, D., Chiovini, B., Vizi, E.S., Roska, B. & Rózsa, B., 2012. Fast two-photon in vivo imaging with three-dimensional random-access scanning in large tissue volumes. *Nature Methods*, 9(2), pp.201–208.
- Katz, B. & Miledi, R., 1967. Ionic requirements of synaptic transmitter release. *Nature*, 215, p.651.
- Kettenmann, H. & Verkhratsky, A., 2008. Neuroglia: the 150 years after. *Trends in Neurosciences*, 31(12), pp.653–659.
- Kofuji, P. & Newman, E. a., 2004. Potassium buffering in the central nervous system. *Neuroscience*, 129, pp.1045–1056.
- Koulakoff, A., Ezan, P. & Giaume, C., 2008. Neurons Control the Expression of Connexin 30 and Connexin 43 in Mouse Cortical Astrocytes. *Glia*, 56, pp.1299–1311.
- Kreft, M., Stenovec, M., Rupnik, M., Grilc, S., Kržan, M., Potokar, M., Pangršič, T., Haydon, P.G. & Zorec, R., 2004. Properties of Ca²⁺-dependent exocytosis in cultured astrocytes. *Glia*, 46(4), pp.437–445.

- Krzysztof, L., Akwasi, M., Escamilla, P., Chan, P., Xenia, A. & Goldberg, M., 2013. Synthesis and properties of Asante Calcium Red- a novel family of long excitation wavelength calcium indicators. *Cell calcium*, 54(4), pp.1199–1216.
- Kuchibhotla, K. V, Lattarulo, C.R., Hyman, B.T. & Bacskai, B.J., 2009. Synchronous hyperactivity and intercellular calcium waves in astrocytes in Alzheimer mice. *Science (New York, N.Y.)*, 323, pp.1211–1215.
- Kuffler, S.W., Nicholls, J.G. & Orkand, R.K., 1966. Physiological properties of glial cells in the central nervous system of amphibia. *Journal of neurophysiology*, 29, pp.768–787.
- Kuga, N., Sasaki, T., Takahara, Y., Matsuki, N. & Ikegaya, Y., 2011. Large-Scale Calcium Waves Traveling through Astrocytic Networks In Vivo. *The Journal of neuroscience*, 31(7), pp.2607–2614.
- Kunishima, N., Shimada, Y., Tsuji, Y., Sato, T., Yamamoto, M., Kumasaka, T., Nakanishi, S., Jingami, H. & Morikawa, K., 2000. Structural basis of glutamate recognition by a dimeric metabotropic glutamate receptor. *Nature*, 407(6807), pp.971–977.
- Lancaster, B. & Batchelor, a M., 2000. Novel action of BAPTA series chelators on intrinsic K⁺ currents in rat hippocampal neurones. *The Journal of physiology*, 522 Pt 2(2000), pp.231–246.
- Lavrentovich, M. & Hemkin, S., 2008. A mathematical model of spontaneous calcium(II) oscillations in astrocytes. *Journal of Theoretical Biology*, 251, pp.553–560.
- Lee, S., Schwaller, B. & Neher, E., 2000. Kinetics of Ca²⁺ binding to parvalbumin in bovine chromaffin cells : implications for [Ca²⁺] transients of neuronal dendrites. *journal of physiology*, 525(2), pp.419–432.
- Lenhossek, M. von, 1895. Die Stutzzellen des Ruckenmarkes. In *Der Feinere Bau des Nervensystems im Lichte neuester Forschungen*. pp. 177–245.
- Lind, B., Brazhe, A.R., Jessen, S., Tan, F.C.C. & Lauritzen, M.J., 2013. Rapid stimulus-evoked astrocyte Ca²⁺ elevations and hemodynamic responses in mouse somatosensory cortex in vivo. *PNAS*, pp.E4678–4687.
- Liu, K., Siebert, M., Mertel, S., Knoche, E., Wegener, S., Wichmann, C., Matkovic, T., Muhammad, K., Depner, H., Mettke, C., Buckers, J., Hell, S., Muller, M., Davis, G.W., Schmitz, D. & Sigrist, S.J., 2011. RIM-Binding Protein, a Central Part of the Active Zone, Is Essential for Neurotransmitter Release. *Science*, 334(December), pp.1565–1570.
- Marchaland, J., Cali, C., Voglmaier, S.M., Li, H., Regazzi, R. & Edwards, R.H., 2008. Fast Subplasma Membrane Ca²⁺ Transients Control Exo- Endocytosis of Synaptic-Like Microvesicles in Astrocytes. *The Journal of Neuroscience*, 28(37), pp.9122–9132.
- Martin, R., Bajo-Graneras, R., Moratalla, R., Perea, G. & Araque, A., 2015. Circuit-specific signaling in astrocyte-neuron networks in basal ganglia pathways. *Science*, 349(6249), pp.730–735.
- Mathiisen, T.M., Lehre, K.P., Danbolt, N.C. & Ottersen, O.L.E.P., 2010. The Perivascular Astroglial Sheath Provides a Complete Covering of the Brain Microvessels : An Electron Microscopic 3D Reconstruction. *Glia*, 58(March), pp.1094–1103.
- Matyash, V. & Kettenmann, H., 2010. Heterogeneity in astrocyte morphology and physiology. *Brain Research Reviews*, 63(1-2), pp.2–10.

- Medvedev, N., Popov, V., Henneberger, C., Kraev, I., Rusakov, D.A. & Stewart, M.G., 2014. Glia selectively approach synapses on thin dendritic spines. *Phil. Trans. R. Soc. B*, 369.
- Meinrenken, C.J., Borst, J.G.G. & Sakmann, B., 2002. Calcium secretion coupling at calyx of held governed by nonuniform channel-vesicle topography. *The Journal of neuroscience*, 22(5), pp.1648–1667.
- Meinrenken, C.J., Borst, J.G.G. & Sakmann, B., 2003. Local routes revisited: the space and time dependence of the Ca²⁺ signal for phasic transmitter release at the rat calyx of Held. *The Journal of physiology*, 547(3), pp.665–689.
- Min, R. & Nevian, T., 2012. Astrocyte signaling controls spike timing–dependent depression at neocortical synapses. *Nature Neuroscience*, 15(5), pp.746–753.
- Mintz, I.M., Venema, V.J., Swiderek, K.M., Lee, T.D., Bean, B.P. & Adams, M.E., 1992. P-type calcium channels blocked by the spider toxin omega-Aga-IVA. *Nature*, 355(6363), pp.827–829.
- Molotkov, D., Zobova, S., Miguel, J. & Khiroug, L., 2013. Calcium-induced outgrowth of astrocytic peripheral processes requires actin binding by Profilin-1. *Cell Calcium*, 53, pp.338–348.
- Morquette, P., Verdier, D., Kadala, A., Féthière, J., Philippe, A.G., Robitaille, R. & Kolta, A., 2015. An astrocyte-dependent mechanism for neuronal rhythmogenesis. *Nature neuroscience*, 18(6), pp.844–854.
- Muller, M.S., Obel, L.F., Waagepetersen, H.S., Schousboe, A. & Bak, L.K., 2013. Complex Actions of Ionomycin in Cultured Cerebellar Astrocytes Affecting Both Calcium-Induced Calcium Release and Store-Operated Calcium Entry. *Neurochemical Research*, 38, pp.1260–1265.
- Mulligan, S.J. & MacVicar, B. a, 2004. Calcium transients in astrocyte endfeet cause cerebrovascular constrictions. *Nature*, 431(September), pp.195–199.
- Nagerl, V., Novo, D., Mody, I. & Vergara, J.L., 2000. Binding Kinetics of Calbindin-D28k Determined by Flash Photolysis of CAged Ca²⁺. *Biophysical journal*, 79, pp.3009–3018.
- Nagy, J.I., Lynn, B.D., Tress, O., Willecke, K. & Rash, J.E., 2011. Connexin26 expression in brain parenchymal cells demonstrated by targeted connexin ablation in transgenic mice. *European Journal of Neuroscience*, 34(2), pp.263–271.
- Nagy, J.I., Patel, D., Ochalski, P.A.Y. & Stelmack, G.L., 1999. Connexin30 in rodent, cat and human brain: selective expression in grey matter astrocytes, co-localization with connexin43 at gap-junctions and late developmental appearance. *Neuroscience*, 88(2), pp.447–468.
- Nakanishi, S., 1992. Molecular diversity of glutamate receptors and implications for brain function. *Science (New York, N. Y.)*, 258(5082), pp.597–603.
- Naraghi, M. & Neher, E., 1997. Linearized Buffered Ca²⁺ Diffusion in Microdomains and Its Implications for Calculation of [Ca²⁺] at the Mouth of a Calcium Channel. *The Journal of Neuroscience*, 17(18), pp.6961–6973.
- Navarrete, M. & Araque, A., 2010. Endocannabinoids Potentiate Synaptic Transmission through Stimulation of Astrocytes. *Neuron*, 68, pp.113–126.
- Navarrete, M., Perea, G., de Sevilla, D.F., Gómez-Gonzalo, M., Núñez, A., Martín, E.D. & Araque, A., 2012. Astrocytes mediate in vivo cholinergic-induced synaptic plasticity. *PLoS Biology*, 10(2).
- Nedergaard, M., 1994. Direct signaling from astrocytes to neurons in cultures of mammalian brain cells. *Science (New York, N. Y.)*, 263(5154), pp.1768–1771.

- Neher, B.Y.E. & Augustine, G.J., 1992. Calcium Gradients and Buffers in Bovine Chromaffin Cells. *Journal of physiology*, 450, pp.273–301.
- Nett, W.J., Oloff, S.H. & McCarthy, K.D., 2002. Hippocampal astrocytes in situ exhibit calcium oscillations that occur independent of neuronal activity. *Journal of neurophysiology*, 87, pp.528–537.
- Newman, E.A., Frambach, D.A. & Odette, L.L., 1984. Control of extracellular potassium levels by retinal glial cell K siphoning. *Science*, 225(4667), pp.1174–1175.
- Nilsson, M., Eriksson, P.S., Ronnback, L.R. & Hansson, E., 1993. GABA Induces Ca²⁺ Transients in Astrocytes. *Neuroscience*, 54(3), pp.605–614.
- Oberheim, N.A., Takano, T., Han, X., He, W., Lin, J.H.C., Xu, Q., Wyatt, J.D., Pilcher, W., Ojemann, J.G., Bruce, R., Goldman, S. a & Nedergaard, M., 2009. uniquely hominid features of adult human astrocytes. *Journal of Neuroscience*, 29(10), pp.3276–3287.
- Ogata, K.Ã. & Kosaka, T., 2002. Structural and Quantitative Analysis of Astrocytes in the Mouse Hippocampus. *Neuroscience*, 113(1), pp.221–233.
- Oliet, S.H.R., Piet, R. & Poulain, D.A., 2001. Control of glutamate clearance and synaptic efficacy by glial coverage of neurons. *Science*, 292(May), pp.923–926.
- Otsu, Y., Couchman, K., Lyons, D.G., Collot, M., Agarwal, A., Mallet, J., Pfrieger, F.W., Bergles, D.E. & Charpak, S., 2015. Calcium dynamics in astrocyte processes during neurovascular coupling. *Nature neuroscience*, 18(2), pp.210–218.
- Panatier, A., Theodosis, D.T., Mothet, J.P., Touquet, B., Pollegioni, L., Poulain, D. a. & Oliet, S.H.R., 2006. Glia-Derived d-Serine Controls NMDA Receptor Activity and Synaptic Memory. *Cell*, 125, pp.775–784.
- Panatier, A., Vallée, J., Haber, M., Murai, K.K., Lacaille, J.C. & Robitaille, R., 2011. Astrocytes are endogenous regulators of basal transmission at central synapses. *Cell*, 146, pp.785–798.
- Pannasch, U., Freche, D., Dallérac, G., Ghézali, G., Escartin, C., Ezan, P., Cohen-salmon, M., Benchenane, K., Abudara, V., Dufour, A., Lübke, J.H.R., Déglon, N., Knott, G., Holcman, D. & Rouach, N., 2014. Connexin 30 sets synaptic strength by controlling astroglial synapse invasion. *Nature neuroscience*, 17(4), pp.549–558.
- Parpura, V., Basarsky, T.A., Liu, F., Jeftinija, K., Jeftinija, S. & Haydon, P.G., 1994. Glutamate-mediated-astrocyte-neuron signalling. *Nature*, 369, pp.744–747.
- Parpura, V., Fang, Y., Basarsky, T., Jahn, R. & Haydon, P.G., 1995. Expression of synaptobrevin II, cellubrevin and syntaxin but not SNAP-25 in cultured astrocytes. *FEBS*, 377, pp.489–492.
- Parpura, V. & Haydon, P.G., 2000. Physiological astrocytic calcium levels stimulate glutamate release to modulate adjacent neurons. *Proceedings of the National Academy of Sciences of the United States of America*, 97(15), pp.8629–8634.
- Parpura, V. & Haydon, P.G., 1999. “Uncaging” using optical fibers to deliver UV light directly to the sample. *Croatian medical journal*, 40(3), pp.340–345.
- Parri, H.R. & Crunelli, V., 2003. The role of Ca²⁺ in the generation of spontaneous astrocytic Ca²⁺ oscillations. *Neuroscience*, 120, pp.979–992.
- Parri, H.R., Gould, T.M. & Crunelli, V., 2001. Spontaneous astrocytic Ca²⁺ oscillations in situ drive NMDAR-mediated neuronal excitation. *Nature neuroscience*, 4, pp.803–812.

- Pasti, L., Volterra, a, Pozzan, T. & Carmignoto, G., 1997. Intracellular calcium oscillations in astrocytes: a highly plastic, bidirectional form of communication between neurons and astrocytes in situ. *The Journal of neuroscience : the official journal of the Society for Neuroscience*, 17(20), pp.7817–7830.
- Patrushev, I., Gavrilov, N., Turlapov, V. & Semyanov, A., 2013. Subcellular location of astrocytic calcium stores favors extrasynaptic neuron-astrocyte communication. *Cell Calcium*, 54(5), pp.343–349.
- Pellerin, L. & Magistretti, P.J., 1994. Glutamate uptake into astrocytes stimulates aerobic glycolysis : A mechanism coupling neuronal activity to glucose utilization. *PNAS*, 91(October), pp.10625–10629.
- Perea, G. & Araque, A., 2007. Astrocytes potentiate transmitter release at single hippocampal synapses. *Science (New York, N. Y.)*, 317(August), pp.1083–1086.
- Perea, G. & Araque, A., 2005. Glial calcium signaling and neuron-glia communication. *Cell Calcium*, 38, pp.375–382.
- Petravicz, J., Boyt, K.M., Mccarthy, K.D. & Stanwood, G., 2014. Astrocyte IP3R2-dependent Ca²⁺ signaling is not a major modulator of neuronal pathways governing behavior. *frontiers in behavioral neuroscience*, 8(November), p.384.
- Petravicz, J., Fiacco, T.A. & Mccarthy, K.D., 2008. Loss of IP3 Receptor-Dependent Ca²⁺ Increases in Hippocampal Astrocytes Does Not Affect Baseline CA1 Pyramidal Neuron Synaptic Activity. *The Journal of Neuroscience*, 28(19), pp.4967–4973.
- Piet, R., Vargova, L., Sykova, E., Poulain, D.A. & Oliet, H.R., 2004. Physiological contribution of the astrocytic environment of neurons to intersynaptic crosstalk. *PNAS*, 101(7), pp.2151–2155.
- Porter, J.T. & McCarthy, K.D., 1997. Astrocytic neurotransmitter receptors in situ and in vivo. *Progress in Neurobiology*, 51, pp.439–455.
- Porter, J.T. & McCarthy, K.D., 1996. Hippocampal Astrocytes In Situ Respond to Glutamate Released from Synaptic Terminals. *The Journal of neuroscience*, 16(16), pp.5073–5081.
- Poser, C. Von, Ichtchenko, K. & Shao, X., 1997. The Evolutionary Pressure to Inactivate. *the journal of biological chemistry*, 272(22), pp.14314–14319.
- Pressman, B.C., 1976. Biological applications of ionophores. *Annual Review of Biochemistry*, 45, pp.501–530.
- Ramon y Cajal, S. & translation by Azoulay, L., 1909. *Histologie du systeme nerveux de l'homme et des vertebres*,
- Rasooli-Nejad, S., Palygin, O., Lalo, U. & Pankratov, Y., 2014. Cannabinoid receptors contribute to astroglial Ca²⁺ -signalling and control of synaptic plasticity in the neocortex. *Phil. Trans. R. Soc. B*, 369(1654).
- Reeves, A., Shigetomi, E. & Khakh, B.S., 2011. Bulk loading of calcium indicator dyes to study astrocyte physiology: key limitations and improvements using morphological maps. *Journal of Neuroscience*, 31(25), pp.9353–9358.
- Reichenbach, A., Derouiche, A. & Kirchhoff, F., 2010. Morphology and dynamics of perisynaptic glia. *Brain Research Reviews*, 63, pp.11–25.
- Reid, C. a., Bekkers, J.M. & Clements, J.D., 2003. Presynaptic Ca²⁺ channels: A functional patchwork. *Trends in Neurosciences*, 26(12), pp.683–687.
- Rizzuto, R. & Pozzan, T., 2006. Microdomains of Intracellular Ca²⁺ : Molecular Determinants and Functional Consequences. *Physiological reviews*, 86(1), pp.369–408.

- Rose, C.R. & Ransom, B.R., 1997. Regulation of intracellular sodium in cultured rat hippocampal neurones. *The Journal of physiology*, 499 (Pt 3, pp.573–587.
- Rosenberg, P. a & Aizenman, E., 1989. Hundred-fold increase in neuronal vulnerability to glutamate toxicity in astrocyte-poor cultures of rat cerebral cortex. *Neuroscience letters*, 103, pp.162–168.
- Ross, W.N., 2012. Understanding calcium waves and sparks in central neurons. *Nature Reviews Neuroscience*, 13(March), pp.157–168.
- Rothstein, J.D., Dykes-Hoberg, M., Pardo, C. a., Bristol, L. a., Jin, L., Kuncl, R.W., Kanai, Y., Hediger, M. a., Wang, Y., Schielke, J.P. & Welty, D.F., 1996. Knockout of glutamate transporters reveals a major role for astroglial transport in excitotoxicity and clearance of glutamate. *Neuron*, 16, pp.675–686.
- Rothstein, J.D., Martin, L., Levey, A.I., Dykes-hoberg, M., Jin, L., Wu, D., Nash, N. & Kuncl, R.W., 1994. localization of Neuronal and Glial Glutamate Transporters. *Neuron*, 13, pp.713–725.
- Rusakov, D. a., 2015. Disentangling calcium-driven astrocyte physiology. *Nature Reviews Neuroscience*, 16(4), pp.226–233.
- Rusakov, D. a., Bard, L., Stewart, M.G. & Henneberger, C., 2014. Diversity of astroglial functions alludes to subcellular specialisation. *Trends in Neurosciences*, 37(4), pp.228–242.
- Rzagalinski, B. a, Weber, J.T., Willoughby, K. a & Ellis, E.F., 1998. Intracellular free calcium dynamics in stretch-injured astrocytes. *Journal of neurochemistry*, 70(6), pp.2377–2385.
- Saleem, H., Tovey, S.C., Molinski, T.F. & Taylor, C.W., 2014. Interactions of antagonists with subtypes of inositol 1,4,5-triphosphate (IP3) receptor. *British Journal of Pharmacology*, 171, pp.3298–3312.
- Schell, M.J., Molliver, M.E. & Snyder, S.H., 1995. D-serine, an endogenous synaptic modulator: localization to astrocytes and glutamate-stimulated release. *Proceedings of the National Academy of Sciences of the United States of America*, 92(April), pp.3948–3952.
- Schiavo, G., Benfenati, F., Poulain, B., Rossetto, O., Polverino, P., DasGuptal, B. & Montecucco, C., 1992. tetanus and botulinum-B neurotoxins block neurotransmitter release by proteolytic cleavage of synaptobrevin. *Nature*, 359, pp.832–835.
- Schneggenburger, R. & Neher, E., 2000. Intracellular calcium dependence of transmitter release rates at a fast central synapse. *Nature*, 406, pp.889–893.
- Schneggenburger, R. & Neher, E., 2005. Presynaptic calcium and control of vesicle fusion. *Current Opinion in Neurobiology*, 15, pp.266–274.
- Schoepp, D.D., Goldsworthy, J., Johnson, B.G., Salhoff, C.R. & Baker, S.R., 1994. 3,5-Dihydroxyphenylglycine Is a Highly Selective Agonist for Phosphoinositide-Linked Metabotropic Glutamate Receptors in the Rat Hippocampus. *Journal of neurochemistry*, 63(2), pp.769–772.
- Scholz, P. & Miller, J., 1995. Developmental Changes in Presynaptic Calcium Channels Coupled to Glutamate Release in Cultured Rat Hippocampal Neurons. *The Journal of Neuroscience*, 15(6), pp.4612–4617.
- Schools, G.P. & Kimelberg, H.K., 1999. mGluR3 and mGluR5 are the predominant metabotropic glutamate receptor mRNAs expressed in hippocampal astrocytes acutely isolated from young rats. *Journal of Neuroscience Research*, 58(4), pp.533–543.

- Schubert, V., Bouvier, D. & Volterra, A., 2011. SNARE protein expression in synaptic terminals and astrocytes in the adult hippocampus: A comparative analysis. *Glia*, 59, pp.1472–1488.
- Scott, R. & Rusakov, D. a, 2006. Main determinants of presynaptic Ca²⁺ dynamics at individual mossy fiber-CA3 pyramidal cell synapses. *The Journal of neuroscience : the official journal of the Society for Neuroscience*, 26(26), pp.7071–7081.
- Scoville, W.B. & Milner, B., 1957. Loss of recent memory after bilateral hippocampal lesions. *journal of Neurology Neurosurgery Psychiatry*, 20, pp.11–21.
- Sheng, J., He, L., Zheng, H., Xue, L., Luo, F., Shin, W., Sun, T., Kuner, T., Yue, D.T. & Wu, L.-G., 2012. Calcium-channel number critically influences synaptic strength and plasticity at the active zone. *Nature Neuroscience*, 15(7), pp.998–1006.
- Sheppard, C.A., Simpson, P.B., Sharp, A.H., Nucifora, F.C., Ross, C.A., Lange, D. & Russell, J.T., 1997. Comparison of Type 2 Inositol 1,4,5-Trisphosphate Receptor Distribution and Subcellular Ca²⁺ Release Sites that Support Waves Ca²⁺ in Cultured Astrocytes. *Journal of neurochemistry*, 68(6), pp.2317–2327.
- Shigetomi, E., Bowser, D.N., Sofroniew, M. V. & Khakh, B.S., 2008. Two Forms of Astrocyte Calcium Excitability Have Distinct Effects on NMDA Receptor-Mediated Slow Inward Currents in Pyramidal Neurons. *Journal of Neuroscience*, 28(26), pp.6659–6663.
- Shigetomi, E., Bushong, E. a, Hausteiner, M.D., Tong, X., Jackson-Weaver, O., Kracun, S., Xu, J., Sofroniew, M. V, Ellisman, M.H. & Khakh, B.S., 2013. Imaging calcium microdomains within entire astrocyte territories and endfeet with GCaMPs expressed using adeno-associated viruses. *The Journal of general physiology*, 141, pp.633–47.
- Shigetomi, E., Jackson-Weaver, O., Huckstepp, R.T., O'Dell, T.J. & Khakh, B.S., TRPA1 Channels Are Regulators of Astrocyte Basal Calcium Levels and Long-Term Potentiation via Constitutive D-Serine Release. *Journal of Neuroscience*, 33(24), pp.10143–10153.
- Shigetomi, E., Tong, X., Kwan, K.Y., Corey, D.P. & Khakh, B.S., 2012. TRPA1 channels regulate astrocyte resting calcium and inhibitory synapse efficacy through GAT-3. *Nature Neuroscience*, 15(1), pp.70–80.
- Sibille, J., Pannasch, U. & Rouach, N., 2013. Astroglial potassium clearance contributes to short-term plasticity of synaptically evoked currents at the tripartite synapse. *journal of physiology*, 592(1), pp.87–102.
- Sloviter, R.S., 1989. Calcium-Binding Protein (Calbindin-D28k) and Parvalbumin Immunocytochemistry : Localization in the Rat Hippocampus With Specific Reference to the Selective Vulnerability of Hippocampal Neurons to Seizure Activity. *the journal of comparative neurology*, 280, pp.183–196.
- Sloviter, R.S. & Lømo, T., 2012. Updating the lamellar hypothesis of hippocampal organization. *frontiers in neural circuits*, 6(December), pp.1–16.
- Söhl, G., Odermatt, B., Maxeiner, S., Degen, J. & Willecke, K., 2004. New insights into the expression and function of neural connexins with transgenic mouse mutants. *Brain Research Reviews*, 47, pp.245–259.
- Sontheimer, H., 1994. Voltage-dependent ion channels in glial cells. *Glia*, 11, pp.156–172.
- Srinivasan, R., Huang, B.S., Venugopal, S., Johnston, A.D., Chai, H., Zeng, H., Golshani, P. & Khakh, B.S., 2015. Ca²⁺ signaling in astrocytes from *Ip3r2*^{-/-} mice in brain slices and during startle responses in vivo. *Nature Neuroscience*, 18(5), pp.708–717.

- Steinhauser, C., 1993. Electrophysiologic characteristics of glial cells. *Hippocampus*, 3, pp.113–123.
- Steinhauser, C., Berger, T., Frotscher, M. & Kettenmann, H., 1992. Heterogeneity in the Membrane Current Pattern of Identified Glial Cells in the Hippocampal Slice. *European Journal of Neuroscience*, 4(February), pp.472–484.
- Sudhof, T., 2012. The Presynaptic Active Zone. *Neuron*, 75, pp.11–25.
- Südhof, T.C., 2012. Calcium control of neurotransmitter release. *Cold Spring Harbor Perspectives in Biology*, 4(1).
- Sugita, S., Shin, O., Han, W., Lao, Y. & Su, T.C., 2002. Synaptotagmins form a hierarchy of exocytotic Ca²⁺ sensors with distinct Ca²⁺ affinities. *the EMBO journal*, 21(3), pp.270–280.
- Sun, M.Y., Devaraju, P., Xie, A.X., Holman, I., Samones, E., Murphy, T.R. & Fiacco, T. a., 2014. Astrocyte calcium microdomains are inhibited by Bafilomycin A1 and cannot be replicated by low-level Schaffer collateral stimulation in situ. *Cell Calcium*, 55(1), pp.1–16.
- Sun, W., McConnell, E., Pare, J.-F., Xu, Q., Chen, M., Peng, W., Lovatt, D., Han, X., Smith, Y. & Nedergaard, M., 2013. Glutamate-dependent neuroglial calcium signaling differs between young and adult brain. *Science (New York, N.Y.)*, 339, pp.197–200.
- Svoboda, K. & Yasuda, R., 2006. Principles of Two-Photon Excitation Microscopy and Its Applications to Neuroscience. *Neuron*, 50, pp.823–839.
- Systema, J., Vroom, J.M., de Grauw, C.J. & Gerritsen, H.C., 1998. Time-gated fluorescence lifetime imaging and microvolume spectroscopy using two-photon excitation. *Journal of Microscopy*, 191(July), pp.39–51.
- Szatkowski, M., Barbour, B. & Attwell, D., 1990. Non-vesicular release of glutamate from glial cells by reversed electrogenic glutamate uptake. *Nature*, 348, pp.443–446.
- Szmacinski, H., Gryczynski, I. & Lakowicz, J., 1993. Calcium-dependent fluorescence lifetimes of Indo-1 for one and two-photon excitation of fluorescence. *photochemistry and photobiology*, 58(3), pp.341–345.
- Tanaka, M., Shih, P.-Y., Gomi, H., Yoshida, T., Nakai, J., Ando, R., Furuichi, T., Mikoshiba, K., Semyanov, A. & Itohara, S., 2013. Astrocytic Ca²⁺ signals are required for the functional integrity of tripartite synapses. *Molecular brain*, 6(1), p.6.
- Tang, W., Szokol, K., Jensen, V., Enger, R., Trivedi, C.A., Hvalby, Ø., Helm, P.J., Looger, L.L., Sprengel, X.R. & Nagelhus, E.A., 2015. Stimulation-Evoked Ca²⁺ Signals in Astrocytic Processes at Hippocampal CA3 – CA1 Synapses of Adult Mice Are Modulated by Glutamate and ATP. *The Journal of Neuroscience*, 35(7), pp.3016–3021.
- Thrane, A., Thrane, V., Zeppenfeld, D., Lou, N., Xu, Q., Nagelhus, E.A. & Nedergaard, M., 2012. General anesthesia selectively disrupts astrocyte calcium signaling in the awake mouse cortex. *PNAS*, 109(46), pp.18974–18979.
- Tønnesen, J. & Nägerl, U.V., 2013. Two-color STED imaging of synapses in living brain slices. In *Nanoimaging, Methods in Molecular Biology*. pp. 65–80.
- Torres, a., Wang, F., Xu, Q., Fujita, T., Dobrowolski, R., Willecke, K., Takano, T. & Nedergaard, M., 2012. Extracellular Ca²⁺ Acts as a Mediator of Communication from Neurons to Glia. *Science Signaling*, 5(208).

- Toyoshima, T., Yamagami, S., Ahmed, B., Jin, L., Miyamoto, O., Itano, T., Tokuda, M., Matsui, H. & Hatase, O., 1996. Expression of calbindin-D28k by reactive astrocytes in gerbil hippocampus after ischemia. *Neuroreport*, 7(13), pp.2087–2091.
- Ullah, G., Jung, P. & Cornell-Bell, a. H., 2006. Anti-phase calcium oscillations in astrocytes via inositol (1, 4, 5)-trisphosphate regeneration. *Cell Calcium*, 39, pp.197–208.
- Vaarmann, A., Gandhi, S. & Abramov, A.Y., 2010. Dopamine induces Ca²⁺ signaling in astrocytes through reactive oxygen species generated by monoamine oxidase. *Journal of Biological Chemistry*, 285, pp.25018–25023.
- Ventura, R. & Harris, K.M., 1999. Three-Dimensional Relationships between Hippocampal Synapses and Astrocytes. *The Journal of Neuroscience*, 19(16), pp.6897–6906.
- Verderio, C., Pozzi, D., Pravettoni, E., Inverardi, F., Schenk, U., Coco, S., Proux-Gillardeaux, V., Galli, T., Rossetto, O., Frassoni, C. & Matteoli, M., 2004. SNAP-25 modulation of calcium dynamics underlies differences in GABAergic and glutamatergic responsiveness to depolarization. *Neuron*, 41(4), pp.599–610.
- Verkhatsky, A. & Kettenmann, H., 1996. Calcium signalling in glial cells. *Trends in neurosciences*, 19(8), pp.346–52.
- Verkhatsky, A. & Parpura, V., 2014. Store-operated calcium entry in neuroglia. *Neuroscience Bulletin*, 30(1), pp.125–133.
- Verkhatsky, A., Rodriguez, J. & Parpura, V., 2012. Calcium signaling in astroglia. *Molecular and Cellular Endocrinology*, 353, pp.45–56.
- Verkhatsky, A. & Steinhäuser, C., 2000. Ion channels in glial cells. *Brain Research Reviews*, 32, pp.380–412.
- Virchow, R., 1856. Über das granulierte Ansehen der Wandungen der Gehirnvventrikel. In *Gesammelte Abhandlungen zur wissenschaftlichen Medizin, Frankfurt*. pp. 885–891.
- Volterra, A., Liaudet, N. & Savtchouk, I., 2014. Astrocyte Ca(2+) signalling: an unexpected complexity. *Nature reviews. Neuroscience*, 15(5), pp.327–35.
- Vuyst, E. De, Wang, N., Decrock, E., Bock, M. De, Vinken, M., Moorhem, M. Van, Lai, C., Culot, M., Rogiers, V., Cecchelli, R., Naus, C.C., Evans, W.H. & Leybaert, L., 2009. Calcium regulation of connexin 43 hemichannels in C6 glioma and glial cells. *Cell Calcium*, 46, pp.176–187.
- Wadel, K., Neher, E. & Sakaba, T., 2007. The Coupling between Synaptic Vesicles and Ca²⁺ Channels Determines Fast Neurotransmitter Release. *Neuron*, 53, pp.563–575.
- Wagner, L.E. & Yule, D.I., 2012. Differential regulation of the InsP3 receptor type-1 and -2 single channel properties by InsP3, Ca²⁺ and ATP. *The Journal of physiology*, 590, pp.3245–59.
- Wallraff, A., Heinemann, U., Theis, M., Willecke, K. & Steinhäuser, C., 2006. The Impact of Astrocytic Gap Junctional Coupling on Potassium Buffering in the Hippocampus. *The Journal of neuroscience*, 26(20), pp.5438–5447.
- Wang, X., Lou, N., Xu, Q., Tian, G.-F., Peng, W.G., Han, X., Kang, J., Takano, T. & Nedergaard, M., 2006. Astrocytic Ca²⁺ signaling evoked by sensory stimulation in vivo. *Nature neuroscience*, 9(6), pp.816–823.
- Wang, X., Takano, T. & Nedergaard, M., 2009. Astrocyte Calcium Signaling: Mechanism and Implications for Functional Btain Imaging. *Methods Molecular Biology*, 489, pp.93–109.

- Wang, Y., Okamoto, M., Schmitz, F., Hofmann, K. & Sudhof, T.C., 1997. Rim is a putative Rab3 effector in regulating synaptic-vesicle fusion. *Nature*, 388, pp.593–598.
- Wang, Z., Tymianski, M., Jones, O.T. & Nedergaard, M., 1997. Impact of cytoplasmic calcium buffering on the spatial and temporal characteristics of intercellular calcium signals in astrocytes. *The Journal of neuroscience : the official journal of the Society for Neuroscience*, 17(19), pp.7359–7371.
- Wilms, C.D. & Eilers, J., 2007. Photo-physical properties of Ca²⁺-indicator dyes suitable for two-photon fluorescence-lifetime recordings. *Journal of Microscopy*, 225(September 2006), pp.209–213.
- Wilms, C.D., Schmidt, H. & Eilers, J., 2006. Quantitative two-photon Ca²⁺ imaging via fluorescence lifetime analysis. *Cell Calcium*, 40, pp.73–79.
- Witcher, M.R., Park, Y.D., Lee, M.R., Sharma, S., Harris, K.M. & Kirov, S., 2010. Three-Dimensional Relationships Between Perisynaptic Astroglia and Human Hippocampal Synapses. *Glia*, 58, pp.572–587.
- Woo, D.H., Han, K.-S., Shim, J.W., Yoon, B.-E., Kim, E., Bae, J.Y., Oh, S.-J., Hwang, E.M., Marmorstein, A.D., Bae, Y.C., Park, J.-Y. & Lee, C.J., 2012. TREK-1 and Best1 Channels Mediate Fast and Slow Glutamate Release in Astrocytes upon GPCR Activation. *Cell*, 151(1), pp.25–40.
- Wu, L.G. & Saggau, P., 1994. Pharmacological identification of two types of presynaptic voltage-dependent calcium channels at CA3-CA1 synapses of the hippocampus. *The Journal of Neuroscience*, 14(9), pp.5613–5622.
- Wu, Y.-W., Tang, X., Arizono, M., Bannai, H., Shih, P.-Y., Dembitskaya, Y., Kazantsev, V., Tanaka, M., Itohara, S., Mikoshiba, K. & Semyanov, A., 2014a. Spatiotemporal calcium dynamics in single astrocytes and its modulation by neuronal activity. *Cell calcium*, 55, pp.119–29.
- Wu, Y.-W., Tang, X., Arizono, M., Bannai, H., Shih, P.-Y., Dembitskaya, Y., Kazantsev, V., Tanaka, M., Itohara, S., Mikoshiba, K. & Semyanov, A., 2014b. Spatiotemporal calcium dynamics in single astrocytes and its modulation by neuronal activity. *Cell calcium*, 55(2014), pp.119–29.
- Xu, J., Pang, Z.P., Shin, O.-H. & Südhof, T.C., 2009. Synaptotagmin-1 functions as a Ca²⁺ sensor for spontaneous release. *Nature neuroscience*, 12(6), pp.759–766.
- Yamamoto, T., Ochalski, A., Hertzberg, E.L. & Nagy, J.I., 1990. On the Organization of Astrocytic Gap Junctions in rat Brain as Suggested by LM and EM Immunohistochemistry of connexin 43 Expression. *the journal of comparative neurology*, 302, pp.853–883.
- Yasuda, R., Nimchinsky, E.A., Scheuss, V., Pologruto, T.A., Oertner, T.G., Sabatini, B.L. & Svoboda, K., 2004. Imaging calcium concentration dynamics in small neuronal compartments. *Science Signaling*, 219, pp.1–20.
- Ye, Z., Wyeth, M.S., Baltan-tekkok, S. & Ransom, B.R., 2003. Functional Hemichannels in Astrocytes : A Novel Mechanism of Glutamate Release. *The Journal of neuroscience*, 23(9), pp.3588–3596.
- Zhang, Q., Fukuda, M., Van Bockstaele, E., Pascual, O. & Haydon, P.G., 2004. Synaptotagmin IV regulates glial glutamate release. *Proceedings of the National Academy of Sciences of the United States of America*, 101(25), pp.9441–9446.
- Zheng, K., Bard, L., Reynolds, J.P., King, C., Jensen, T.P., Gourine, A. V & Rusakov, D.A., 2015. Time-Resolved Imaging Reveals Heterogeneous Landscapes of Nanomolar Ca²⁺ in Neurons and Astroglia. *Neuron*, 88, pp.277–288.

Zhou, M., Schools, G.P. & Kimelberg, H.K., 2006. Development of GLAST(+) astrocytes and NG2(+) glia in rat hippocampus CA1: mature astrocytes are electrophysiologically passive. *Journal of neurophysiology*, 95(August 2005), pp.134–143.

Zurborg, S., Yurgionas, B., Jira, J.A., Caspani, O. & Heppenstall, P.A., 2007. Direct activation of the ion channel TRPA1 by Ca²⁺. *Nature neuroscience*, 10(3), pp.277–279.